Heavy ion irradiation as a proxy to neutron irradiation in impure Fe and Fe-Cr alloys



Luke Hewitt
Corpus Christi College
University of Oxford

A thesis submitted for the degree of
Doctor of Philosophy

Michaelmas Term 2018

Abstract

The realisation of nuclear fusion energy will require materials that can withstand high doses of neutron irradiation, and one class of candidate materials for structural applications is reduced-activation ferritic-martensitic (RAFM) steels containing around 9% Cr. The present lack of a fusion neutron source has meant that much of the research into radiation damage has been conducted using specimens irradiated in fission test reactors, or by using heavy ion irradiation as a simulation method. This work explores details of the use of this emulation technique, alongside the effect of composition and impurities on radiation damage in these materials.

Beam rastering is often employed during heavy ion irradiation in order to deliver a more uniform dose across the target area in comparison to continuous irradiation with a defocused beam, but this practice has been reported to alter the radiation-induced microstructural changes. This work investigated this in Fe and Fe-Cr alloys, using nanoindentation. No difference in post-irradiation hardness was observed between samples irradiated with a rastered or defocussed beam.

A direct comparison of the microstructure and mechanical properties of heavy ion and neutron irradiated Fe-9Cr samples was made, and it was found that the segregation to dislocation loops and clustering of impurity elements Si and P reported in the neutron irradiated specimen was also present in the ion irradiated specimen. The α' precipitation reported after neutron irradiation did not occur after ion irradiation. The post-irradiation increase in hardness and yield stress of both samples were found to be the same, measured by nanoindentation and microcantilever testing. An increase in hardness of 0.88 ± 0.21 and 0.81 ± 0.26 GPa was found in the ion and neutron irradiated specimens respectively.

The increase in hardness for the neutron irradiated specimen was found to be less then the 1.5 ± 0.28 GPa reported for an identically irradiated Fe-6Cr sample.

The impact of carbon concentration on irradiation hardening in Fe was investigated by ion irradiating a high purity Fe sample containing regions of varying carbon concentration. Two samples were irradiated at two different dose rates, but no dose rate effect was observed. The increase in hardness however was found to increase with increasing carbon concentration, with a maximum increase of around 3 times that observed in pure Fe.

This work has identified some limitations of and future challenges for the use of heavy ion irradiation as a surrogate to neutron irradiation in the absence of a dedicated fusion materials testing facility.

Preface

This thesis describes work carried out by the author in the Department of Materials, University of Oxford from October 2013 to December 2018 under the supervision of Prof. Steve G. Roberts and Dr. Chris D. Hardie. Funding was provided by the Culham Centre for Fusion Energy (CCFE) in the form of a CASE studentship.

No part of this thesis has been previously submitted for a degree at this or any other university. The work of other authors has been drawn upon and has been referenced and acknowledged in the text. A list of references is given at the end of the thesis.

Acknowledgements

Firstly, I would like to thank my supervisors Prof. Steve Roberts and Dr. Chris Hardie for their continual support, guidance, and encouragement throughout my PhD. Despite having many other commitments (and retiring), they would both regularly go the extra mile to help me and for this I am grateful.

This work would not have been possible without the assistance of many members of the department. I would like to thank all those from electron microscopy for training, technical support, and advice. I would also like to thank all those in the atom probe group, in particular Dr. Tomas Martin and Dr. Maria Auger for help with sample preparation and LEAP training, and Dr. Daniel Haley and Dr. Andrew London for useful discussions and help with analysis. I also thank Laurie Walton for help in the workshop, and Bob Lloyd, Tony Wheeler and Paula Topping for their assistance in using the furnaces.

My thanks also go to the staff at the Surrey Ion Beam Centre and JANNuS irradiation facilities for making the ion irradiation experiments possible, to Bob Odette at UCSB for providing access to the neutron irradiated sample, and to staff at CCFE and CAES for assistance in handling it.

Thank you to my friends and colleagues in MFFP, Watanabe Office, and from college for interesting discussions and for making my time in Oxford so enjoyable.

Thank you also to my friends at home in 😌, P5, and Gothic Collectables for keeping me sane.

And finally to my family, I will always be grateful for your continued support and encouragement.

Contents

1 Introduction **10**

2 Literature Review **16**

2.1 Displacement Damage 16

2.1.1 Quantifying Dose 16

2.1.2 Displacement Cascades 18

2.2 Radiation Damage in Fe & Fe-Cr 21

2.2.1 Dislocation Loops 21

2.2.2 Void Growth & Swelling 23

2.2.3 Phase Stability 24

2.2.4 Mechanical Properties 29

2.3 Influence of Carbon on Radiation Damage in Fe 35

2.3.1 Carbon - Point Defect Interactions 35

2.3.2 Carbon - Loop Interactions 37

2.3.3 Mechanical Properties 38

2.3.4 Carbon Contamination During Ion Irradiation 40

2.4 Neutron-atypical Aspects of Heavy Ion Irradiation 42

2.4.1 Recoil Energy Spectrum 42
2.4.2 Dose Rate 49
2.4.3 Injected Interstitials 63
2.4.4 Transmutation Gases 72
2.4.5 Beam Rastering 78
2.5 Heavy Ion vs Neutron Irradiation Comparison Experiments 93
2.5.1 Summary 97
2.6 Summary & Work Outline 98

3 Materials & Methods 100

3.1 Nanoindentation 100
3.1.1 Introduction 100
3.1.2 Instrumentation 101
3.1.3 Data Analysis 102
3.2 Microcantilevers 108
3.2.1 Introduction 108
3.2.2 Manufacture 109
3.2.3 Measurement 110
3.2.4 Testing 112
3.2.5 Simple Beam Theory Analysis 116
3.2.6 Finite Element Analysis 120
3.3 Size Effects 127
3.3.1 Mechanisms of Plasticity Size Effects 127
3.3.2 Size Effects in Nanoindentation & Microcantilevers 129

3.4 Atom Probe Tomography 130
3.4.1 Introduction 130
3.4.2 Reconstruction Using Crystallography 132
3.4.3 Crystallography of Features 137
3.4.4 Atom Probe Sample Preparation 139
3.5 SRIM Damage Calculations 141
3.6 Materials 142
3.6.1 EFDA Alloys 142
3.6.2 UCSB Alloy 143
3.6.3 Sample Preparation 144
3.6.4 Irradiation Conditions 144

4 Effect of Beam Rastering on Irradiation Hardening in Fe-Cr alloys 146

4.1 Introduction & Background 146
4.2 Experimental 150
4.2.1 Defocussed Setup 154
4.2.2 Beam Scanning Details 155
4.2.3 Post-Irradiation Analysis 159
4.3 Results 159
4.4 Discussion 163
4.4.1 Dose Rate 163
4.4.2 Beam Rastering 169
4.5 Conclusions 170
4.6 Further Work 171

5 Heavy Ion vs Neutron Irradiation in an Fe-9Cr Alloy 172

5.1 Introduction & Background 172

5.2 Experimental 175

5.2.1 Neutron Irradiation 175

5.2.2 Ion irradiation 175

5.2.3 Post-Irradiation Analysis 181

5.3 Results 183

5.3.1 Nanoindentation 183

5.3.2 Microcantilevers 185

5.3.3 Atom Probe Tomography 200

5.4 Discussion 212

5.4.1 Microstructure 213

5.4.2 Mechanical Properties 222

5.5 Conclusions & Further Work 234

6 Effect of Carbon on Irradiation Hardening in Fe 237

6.1 Introduction & Background 237

6.2 Experimental 239

6.2.1 Materials 239

6.2.2 Ion irradiation 250

6.2.3 Post-Irradiation Analysis 250

6.3 Results & Discussion - Atom Probe Tomography 255

6.3.1 Composition 255

6.3.2 Spatial Distribution of C 265

6.3.3 Nitrogen 269
6.3.4 Carbon Contamination 272
6.4 Results & Discussion - Nanoindentation 274
6.4.1 Unirradiated Behaviour 274
6.4.2 Irradiated Behaviour 276
6.4.3 Dose rate 281
6.5 Conclusions & Future Work 282

7 Summary, Discussion, & Conclusions 284
7.1 Emulation of Irradiation-induced Microstructural Changes 285
7.2 Emulation of Mechanical Property Changes 287
7.3 Effect of Impurities 291
7.4 Conclusions 294
7.5 Recommendations & Considerations 296

Appendices 299

A APT ranges for UCSB Fe-9Cr alloy 300

B Nanoindentation results of Fe-Cr-C alloys 301

Chapter 1

Introduction

Human activities have already caused around 1.0°C of global warming above pre-industrial levels, and this will likely reach 1.5°C by 2030-2052 at the current rate [1]. In order to reduce emissions and limit global temperature rises, a transition away from fossil fuels towards clean, renewable energy sources is required. One such potential energy source is nuclear fusion.

Nuclear fusion is the process that powers the sun, and involves the fusion of two smaller nuclei into a single, larger one. Energy is released due to the difference in total mass between the reactants and the products [2]. High temperatures (i.e. particle energies) and/or pressures are required to facilitate this type of reaction, as the Coulomb forces that act to repel nuclei from each other need to be overcome. The most easily achievable of such reactions at temperatures and pressures attainable under terrestrial conditions is the fusion of two isotopes of hydrogen - deuterium and tritium, to form helium [3], requiring temperatures around 150 million K [4] to occur.

The reaction is shown below [5]:

$$^{2}\mathrm{D} + {}^{3}\mathrm{T} \longrightarrow {}^{4}\mathrm{He}(3.56\mathrm{MeV}) + \mathrm{n}(14.03\mathrm{MeV}) \tag{1.1}$$

At present the most promising way to recreate this process and harness its energy on earth is using a device called a tokomak, where a deuterium-tritium plasma is confined in a toroidal-shaped vacuum vessel using magnetic fields.

One significant challenge to the viability of fusion power is the structural integrity of materials in the environment created by such a device. The 14 MeV neutrons produced in the fusion reaction can collide with atoms from components of the reactor, displacing them from their lattice sites and creating point defects. The unit of dose for this displacement damage is dpa - displacements per atom, the number of times on average each atom is displaced from its lattice site. In addition to displacing atoms, the neutrons can also cause transmutation through nuclear reactions, inducing radioactivity in the material, and producing He and H gas. The overall effect of these processes is to cause hardening, embrittlement, and swelling of the material, which poses a problem for the structural integrity of components. The displacement of atoms and radiation damage are discussed in detail in sections 2.1 and 2.2 respectively.

The expected conditions for structural materials in fusion reactors, alongside those for generation IV fission reactor concepts are shown in figure 1.1. The fusion reactor environment is extreme even by these standards.

A schematic showing the main components in a magnetic confinement fusion reactor is shown in figure 1.2. One class of candidate materials for components in the first wall is reduced-activation ferritic-martensitic steels with Cr contents around 9 wt.%,

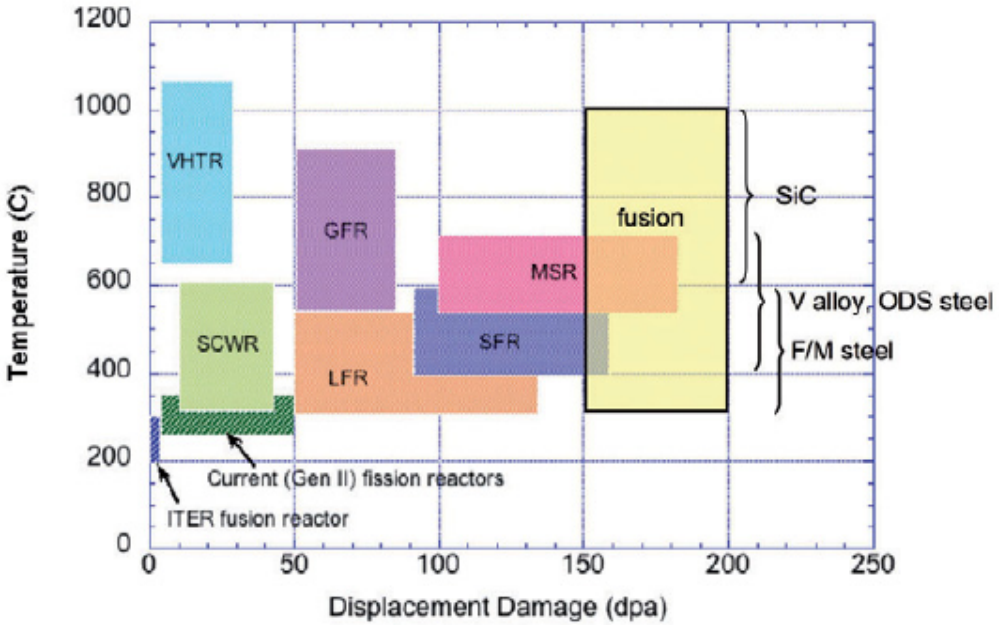


Figure 1.1: The expected conditions to be faced by structural materials in fusion reactors, and a number of generation IV fission reactor concepts. Figure taken from [6].

chosen for their technological maturity [7], superior swelling resistance compared to austenitic steels [7, 8], and low long term radioactivity. Their reduced activation is due to replacement (Mo and Nb with W and V [7]) or careful control (Co, Cu, Ni, Al, N [9]) of the composition with regards to elements that transmutate to highly radioactive or long term radioactive nuclides, which are undesirable in the event of an accident or would prevent recycling or shallow land burial at end of life.

Several authors have highlighted the need for a facility able to recreate fusion-relevant conditions in order to test the performance of materials and components [4, 10, 11], but at present no such facility exists. Currently fission test reactors are used in its place, but differences in neutron energy spectra mean these facilities are not able to recreate the same levels of transmutation gas as will be present in fusion reactors [11]. The effects of transmutation gases are discussed in section 2.4.4.

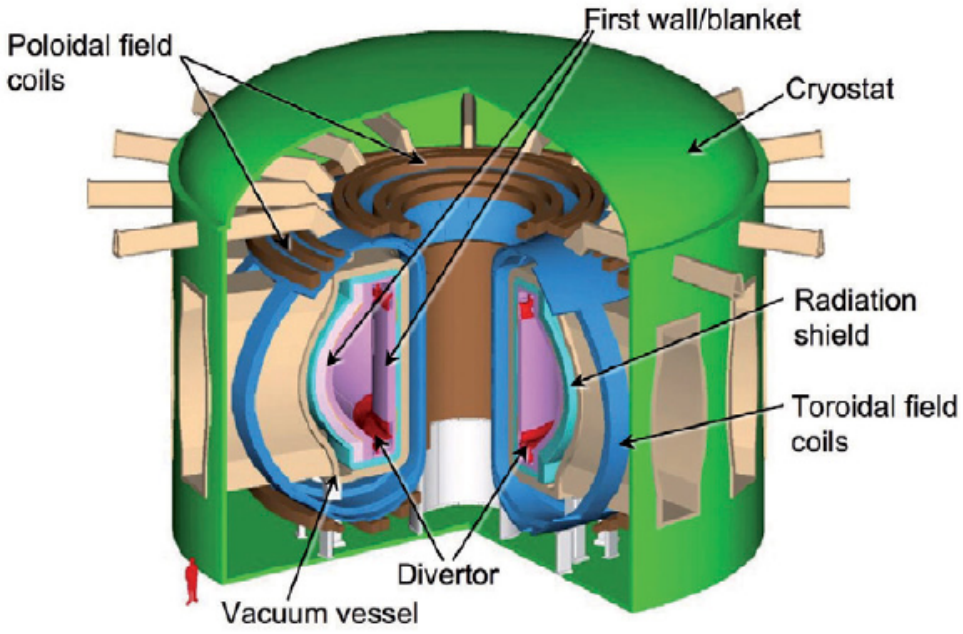


Figure 1.2: Schematic (taken from [6]) showing the main components in a tokomak, with figure in red for scale.

As well as gases, neutron-induced transmutation can produce radioactive nuclides, inducing radioactivity in the material. Analysis of radioactive samples requires specialist facilities such as those at the Materials Research Facility (MRF) at the Culham Centre for Fusion Energy (CCFE), and are generally not present at universities. This, alongside the high costs, long duration, and limited flexibility of neutron irradiation experiments has meant that alternatives have been sought.

Heavy ion irradiation is frequently used to generate the same displacement of atoms as neutron irradiation, but without the induced radioactivity. This technique also offers greater experimental flexibility, is cheaper, and can deliver high doses of damage in much shorter periods of time than fission test reactor neutron irradiation experiments. There are however differences between the two irradiation methods, including dose rate, primary knock-on atom energy spectra, transmutation gas production, the injection of

additional interstitial atoms, and the presence of pulsing due to ion beam rastering; all of which are discussed in section 2.4. These differences raise questions about the equivalence of the damage produced by the two methods.

The work in this thesis is concerned with the use of heavy ion irradiation to simulate neutron irradiation damage in Fe and Fe-Cr alloys, and the influence of composition (including impurities) on this.

Nanoindentation and microcantilever testing are used to measure the hardness, elastic modulus, and yield stress of samples. These properties are key for the design of structural components, defining maximum allowable stresses and safety margins throughout their service, and for deterimination of component lifetimes. Strengthening of materials by irradiation may also lead to embrittlement, and a reduction in the ductile to brittle transition temperature, meaning components may no longer perform as required under operating conditions or during a shutdown period where temperatures are reduced. Microstructures are also examined using atom probe tomography, a technique with excellent chemical resolution able to resolve clusters on the atomic scale.

An overview of the relevant literature is given in chapter 2, and a description of the materials and methods used in this thesis in chapter 3. The experimental chapters then follow.

In chapter 4 the influence of beam scanning on the irradiation hardening of Fe and Fe-Cr alloys if investigated. Recently there has been renewed concern over the use of beam rastering in ion irradiation experiments, with reports of differences in void microstructure between irradiation with defocussed and scanned beams [12, 13]. Beam rastering is a common practice, used to achieve a more uniform dose over the target area compared to a static defocussed beam, and so any influences it has on radiation damage

microstructure need to be understood.

In chapter 5, a direct comparison of the effects of heavy ion and neutron irradiation on the microstructural and mechanical property changes of an Fe-9Cr alloy is made, using atom probe tomography, nanoindentation, and microcantilever testing. Few such direct comparisons have been reported in the literature, particularly concerning the mechanical properties of the fusion-relevant Fe-9Cr composition. The results are compared to a similar study on an Fe-6Cr alloy [14].

Chapter 6 reports the results of a study into the effects of carbon concentration on radiation damage in Fe. Carbon is added to steels to increase strength [15], as well as being a common impurity. It is important to understand its influence on radiation damage, both from the point of view of alloy design, and for when comparing experiments on alloys of differing purity.

All of this work is then summarised and discussed as a whole in chapter 7, where conclusions and suggestions for further work are also given.

Chapter 2

Literature Review

2.1 Displacement Damage

When an irradiating particle (e.g. a proton, neutron, electron, or ion) collides with an atom, it imparts energy T. If this energy is higher than a threshold energy, E_d (on average 40 eV for Fe [16]), the struck atom will be displaced from its lattice site, leaving behind a vacancy and forming a self interstitial atom (SIA) where it comes to rest. This struck atom is called a primary knock-on atom (PKA), and often has sufficient energy to displace additional atoms in further collisions, resulting in a displacement cascade.

2.1.1 Quantifying Dose

In radiation materials science, dose is commonly quantified in terms of displacements per atom (dpa) - the number of displacements produced in a volume divided by the

atomic number density. 1 dpa represents the dose at which each atom is displaced from its lattice site on average once.

It provides a useful measure to compare the *dose* received between irradiation under different neutron energy spectra, or between different irradiating particles, but does not imply equivalence of the *damage* produced, for reasons discussed in detail in section 2.4.

In order to quantify dose, a solution to the damage rate equation must be found [16]:

$$R_d = N \int_{\check{E}}^{\hat{E}} \phi(E_i)\sigma_D(E_i) d E_i \tag{2.1}$$

where N is the atomic density, and $\phi(E_i)$ the energy dependent incident particle flux.

$\sigma_D(E_i)$ is the energy dependent displacement cross-section - the probability for the displacement of lattice atoms by incident particles:

$$\sigma_D(E_i) = \int_{\check{T}}^{\hat{T}} \sigma(E_i, T)\nu(T) dT \tag{2.2}$$

where $\sigma(E_i, T)$ is the probability that a particle of energy E_i will impart energy T to a struck lattice atom, and the $\nu(T)$ is the number of displacements resulting from such a collision.

The most commonly used form of $\nu(T)$ is the so called NRT model, named after its creators Norgett, Robinson and Torrens [17]. It is based on the Kinchen-Pease model [18].

The number of displacements, N_d is given by:

$$N_d = \frac{\kappa E_D}{2E_d} \tag{2.3}$$

where κ is the damage efficiency, which takes into account realistic non hard-sphere scattering and based on simulations of binary collision models has a value of 0.8 [19]. E_D is the damage energy, the energy available to produce displacements by elastic collisions, and is equal to $T - \eta$, where η is the energy lost to electronic excitation. η is calculated using the model of Lindhard [20].

The Monte Carlo code SRIM (stopping range of ions in matter) [21] is commonly used to estimate dpa for ion irradiation experiments. In 2013 Stoller et al. [22] made recommendations for a standardised protocol for its use. This was used in this work, and is described in section 3.5.

2.1.2 Displacement Cascades

The transfer of energy from the irradiating particle to the struck atom, the formation of a displacement cascade and subsequent recombination and clustering of point defects takes place over time and length scales on the order of 10^{-11} s and 10^{-8} m [16, 23]. These time and length scales are inaccessible to physical experiments, so study of this process has relied on modelling efforts.

Stoller et al. [23–25] performed molecular dynamics (MD) calculations to investigate the effects of a number of parameters on defect survival and clustering fractions in Fe. The defect survival fraction is defined as the number of defects present at the end of the simulation divided by those calculated by the NRT model.

The survival fraction is < 1 due to the widespread recombination of vacancies and self-interstitials in the wake of the cascade. Computational resources limit MD simulations to timescales of around 200 ps [24], and additional recombination may take place after this time.

The defect survival fraction was found to decrease with increasing PKA energy up until about 10 keV where it reached a constant value of around 0.3. This is thought to be due to subcascade formation at these energies [25–28], where multiple smaller cascades tend to form rather than one large cascade.

Of the surviving defects for PKA energies above 10 keV, around 60% of the interstitials were found to be clustered, and between 10-50% of the vacancies depending on the clustering criterion.

PKA energy effects are discussed in detail in section 2.4.1.

PKA crystallographic direction was also found to influence in the interstitial surviving fraction for 1 keV cascades, as shown in figure 2.1. Although the error bars are large, more defects were found to survive for PKAs in directions with higher displacement threshold energies [29].

Vörtler et al. [30] and Terentyev et al. [31] investigated the effect of Cr concentration on primary damage formation. The presence of Cr was not found to change the point defect survival or clustered fraction in either study. It was however observed that the fraction of Cr in the surviving self interstitial population was larger than that in the matrix.

5 nm Cr precipitates (see section 2.2.3) were not dissolved or modified in any significant way by 20 keV cascades, and were also found to not affect point defect survival or clustering fractions [30].

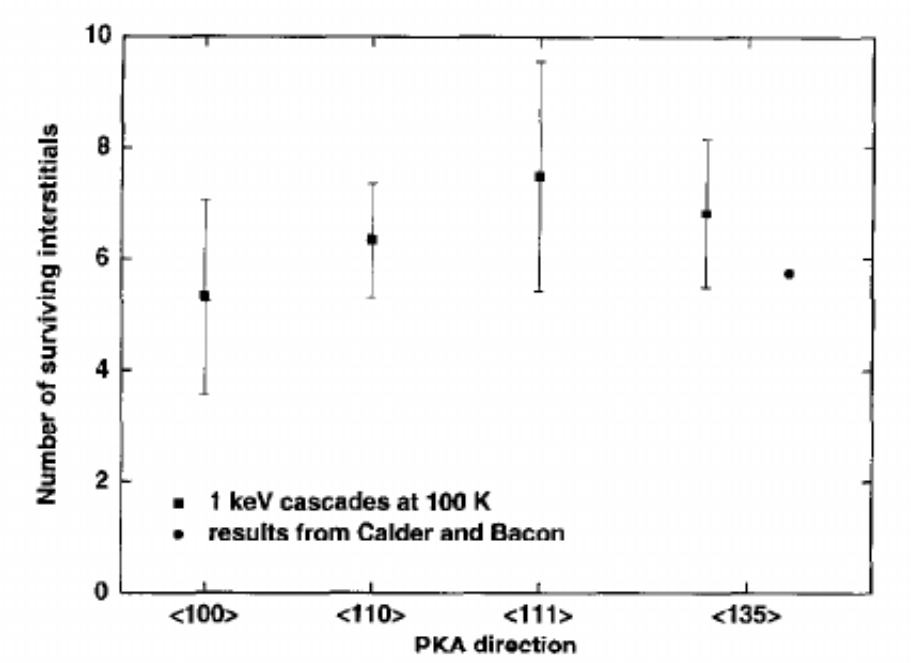


Figure 2.1: Interstitial surviving fraction for different PKA directions in Fe. Averages and standard deviations from 6 cascades. Figure from [23].

2.2 Radiation Damage in Fe & Fe-Cr

The production of individual point defects from displacement cascades is discussed in section 2.1 above. This section discusses the microstructural and material property changes caused by the accumulation and agglomeration of these point defects. The discussion will focus on radiation damage in Fe, with changes due to the presence of Cr highlighted where relevant.

The influence of Cr can be understood through its interaction with individual point defects and clusters. DFT calculations by Olsson et al. [32] found weak interaction between Cr atoms and vacancies, but significant attraction between Cr and interstitials. This is supported by resistivity recovery experiments discussed in [33], where Terentyev et al. use MD simulations to interpret the results.

2.2.1 Dislocation Loops

Below a threshold dose, no damage is visible in TEM in Fe. Robertson et al. [34] found this to be 4×10^{23} neutrons/m^2 in pure Fe at 80 °C. For self-ion irradiation at 40K, Robertson et al. [35] found the threshold dose to be around 10^{16} ions/m^2. More recent in situ heavy ion irradiations (Xe and Fe) of Fe and Fe-Cr alloys at room temperature and 300 °C by Yao et al. [36] found visible damage only above a dose of 10^{16}-10^{17} ions/m^2, corresponding to a dose of around 0.01 dpa.

This threshold dose is thought to correspond to the cascade overlap dose, and that visible loops do not form within single cascades in self-ion irradiation in Fe, only when subsequent cascades interact with debris from previous cascades [35, 36].

Beyond this threshold dose, visible damage takes the form of dislocation loops, typically reported to be interstitial in nature (e.g. [34, 37, 38]). Vacancy loops have been reported by some studies [36, 39, 40], however two of which [36, 40] used ion irradiation with ions heavier than Fe, for which the cascade morphologies are different to those produced by self-ion irradiation [40].

In Fe dislocation loops with Burgers vectors of <100> and $\frac{1}{2}$<111> have been observed. The relative number of each population depends on the temperature, with $\frac{1}{2}$<111> Burgers vectors generally being more prevalent at lower temperatures (<300°C) [34, 35, 38], and <100> Burgers vectors at higher temperatures (≥400°C) [36–38, 41].

Dudarev et al. [42] explained these observations, linking a reduction in the shear stiffness constant $c' = \frac{(c_{11}-c_{12})}{2}$ near the γ phase transition temperature (912°C) to the relative stability of the two types of loop. Their work predicts an increasing preference for <100> loops with increasing temperature beginning at around 300°C, broadly in line with experimental observations [43].

TEM observations of neutron irradiation experiments on Fe-Cr binary alloys in the temperature range 300-450°C have found an increase in the relative population of dislocation loops with $\frac{1}{2}$<111> type Burgers vectors with increasing Cr content [41, 44–46]. Some heavy ion irradiations at 300-460°C [47] and at RT and 300°C [36] found similar trends, but others at 300 °C did not [48].

TEM in-situ self-ion irradiation of thin foils [36, 38] found the number of loops retained and not lost to the surface was strongly orientation dependent in pure Fe but less so in Fe-Cr. This was understood to be due to lower loop mobility in Fe-Cr, due to pinning by Cr. The pinning of dislocation loops and small interstitial clusters by Cr is also supported by MD simulations [49].

Modelling has shown that loops with Burgers vector of <100> type can form through the interaction of two $\frac{1}{2}$<111> loops [50,51]. The increased number of observed $\frac{1}{2}$<111> loops with increasing Cr content can be explained due to pinning by Cr, reducing the number that can interact to form <100> loops. The reduction in loop mobility may also cause fewer $\frac{1}{2}$<111> loops to be lost to surfaces due to image forces [37].

Mean loop size is generally observed to be decreased [41, 45, 46, 52, 53], and the loop number density increased [41, 45, 46, 52–54] with the presence of Cr compared to pure Fe, but no clear dependence on Cr content is seen.

2.2.2 Void Growth & Swelling

The presence of a supersaturation of vacancies during irradiation causes the formation and growth of voids leading to swelling, first observed by Cawthorne and Fulton in 1967 [55] in type 316 stainless steel.

The growth of voids is usually treated using a rate theory approach [56]. Growth occurs once a void reaches a critical size at which it becomes stable, where thermal emission of vacancies is equal to the influx [57]. A typical size is between 0.1-10 nm [57]. This critical size depends on a variety of experimental conditions, including temperature, dose rate (section 2.4.2), the presence of beam scanning or pulsing (section 2.4.5) and the presence of transmutation gases (section 2.4.4) [57–59].

Ferritic steels have been observed to swell considerably less than austenitic steels, primarily due to longer transient regimes (void nucleation) before the onset of steady state swelling (void growth) [8].

The addition of Cr was found to suppress swelling in Fe-Cr binary alloys compared

to pure Fe after neutron irradiation to 5.5-7.1 dpa at 400°C by Porollo et al. [46]. A similar finding was made by Konobeev et al. [52] after neutron irradiation at 400°C to 26 dpa, and by Bhattacharya et al. [60] after single and dual beam heavy ion irradiation at 500°C to >100 dpa.

A compilation of neutron irradiated swelling data for low and high doses with varying Cr contents at around 420°C by Bhattacharya et al. [60] shown in figure 2.2 shows a complex relationship, with peak swelling occurring for around 9%Cr at high doses.

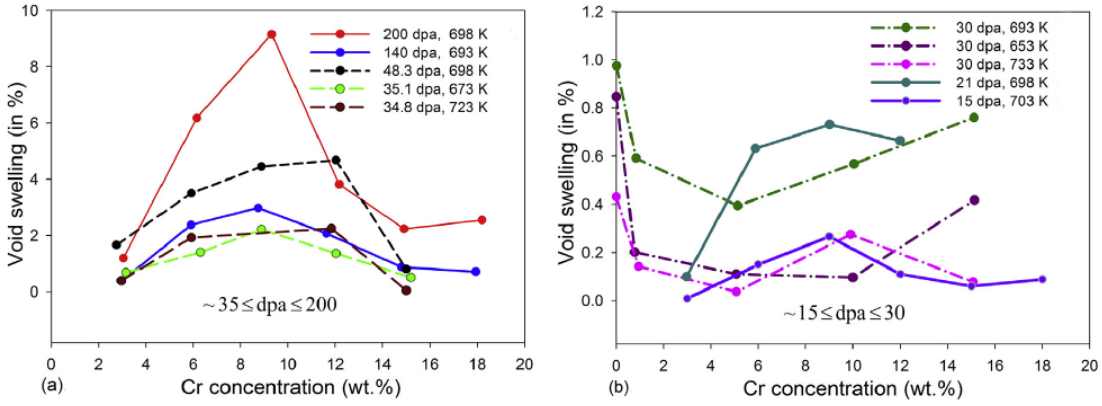


Figure 2.2: Compilation of neutron irradiated swelling data for Fe-Cr alloys at low (b) and high doses (a) by Bhattacharya et al. [60]. Data from [8, 44, 46, 61–63]

2.2.3 Phase Stability

Figure 2.3 shows the CALPHAD handbook phase diagram for the Fe-Cr system [64]. At low temperatures there is a miscibility gap, where the bcc Fe α phases exists alongside a bcc Cr phase α'. The precipitation of Cr in this phase is responsible for 475°C embrittlement [65], and as such it is important that it is avoided in nuclear applications.

The region of the phase diagram of particular interest for nuclear relevant ferritic-martensitic steels is at temperatures 250-500°C, and compositions of 9-12%Cr [66].

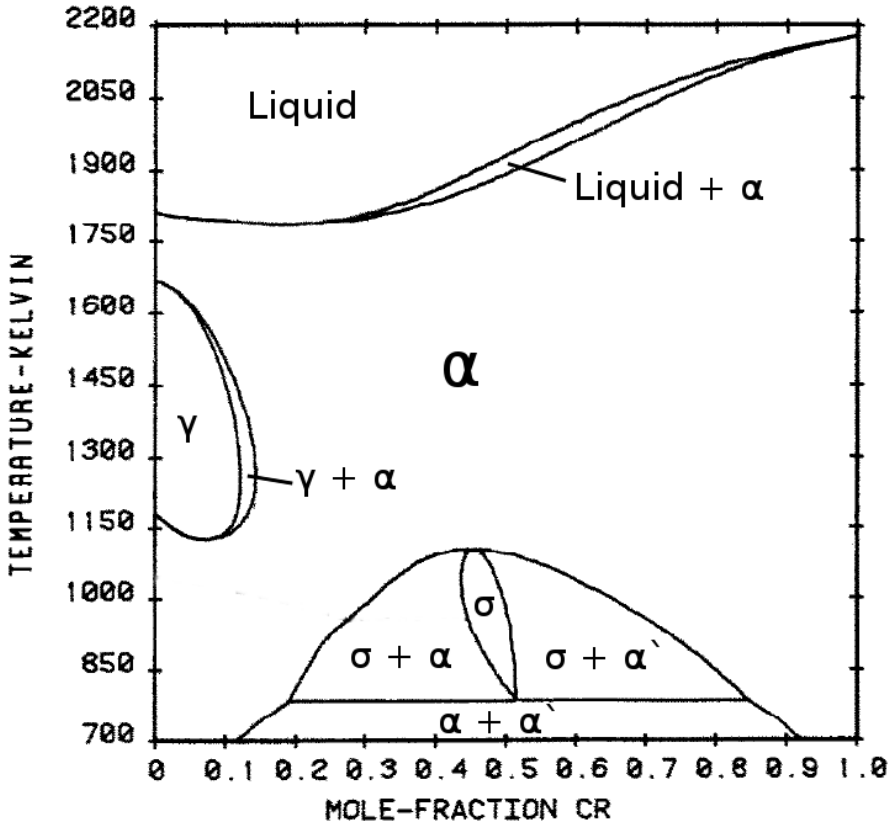


Figure 2.3: CALPHAD Fe-Cr phase diagram, from [64]. The α phase is a bcc solid solution, γ fcc solid solution, and σ an intermetallic phase. α' is a bcc Cr phase, and exists in the miscibility gap present at low temperatures.

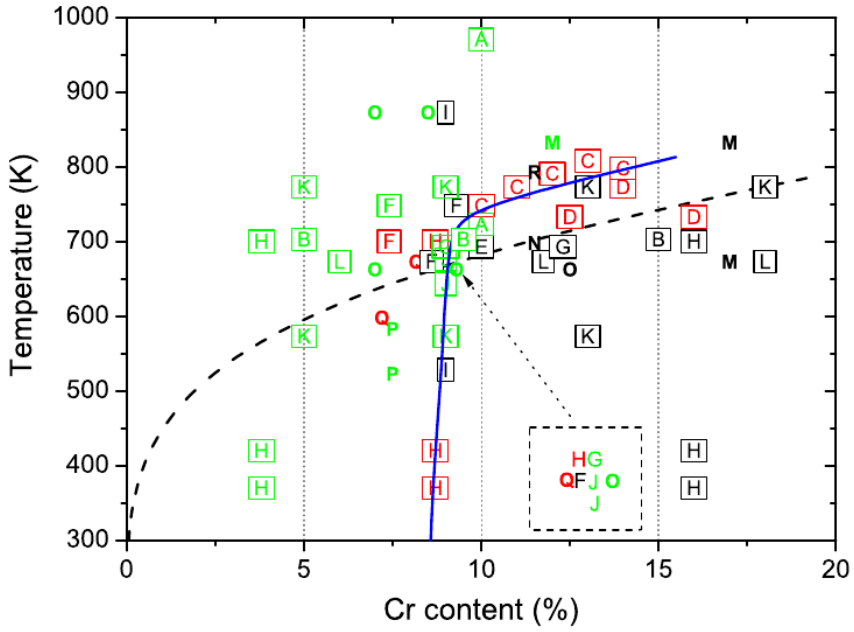


Figure 2.4: Figure taken from [69], a compilation of irradiation and thermal aging data for Fe-Cr binary alloys and steels by Bonny et al. Green points correspond to observation of Cr ordering (solid solution), black to α‘ precipitation, and red to suggested phase boundary. The black dashed line represents the standard CALPHAD diagram boundary [64], and the blue line the boundary proposed by Bonny et al. [69].

Due to the slow diffusion of Cr in Fe [67, 68], low temperature annealing studies are infeasible so this area of the diagram is produced from extrapolation of higher temperature experiments (700 K and above [64]).

During irradiation however, an increase in the number of vacancies and interstitials can increase the rate of Cr diffusion, allowing equilibrium to be reached more rapidly. Bonny et al. [69] compiled literature data of observations of precipitation or ordering for irradiated Fe-Cr binary alloys and steels, in an effort to determine the boundary for Fe rich side of the miscibility gap for nuclear applications. Their findings are shown in figure 2.4, where significant disagreement with the CALPHAD diagram of Andersson et al. [64] can be seen - particularly for the solubility of Cr at low temperatures.

Xiong et al. [70] were critical of Bonny et al.'s [69] work, taking issue with the use of irradiated samples to determine thermal equilibrium states. They argued that the observed phase change could be radiation induced - that radiation damage could provide nucleation sites, or support non-equilibrium states - rather than radiation enhanced.

DFT calculations however support the change in phase boundary proposed by Bonny et al. [69], predicting a negative mixing enthalpy at low Cr concentrations [71,72]. This is understood physically to be due to electron band properties [72] and magnetic frustration [73]. Fe is ferromagnetic, meaning it prefers its magnetic moments to be parallel to its neighbours', and Cr is anti-ferromagnetic, meaning it prefers its magnetic moments to be aligned anti-parallel to its neighbours'. Magnetic frustration occurs when 2 Cr atoms are close to each other, and cannot align their magnetic moments anti-parallel to both the surrounding Fe atoms and each other. In dilute alloys the most energetically favourable situation is one where the Cr atoms are distributed sufficiently far from each other such that magnetic frustration doesn't occur, in short range order [74]. As the Cr concentration is increased, this magnetic frustration cannot be avoided and α' precipitation becomes favourable.

Bonny et al. [75] reparametrised the Gibbs free energy to produce an updated Fe-Cr phase diagram, shown in figure 2.5.

Experimental observations of neutron irradiated Fe-Cr alloys with a range of Cr contents also suggest a radiation-enhanced mechanism - i.e. that the effect of irradiation is to achieve the equilibrium state more rapidly, and the phase boundary is not significantly altered. A small angle neutron scattering (SANS) experiment by Mathon et al. [76] estimated the threshold for α' precipitation under neutron irradiation to be ~7.2 at% Cr at 325°C and 8.3 at% Cr at 400°C, and argued that this is not significantly different from the standard phase diagram, suggesting a kinetics origin.

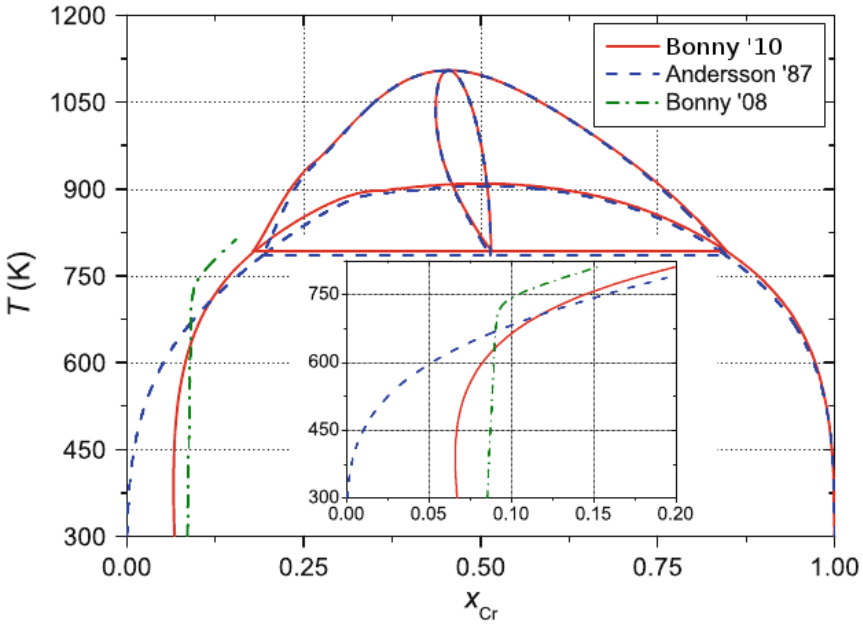


Figure 2.5: Updated Fe-Cr phase diagram by Bonny et al. [75] (red line). The blue line is the original CALPHAD diagram by Andersson et al. [64], and the green line from Bonny et al.'s earlier compilation of experimental data [69]. Figure from [75].

Furthermore, two separate neutron irradiation studies of Fe-Cr binary alloys with a range of Cr contents at 290 [77] and 300°C [78, 79] found α' precipitation only in those alloys with Cr concentrations above 9%, also suggesting a radiation enhanced mechanism rather than a radiation-redefined phase boundary.

α' precipitation has also been observed in an Fe-15Cr alloy after electron irradiation at 300°C [80]. The precipitation occurred more rapidly under electron irradiation than under neutron irradiation, with a 6.7% volume fraction of α' observed at 0.7 dpa compared to 3.8% after 1.82 dpa in the neutron irradiated case. Tissot et al. [80] suggested that this is likely due to the increased efficiency at which freely migrating defects are produced per dpa for electron irradiation, where individual Frenkel pairs are created, compared to the larger cascades produced by neutron irradiation where more recombination and clustering of point defects occurs (see section 2.4.1). These freely migrating

defects are what enhance diffusion, leading to the α' precipitation. This also strongly suggests a solely radiation enhanced mechanism.

To date there has been only 1 observation of α' precipitation after heavy ion irradiation, made by Tissot et al. [81]. An Fe-15Cr alloy was irradiated with 2 MeV Fe ions at 300°C at a dose rate of $3 - 6 \times 10^{-5}$ dpa/s. α' precipitation was observed only in regions away from the injected interstitial (see section 2.4.3) peak. The combination of a relatively low dose rate and absence of injected interstitials appear to be the factors leading to the observation, unlike other studies where no α' was observed in Fe-9Cr and Fe-12Cr [82] and Fe-9Cr [83] irradiated under similar conditions.

2.2.4 Mechanical Properties

Modelling has shown that dislocation loops [84], voids [85], and α' precipitates [86], all present significant barriers to dislocation glide, leading to hardening.

Perhaps the most serious consequence of irradiation induced hardening is embrittlement, and an increase in the ductile to brittle transition temperature (DBTT). The radiation-induced increase in DBTT for low activation ferritic steels irradiated in the fast flux test facility (FFTF) are shown in figure 2.6, taken from a review by Kohyama et al. [87]. A clear minimum can be seen for alloys containing around 9%Cr.

A similar trend with Cr content was observed in post-irradiation yield stress of low activation ferritic steels irradiated in the FFTF and the High Flux Isotope Reactor (HFIR) [87], with alloys with 7-9% Cr having a lower yield stress than those with 2.5 and 12% Cr (figure 2.7).

Matijasevic et al. [45] irradiated Fe and Fe-Cr model alloys with 2.5, 5 , 9, and 12%

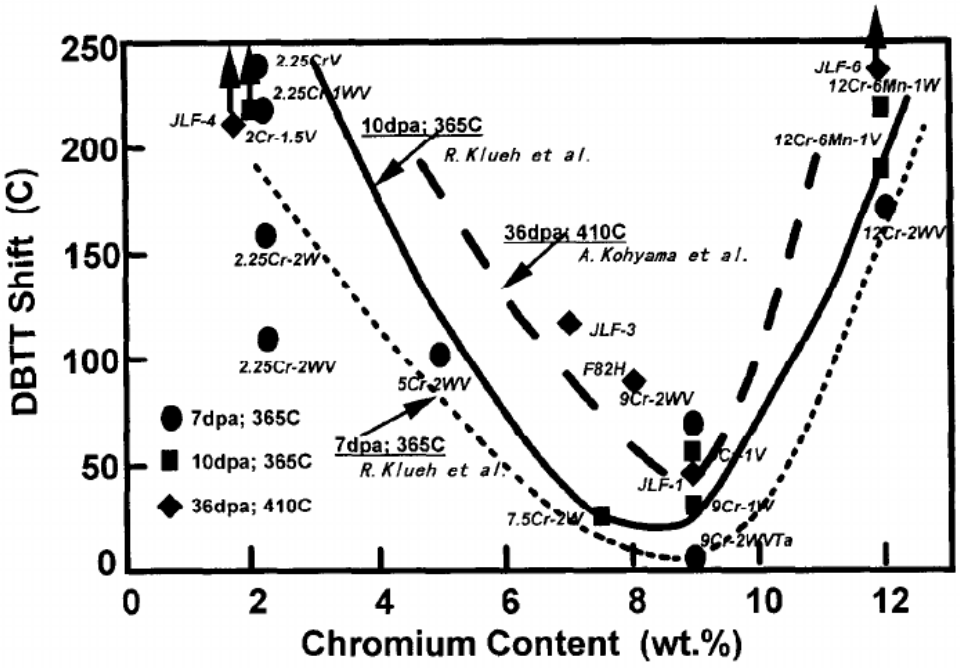
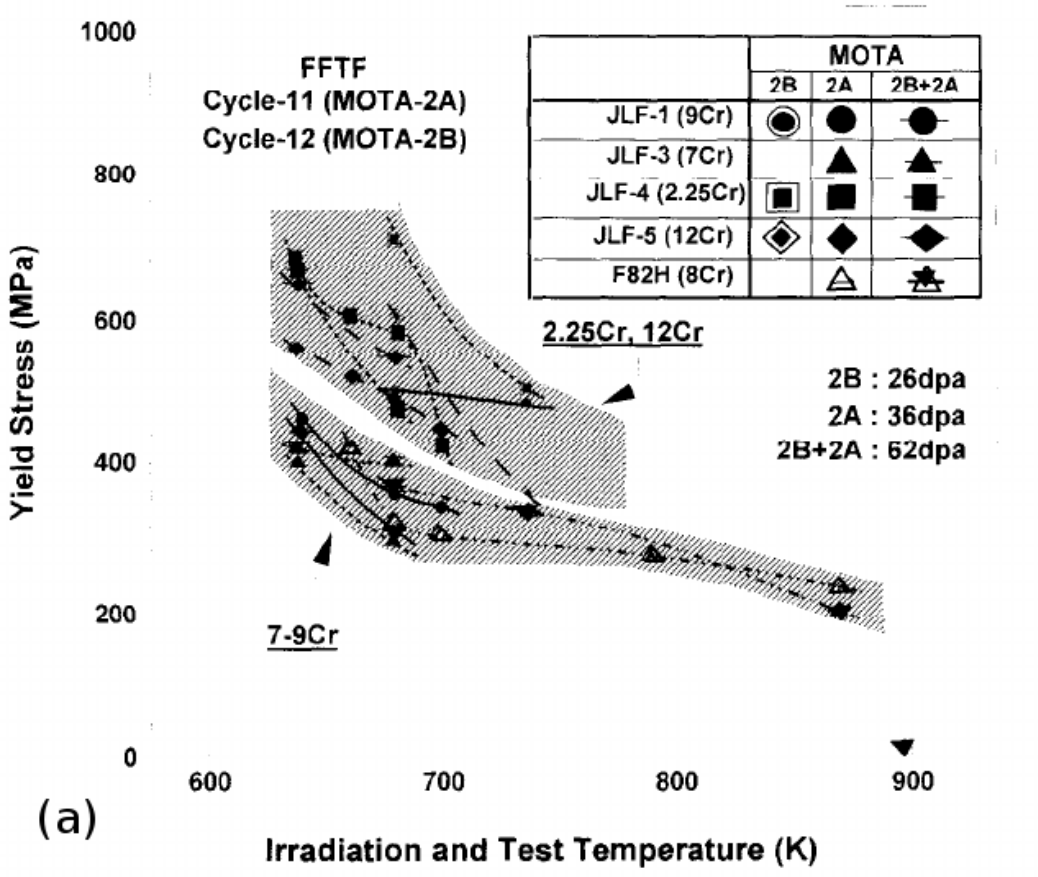


Figure 2.6: Change in DBTT vs Cr content for low activation ferritic steels irradiated in the FFTF. Figure from [87], data from [88, 89].

Cr at 300°C to 0.06, 6 and 1.5 dpa in the SCK-CEN BR2 reactor, and found those alloys containing Cr hardened more than the pure Fe. A minimum in hardening was found for the alloy containing 9% Cr.

Porollo et al. [46] found Fe-Cr alloys to harden more than pure Fe, but that yield strength increased with increasing Cr content after neutron irradiation to 5.5-7.1 dpa at 400°C in alloys containing 2, 6, 12, and 18% Cr. Severe embrittlement was found in the 18% Cr alloy.



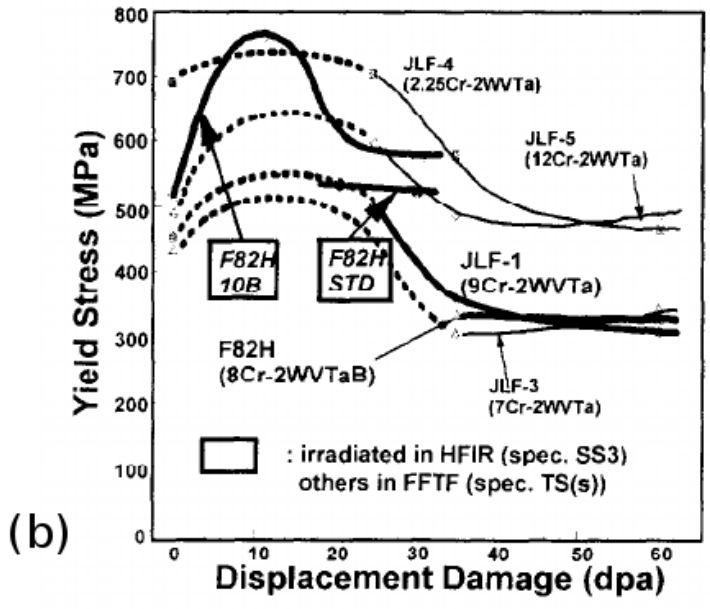


Figure 2.7: (a) Yield stress for samples irradiated in the FFTF. (b) Yield stress for samples irradiated in the HFIR and FFTF at 410°C as a function of dose. Both figures from [87].

An Orowan model is often used to predict the contribution to hardening of a population of a class of defects (eg. [41, 45, 90, 91]). In this model, hardening results from the additional stress required for dislocations to bow into a semi-circle in order to bypass obstacles pinning it. TEM analysis can determine whether this is the appropriate hardening model, using in-situ deformation and looking for the pinning of line dislocations and the formation of Orowan loops around obstacles, as was observed for Cu-rich precipitates in Fe [92].

In terms of yield stress, the stress ($\Delta\sigma_x$) required for a dislocation to pass a periodic array of obstacles of type x:

$$\Delta\sigma_x = \alpha_x M \mu b \sqrt{N_x d_x} \tag{2.4}$$

where α is the obstacle strength, M the Taylor factor, μ the shear modulus, b the Burgers vector, and N and d the obstacle number density and average diameter.

Contributions from multiple populations of obstacles are typically summed linearly, but modelling has shown summation in quadrature to be valid when obstacle strengths are small and nearly the same [93].

According to this Orowan model, the yield stress can be increased by either adding a new class of obstacle, increasing the number density(N) or the average diameter(d) of existing obstacles, or by increasing their strength (α).

There are a number of plausible explanations for the increased hardening in alloys containing Cr compared to pure Fe [41]. Cr increases the proportion of loops with $\frac{1}{2}$<111> type Burgers vectors, which have been shown to be stronger obstacles than those with <100> type Burgers vectors [84]. Cr also increases the loop number density

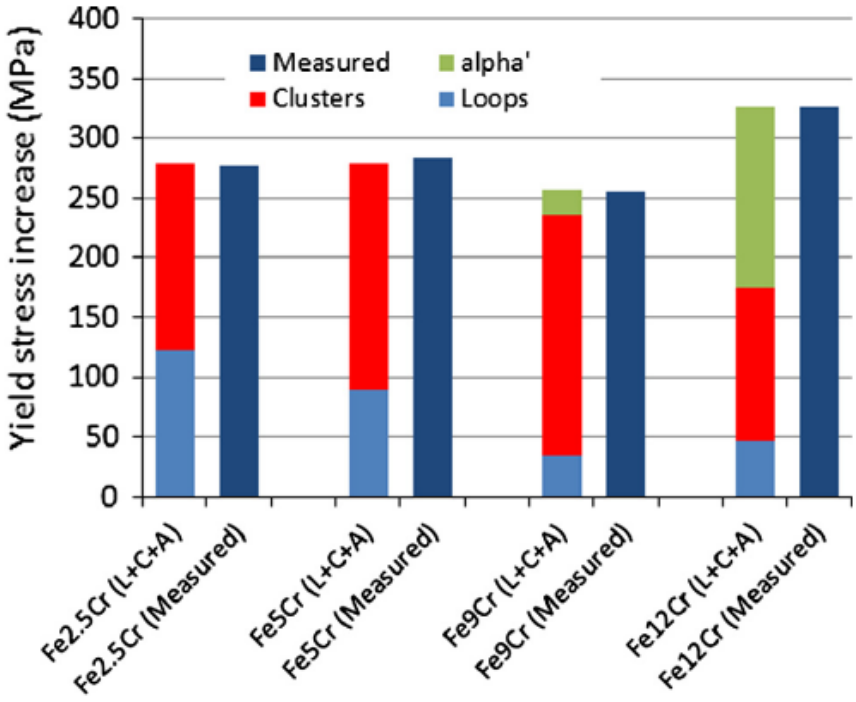


Figure 2.8: Contribution to increase in yield stress predicted for each class of defect alongside measured yield stress increase for Fe-Cr model alloys neutron irradiated to 0.6 dpa at 300°C. "Clusters" are NiSiPCr-rich clusters. Figure from [90].

compared to pure Fe [41, 45, 46, 52–54]. The decoration of loops by Cr (observed in neutron irradiation Fe-6Cr at 290°C [94]) has also been shown to increase their strength [95]. For alloys containing above ~9% Cr, the formation of α' will also lead to increased hardening.

Bergner et al. [90] applied an Orowan type model to the data produced by Matijasevic et al. from irradiation of Fe-Cr model alloys at 300°C to 0.6 dpa [45]. Contributions to the yield stress increase from each class of obstacles is shown in figure 2.8.

Their analysis showed that loops were the strongest obstacles, α' precipitates were the weakest, and that NiSiPCr clusters formed from impurities play an important role. The observed increase in yield stress was well explained by these 3 classes of defects.

The authors also suggested that the minimum increase in yield stress at around 9% Cr

results from a competition of a reduced influence of loops as Cr concentration increases (loops were observed to decrease in size and number density with increasing Cr [45]), and the increasing influence of α' precipitation at higher Cr concentrations.

2.3 Influence of Carbon on Radiation Damage in Fe

The work by Bergner et al. [90] showed that Ni, Si, and P impurities can have a significant effect on the mechanical properties of ferritic steels after irradiation. Another common impurity is carbon, which has long been known to interact with point defects.

2.3.1 Carbon - Point Defect Interactions

In the 1960s, analysis of an Fe-0.01wt%C alloy neutron irradiated at -73 and 57°C by internal friction [96], electrical resistivity [97], calorimetry [98] and electron microscopy [99] showed that carbon atoms strongly interact with vacancy defects - with a binding energy measured to be 0.41 eV [98] .

In the 1980s, two similar but separate studies of electron irradiated pure Fe and Fe-C alloys using positron lifetime measurements [100], and resistivity recovery [101] demonstrated the presence of vacancy-carbon complexes, where more than one carbon atom can be bound to a vacancy. This, alongside the observation of vacancy migration at 220 K rather than the previously thought 520 K (due to the presence of C), provided a revised interpretation of the earlier experiments. The earlier value of 0.41 eV for the binding energy of a carbon atom with a vacancy was now assigned to the binding energy of an additional C atom to a C-V pair, and values of 0.85 eV [100] and 1.1 eV [101] were found for the carbon-vacancy binding energy. A carbon-interstitial binding energy of 0.11 eV was reported in [101].

More recently, modern density functional theory calculations have been performed [102–106] detailing the binding energies of carbon-vacancy complexes in different configurations. Carbon-vacancy binding energies in the range 0.41-0.65 eV were reported.

C_2-V and C_3-V were found to be stable with total binding energies of 1.18-1.65 eV and 1.3-1.82 eV respectively, but C_4-V was found to decay spontaneously. Stable complexes containing multiple vacancies were also found, the most stable of which was V_2C_4, with a dissociation energy of 1.92 eV [107].

A number of studies have coupled these ab initio calculations with simulations in an attempt to reproduce experimental results [106–109]. Some success was found, although different parameters were used between studies.

For example with a rate theory model, Tapasa et al. [108] were able to reproduce the recovery stages in Vehanen et al.'s [100] experiment using DFT calculated values [102] for vacancy migration of 0.65 eV, V-C binding energy of 0.47 eV, and an additional binding energy of 0.8eV between a V-C pair and additional C atom.

Terentyev et al. [107] and Fu et al. [109] however found that the temperature of the recovery stage corresponding to vacancy migration could not be reproduced with a realistic attempt frequency prefactor for a vacancy migration energy of 0.65 eV. Terentyev et al. [107] instead used the experimentally measured value of 0.55 eV in their object Monte Carlo simulations. They argued that the model in [108] used an unreasonably high dislocation density in order to match the experimental results using a V-C binding energy of 0.47 eV, and that a value of 0.65 eV better matched the observed migration energies of vacancies in low purity Fe [110, 111]. Using this value however, the experimentally observed recovery at 450 K was not reproduced by the simulation. The authors proposed some alternative causes for the recovery at this temperature, which do not contradict available DFT or experimental data.

The additional detail provided by these modelling experiments has reopened uncertainty of the interpretation of the experimental results, in particular the identities of

the species remaining at higher temperatures, above ~450 K [107]. A discrepancy still remains between the DFT calculated value for the vacancy migration energy of ~0.65 eV [106, 112], and the experimentally measured value of 0.55 eV [100, 101, 107–109].

Calder et al. [113] performed molecular dynamics simulations of displacement cascades in α-Fe containing up to 1 at% C in solution. Cascade energies in the range 5 - 20 keV were tested at 100 and 600 K but no effect of C was found on the number of surviving defects or the clustered fraction. A large number of the defects were however found to be trapped by C atoms, independent of temperature for vacancies but increased with increasing temperature for self interstitials.

The experimental and modelling work both demonstrate the strong interaction of carbon with vacancies in α-Fe and the formation of carbon-vacancy complexes, which can remain stable up to 580 K [114].

2.3.2 Carbon - Loop Interactions

Satoh et al. [115, 116] observed 1D loop hopping during in-situ electron irradiation of Fe samples of varying purity at room temperature. Under irradiation loops were seen to jump between different positions, and the distance between jumps was found to be smaller for samples of lower purity. The authors suggest that loops are initially trapped by impurities, and are freed by the electron irradiation. The loops then migrate with low activation energy [117–119] along their glide cylinders until they reach another impurity and become trapped again.

Terentyev et al. [114,120] studied the interaction of carbon with dislocation loops by molecular dynamics. In [120] carbon was found to interact more strongly with <100>

loops than $\frac{1}{2}$<111> loops, with a maximum binding energy of 1eV. In [120] carbon-vacancy complexes (C-V complexes) were found to be potential traps for $\frac{1}{2}$<111> loops, with an interaction energy of ~1 eV.

More detailed calculations by Aneto et al. [121] confirmed this, and found a binding energy of 1.5 eV between a 61 self interstitial $\frac{1}{2}$<111> cluster and a C_2-V complex. Similar results were found by Abe et al. [122].

Janssson et al. [123–125] used object kinetic Monte Carlo simulations to recreate experimental observations of irradiated Fe-C. By modelling C-V complexes as generic traps, with binding energies that vary with cluster sizes based on simulations [114, 121], they were able to match the experimentally observed cluster and loop sizes and number densities after irradiation.

In [124] and [125], the effect of carbon concentration on these loop and cluster populations was also studied by adjusting the number of traps. Simulations were made up to 1 dpa for carbon concentrations in the range 1-300 appm. For greater C concentrations: the visible SIA and vacancy cluster density was found to increase, and the mean cluster sizes to decrease - more for the SIA clusters.

2.3.3 Mechanical Properties

Lambrecht et al. [126, 127] studied the effects of different element additions to Fe on post irradiation tensile behaviour. Among the samples were pure Fe (<20 ppm C) and an Fe-C alloy containing ≥50 ppm C, which were irradiated to 0.1 dpa [126] and 0.2 dpa [127] at 290-295°C in the BR2 test reactor at SCK-CEN. Results of tensile testing are shown in figure 2.9, showing that the Fe-C alloy hardened more than the pure Fe sample.

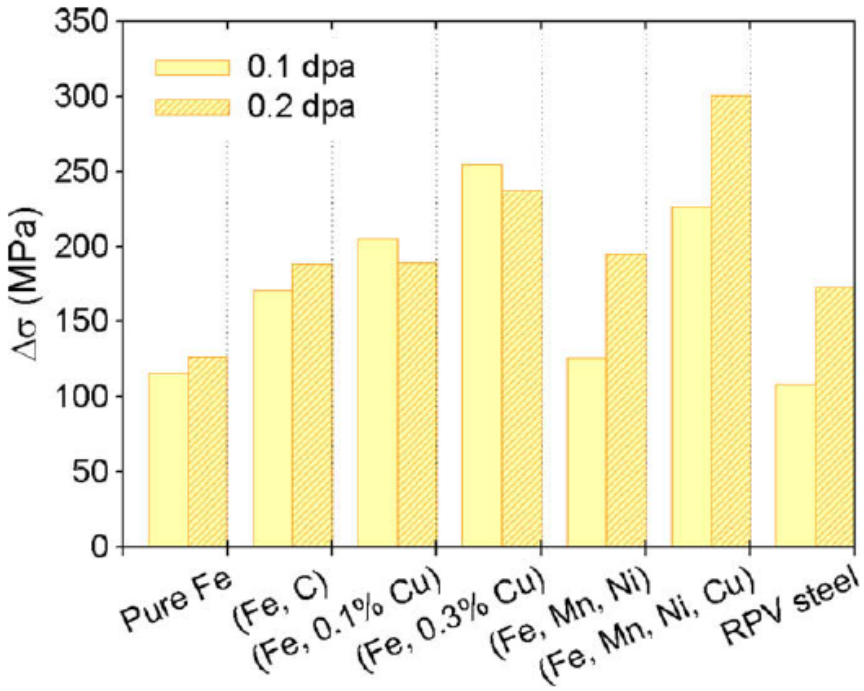


Figure 2.9: Work by Lambrecht et al. [127] showing the change in yield stress vs unirradiated condition by tensile testing. The Fe-C alloy can bee seen to harden significantly more than the pure Fe alloy. Figure from [127].

Positron annihilation spectroscopy analysis suggested that the number of vacancies was slightly reduced by the presence of C. The authors suggest this could be due to enhanced recombination due to trapping of vacancies by C. They suggest the increase in hardening observed must be due to differences in loop population, and that trapping of self interstitial clusters by C will increase the number of nucleation sites for clusters, and that the reduced mobility will mean coalescence to form loops is reduced, keeping the loop number density higher.

Terentyev et al. [128] investigated the interaction of edge dislocations with $\frac{1}{2}$<111> loops decorated with carbon using the model of Osetsky and Bacon [129]. At 300 K, 1 nm loops (TEM invisible) decorated with C were found to have a strength to be absorbed into a glissile superjog at least twice as high as undecorated loops. For 3.5 nm loops (TEM visible), C decoration increased the strength by 25-40% compared to naked loops.

2.3.4 Carbon Contamination During Ion Irradiation

Recently a number of studies have been carried out on the subject of carbon contamination during ion irradiation.

Marquis et al. [130] found the Gibbsian excess of C at grain boundaries in ion irradiated Fe-Cr alloys to decrease with increasing sample depth. The results are shown in figure 2.10. It was suggested that this was due to carbon being unintentionally implanted during ion irradiation.

Gigax et al. [131] irradiated the ferritic-martensitic steel HT9 with 3.5 MeV Fe ions at 450°C both with and without a beam filtering technique including a liquid nitrogen cold trap designed to reduce carbon contamination. Doses of 200, 400, and 600 dpa were produced with the unfiltered beam, and 200, 600, and 800 dpa with the filtered beam, all at 1.74×10^{-3} dpa/s.

The carbon concentration as a function of depth as measured by SIMS for the 600 dpa samples is shown in figure 2.11, alongside the SRIM calculated dpa and injected ion profiles. It can be seen both that significant carbon contamination occurred throughout the irradiated depth, and that this was significantly reduced by the beam filtering process.

The implanted carbon was found to form carbides, and to greatly reduce void swelling. This is thought to be due to carbides acting as defect sinks.

Was et al. [132] observed similar contamination in 800H irradiated to 20 dpa with 5 MeV Fe^{2+} ions at 440°C, measured using nuclear reaction analysis, SIMS and APT. It was found that source of carbon was hydrocarbons present in the vacuum and on the sample and stage surfaces. These hydrocarbons crack under irradiation, are adsorbed onto the sample surface, and then injected into the sample with irradiation. The use of plasma cleaning and liquid nitrogen cold traps was found to significantly reduce this carbon implantation.

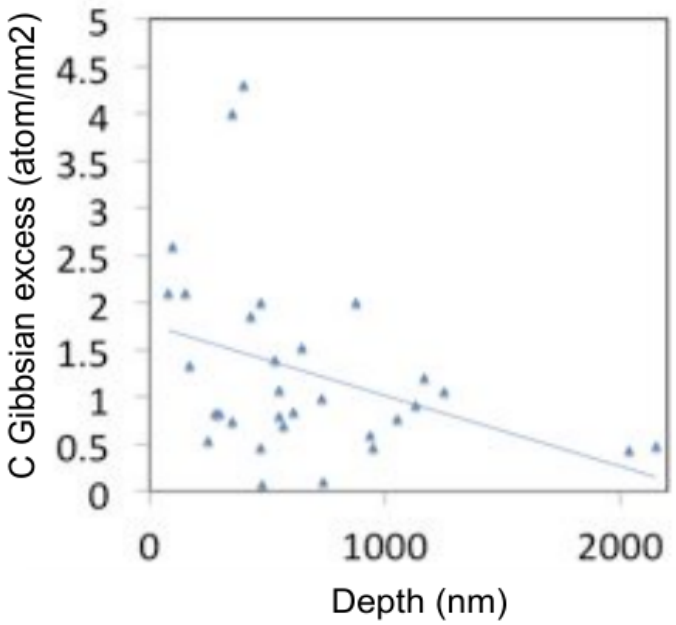


Figure 2.10: Gibbsian excess of C at grain boundaries in ion irradiated Fe-Cr alloys as a function of depth. Figure from [130].

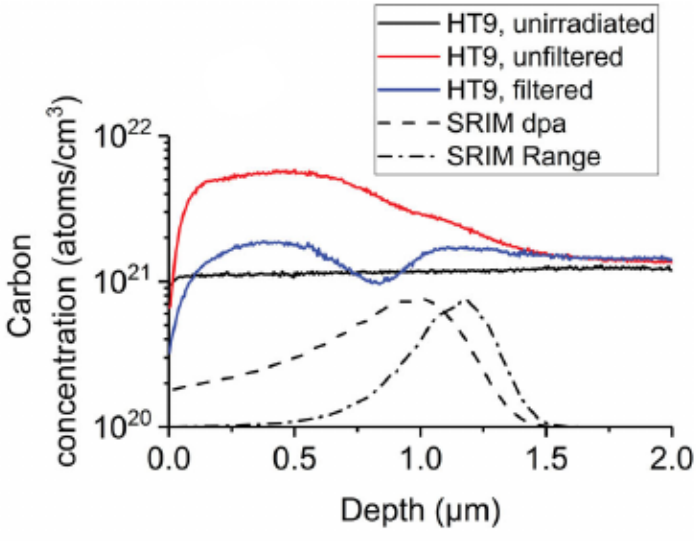


Figure 2.11: Carbon concentration as a function of depth measured using SIMS for unrradiated and ion irradiated HT9 samples using an filtered and unfiltered 3.5 MeV Fe^{+} beam. 10^{21} and 10^{22} C atoms/cm^3 is around 1.17 and 11.7 at% respectively. Also shown is the SRIM calculated dpa and injected ion profiles. Both irradiated samples received a dose of 600 dpa. Figure from [131].

2.4 Neutron-atypical Aspects of Heavy Ion Irradiation

Heavy ion irradiation has a number of practical advantages over neutron irradiation including increased speed, lower cost, greater control over experimental parameters, and a lack of induced radioactivity. For these reasons it is frequently used in the place of neutron irradiation to study radiation damage.

There are however certain differences between the two irradiation methods, which need to be well understood if heavy ion irradiation is to be used to predict material behaviour under neutron irradiation. In this section the influence of these neutron-atypical effects are discussed.

2.4.1 Recoil Energy Spectrum

As discussed in section 2.1, a lattice atom struck by an irradiating particle recoils with an energy which depends on the angle it is struck and the nature of the irradiating particle and its energy. This first struck atom that initiates a displacement cascade is known as a primary knock on atom (PKA). Neutrons from both fission and fusion reactors are produced with a range of energies, and will therefore produce PKAs with a range of energies. An understanding of the effect of PKA energy on the final damage produced is important for comparing irradiations of different energy spectra.

The PKA spectrum for an Fe-Cr alloy in the ATR fission test reactor was calculated by Dr M Gilbert (CCFE), and is shown alongside the neutron spectrum in figure 2.12. It can be seen that recoiling atoms are produced with a wide range of energies, from a few eV to ~1 MeV.

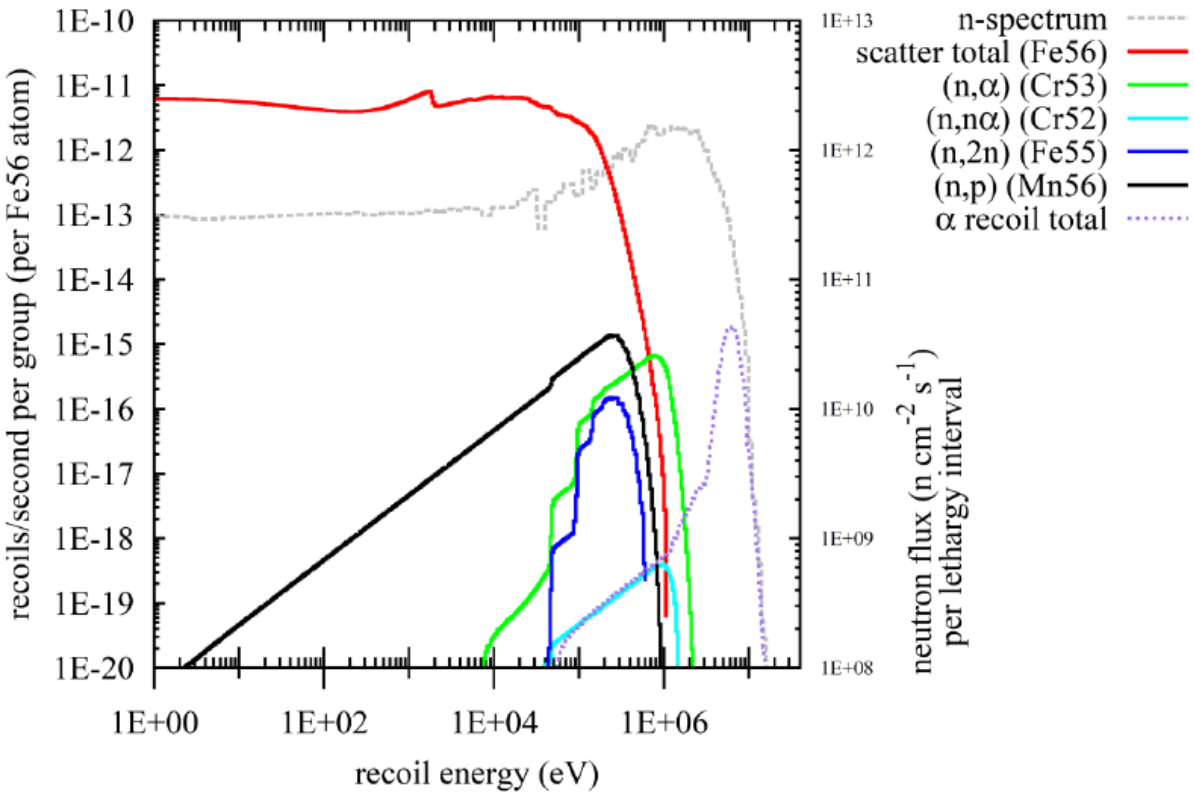


Figure 2.12: PKA and neutron energy spectra for material irradiated in the ATR reactor. Data produced by Dr M Gilbert (CCFE), figure from [14].

Molecular dynamics (MD) has been the main tool used to study displacement cascades as it allows access to the relevant small time and length scales, and can provide a detailed picture of the damage on an atomic scale. However, results can be sensitive to the choice of potential as discussed by Malerba [133] and Terentyev et al. [134]. The technique is also computationally expensive, which limits the number of atoms and hence the energy of cascade that can be simulated. Nonetheless, simulations of relatively low energy cascades have provided significant insights into the effect of PKA energy on defect formation. These are discussed, with the implications for heavy ion - neutron correlation considered in section 2.4.1.3.

2.4.1.1 Surviving Defect Fraction

Stoller et al. [24, 25, 135] performed MD simulations in Fe with a cascade energy up to 50 keV at 100 K, up to 20 keV at 600 K and up to 10 keV at 900 K. The surviving defect fraction, defined as the number of defects remaining at the end of the simulation compared to those calculated using the NRT model [17] (see section 2.1), is plotted against the cascade energy in figure 2.13.

The trend towards an energy independent value of ~0.3 for cascades above around 10 keV is in agreement with simulations using other potentials [133] and experiment (see the discussion in section 2.4.3.1), and is thought to be due to subcascade formation at around this energy [26–28].

More recent simulations however, suggest a tendency towards a more continuous cascade structure for higher energy cascades of 0.2 and 0.5 MeV in Fe [136]. Nonetheless the survival fraction was found to be 0.3-0.4, similar to that observed for 10-50 keV cascades.

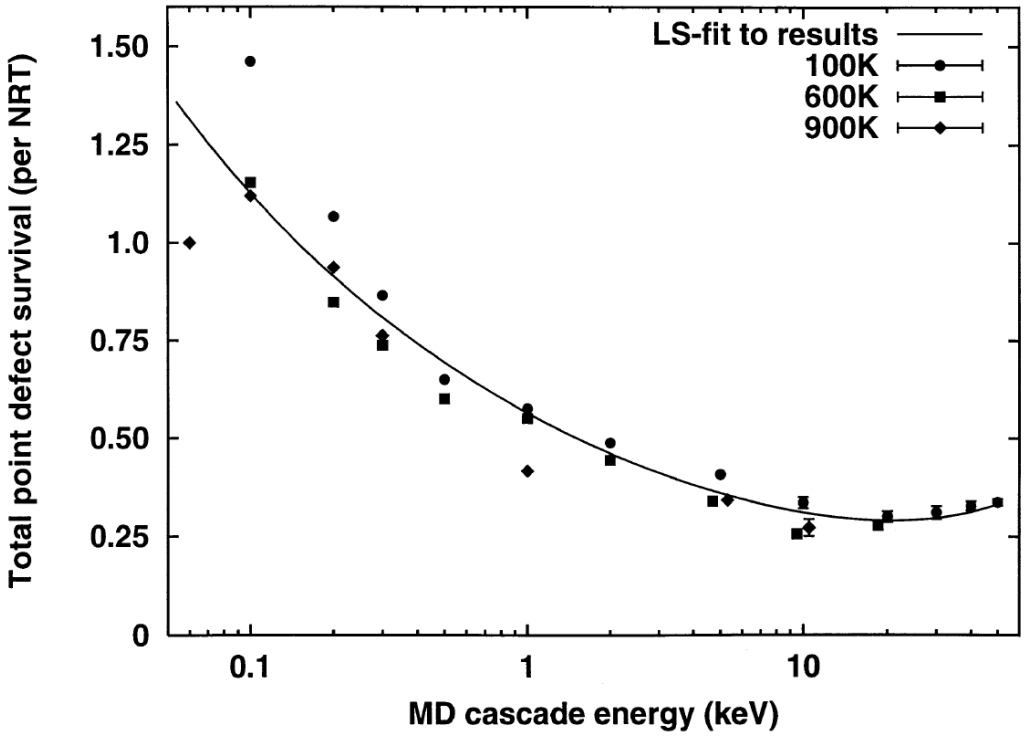


Figure 2.13: Ratio of surviving defects as calculated by MD to NRT displacements as a function of cascade energy in Fe. Figure from [25].

2.4.1.2 Clustered Fraction

The fraction of surviving defects in clusters for the same simulations by Stoller et al. [24, 25, 135] is shown in figure 2.14.

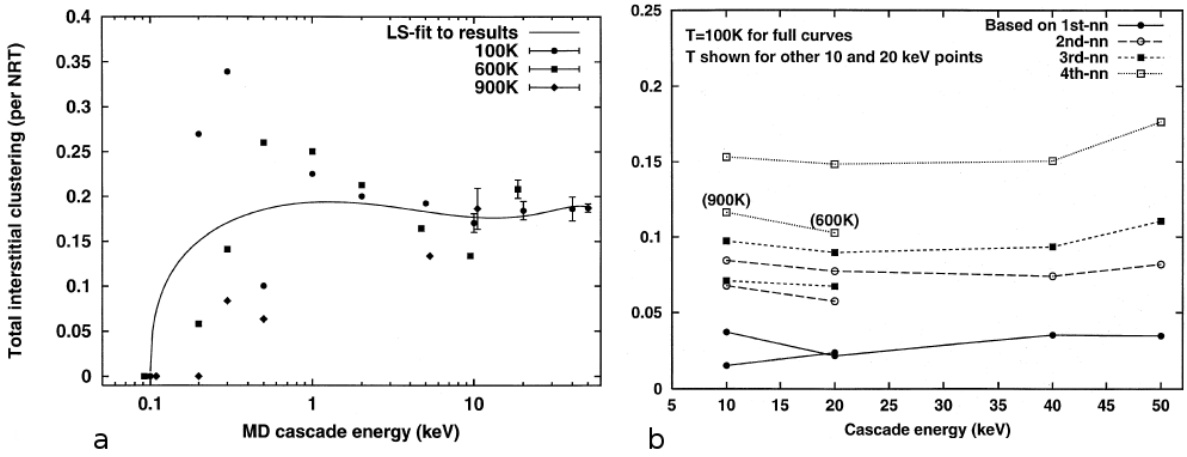


Figure 2.14: Ratio of clustered defects per NRT displacement as a function of cascade energy for (a) interstitials and (b) vacancies in Fe. Figure from [25].

For lower energy cascades (below 1 keV) there is a tendency for fewer of the surviving self interstitials to be clustered. This is again in broad agreement with simulations performed using different potentials [134, 137]. For the higher energy cascade simulations of 0.2 and 0.5 MeV, Zarkadoula et al. [136] reported a surviving defect fraction of 0.3-0.4 and the fraction of surviving self interstitials in clusters as 0.58-0.52. As a fraction of NRT as plotted in figure 2.14 this is 0.16-0.21, similar to cascades of energy 10-50 keV.

A reduced clustering fraction means and more of the defects are freely mobile [138–140] and able to participate in RIS, creep and swelling.

2.4.1.3 Ion Irradiation

As discussed above, differences in the primary recoil spectrum can cause different fractions of defects surviving and clustering after the initial displacement cascade, leading to potential implications for ion-neutron irradiation correlation.

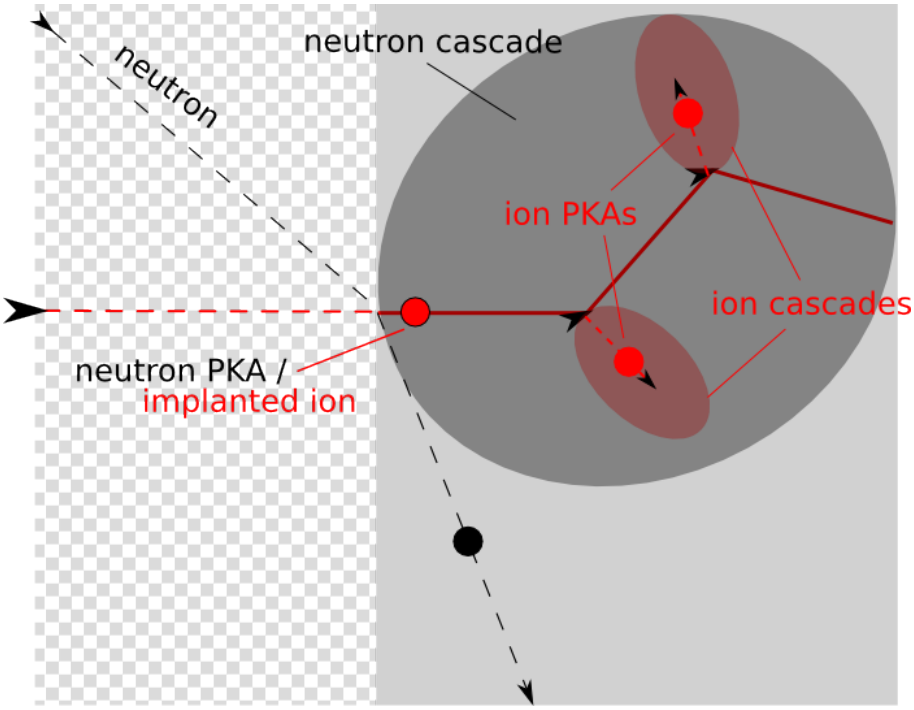


Figure 2.15: Depiction of possible definitions of PKA for ion irradiation.

For neutron irradiation, it is clear what is meant by the primary recoil spectrum - but for self ion irradiation it is less obvious. This is illustrated in figure 2.15, where two equivalent situations leading to the same displacement cascade are depicted, with two apparently different definitions of PKA:

1. During a self ion irradiation experiment an incident ion with energy T_1 collides with a lattice atom imparting energy T_2 and then later again with another imparting energy T_3 and so on to T_n. In this viewpoint, the atoms recoiling with energies T_2 ... T_n would be the PKAs.

2. Equivalently, during a neutron irradiation experiment a neutron could collide with a lattice atom at the surface, imparting energy T_1. In this viewpoint, the atom recoiling with energy T_1 would be the PKA, equivalent to the incident ion in viewpoint 1.

In the case of viewpoint 1, the nature of the particle interaction should be considered. Work by Averback [141] shows that the screened Coulomb interaction between heavy ions and lattice atoms produces recoils with a greater spread of energy than produced by a neutron of the same energy, which interacts as a hard sphere. The weighted recoil spectra, defined as the fraction of damage energy deposited in recoils of energy T, is shown in figure 2.16.

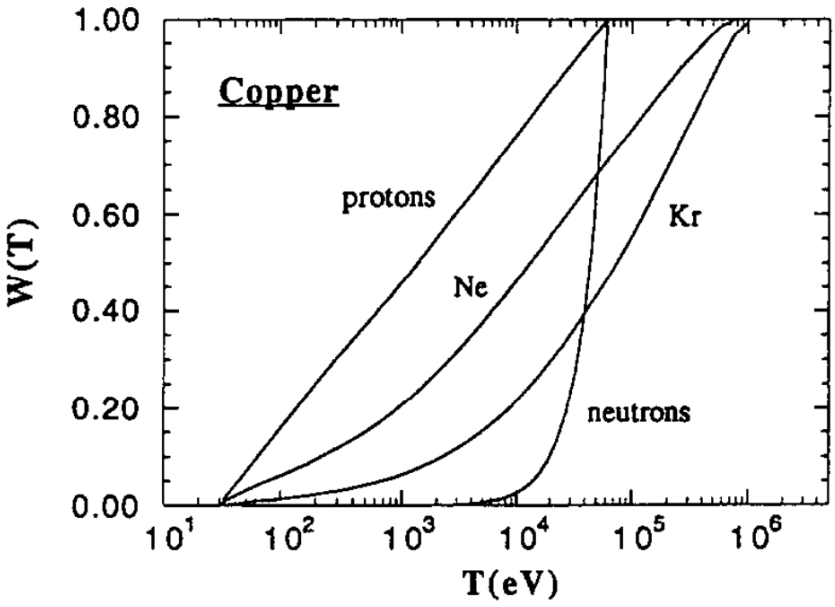


Figure 2.16: Weighted recoil spectra for 1 MeV particles in Cu. From [141].

Zinkle and Snead [142] subscribe to viewpoint 1, and suggest that the nature of screened Coulomb interaction could mean a higher surviving defect fraction per dpa for heavy ion irradiation compared to neutron irradiation, due to a larger number of lower

energy PKAs. The difficulty with this view, and discussed by Averback [141], is the implicit assumption that these lower energy cascades are produced in isolation (as they are modelled in MD). The work by Zarkadoula et al. [136] modelling implantation relevant 0.2 and 0.5 MeV cascades suggest that at these higher energies, cascades tend to be more continuous rather than branched, implying that this assumption may be incorrect and that viewpoint 2 may be more appropriate.

In viewpoint 2 the recoil energy spectrum is taken to be the ion implantation energies, as asserted in eg. [14, 143, 144]. Hardie et al. [14] argue that this means that heavy ion irradiation fails to reproduce the low energy PKAs produced in neutron irradiation (see figure 2.12) and therefore produces fewer freely migrating defects for the same dpa. It was suggested that this could be part of the cause of the reduced RIS observed for heavy ion irradiation compared to neutron irradiation.

2.4.2 Dose Rate

Structural components in any nuclear reactor are expected to last decades. Clearly it is not practical to test candidate materials over these timescales and some acceleration of the process is necessary. Figure 2.17 shows the typical range of dose rates achievable in Fe-based alloys for different irradiation techniques. Of particular relevance to this work is the distinct dose rate ranges available with heavy ion and test reactor facilities.

In a test reactor it may take months or years for specimens to receive a significant number of displacements per atom, whereas the same dose can be achieved with heavy ion irradiation in a matter of hours. This is clearly a practical advantage as it allows rapid completion of experiments. However, any effects of differing dose rates on microstructural evolution need to be understood if heavy ion irradiation is to be a useful surrogate for neutron irradiation.

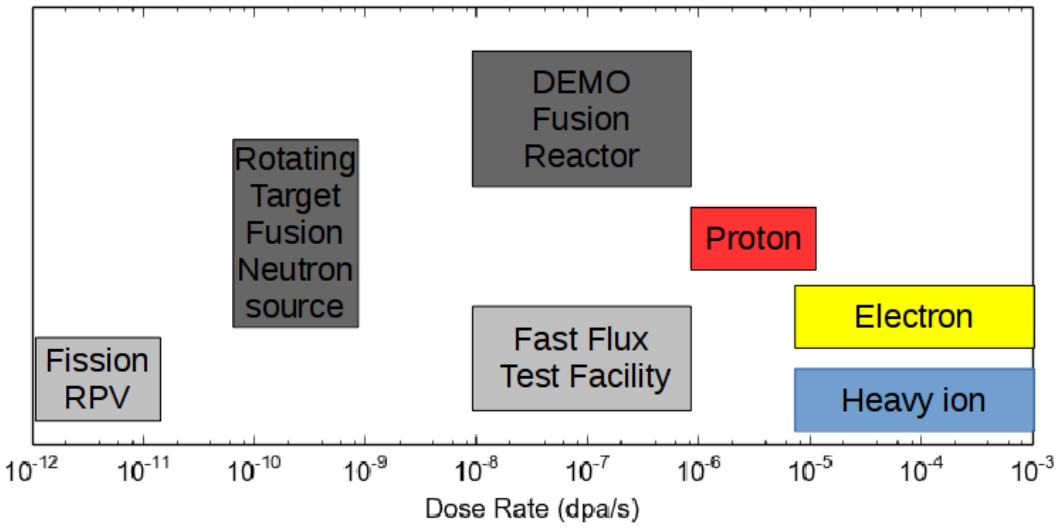


Figure 2.17: Achievable dose rates in Fe-based alloys for commonly used irradiation facilities

Point defects produced by irradiation can have one of three fates [145]:

i Loss at extended sinks such as dislocations or grain boundaries

ii Contribute to growth or shrinkage of defect clusters

iii Annihilation by mutual recombination

The evolution of damage is determined by the relative distribution of point defects among these paths. The influence of dose rate can be understood by its effect on this distribution. For low defect mobility and high defect concentration, mutual recombination tends to dominate. Conversely for high mobilities and low defect concentrations, loss to sinks tends to be the dominant reaction pathway [145]. A higher dose rate means higher defect concentration, and therefore an increase in mutual recombination.

This concept is well established, and is shown plainly by a shift in peak swelling

temperature with dose rate e.g. in work by Packan et al. [146] (figure 2.18). A peak swelling temperature exists because at too low a temperature mutual recombination limits the number of vacancies available to form voids, whereas at too high a temperature the increase in flux of vacancies is negated by their thermal emission from voids [147]. A shift in peak swelling temperature with dose rate occurs because at constant temperature a higher dose rate means increased recombination, so the number of free point defects is decreased, and an increase in temperature is required to maintain the same flux of vacancies to voids. The effect of thermal emission at higher temperatures is diminished for higher dose rates, as the voids grow more rapidly [148].

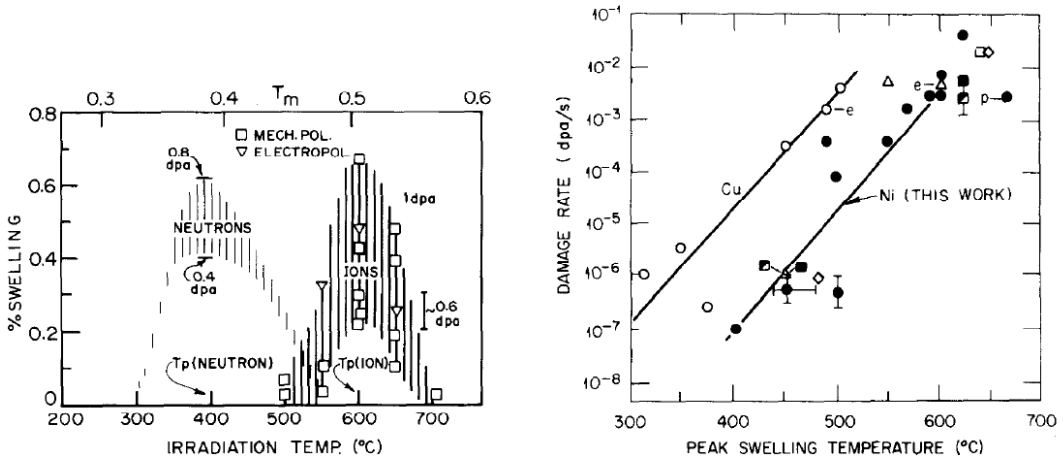


Figure 2.18: (Left) swelling as a function of temperature in pure nickel at ~1 dpa for neutron and nickel ion irradiation with dose rates of 1×10^{-7}dpa/s and 3×10^{-3}dpa/s respectively. (Right) Peak swelling temperature vs dose rate for a variety of fcc materials from literature. ◩- 316 SS; ■ - 316 SS;◯ - Cu; △ - A286 STA; ◇ - 304 SS; ● - Ni; □ - 316 SS. Both figures taken from [146], detailed references therein.

2.4.2.1 Austenitic Alloys

Okita et al. [149,150] compared swelling and microstructure of solution annealed model Fe-15Cr-16Ni alloy samples neutron irradiated at different positions and for either one

or both of cycles 11 and 12 in the materials open test assembly (MOTA) at the fast flux test facility (FFTF). This resulted in a matrix of samples irradiated at a range of dose rates (1.0×10^{-6} - 1.9×10^{-9} dpa/s) at around 400°C, each to 2 different doses corresponding to those exposed to 1 or 2 cycles. Both nucleation and growth of cavities were found to be enhanced at lower dose rates. The incubation dose to achieve steady state swelling was also found to decrease with decreasing dose rate, thought to be due to more rapid formation and unfaulting of dislocation loops at lower doses [149, 151]. A similar observation was made by Allen et al. [152] in 304 and 316 steels.

Later Okita et al. [151] performed Ni ion irradiation on the same model Fe-15Cr-16Ni material at a 300-600°C using dose rates 1.0×10^{-4}, 4×10^{-4}, and 1×10^{-3} dpa/s. Dislocation loop density was found to increase with increasing dose rate.

Muroga et al. [153] compared the saturation loop density for similar Fe-Cr-Ni alloys irradiated over a wide range of dose rates at around 450°C. Samples were irradiated with fusion neutrons at the rotating target neutron source (RTNS-II), with fast neutrons at the JOYO Japanese experimental fast reactor, and with electrons with a JEM-1000 HVEM, enabling a range of dose rates from 1×10^{-3} - 1×10^{-9} dpa/s to be studied. Figure 2.19 shows the strong increase in saturation loop density with increasing dose rate.

As pointed out by Hardie et al. [154], the low PKA energy spectrum produced by electron irradiation likely increases the amount of recombination, lowering the rate of production of defect clusters directly by collision events compared to the data sets from neutron irradiation. Indeed, the data from Okita et al's study [151] using heavy ion irradiation for similar materials and conditions show even higher loop densities: for 1×10^{-4} dpa/s, at 673K and 773K saturation loop densities of $6.10 \times 10^{22}\text{m}^{-3}$ and $2.09 \times 10^{22}\text{m}^{-3}$ are reported, suggesting the impact of dose rate is underestimated - partially masked by the additional effect of the different PKA spectrum for the electron irradiation data.

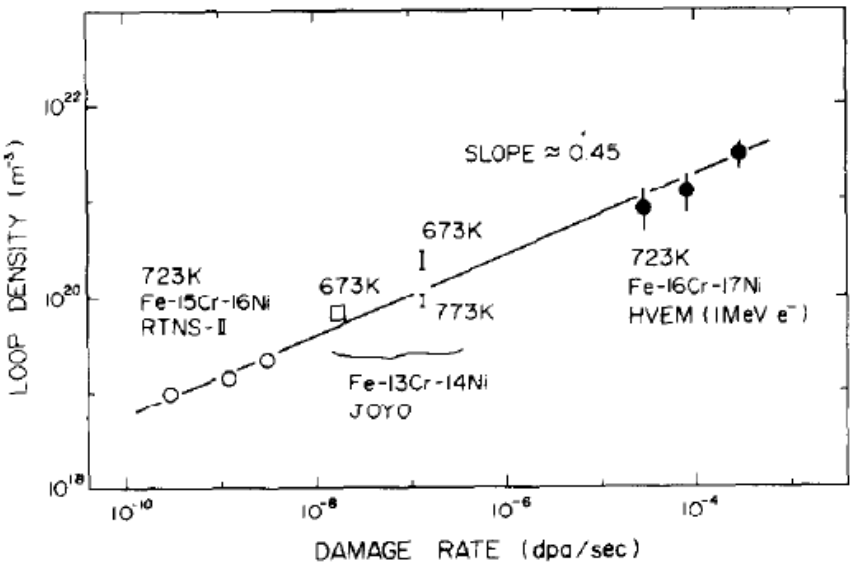


Figure 2.19: Saturation loop density as a function of dose rate in Fe-Cr-Ni alloys, from [153].

Allen et al. [152] examined 304 and 316 stainless steel samples retrieved from different positions within the Experimental Breeder Reactor-II. Alongside the swelling results mentioned above, radiation induced grain boundary segregation was also studied. Figure 2.20 shows changes in grain boundary concentrations of Cr and Ni after irradiation, showing an increase in segregation for decreasing dose rate. There are small variations in the composition of the specimens examined from different positions, but there was no correlation found between bulk composition and the amount of segregation observed that would suggest that these minor variations had any significant effect on the segregation.

Lewthwaite and Mosedale [155] studied creep rates in a range of austenitic steels neutron irradiated in the Dounreay Fast Reactor. The strain per unit dose was found to increase with decreasing dose rate, due to greater levels of mutual recombination meaning fewer freely migrating defects are available to participate in creep.

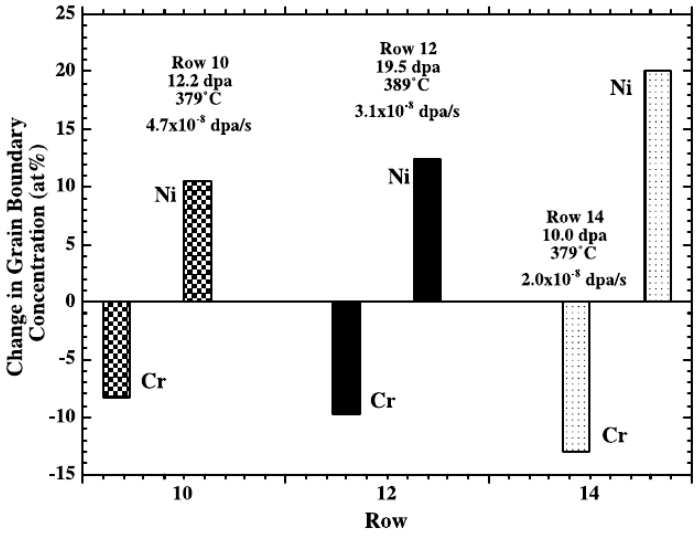


Figure 2.20: Change in grain boundary concentration in 304 stainless steel after neutron irradiation in different positions in EBR-II, showing the influence of dose rate. From [152].

2.4.2.2 Ferritic Alloys

The above work all relates to austenitic steels. A more limited amount of work has been performed on ferritic alloys.

Okita et al. [156] analysed swelling of Fe-Cr binary alloys irradiated in the same MOTA FFTF campaign as the model Fe-Cr-Ni alloys mentioned in section 2.4.2.1. Samples received doses in the range 0.37 - 67.8 dpa, at dose rates varying from 1.4×10^{-8} to 1.7×10^{-6} dpa/s. In contrast to the austenitic alloys, no effect of dpa rate on the amount of swelling observed was found. The authors suggested that this is because the samples were still in the transient regime, and steady state swelling had not yet been achieved at these doses. Garner et al's [8] comparison of swelling in austenitic and ferritic steels concludes that ferritic steels swell less than austenitic steels primarily due to a much longer transient regime prior to steady state swelling. In support of Okita et al's expla-

nation, data from another FFTF irradiation at higher flux shows the transition to steady state seems to occur at doses >100 dpa [8], higher than received by these specimens.

Boulanger and Serruys [157] irradiated thin foils of Eurofer97 and a model Fe-9Cr alloy to 3 dpa at 350 and 550°C at two dose rates, 2.8×10^{-3} and 1.4×10^{-4} dpa/s, with Kr ions and analysed the samples by TEM. At 350°C no defects were observed in Eurofer97 at the higher dose rate, but at the lower dose rate loops were seen. The model alloy showed an increase in loop size for the lower dose rate - a bimodal distribution of 7 and 28 nm loops compared to < 5 nm loops for the higher dose rate. At 550°C loop sizes were much larger than at 350°C, and both alloys showed an increase in both loop size and density for the lower dose rate. At the higher dose rate loops had a maximum size of 150 nm in both alloys, and at the lower dose rate the maximum observed sizes were 300 and 400 nm in Eurofer and the model alloy respectively. For the lower dose rate the loop number density was at least double that of the higher dose rate in both alloys. There was a discrepancy in damage level between the two dose rates, with the lower dose rate receiving a higher dose than the higher dose rate, so it is difficult to draw firm conclusions about the effect of dose rate from this experiment.

Hardie et al. [154] irradiated ultra high purity Fe, Fe-5Cr, Fe-10Cr and Fe-14Cr alloys at 300, 400, and 500°C with Fe ions at two dose rates, 6×10^{-4} and 3×10^{-5} dpa/s. The total dose received was 0.6 dpa as calculated using the full cascade option in SRIM [22]. Nanoindentation showed a greater increase in hardness for the Cr containing materials irradiated at the lower dose rate than at the higher dose rate at 300°C (figure 2.21). The influence of dose rate was found to reduce with increasing Cr content. No difference in hardening due to dose rate was observed in pure Fe or Fe-14Cr. The trend regarding Cr was thought to be due to trapping of point defects by Cr [31,32,36,38], and supported by an appearance of a dose rate effect in Fe-14Cr at 400°C (but not 300°C), where defects are more mobile.

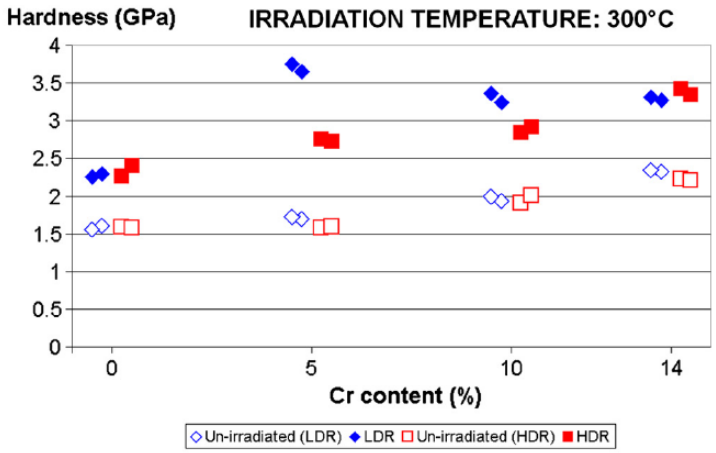
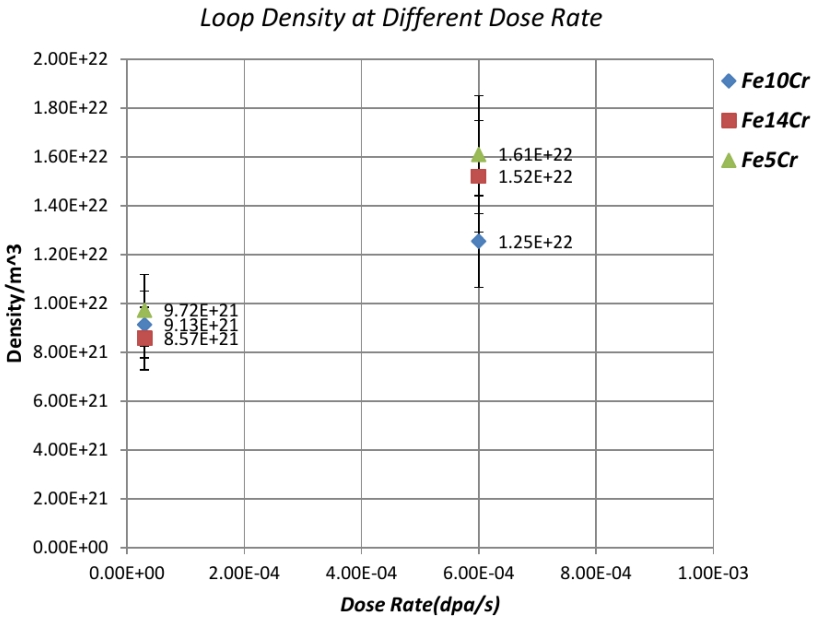


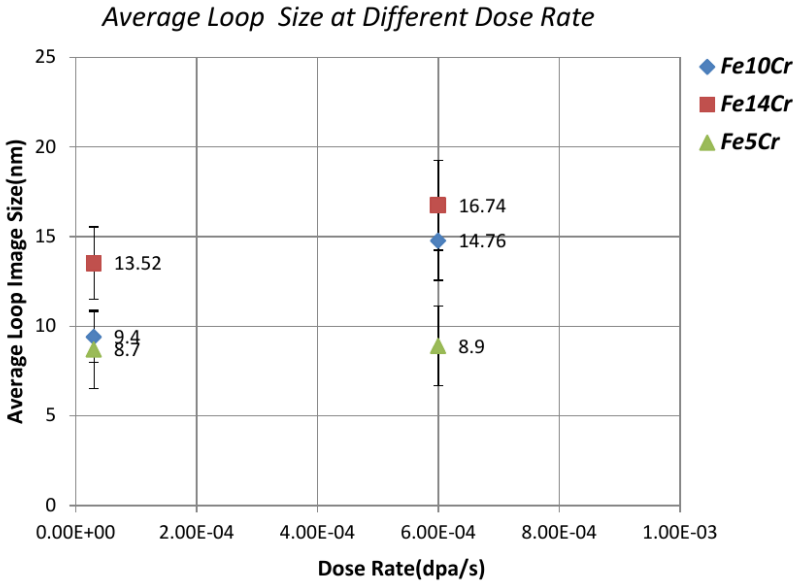
Figure 2.21: Nanoindentation hardness of ultra high purity Fe and Fe-Cr alloys irradiated at 2 dose rates at 300°C. A pronounced effect of dose rate on the post-irradiation hardness of the Fe-5Cr sample can be seen, with a lesser effect for higher Cr concentrations. From [154].

TEM analysis of the 300°C Fe-Cr samples (additional details in [47]) revealed an increase in average loop size and density for all materials at higher dose rate, as shown in figure 2.22. This is in contradiction to the Boulanger study [157], possibly due to the uncertainty in dose measurement reported there for the lower dose rate. The two studies may not be directly comparable, as Boulanger irradiated samples as thin foils and Hardie et al. irradiated bulk samples which were later thinned. The free surface can have a strong effect on vacancy cluster formation in Fe [158], and act as a sink for point defects. Hardie et al.'s work is therefore more likely to be relevant to real bulk irradiations than Boulanger et al.'s.

Regarding the mechanical properties, this means that the dose rate effect is likely caused by obstacles other than simple dislocation loops, which present a stronger barrier to dislocation glide. Atom probe tomography performed on the Fe-5Cr sample irradiated at 400°C revealed areas of Cr enrichment, possibly associated with dislocation loops, which had a larger size and higher number density for the lower dose rate sam-



(a)



(b)

Figure 2.22: (a) Loop densities and (b) average sizes for Fe-Cr alloys irradiated at different dose rates at 300°C, showing an increase in size and density at higher dose rate. Figures from [47].

ple [154]. These are thought to be responsible for the increase in hardness. The enriched regions/precipitates may be suppressed at higher dose rate where mutual recombination is increased, and so point defects migrate over shorter distances on average before annihilating. Similar behaviour was noted in grain boundary segregation in austenitic alloys by Allen et al. [152].

2.4.2.3 Mansur Shift

The review of work presented above demonstrates that dose rate can significantly affect both the microstructure and mechanical properties of irradiated materials. Mansur [147, 159] presented a method whereby a difference in dose rate can be compensated by a shift in temperature (or dose). In [159] expressions are derived for the number of point defects lost to sinks or recombination for sink-dominated and recombination-dominated regimes as well as for the intermediate case. A framework is defined where the change in dose, temperature, or dose rate required to maintain the same loss of point defects to either sinks or recombination as for another dose/temperature/dose rate combination can be calculated. In [147] a temperature shift for maintaining the net flux of vacancies to voids is given, which is related to the swelling rate.

For a recombination dominant system, the temperature shift to maintain the number of defects absorbed at sinks constant for two different dose rates is given by equation 2.5 [159]:

$$T_2 - T_1 = \frac{\frac{kT_1^2}{E_v^m} \ln\left(\frac{G_2}{G_1}\right)}{1 - \frac{kT_1}{E_v^m} \ln\left(\frac{G_2}{G_1}\right)} \tag{2.5}$$

where k is Boltzmann's constant, T is temperature, E_v^m the vacancy migration energy, and G the point defect generation rate - derived from the dose rate.

Was et al. performed experiments using a temperature shift to compare neutron irradiation with proton irradiation in austenitic steels; and with Fe ion irradiation in ferritic/martensitic steel. Unfortunately details of how the magnitude of temperature shifts were selected were not given for either experiment.

Was et al.'s first study [160] used proton irradiation with a dose rate of ~7×10^{-6} dpa/s at 360°C to emulate neutrons irradiation with a dose rate of 2 - 10×10^{-8} dpa/s at 270 - 284°C in 304SS and 316SS. Several doses were produced, ranging from 0.3 to 5.0 dpa. A wide range of post irradiation characterisation was carried out and good agreement was found between the two irradiation modes. A slightly smaller and less dense loop population was observed for the proton irradiated samples; but grain boundary chemistry, hardening, and susceptibility to irradiation assisted stress corrosion cracking were well reproduced.

The authors discuss potential proton irradiation neutron-atypical effects, including lower PKA energies with lower intra-cascade recombination producing a greater number of freely migrating defects per dpa [139, 140, 161]. This raises questions of dose equivalence when compared to neutron irradiation to the same nominal dpa level. The method of dose calculation used a displacement energy of 25 eV, and was reported as resulting in a dose about a factor of 1.8 smaller than when using the commonly recommended 40 eV for Fe-based alloys [22]. Hydrogen retention may also be an issue, where the irradiated protons persist and are retained within the material after irradiation, although no cavities or bubbles were reported.

The second study [162] used 5 MeV Fe ions at 460°C to 188 dpa with He pre-

implantation to emulate neutron irradiation at 443°C to 155 dpa in HT9. Figures 2.23 and 2.24 describe the post irradiation microstructure for both conditions. Overall the ion irradiation experiment reproduces the neutron irradiated microstructure well.

The authors raise the question of how close the agreement should reasonably be expected to be. Neutron irradiations can span a significant period of time, and temperatures may vary over the duration (estimated by the authors to be 40 - 50°C in this case). Kiritani et al. [163] demonstrated the importance of avoiding the exposure of samples to low temperature neutrons during start up which can significantly effect the final damage microstructure. Figure 2.25 shows a dramatic difference in void size and number density in Ni at 400°C between samples exposed to neutrons at a lower temperature during reactor start up ("conventional control") and shutdown and those held at a more constant temperature ("improved control").

Both the above studies appear to successfully use ion or proton irradiation to reproduce the neutron irradiated microstructure, overcoming differences in dose rate by employing a temperature shift. The lack of data from an ion irradiation with no temperature shift casts doubt over the particular importance of the change in temperature in reproducing the microstructure, the inclusion of which would convincingly demonstrate. A limitation of this approach is that with a single temperature shift, only one aspect of the damage (e.g. number of defects lost to sinks) can be targeted to be kept invariant. This may be the reason the dislocation structure was less well reproduced than the void structure in both cases.

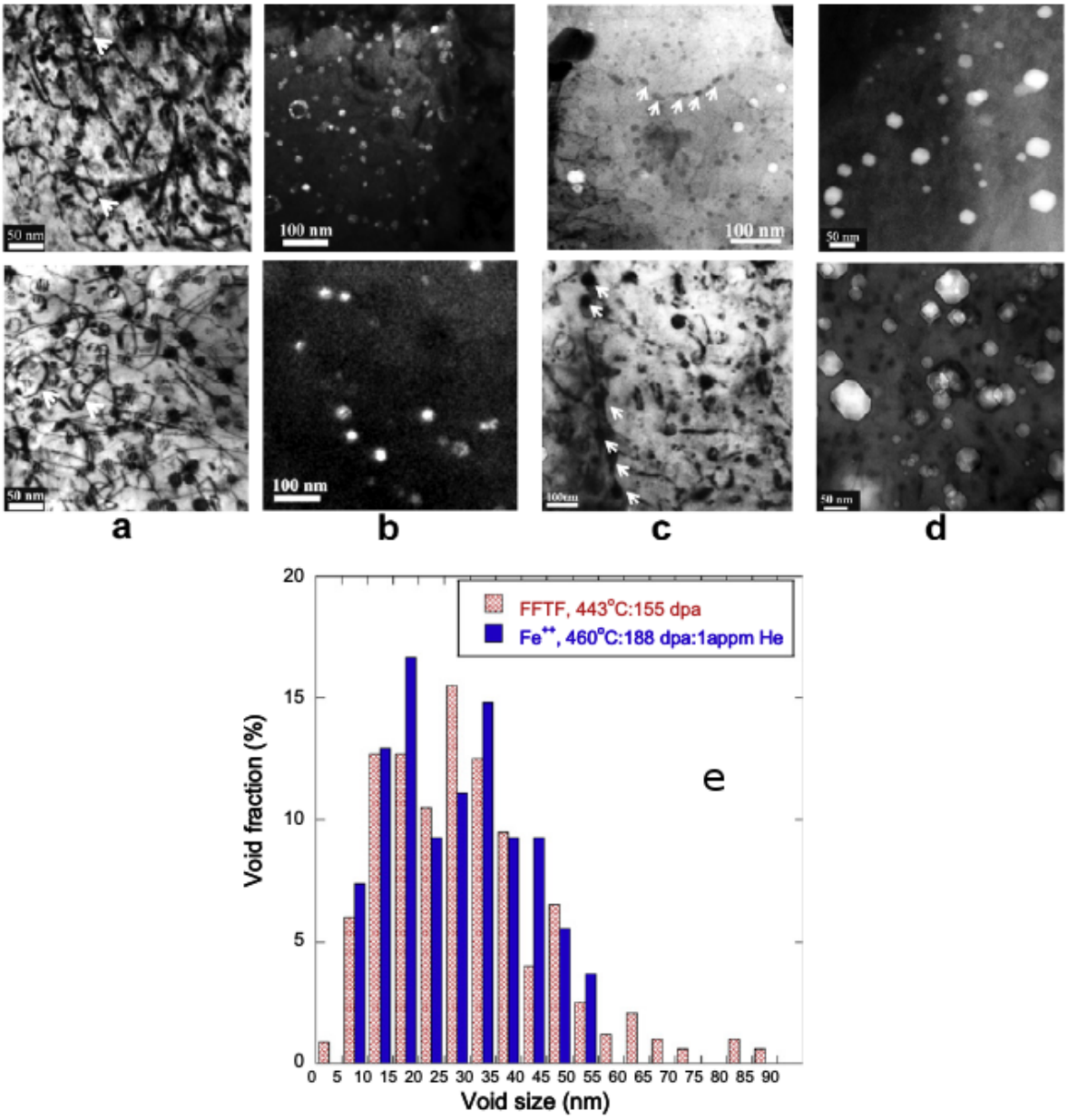


Figure 2.23: Comparison of microstructure ion irradiated (top row) and neutron irradiated (bottom row) HT9. (a) bright field TEM of dislocations and loops, (b) dark field TEM of G-phase precipitates, (c) bright field TEM of G-phase precipitates on grain boundaries, (d) voids, and (e) void size distributions. Figure from [162].

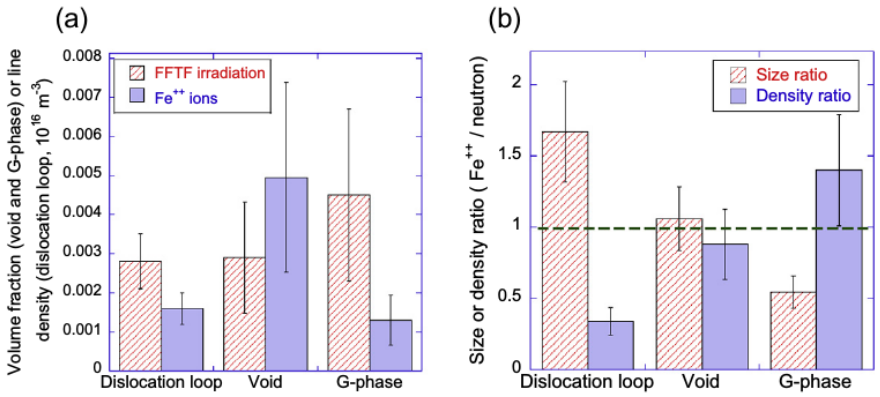


Figure 2.24: Comparison of (a) volume fraction/line density and (b) size and number density ratios for ion and neutron irradiated HT9. Figure from [162].

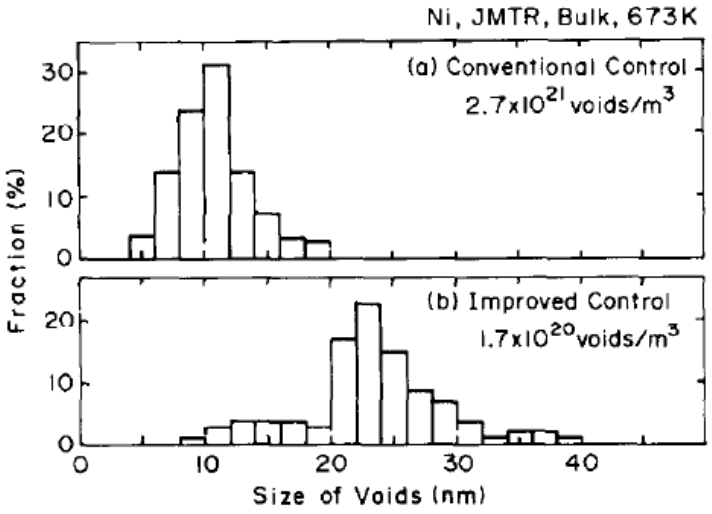


Figure 2.25: Void size and number density in neutron irradiated Ni with conventional and improved temperature control. From [163].

2.4.2.4 Summary

Dose rate has been shown to affect a wide range of radiation damage microstructures. In austenitic steels: swelling is affected by dose rate - both through a shift in peak swelling to higher temperature with higher dose rate [146], and reduction in incubation dose with lower dose rate [149, 150]. Dislocation loop density is seen to increase with increasing dose rate [153], and radiation induced segregation [152] and radiation creep rate [155] found to be enhanced at lower dose rate. Similarly in ferritic steels dislocation loop size and number density were increased at higher dose rate [47] and radiation induced segregation/precipitation enhanced at lower dose rate [154].

The influence is understood through changes in the proportion of point defects undergoing mutual recombination or loss at sinks due to changes in their concentration with dose rate.

Understanding these changes is important for ion-neutron irradiation correlation, which necessarily use vastly different dose rates. Theory [147, 159] suggests a change in temperature can be used to compensate for a difference in dose rate, and experiment [160, 162] has validated this to a degree, although further more methodical experiments are required.

2.4.3 Injected Interstitials

Injected interstitials are an artefact unique to heavy ion irradiation. Incident ions come to rest within the sample, becoming an additional interstitial that would not be there under neutron irradiation. This leads to an imbalance in the number of vacancies and interstitials produced by heavy ion irradiation.

Figure 2.26 shows the damage and implanted ion profiles of a 2 MeV Fe irradiation into Fe predicted by SRIM [21]. It can be seen that both profiles are peaked with ions coming to rest slightly deeper than the damage peak, and that there is strong overlap between the two.



Figure 2.26: Displacements per atom and injected-interstitials per atom as a function of depth for 2 MeV Fe ions implanted into Fe, as predicted by SRIM.

The effect of this defect imbalance on void swelling has been modelled using rate theory. Brailsford et al [164] found injected interstitials can reduce void growth rate, particularly at lower temperatures where mutual recombination is dominant. Plumton et al [165] showed that for injected interstitials to suppress void swelling there must be overlap between the damage region and implanted ion region, and that recombination must be a significant point defect loss mechanism. In another study they showed there was also a reduction of void nucleation, and discussed interplay with dose rate effects [166]. It was suggested that at higher dose rates recombination becomes increasingly important, and therefore so does the injected-interstitials' influence, as they become a

higher fraction of the surviving interstitials. It is also stated that at lower implantation energies there is greater overlap between damage and implanted regions and so greater injected-interstitial influence.

Experimental evidence also suggests a strong injected-interstitial reduction in void swelling. Lee et al. [167] irradiated a previously neutron irradiated austenitic 316 steel sample with 4 MeV Ni ions. The neutron irradiation produced a uniform void structure, so the effect of injected interstitials on void growth could be isolated from void nucleation. A reduction in additional swelling was found in the region of the injected peak.

More recently and in ferritic structured material, Shao et al. [168] irradiated pure Fe with 3.5 MeV Fe ions at 450°C, and measured swelling as a function of depth. An almost complete suppression of swelling was found near the injected peak, as shown in figure 2.27.

Another recent study by Tissot et al. [81] looked at the effect of injected interstitials on chromium precipitation. An Fe-14Cr alloy was irradiated with 2 MeV Fe ions at 300°C, and analysed with atom probe tomography at different depths along the damage profile. It was found that chromium precipitation was suppressed in the region of the injected peak (figure 2.28).

A problem with using single energy implantations with a peaked damage profile is that the dose rate also varies with depth. In both studies [81,168] the observations can be confidently be ascribed to injected interstitials rather than dose rate because areas either side of the peak at similar damage(and therefore dose rate) show different behaviour.

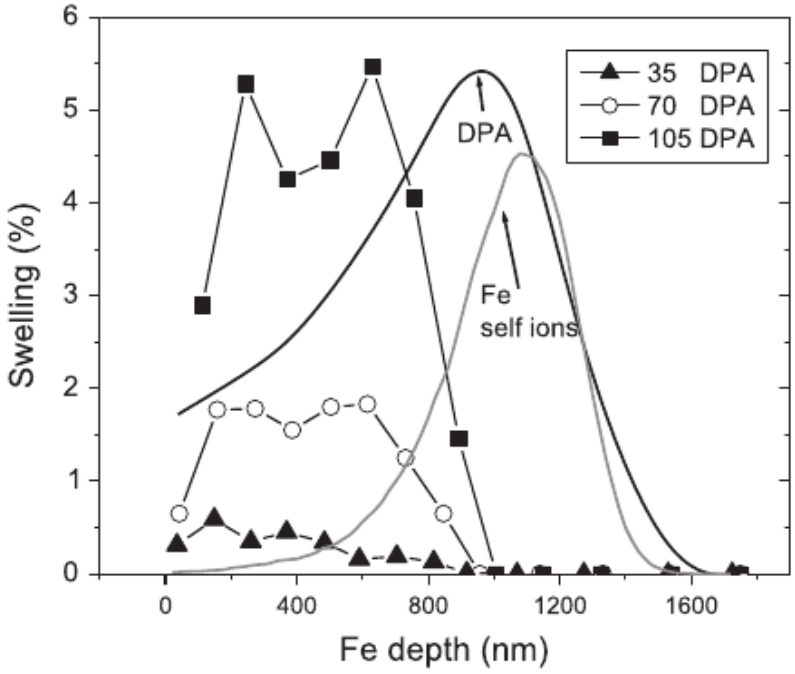


Figure 2.27: Swelling as a function of depth in ion irradiated pure Fe. Specimens were irradiated with 3.5 MeV Fe ions at 450°C. From [168]

2.4.3.1 Discussion

A simple comparison of the damage and implanted ion profiles in figure 2.26 would suggest that the number of defects caused by displacement cascades far outnumber those which are implanted, around 5000:1 at the dpa peak, meaning they should have little effect.

However not all point defects survive the displacement cascade; many quickly recombine as the lattice reforms in its wake. The defect production efficiency is defined as the ratio of the Frenkel pairs that survive the cascade to those predicted by the NRT model, and has been studied by molecular dynamics in Fe (eg [25, 134]), and reviewed by Malerba [133]. The results are summarised in figure 2.29, taken from Malerba's article. A variety of potentials predict a defect production efficiency of around 0.3 for implantation relevant energies.

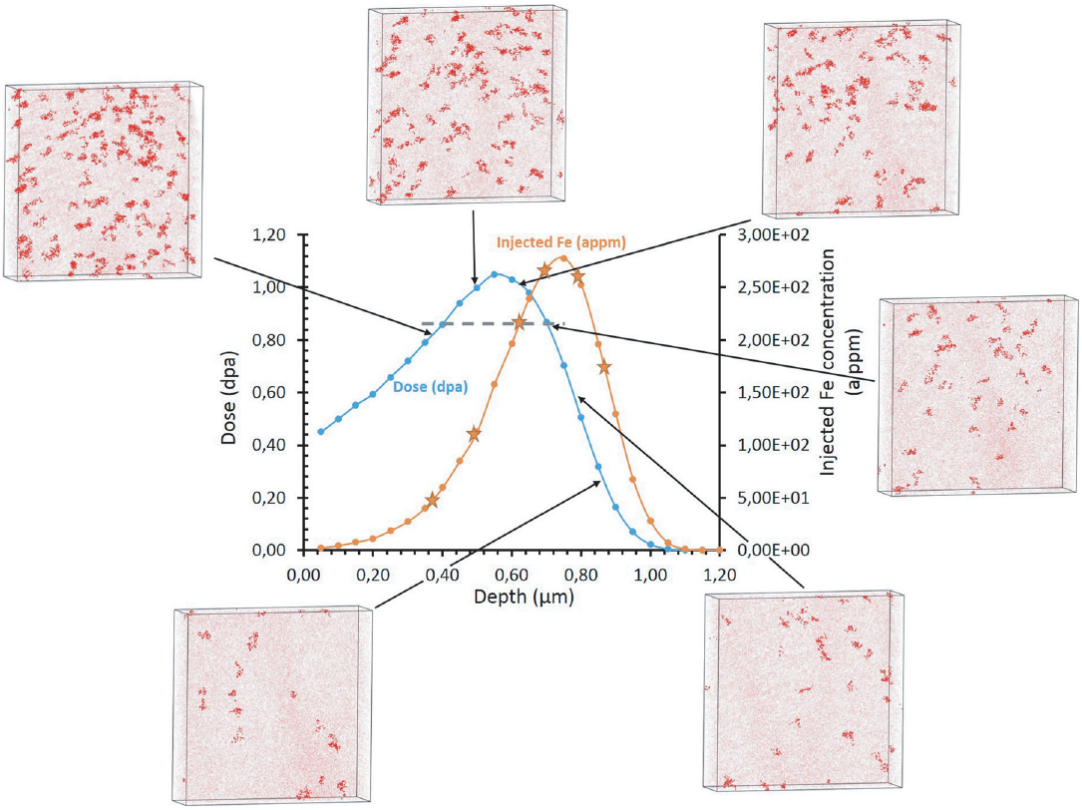


Figure 2.28: From [81], showing α' precipitation as a function of depth in an ion irradiated Fe-14Cr alloy. Concentrations above 24 at% are highlighted. α' precipitation can be seen to be suppressed in regions of high injected interstitial concentrations.

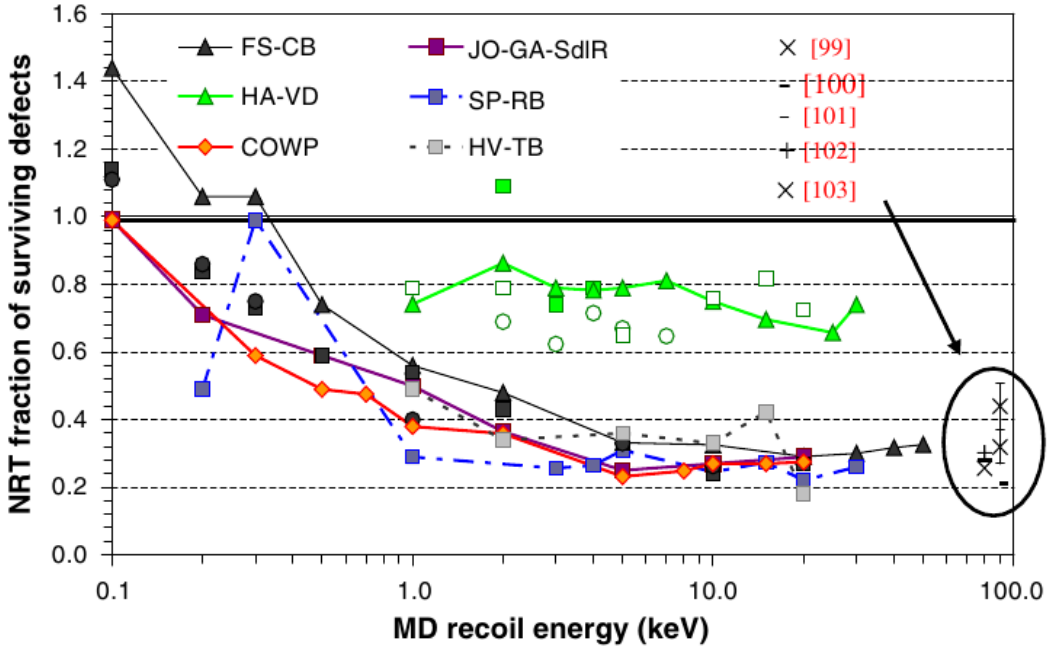


Figure 2.29: Efficiency of point defect production as a function of recoil energy, taken from [133]. Each colour represents a different potential, and triangles, diamonds and squares represent simulations at 100, 300 and 600 K. The group of markers circled correspond to experiments [169–173].

This is in agreement with the cryogenic temperature in-situ irradiation resistivity experiments, which are also plotted. These experiments [169–173] and others [174, 175] measure the resistivity of samples during neutron irradiation at low temperature (5 K). The change in resistivity is divided by the resistivity of a Frenkel pair to calculate the number of Frenkel pairs. This is compared to the number expected to have been produced for a given fluence of the well characterised neutron source. These studies found defect production efficiencies for Fe in the range of 0.22 to 0.48, in agreement with the above molecular dynamics work.

Due to the short timescales in molecular dynamics (< 200 ps), and the low temperatures in the resistivity experiments (a few K) that prevent diffusion, neither of these methods account for further subsequent recombination. Both methods also only consider individual cascades - explicitly in molecular dynamics, and through the use of the initial damage rate in the resistivity experiments - and so neglect additional recombination during the overlap of cascades. The amount of recombination depends on point defect mobility and concentration, and so on irradiation temperature and dose rate, and also on the availability of sinks. This is discussed further in section 2.4.2. There is evidence [150] to suggest that mutual recombination is dominant even at the moderately high temperature and low dose rate (400°C and 10^{-7} dpa/s) and where sinks (dislocation network) are well developed.

Taking into account only intra-cascade recombination leaves the number of displacement induced defects outnumbering injected defects by around 1000:1. This will be reduced significantly for systems where mutual recombination of point defects dominates over their loss to sinks.

Quantification of the fraction of point defects that recombine rather than accumulate and participate in radiation damage is difficult. An outline of an estimate is given below,

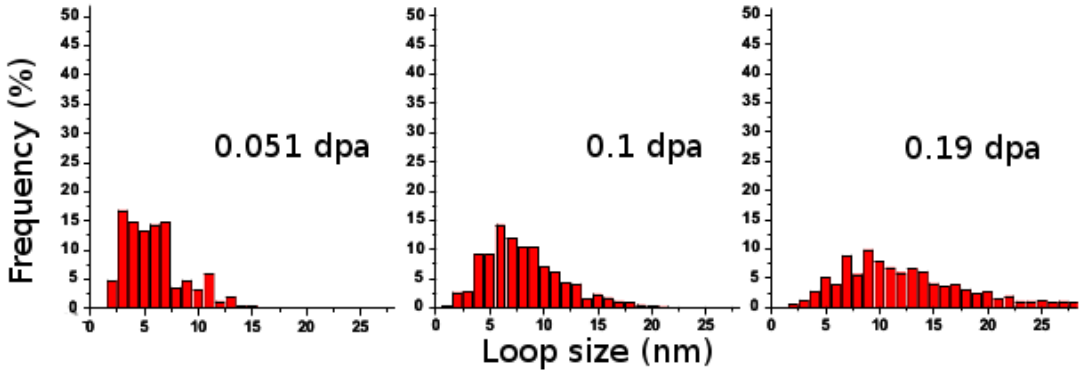


Figure 2.30: Loop size distributions for pure Fe neutron irradiated to various doses at 300°C. Taken from [176].

using TEM data from Hernández-Mayoral and Gómez-Briceño's work [176] on high purity iron neutron irradiated to low doses at 300°C.

Using the size distribution (figure 2.30) and total number of loops reported for each dose, the number distribution of loops as a function of size was obtained. It was stated that 86% of loops were <100>type, so an estimate for the number of defects contained in a loop of a given size was calculated using equation 2.6, treating loops as 2d objects with standard α-Fe packing. N is the number of defects contained in a loop of diameter d, and a_0 is the lattice spacing for Fe.

$$N(d) = \pi \frac{d}{2}^2 \frac{1}{a_0^2} \tag{2.6}$$

The efficiency is defined as this number of visible defects divided by the number expected to be produced for the displacements per atom and number of atoms in the examined volume. For the lowest dose (0.051 dpa) the efficiency is 7×10^{-5}, for the middle dose (0.1 dpa) it is 1×10^{-4} and for the highest dose (0.19 dpa) 3.0×10^{-4}. The reason for the increase in efficiency with increasing dose is probably due to the resolution limit of the TEM. Loops below a certain size are not visible, and those slightly

larger and barely visible are difficult to discern from background noise. As the dose increases the mean size of loops increases, so more of the defects are in larger loops that are visible in the TEM. A typical resolution limit for loops is around 2-5 nm. A certain number of loops can also be lost to the surface of foils. As a rough estimate, this analysis suggests of the order of 1 in 10000 defects produced by displacement damage end up in visible damage, with the rest either recombining or being lost to sinks. This analysis neglects small invisible defects, of which there could be many, and so is likely an overestimate. Numbers in this range mean that injected interstitials can form a significant fraction of the active point defects involved in radiation damage.

2.4.3.2 Summary

Rate theory predicts that injected interstitials can have a strong impact on void swelling, affecting both nucleation [166] and growth [164, 165]. This is supported by experiment [167, 168]. There is also recent experimental evidence to suggest that injected interstitials can suppress α' precipitation in Fe-14Cr [81]. Such pronounced effects from a very small induced point defect imbalance can be conceptually understood due to a large proportion of the defects created undergoing mutual recombination, leading to a greatly increased influence of the extra interstitials.

This has important implications for correlation of ion irradiation to neutron irradiation experiments, particularly where multiple energies are used and so the whole damaged depth contains large numbers of additional interstitials and the injected peak cannot be avoided.

There may also be an interplay between this effect and other factors that influence the proportion of mutual recombination, including dose rate [166].

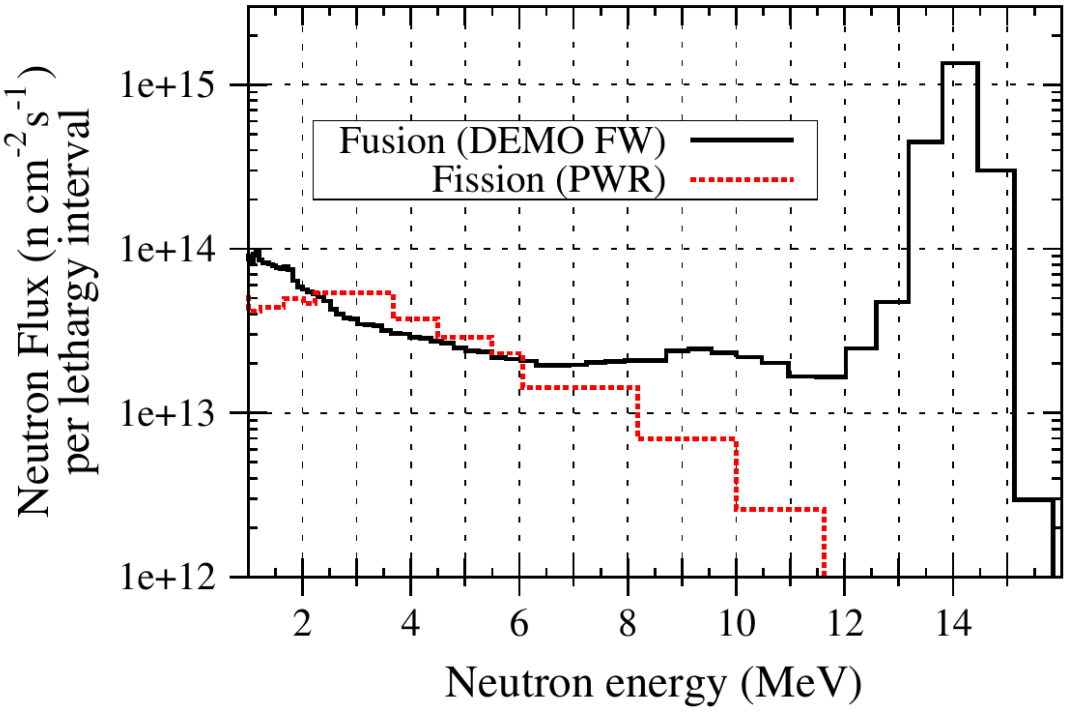


Figure 2.31: Comparison of neutron energy spectra for a fuel assembly in a PWR fission reactor, and outboard equatorial first wall spectrum for a DEMO model. Figure from [179].

2.4.4 Transmutation Gases

Unlike heavy ion irradiation, neutron irradiation can cause transmutation of the struck atom leading the production of He and H. In Fe-Cr alloys, the main nuclear reactions responsible for the production of these gases are ^{56}Fe(n,α)^{53}Cr and ^{56}Fe(n,p)^{56}Mn, with threshold energies of around 3.7 MeV and 2.9 MeV respectively [177]. As can be seen in figure 2.31, a fusion environment will expose materials to a significantly higher flux of neutrons with energies above these threshold values compared to a fission environment. This will result in greater production of gases, around 10-15 appm per dpa of He and 40-50 appm per dpa of H for fusion, compared to approximately 1 and 10 appm per dpa for fission [178].

The lack of a fusion neutron source has meant that most of the neutron irradiation experiments have been performed in a fission environment, with corresponding low levels of gas production. Methods have been used to increase the gas production under a fission spectrum including doping samples with B or Ni [180], and NiAl coating [181]. For heavy ion irradiation where no transmutation occurs, dual/triple beam irradiations have been used where He and H are co-implanted [182]. These techniques have provided insights into the effects of transmutation gases on radiation damage, an understanding of which is important for fusion applications.

2.4.4.1 Microstructure

Prokhodtseva et al. [183] ion-irradiated UHP Fe to 1 dpa with and without simultaneous injection of 1000 appm He at room temperature. It was found that dual beam irradiation (Fe + He) of UHP Fe produced a loop population dominated by $\frac{1}{2}a_0\langle 111\rangle$ loops, as opposed to the $a_0\langle 100\rangle$ dominated population produced by Fe^+ irradiation alone. It was suggested that trapping of $\frac{1}{2}a_0\langle 111\rangle$ type loops by He inhibited their ability to interact to form $a_0\langle 100\rangle$ type loops. Defect density was also observed to be higher in the dual beam case. Similar observations were made by Brimbal et al. [184] at 500°C.

Due to low solubility He tends to combine with irradiation-induced voids and precipitate as bubbles in steels. This has been observed in TEM e.g. [184–187]. Kaiser et al. [185] irradiated Eurofer97 with Fe and He ions at 330,400, and 500°C, producing 26 dpa and implanting 450 appm He. Bubbles were found to be homogeneously distributed at 330 and 400°C, but located at extended sinks such as grain boundaries, dislocation lines and precipitates at 500°C. This is similar to that observed by Yamamoto et al. [186] in a high Ta variant of a tempered martensitic steel, designated F82H-mod3, after neu-

tron irradiation in the HFIR JP26 experiment at 500°C. A Ni-Al coating was used to act as an in-situ He implanter, with thicknesses of 1, 2 and 4 μm producing He/dpa ratios of 10, 20 and 40 all at 9 dpa. A TEM image highlighting the segregation of bubbles to sinks is shown in figure 2.32.

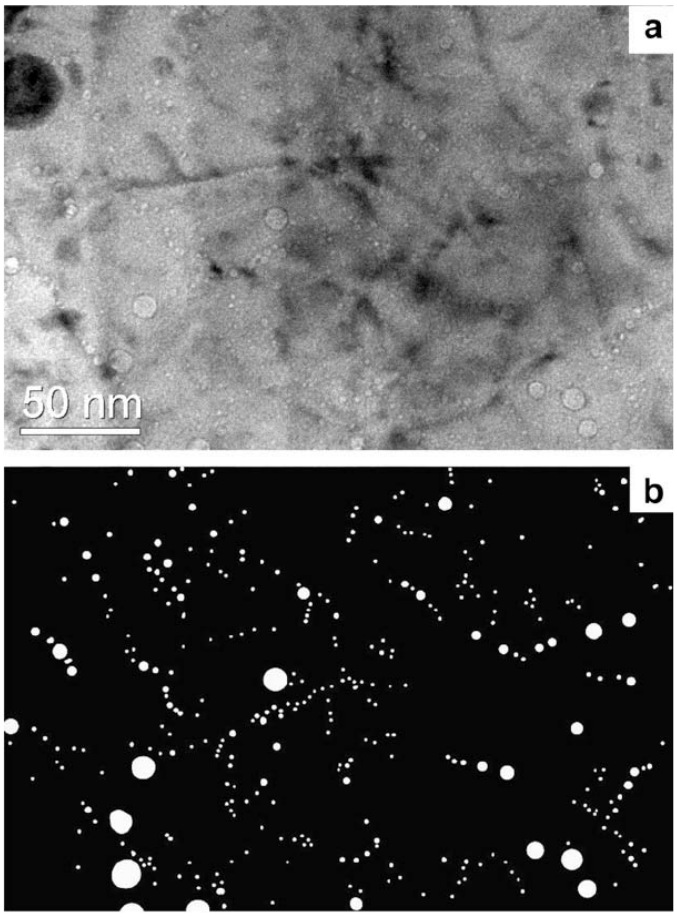


Figure 2.32: (a) 512nm underfocussed TEM image of as tempered F82H-mod3 irradiated to 9 dpa and 380 appm He at 500°C and (b) features identified as bubbles by through-focus image analysis, clearly showing their association with dislocation lines. Figure taken from [186].

2.4.4.2 Mechanical Properties

He bubbles have been observed to have a hardening effect [188]. Grieveson et al. [187, 189] implanted Eurofer with 75 and 2000 appm He at 300°C. A significant in-

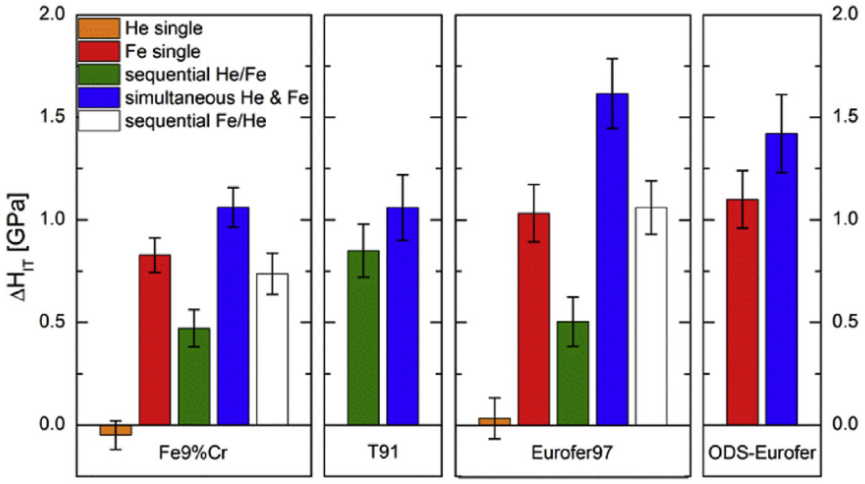


Figure 2.33: Change in nanoindentation hardness at 150 nm after different combinations of Fe irradiation to 5 dpa and He implantation to 100 appm. Figure from [83]

crease in hardness was observed in the 2000 appm He sample, and bubble-like features were seen in TEM. No significant hardening was observed in the 75 appm sample. Molecular dynamics simulations have shown that He bubbles can be strong obstacles to dislocations [190, 191], particularly when the He to vacancy ratio is above ~5, where significant loop punching occurs [191]. Loop punching is the stress induced emission of a dislocation loop by a precipitate, and has been experimentally observed in He bubbles in copper [192] and an aluminium-lithium alloy [193].

Heintze et al. [83] investigated effects of implanted He and heavy ion irradiation at 300°C in Fe-9Cr based alloys. Irradiation with Fe ions to 5 dpa, and He implantation to 100 appm were performed individually, sequentially in both orders, and simultaneously. Changes in nanoindentation hardness are shown in figure 2.33.

Similar to that observed by Grieveson et al., the He implantation to 100 appm alone didn't result in an increase in hardness, but caused a significant increase in hardness over the single Fe irradiation for all materials when injected simultaneously. It was suggested that the simultaneous damage may have assisted the formation of He bubbles.

From the point of view of simulation of neutron damage the presence of He changing the amount of hardening observed is important, as is the fact that pre or post He implantation doesn't appear to reproduce the same hardening as simultaneous implantation.

He has also been observed to have a deleterious effect on the fracture properties of ferritic martensitic steels. Dai et al. [194] implanted T91 with He and performed 3 point bend tests on sub-sized Charpy specimens. The He was implanted in a region below the notch. Pop-in events were observed during tests, where brittle crack initiation and propagation occurred within the He implanted zone, followed by crack arrest in the unimplanted region. Analysis of the crack surface showed two zones, one fully brittle with a significant amount of intergranular fracture as well as cleavage. The depth of the brittle zone corresponded to the depth of He implantation. The second zone was fully ductile in appearance.

Low temperature tests on the same unimplanted material showed a purely cleavage fracture mode. Finite Element (FE) analysis suggests that the principal fracture stress for the implanted material was lower than for the low temperature unimplanted material. Together with the intergranular fracture surface (also observed by Jung et al. [195] in tensile tests of He implanted T91), this suggests that He lowers grain boundary cohesion. This is also supported by modelling work [196].

2.4.4.3 Swelling

Swelling has also been observed to be affected by He. Wakai et al. [197] compared B doped and undoped samples of F82H irradiated in the HFIR reactor at 400°C to 51 dpa. Swelling and cavity formation was found to be enhanced by the presence of He pro-

duced by transmutation of the dopant. Garner et al. [198] also suggested the difference in swelling behaviour observed for FeCr alloys at ~400°C between experiments in the EBR-II and FFTF reactors were due to different He generation rates.

Triple beam ion irradiation experiments have shown there is also a synergistic effect with H on swelling [182, 199, 200]. Tanaka et al. [182] (Fe-Cr alloys) and Wakai et al. [199,200](F82H) both found swelling to be significantly enhanced under triple beam irradiation (Fe+He+H) compared to dual beam irradiation (Fe+He) (Figure 2.34). In [199, 200] the H content was measured during and after implantation (at 470°C), but could not be detected afterwards, likely due to diffusion away of the H.

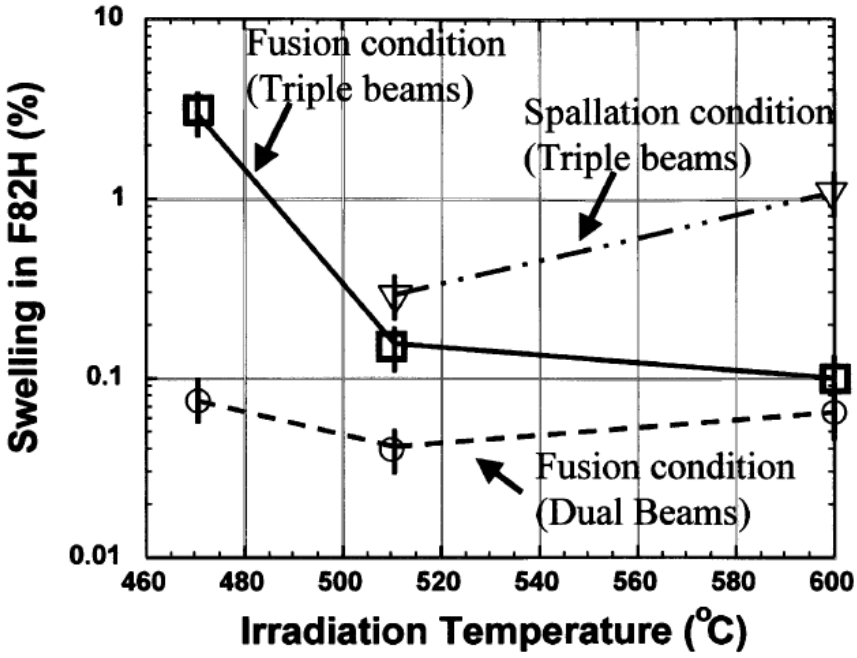


Figure 2.34: Swelling in F82H at different temperatures at 50 dpa with dual (Fe+He) and triple (Fe+He+H) ion beams. Fusion condition refers to 70 appm H/dpa and 18 appm He/dpa. The spallation condition is 1700 appm H/dpa and 180 appm He/dpa. The damage rate was about 1.6×10^{-3} dpa/s in all cases. Figure taken from [199].

2.4.4.4 Heavy Ion - Neutron Correlation

For the study of the effects of transmutation gases, ion irradiation has advantages over neutron irradiation in that it provides an opportunity to study both sequential and synergistic effects, as well as allowing good control over He/dpa ratio. Studies have shown differences in hardening depending on whether gases are injected simultaneously or sequentially, and on the order of injection [83]. A synergistic influence of H and He on swelling has also been demonstrated [182, 199, 200].

Both these results highlight the need for triple beam lines where H and He can be injected simultaneously in order to recreate transmutations in neutron irradiation. Triple beam heavy ion irradiation does however still involve other neutron a-typical effects discussed elsewhere in this section (2.4). The lack of a fusion neutron source and potential severity of the effect of the additional production of gas on fracture toughness [194, 195] presents perhaps the biggest uncertainty in predicting material behaviour in a fusion environment for future reactors.

Differences in neutron energy spectra and dose rates also raises concerns for fission-fusion neutron irradiation correlation, and work is required in this area.

2.4.5 Beam Rastering

For ion irradiation a focussed, scanned beam (also referred to as a rastered beam) is often used, in preference to a defocussed, static beam, to ensure a uniform dose is delivered across the whole target area. ASTM standard E521-77 recommends against this practice; however, this is largely based on a limited set of early experiments from the 1970's which found differences in swelling in pure Ni between samples irradiated with the two

modes [201]. There has recently been a renewed interest in these scanning effects in nuclear relevant steels [12,13], and the implications for heavy ion - neutron correlation.

2.4.5.1 Theory

A rastered beam can be thought of as operating as a pulsed source, where each volume element is irradiated by the beam intermittently - with off periods while the beam scans over the rest of the sample. This causes it to differ from steady state irradiation in 3 ways:

i An increase in instantaneous dose rate due to the dose delivered per unit time being compressed into only the "beam on" periods

ii An induced temporal variation in flux of point defects

iii The presence of "beam off" periods where annealing can occur

For **i**, the degree to which the instantaneous dose rate is increased depends depends on the scanning conditions used. An increase in dose rate causes an increase in point defect concentrations, and therefore an increase in mutual recombintation. This can cause a shift to a higher peak swelling temperature [146], an increase in incubation dose to reach steady state swelling [149, 150], an increase in dislocation loop density [47, 153], and a reduction in RIS [152, 154] and creep rates [155]. Dose rate effects are discussed in detail in section 2.4.2.

Implications of **ii** and **iii** for defect populations and microstructure may be considered by using the Fully Dynamic Rate Theory developed by Ghoniem and Kulcinski [202]. These are discussed, beginning with **ii**, below.

Unlike conventional rate theory, the Fully Dynamic Rate Theory [202] allows interstitial and vacancy concentrations to vary with time, providing insight into non steady-state conditions. As with much of the early work it was motivated by the prospect of pulsed (inertial confinement) fusion reactors and understanding the impact of this pulsed irradiation on damage microstructure. The theory and effects were reviewed by Simonen et al. [203], with figure 2.35 showing changes in defect concentration with time in a pulsed irradiation environment for different vacancy lifetimes and dominant point defect reactions.

For sink dominant conditions (figure 2.35 (a)): when the vacancy lifetime is short compared to the pulse period, their concentration quickly rises and falls to a thermal equilibrium value during the on and off periods. The interstitials have short lifetimes compared to the vacancies [204], so their concentration also rapidly reaches thermal equilibrium values. When the vacancy lifetime is long, there isn't sufficient time for their concentration to fall back to thermal equilibrium values during the off period, so some are retained from the previous pulse and their concentration accumulates over time.

For recombination dominant conditions (figure 2.35 (b)): when the vacancy lifetime is short, again an equilibrium value is quickly reached during on and off periods. The interstitial lifetime is shorter than the vacancy lifetime, so during on period there is a loss of interstitials to sinks, causing the vacancy concentration to grow until the vacancy lifetime, where a steady state is reached due to mutual recombination. When the vacancy lifetime is long compared to the pulse length (figure 2.35 (c)), their concentration builds during the on period and remains approximately constant during the off period, and so builds over each cycle. The interstitial concentration builds at the beginning of the on period and falls due to recombination during it, and rapidly to the thermal equi-

librium value during the off period. Because mutual recombination dominates and the vacancy concentration hasn't appreciably changed during the off period, the interstitial concentration builds to where it was at the end of the last on period, declining with each cycle.

Trinkaus and Ullmaier [204, 206] discussed the processes that are sensitive to these pulsing effects on defect concentrations. Insensitive processes are those which mainly depend on the total dose accumulated - the growth of stable structures (cavities, precipitates), and the segregation of impurity atoms to interfaces and grain boundaries. Processes that require surmounting of a physical or energetic barrier, such as in creep by climb controlled dislocation glide or in nucleation processes, can be sensitive to pulsing effects.

Their work also discusses the conditions under which these pulsing effects can occur, termed absolute dynamic bias and relative dynamic bias. Absolute dynamic bias, Δ, is defined as the magnitude of the excess defect flux integrated over time:

$$\Delta = Ampl\left\{ \int (D_i c_i - D_v c_v) dt \right\} \tag{2.7}$$

where D and c are the diffusivities and concentrations with subscripts i or v designating interstitials or vacancies.

Relative dynamic bias, δ is defined as Δ divided by the integral of the average flux of both defect types over one pulsing period:

$$\delta = \Delta\nu/(D_{i,v}\langle c_{i,v}\rangle) \tag{2.8}$$

where ν is the pulse frequency and $\langle c_{i,v}\rangle$ the average defect concentrations.

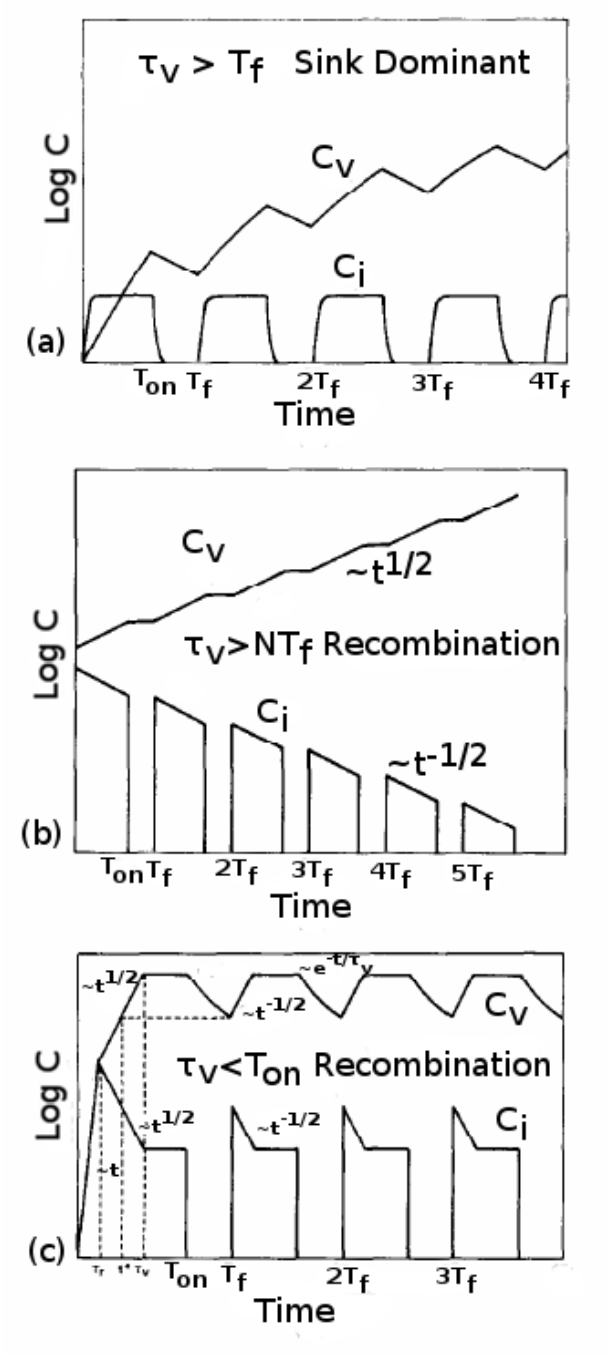


Figure 2.35: Defect concentrations as a function of time under pulsed irradiation. T_{on} and T_f represent beam on duration and total pulse cycle time, C_i and C_v interstitial and vacancy concentrations, and τ_v the vacancy lifetime. (a) depicts sink dominant conditions for long vacancy lifetimes, (b) for recombination dominant conditions and vacancy lifetimes longer than the period of examination, and (c) for recombination dominant conditions and short vacancy lifetimes. Figure from [203] (originally from [205]).

δ varies from 0 for continuous irradiation to 1 for extreme pulsing, giving a measure of relative changes in defect flux over a pulsing period. Δ is a measure of the magnitude of the variation.

The authors argue that a sufficiently large value of both of these quantities is necessary to observe any differences with continuous irradiation - δ so that the pulsing creates significant variations, and Δ so that these variations are large enough to have an impact on microstructure. In [206] it was concluded that for a planned European Spallation Source (ESS) at relevant temperatures, with a pulse length of $1\mu s$ and a repetition frequency of 50Hz, the δ condition was fulfilled, but with an average damage rate of 2×10^{-6} dpa/s, the damage per pulse of 4×10^{-8} dpa was too low to fulfil the Δ condition to affect either cavity nucleation or irradiation creep.

Point **iii**, inter-pulse annealing, is also treated by the Fully Dynamic Rate Theory, and discussed by Simonen et al. [203]. Non-equilibrium microstructures can anneal during beam off periods, with higher sensitivity at lower doses where defect sizes are smaller so can anneal more quickly, and for longer off periods and higher temperatures where annealing is enhanced.

Void nucleation can be reduced under pulsed conditions if small, subcritical [57] voids are able to anneal during beam off periods, effectively meaning an increase in the critical void size. Pulsed irradiation can also promote thermally stable phases and inhibit irradiation induced phases compared to steady irradiation, if significant recovery towards the equilibrium state can occur during the beam off periods.

2.4.5.2 Experiments - Pulsed Irradiation

A number of studies were conducted during the late 1970s and '80s to study the influence of pulsing on radiation damage in a variety of materials. As mentioned in section 2.4.5.1, this work was motivated by the prospect of fusion reactors operating in a pulsed fashion, and so beam on and off times are considerably longer than would generally be found for irradiation using a scanned beam. A summary of changes in microstructure found in these experiments is given below.

In Ni, Brimhall et al. pre-irradiated specimens at high (775-975 K) [207] and low (675, 725 K) [208] temperatures, and compared the microstructure by TEM analysis after subsequent irradiation in a continuous and pulsed manner. Pulsed irradiations were 10 s on and off periods, produced by beam blanking.

For the samples pre-irradiated at the high temperature [207], no discernible effect of pulsing was found in the subsequent irradiation. However for those pre-irradiated at the lower temperature [208], subsequent pulsing lead to a coarser void population, with the biggest effect at high temperatures.

These observations were explained in terms of interpulse annealing. The void population produced by the lower temperature pre-irradiation consisted of a higher number density of smaller voids. These smaller voids are more easily annealed, with a greater effect at higher temperatures. Indeed, an annealing study of these samples found after 90 minutes at 1000 K all voids were removed, with a measurable decrease after 10 s. After 10 s at 975 K almost all < 5 nm voids were annealed. Annealing after continuous irradiation for the sum of the beam off time didn't appreciably change the void population, demonstrating that annealing rate is a function of void size.

Brimhall et al. [209] also investigated pulsed effects in Mo. Samples were irradiated with Ni at 1025-1225 K, continuously and with 5 s beam on and off time. Void nucleation was observed to be delayed by pulsing, thought to be due to interpulse annealing of subcritical voids.

The dislocation structure was found to develop more rapidly under pulsing.

This was the opposite to that found by Lee et al. [210] and Hishinuma et al. [211] in studies on similar austenitic steels, where the dislocation structure developed more slowly under pulsing. Both studies used similar materials, and irradiated with Ni at 950/958 K continuously and with 60 s beam on and off periods. A more refined loop structure was seen by both authors for pulsed irradiation, explained in terms of point defect concentration changes caused by pulsing. Both suggested that loops form quickly during beam on periods where interstitial concentrations are high, and then are eroded freely by vacancies during beam off periods where the interstitial concentrations are very low, leading to larger numbers of smaller loops.

In Lee et al.'s [210] Ti modified stainless steel a difference in precipitate formation was observed after irradiation, with pulsing enhancing carbide (MC) formation and retarding the subsequent G phase formation. This is explained by the beam off periods allowing a relaxation towards thermal equilibrium, where the MC phase is favoured.

Lee et al. [210] also found that simultaneous injection of helium to enhanced the pulsing effects, producing a smaller loop population, and enhanced MC stability.

These early experiments demonstrated that pulsing can effect many aspects of damage microstructural development, including dislocation loop and void populations, and precipitate formation. However unlike with beam scanning, these studies used beam blanking to generate the pulsing, meaning there was no change in instantaneous dose

rate for the pulsed condition, and that these samples were irradiated on average more slowly and so exposed to temperature for a longer time. Beam off and on times are also significantly longer than would be typically found for a scanned beam.

2.4.5.3 Experiment - Scanned vs Defocussed

A more limited set of experiments has been performed directly comparing irradiation with scanned and defocussed beams. Results from these studies will be presented below, and then compared to theory. The implications for heavy ion-neutron correlation will then be discussed.

In 1973 Sprague et al. [201] irradiated pure Ni with 2.8 MeV self ions to 16 dpa at temperatures between 350 and 750°C using rastered and defocussed beams. Rastered irradiations were performed with average dose rates of 1.4×10^{-2} and 8.3×10^{-2} dpa/s, and defocussed irradiations at 8.3×10^{-2} dpa/s. Beam scanning resulted in pulses of 2.5 ms on and off, with each on pulse being comprised of 2.5 μs on/off sub pulses [212].

As shown in figure 2.36 (a), beam scanning was found to reduce mean void diameters compared to continuous irradiation with a defocussed beam. Different trends for void sizes with temperature were also found for the two conditions, with defocussed irradiation displaying the expected increase in size with temperature, and the scanned irradiation showing the opposite. It was suggested that time-dependent fluctuations in defect populations could interfere with void nucleation, and that the magnitude of these fluctuations would increase with increasing temperature so could be responsible for the unexpected trend.

Figure 2.36 (b) shows overall swelling as a function of temperature. Data from both

irradiation conditions appear to lie on a single curve, suggesting that beam scanning under these conditions doesn't effect the overall swelling, in that the total flux of vacancies to sinks remains the same. However, some of the data were produced using different dose rates, which shift the peak swelling temperature (see section 2.4.2), and so would not necessarily be expected to fit on a single curve.

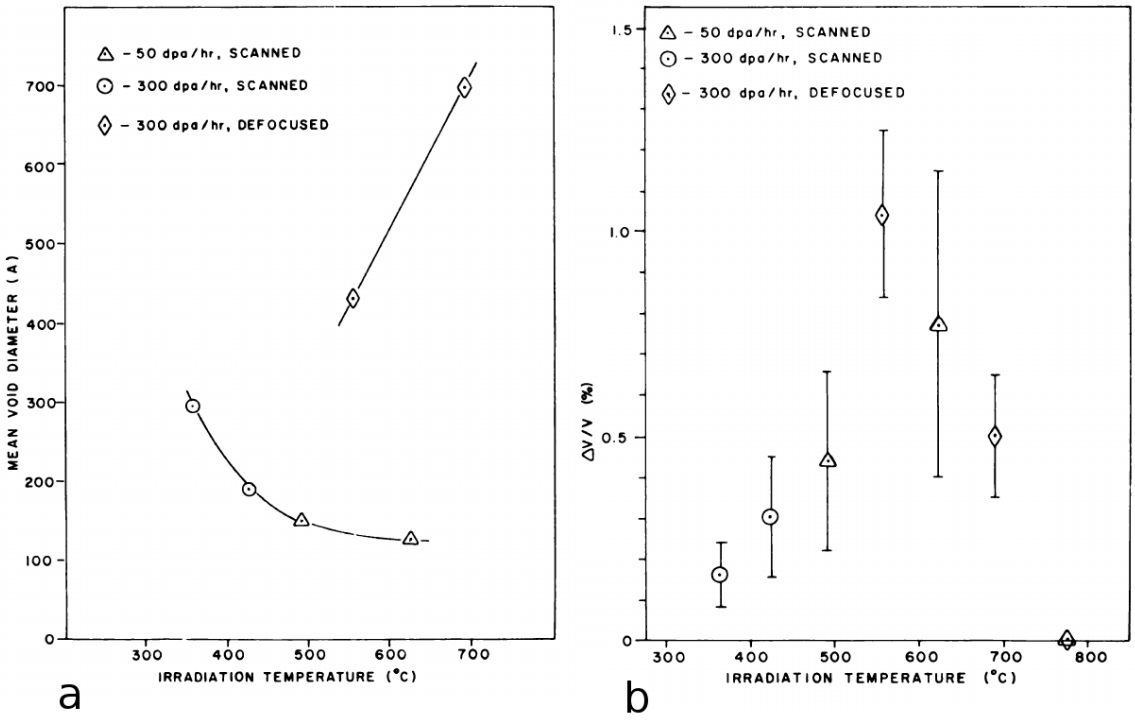


Figure 2.36: (a) Mean void diameter and (b) swelling as a function of temperature for rastered and defocussed irradiation of Ni to 16 dpa. Figure from [201].

More recently Getto et al. [13] investigated beam scanning effects in ferritic-martensitic alloys T91 and HT9. Samples were irradiated with 5 MeV Fe ions to 140 and 150 dpa at 440°C with a dose rate of between 0.792×10^{-3} and 1.92×10^{-3} dpa/s using rastered and defocussed beams. Helium was pre-injected at concentrations of 0, 10, 100 appm.

The beam was scanned at 2061Hz in one direction and 255Hz in the other. Detailed pulse times were not given, but from the beam path irradiation would consist of a similar

pulse/sub-pulse structure to that of Sprague et al. [201] with sub-pulses generated by the faster scanned direction with widths dictated by beam dimensions. Full coverage was achieved every 3.92ms. Microstructures were analysed by TEM at a depth such to avoid influence of the injected interstitial peak (see section 2.4.3).

Both the number and size of voids in these F/M steels were found to be significantly decreased in the samples irradiated in the rastered condition compared to those in the defocussed. The differences were greatest without pre-injected He, where very few voids were observed for the rastered condition, with smaller differences found in samples preinjected with 100 appm He.

Ni/Si rich G-phase precipitates were also formed after irradiation. Samples irradiated with the rastered beam showed smaller and fewer precipitates than those irradiated with the defocussed beam.

A slightly smaller loop size was observed for rastered samples.

As shown in figure 2.37, overall swelling was reduced with rastering for all samples.

Analysis of the ratio of dislocation sink strength to cavity sink strength [213] suggested that those samples irradiated with the defocussed beam were closer to the steady state swelling regime, and that both irradiation modes cause the microstructure to evolve similarly, with beam scanning slowing progression.

Gigax et al. [12] irradiated pure Fe with 3.5 MeV self ions at 450°C to 50 and 150 dpa with scanned and defocussed beams. Scanning was only performed in 1 direction for simplicity, at 0.244, 1.93 and 15.625 Hz. The time averaged dose rate was 1.74×10^{-3}dpa/s for all conditions, with an instantaneous dose rate of 6.26×10^{-3}dpa/s for the scanned irradiations.

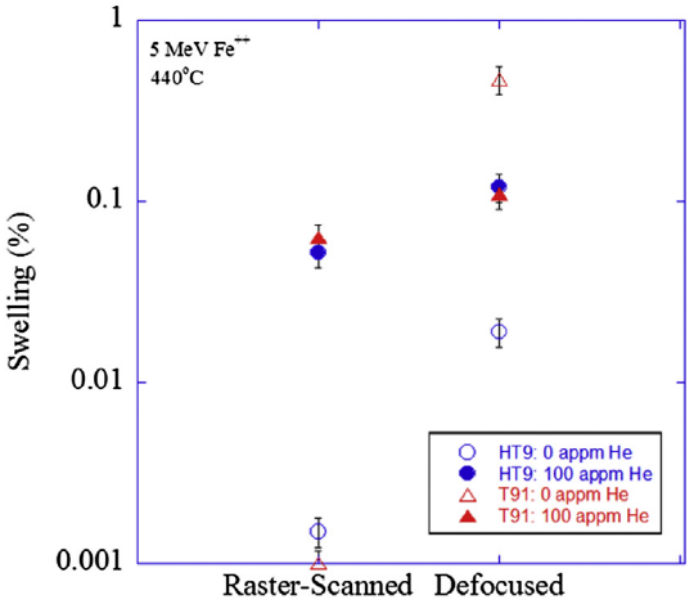


Figure 2.37: Swelling of HT9 and T91 ferritic/martensitic steels irradiated to 140 dpa at 440°C with 5 MeV Fe ions using rastered and defocussed beams. Figure from [13].

As can be seen in figure 2.38, void microstructure was significantly altered by beam rastering. With decreasing scanning frequency voids tended to become smaller and more numerous, compared to the larger voids seen under defocussed beam irradiation. Overall swelling was reduced by beam scanning.

The lower frequency scanned irradiations also produced voids deeper into the sample, suggesting a possible interplay between pulsing and the injected interstitial effect (see section 2.4.3).

2.4.5.4 Discussion

Here the results will be discussed in terms of the scanning induced artefacts outlined in the theory section (section 2.4.5.1): **i** change in instantaneous dose rate, **ii** temporal variation of point defect fluxes, and **iii** annealing during "beam off" periods.

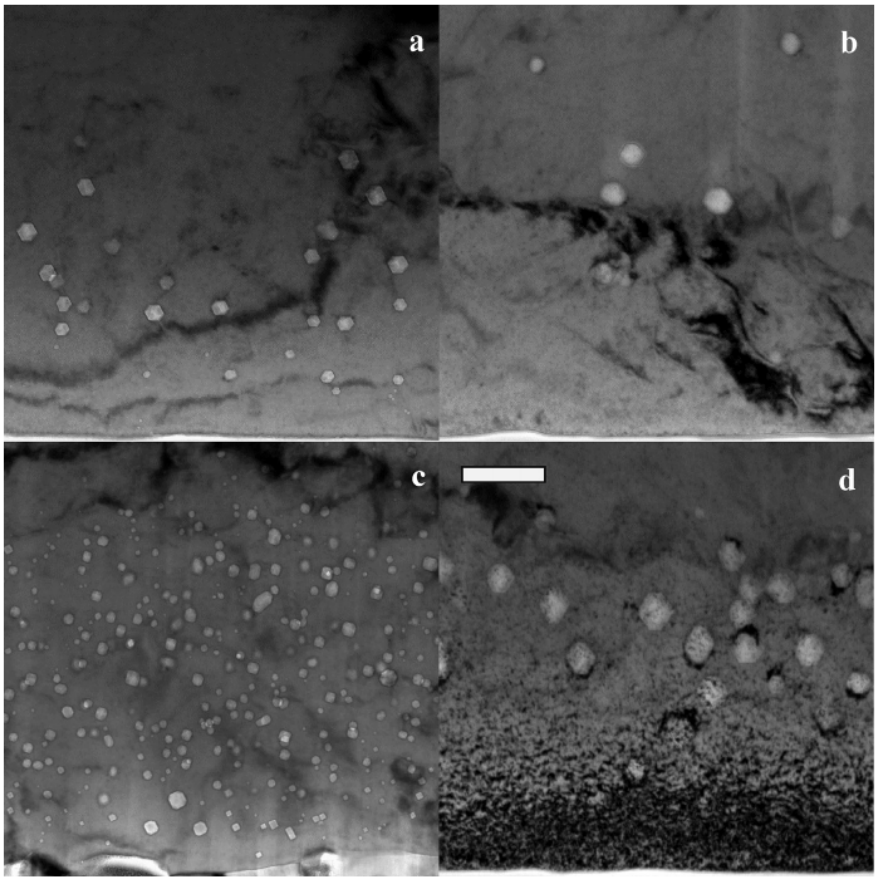


Figure 2.38: Micrographs showing voids in Fe irradiated at 450°C to 150 dpa using beams rastered with frequencies of (a) 15.93 Hz, (b) 1.95 Hz, (c) 0.244 Hz and (d) with a defocussed beam. The time averaged dose rates were 1.74×10^{-3} dpa/s for all conditions, with an instantaneous dose rate of 6.26×10^{-3} dpa/s for the scanned irradiations. The scale bar denotes 250 nm. Figure from [12].

In Gigax et al's [12] study, beam scanning produced the same instantaneous dose rate for all frequencies used. As can be seen in figure 2.38, the void structures are markedly different for different scanning frequencies, suggesting that the increase in instantaneous dose rate over that of the defocussed irradiation is not solely responsible.

This frequency sensitivity is a significant observation, and further work is required to fully understand this in terms of defect fluxes and annealing during beam off periods. For emulation of steady state neutron irradiation it is important to establish experimentally whether there are bounds to the range of frequencies where pulsing effects occur.

In their paper Getto et al. [13] considered the scanning frequency below which local heating by the beam becomes significant, by calculating the fraction of heat lost between on periods. For ferritic-martensitic alloys, it was found that pulses with frequency >2 Hz should result in <0.03 of the heat applied by the beam to be lost between pulses, and so negligible changes in temperature or associated effects.

Gigax et al. [12] used frequencies below this, but thermal imaging only measured a maximum temperature rise of 4-6°C due to beam heating, so is unlikely to have had a significant impact on the damage microstructure. For experimental conditions where a significant fraction of the heat supplied to the specimen is deposited by the beam however, this temperature pulsing could become significant.

An upper frequency limit for pulsed effects of 500 Hz for a dose rate of 10^{-6}dpa/s in stainless steels is given by the Fully Dynamic Rate Theory [214]. However, this is a continuum rate theory and doesn't consider nucleation processes. Mansur et al. [215] considered the effect of temporally and spatially inhomogeneous point defect production by cascades. Their analysis suggested the arrival of point defects to any point was inherently pulsed due to the intermittent production of nearby cascades. A more complete theory including this effect and nucleation processes would provide a better understanding.

2.4.5.5 Summary

A limited number of static/scanned beam irradiation comparison experiments have shown that beam scanning can influence damage microstructure [12, 13, 201].

Void sizes were found to be reduced by beam scanning in all 3 experiments, in agreement with other simple pulsing experiments [208, 209]. Overall swelling was reduced in 2 cases [12, 13] and in the 3rd [201] it appeared to remain unchanged, but differences in dose rates cloud the interpretation.

G-phase precipitate sizes and number densities were found to be reduced by beam scanning [13], again in agreement with simple pulsing experiments [210].

Loop sizes were only reported by one beam scanning study, and were found to be unchanged within experimental error [13]. Earlier pulsing experiments found dislocation structure to develop more slowly under irradiation in austenitic steels [210, 211], and more rapidly in Mo [209].

Pulsed flux effects are understood through fully dynamic rate theory [202], and occur because of changes in instantaneous dose rate, temporal variations in point defect fluxes, and thermal annealing during "beam off" periods. The reported frequency sensitivity [12] suggests that changes in dose rate are not the sole factor. The rate theory is a continuum model, and so doesn't take into account the inherently pulsed arrival of defects produced by nearby individual cascades [215] for all irradiation conditions.

Further work is required to understand the effect of additional pulsing on nucleation and damage processes and the relation to damage microstructure. For neutron irradiation emulation by heavy ions, it is important to establish both theoretically and experimentally the conditions under which beam scanning can affect damage microstructure,

which damage processes are sensitive, and any synergistic effects with other neutron atypical effects (e.g. injected interstitials [12] and He).

2.5 Heavy Ion vs Neutron Irradiation Comparison Experiments

A relatively small number of studies have been made directly comparing the effects of heavy ion and neutron irradiation in Fe-Cr model alloys. They do however analyse a range of microstructural features.

Pareige et al. [82] irradiated Fe-9Cr and Fe-12Cr alloys at 300°C to 0.5 dpa using Fe ions with energies of 0.5, 2.0, and 5.0 MeV. The microstructure of these materials was characterised by APT, and compared to samples neutron irradiated to 0.6 dpa at 300°C (characterised in [78, 216, 217]).

3D reconstructions for the Fe-12Cr alloy after both ion and neutron irradiations are shown in figure 2.39.

The most notable observation was that Cr enriched α' clusters were not found after ion irradiation, but were present after neutron irradiation. The authors suggested that the difference in dose rate by a factor of ~1000 meant that the clusters had insufficient time to form in the ion irradiated case.

P and Si enriched clusters were observed under both irradiation species, and with similar number density and radii. The enrichment however was found to be higher under neutron irradiation.

Hernandez-Mayoral et al. [218] examined the same materials as Pareige et al. [82]

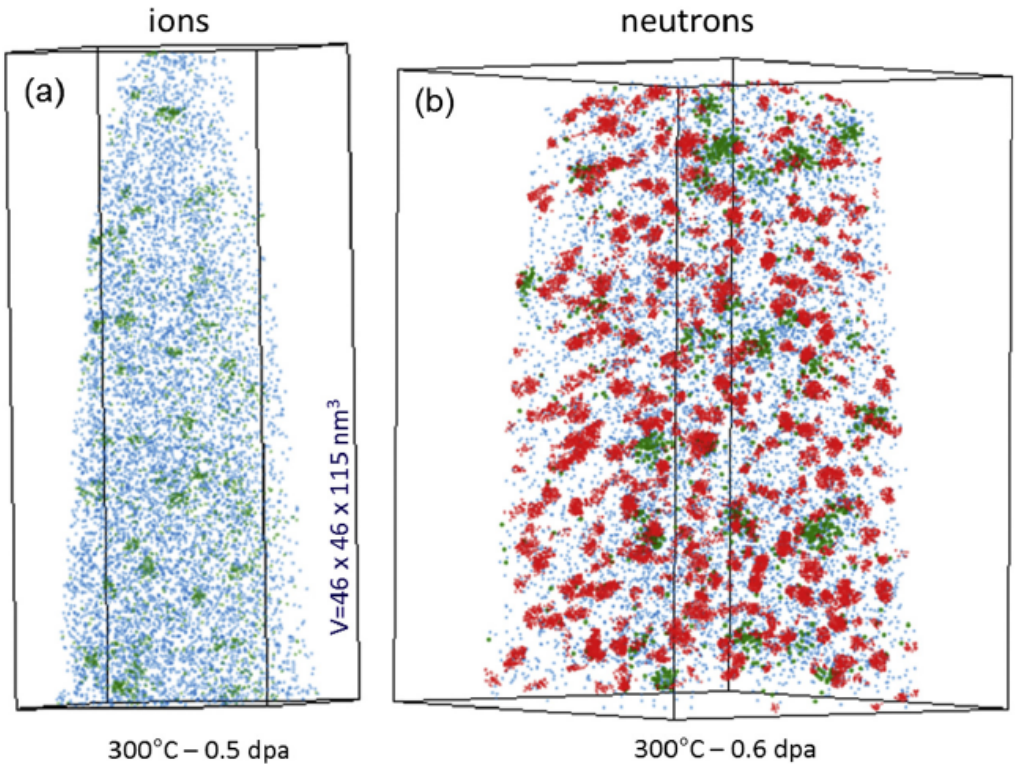


Figure 2.39: 3D APT reconstructions of an Fe-12Cr alloy irradiated with (a) ions and (b) neutrons. Si atoms are marked in blue, and P atoms in green. Red denotes Cr clusters with composition greater than 28%. Figure from [82].

with TEM, studying the full range of Cr contents: 2.5, 5, 9 and 12% Cr. The most striking finding was related to the spatial distribution of dislocation loops. In the neutron irradiated specimens, loops were found to be homogeneously distributed only in the 2.5% Cr alloy, and preferentially located close to dislocation lines and grain boundaries in the 5, 9 and 12% Cr alloys. In the ion irradiated specimens however, loops were found to be spatially homogeneous in all alloys.

The authors suggest that the ~1000 times difference in dose rate is the likely cause of this observation. They argue that for a high dose rate (ion irradiation) the concentration of point defects is high, and so loops can grow to TEM visible sizes close to where they are nucleated - leading to a homogeneous spatial distribution. For a low dose rate (neutron irradiation) the concentration of point defects is lower, and small loops have a reduced chance to interact with point defects and grow. They are mobile and so can migrate to a dislocation line or grain boundary, where they can grow to TEM visible sizes.

Hardie et al. [14] compared the mechanical properties of an Fe-6Cr alloy irradiated with heavy ions and neutrons. The neutron irradiated specimen received a dose of 1.7 dpa at 288°C. Fe ions with a range of energies from 0.5 - 9 MeV were used to irradiate another specimen also at 288°C. Due to discrepancies between models within the SRIM code [22] the ion irradiated specimen received a dose equivalent to the neutron dose of only 0.82 dpa.

Nanoindentation and microcantilever testing were performed to measure the hardness and proof stress respectively. The results are shown in figure 2.40.

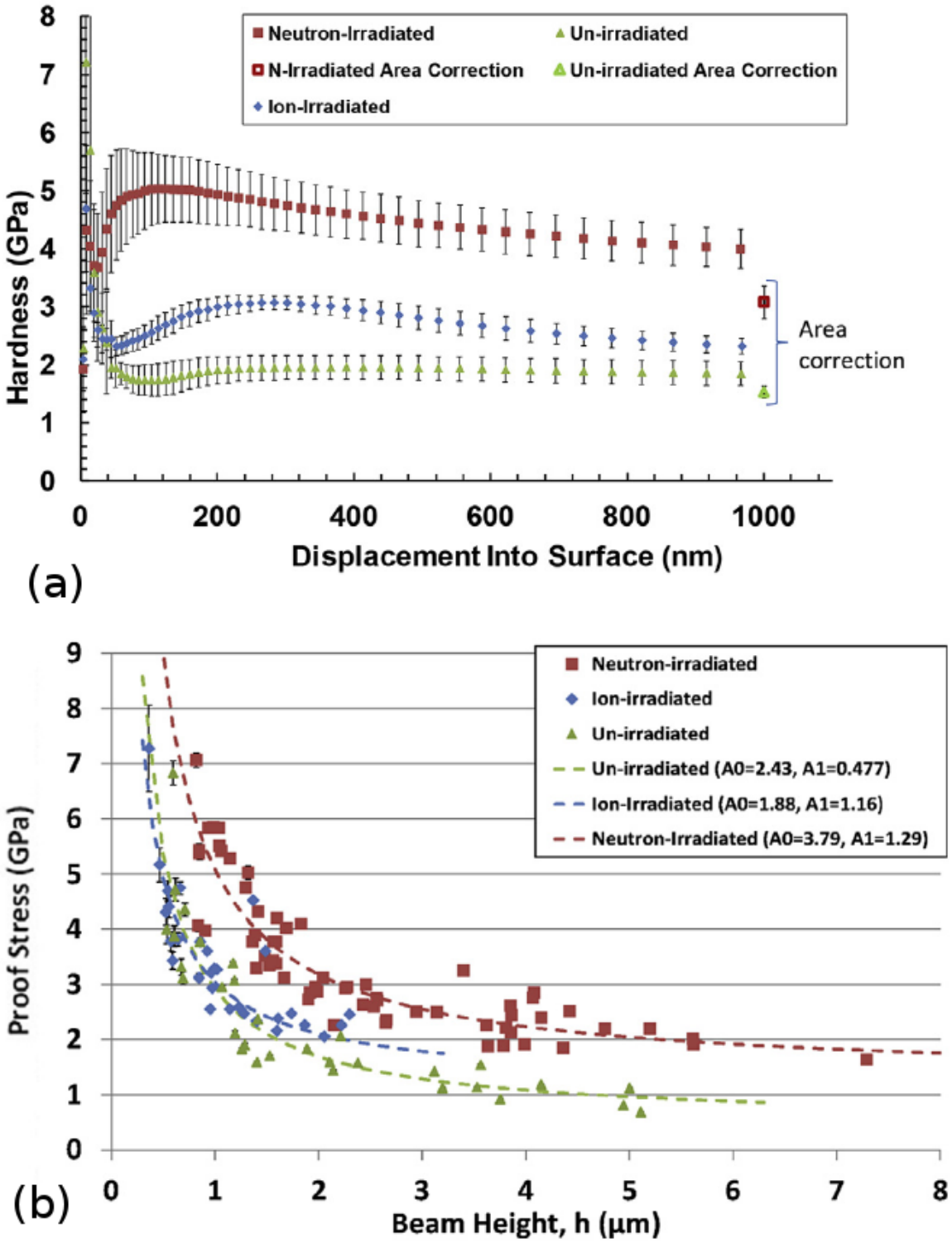


Figure 2.40: (a) Nanoindentation hardness of heavy ion-, neutron-, and unirradiated Fe-6Cr. (b) Proof stress from microcantilever testing of same materials. Figure from [14].

The neutron irradiated specimen was found to have a significantly higher hardness and proof stress than the ion irradiated specimen. TEM [219] and APT [94] analysis of the same materials showed dislocation loops decorated with Si for both specimens. In the neutron irradiated specimen the loop density was found to be higher, and also decorated with Cr.

Orowan analysis showed that the obstacle spacing was significantly less in the neutron irradiated specimen, and that the obstacles were also stronger than in the ion irradiated specimen. It was suggested that this was likely due to the Cr decoration observed only after neutron irradiation.

The authors argued that a combination of differences in PKA energy (see section 2.4.1) and dose rate (see section 2.4.2) lead to a reduction in the number of freely migrating defects and the distance they travel before recombination in the ion irradiated case as compared to the neutron irradiated, and that this was the cause of the lack of Cr (and possible reduction in Si) segregation to loops.

2.5.1 Summary

Only a small number of studies have been performed directly comparing irradiation damage caused by heavy ion and neutron irradiation in Fe-Cr alloys [14, 82, 218], but they have all revealed significant differences between the two.

A more substantial body of work exists in the literature on the impact of the characteristic differences between the two types of irradiation, and this provides a framework within which to understand the observations made in the comparison studies.

Differences in dose rate were highlighted in all the comparison studies as a likely key

factor in the observed microstructural disparity. It is essential that dose rate effects are well understood, as some form of accelerated irradiation is necessary for any predictive studies of in-use reactor components. Some progress has been made using Mansur [147, 159] temperature shifts [160, 162, 220], but no work has yet been performed in model Fe-Cr alloys.

In order for ion irradiation to be proven to be a useful analogue to neutron irradiation for the development and testing of materials there is a need for further comparison studies, with a particular focus on fusion relevant alloy compositions and irradiation conditions.

2.6 Summary & Work Outline

Nuclear fusion will expose materials to high levels of neutron irradiation damage, and the effects of this need to be well understood for the safe and economical running of such reactors.

Heavy ion irradiation has practical advantages over neutron irradiation including lower cost, lack of induced radioactivity, and shorter irradiation times. The quicker turnaround and more precise control over experimental parameters are also strategical and scientific advantages, and mean that without a fusion neutron source, heavy ion irradiation will, alongside neutron irradiation in fission test reactors, play a key role in the investigation of radiation damage for fusion applications.

There are however neutron-atypical aspects to heavy ion irradiation, and these need to be well understood if heavy ion irradiation is to be a suitable emulation technique.

A fairly substantial body of literature exists investigating these aspects, and they are discussed in section 2.4.

One lesser-studied aspect is the impact of beam rastering during heavy ion irradiation (section 2.4.5), and in particular the potential effect of differences in instantaneous dose rate between defocussed and scanned beams. In chapter 4 this is investigated in Fe-Cr alloys.

There have also been relatively few direct comparisons of samples irradiated with heavy ions and neutrons under the same conditions (section 2.5). In chapter 5 a direct comparison is made between the mechanical properties and microstructure of a fusion relevant Fe-9Cr alloy irradiated with heavy ions and with neutrons.

Impurities, and in particular carbon (section 2.3), have been shown to have an influence on radiation damage in steels. The effect of concentration and sensitivity to irradiation parameters need to be well understood, both for comparisons between experiments with samples of different purity, and for alloy design. The effect of carbon concentration and dose rate on radiation damage in Fe are investigated in chapter 6.

Chapter 3

Materials & Methods

3.1 Nanoindentation

3.1.1 Introduction

Nanoindentation was first used by Pethica et al. [221] to measure properties of N irradiated stainless steel in 1982. The technique has since been used in a wide range of applications [222] including to measure properties of thin films and surface coatings.

In relation to the present work, it is a useful technique as it can measure the mechanical properties of the ~1 μm damage layers produced by ion implantation.

Much of the now widely used methodology for data analysis was developed by Oliver and Pharr [223] in 1992, and is described in section 3.1.3.

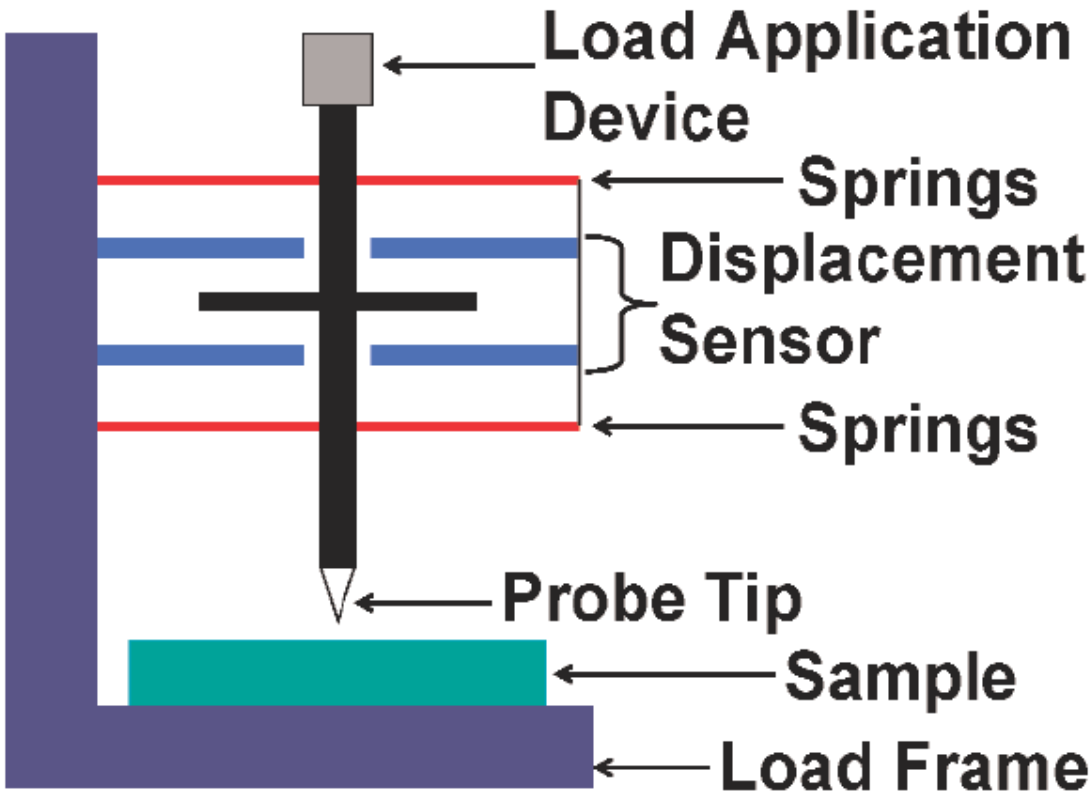


Figure 3.1: Schematic of a nanoindenter, taken from [224].

3.1.2 Instrumentation

An Agilent G200 indenter equipped with both an XP head and the NANO CSM (continuous stiffness measurement) system was used for all work in this thesis. A schematic illustration of the hardware is shown in figure 3.1. Load is applied using electromagnetic actuation, and displacement measured by a capacitive displacement sensor. The manufacturer stated load resolution is 50 nN and displacement resolution < 0.01 nm. The system is inherently load controlled, but pseudo displacement control can be achieved by using a feedback loop. Leaf springs hold the indenter column in place, and prevent lateral movement.

The raw load measured by the machine is a combination of the load on the sample

and the load required to displace the indenter column support springs. The load on the sample, P, is given by equation 3.1:

$$P = (P_{raw} - P_0) - (h_{raw} - h_0)K_s \tag{3.1}$$

where P_{raw} is the raw load, P_0 the raw load at the sample surface, h_{raw} the raw displacement, h_0 the raw displacement at the sample surface, and K_s the stiffness of the support springs. $K_s = \frac{dP_{raw}}{dh_{raw}}$, and is calculated from the data collected before the tip contacts the surface.

The raw displacement also needs to be corrected for frame compliance and thermal drift. The displacement into the sample surface, h, is given by equation 3.2:

$$h = (h_{raw} - h_0) - \frac{P_{raw} - P_0}{K_f} - (t - t_0)Q \tag{3.2}$$

where h_{raw} is the raw displacement and h_0 the displacement at the sample surface. K_f is the frame stiffness, and is measured when calibrating the tip geometry (see section 3.1.3.2). t and t_0 are the times at the end and beginning of the test respectively, and Q the thermal drift. The thermal drift is measured during the unload part of the indentation, in a hold segment at 10% maximum load.

3.1.3 Data Analysis

Common properties measured using nanoindentation include the elastic modulus, E, and the hardness, H, and are extracted from the load-displacement data using methods outlined by Oliver and Pharr [223].

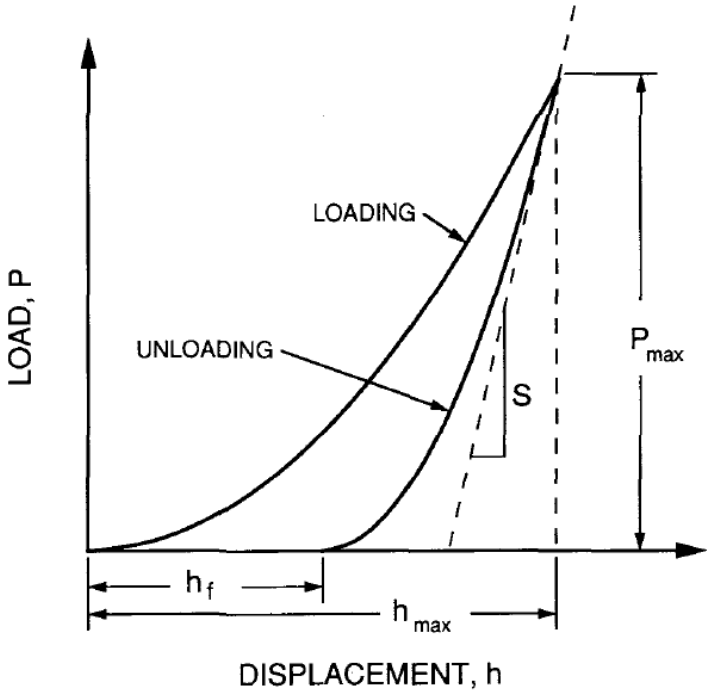


Figure 3.2: Typical load-displacement curve from a nanoindentation test, taken from [223].

Figure 3.2 shows a typical load-displacement curve from a nanoindentation test, with key parameters labelled.

Hardness is given by equation 3.3:

$$H = \frac{P}{A} \tag{3.3}$$

where P is the load and A is the contact area.

$$S = \frac{dP}{dh} = \frac{2}{\sqrt{\pi}} E_r \sqrt{A} \tag{3.4}$$

Equation 3.4 relates the stiffness, S (the change in load, P, with displacement, h), to

the reduced modulus, E_r, and the contact area, A, and was first derived by Sneddon for a circular flat punch [225]. It was later shown to apply more generally to any axisymmetric shape indenter by Pharr, Oliver and Brotzen [226]. Calculations by King [227] have also shown only small deviations for square and triangular flat punches.

The reduced modulus, E_r, is so called because the stiffness contains contributions from both the sample and the indenter tip. They can be separated using equation 3.5:

$$\frac{1}{E_r} = \frac{(1-\nu^2)}{E} + \frac{(1-\nu_i^2)}{E_i} \tag{3.5}$$

where ν and E are the sample's Poisson's ratio and elastic modulus respectively, and those with the i subscript relate to the indenter tip - known to be 0.07 and 1141 GPa for diamond [223].

The stiffness can found by first fitting equation 3.6 to the unloading data:

$$P = B(h - h_f)^m \tag{3.6}$$

where B,h_f and m are all constants determined using a least squares fitting procedure. The equation is then differentiated, and solved for the peak load to find the initial unloading stiffness.

3.1.3.1 Continuous Stiffness Measurement

For all work in this thesis continuous stiffness measurement (CSM) was used to measure the stiffness continually throughout the test, allowing hardness and elastic modulus to

be measured as a function of depth. This technique was developed by Oliver and Pharr [223], and is achieved by applying a small sinusoidal oscillation in force and measuring the corresponding displacement signal.

Determination of the contact stiffness requires the response of the entire system to be taken into account. A dynamic model is shown in figure 3.3.

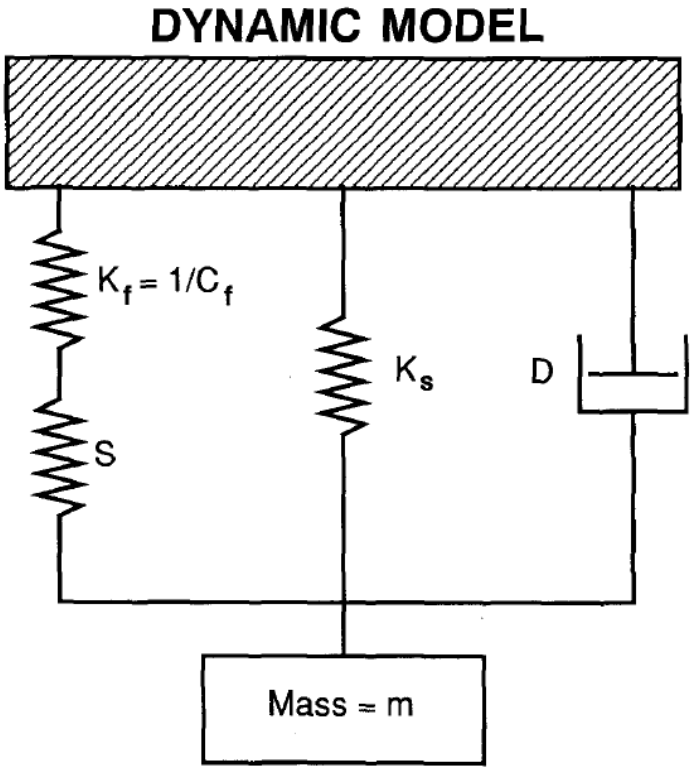


Figure 3.3: Dynamic model of the nanoindenter system, taken from [223]. K_f is the frame stiffness, S the contact stiffness, K_s the support spring stiffness, D the damping coefficient, and m the indenter mass.

The stiffness can be calculated from the amplitude of the displacement signal from:

$$\left|\frac{P_{os}}{h(\omega)}\right| = \sqrt{\{(S^{-1} + C_f)^{-1} + K_s - m\omega^2\}^2 + \omega^2 D^2} \tag{3.7}$$

or from the phase difference between the force and displacement signals:

$$\tan\phi = \frac{\omega D}{(S^{-1} + C_f)^{-1} + K_s - m\omega^2} \tag{3.8}$$

where

P_{os} = the magnitude of the force oscillation

$h(\omega)$ = the magnitude of the displacement oscillation

ω = the oscillation frequency

S = the contact stiffness

C_f = the frame compliance

K_s = the indenter support spring stiffness

m = the indenter mass

D = the damping coefficient

ϕ = the phase difference between force and displacement signals

D and K_s are measured whilst the tip is not in contact with the surface, and C_f is measured during the tip calibration procedure described below.

3.1.3.2 Tip area function

The tip contact area is required to measure both the hardness (equation 3.3) and elastic modulus (equation 3.4). Oliver and Pharr [223] developed a technique whereby an area function, $A(h_c)$, is found that describes the contact area of the tip as a function of displacement into the sample surface, h_c. This is achieved through indentation of a reference material of known elastic modulus and Poisson's ratio (fused silica was used for this work, with an elastic modulus of 72 GPa and Poisson's ratio of 0.170 [223]) -

allowing the reduced modulus E_r (equation 3.5) to be known, and assuming that it is independent of indentation depth.

The measured compliance of the system, $C = \frac{1}{S}$, is composed of the sample compliance, C_s and the frame compliance C_f:

$$C = C_s + C_f \tag{3.9}$$

Combining equations 3.4 and 3.9 gives

$$C = C_f + \frac{\sqrt{\pi}}{2E_r}\frac{1}{\sqrt{A}} \tag{3.10}$$

If the reduced modulus, E_r, is constant, a plot of C vs $A^{-\frac{1}{2}}$ will be linear with an intercept of C_f.

Rearranging equation 3.10 allows the contact area to be calculated for all depths:

$$A = \frac{\pi}{4}\frac{1}{E_r^2}\frac{1}{(C - C_f)^2} \tag{3.11}$$

and for a Berkovich tip fitted to a function of the form:

$$A(h_c) = 24.5h_c^2 + C_1h_c + C_2h_c^{\frac{1}{2}} + C_3h_c^{\frac{1}{4}} + ... + C_8h_c^{\frac{1}{128}} \tag{3.12}$$

where C_n are constants. The lead term describes the shape of a perfect tip, with subsequent terms describing deviations due to tip blunting. The exact form of the area

function influences both C_f and E_r, so an iterative process is followed until convergence is achieved.

3.1.3.3 Tip Calibration

For the work in this thesis, prior to each batch of indents the tip and frame stiffness were calibrated by performing indents on a reference fused silica sample. This sample has a known elastic modulus and Poisson's ratio of 72 GPa and 0.170 respectively [223].

A 4x4 array of indents with a depth of 3000 nm are made in this reference material, and the frame compliance and tip area function are calibrated according to the principles outlined in section 3.1.3.2 using the *Tip Configuration* tool in the Nanosuite software. The nominal modulus of the tested material is set to 72 GPa, the range of depth for area calculation set to 20 - 3000 nm (to avoid using any blunt region at the end of the tip), the range of depth for load frame stiffness calculation set to 500 - 3000 nm, using 5 coefficients, and without keeping the lead term fixed (to allow for non-perfect tip geometry).

3.2 Microcantilevers

3.2.1 Introduction

The invention of the nanoindenter and widespread use of Focussed Ion Beam (FIB) equipment has made possible the field of micromechanics, where micron-scale specimens can be manufactured and mechanically tested.

The first use of FIB to wholly manufacture microcantilevers from "bulk" material was by Di Maio and Roberts [228], who measured the fracture toughness of Si, and a WC coating on a steel substrate.

Armstrong [229, 230] developed techniques for measuring elastic and plastic properties from microcantilever beams, and alongside further development by Hardie [231] and the Di Maio-Roberts work, these techniques were applied to study irradiation damage effects in Fe-12Cr and W [232]. They were also used by Hardie [14] to compare mechanical properties of heavy ion and neutron irradiation in Fe-6Cr.

These techniques are the basis of the microcantilever work performed in this thesis, and are outlined below.

3.2.2 Manufacture

Microcantilevers were manufactured using a Focussed Ion Beam (FIB), where a 30 kV Ga^+ beam is used to sputter away material. A procedure similar to that used by Di Maio and Roberts [228] and Armstrong et al. [230] was followed, and is outlined in figure 3.4 (from [230]) and detailed below.

First a U-shaped trench is milled (using a beam current of ~5000pA) to sufficient depth, and leaving a rectangular section with dimensions larger than those desired for the cantilever (a).

Next, the stage is tilted to 30°, and the rectangular section is undercut from one side (b), then rotated 180° and undercut from the other side (c), leaving a triangular cross-sectioned beam with dimensions still larger than those required.

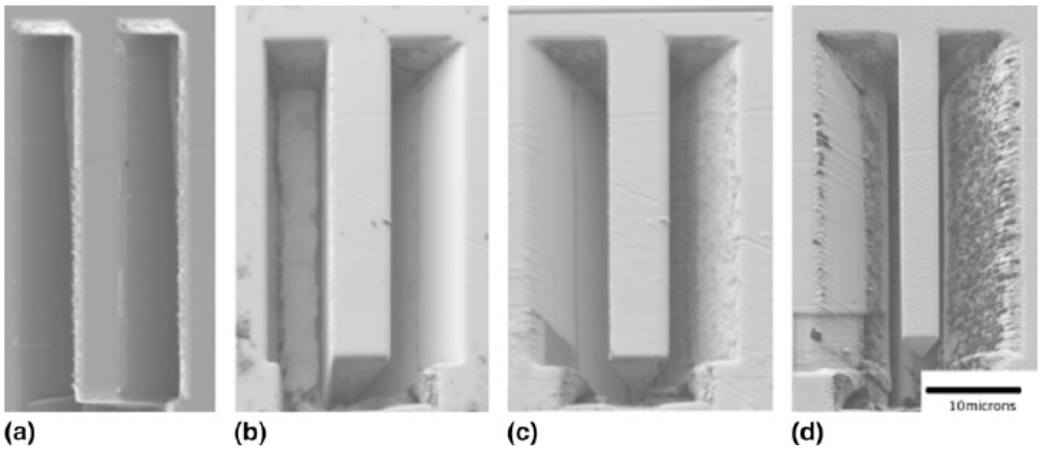


Figure 3.4: From [230], FIB images illustrating the procedure used to mill microcantilever specimens. See text for description.

The stage is then returned to 0° tilt, and the cantilever beam milled to the desired width and length using a lower beam current (500pA or less). This is to ensure sharp edges, reducing the effect of "beam tails" at larger currents.

Final undercutting is again performed at a stage tilt of 30° using the same low beam current.

3.2.3 Measurement

As is discussed below in section 3.2.5, the values of material properties extracted through analysis of load-displacement data of cantilever beams are highly sensitive to the measured beam dimensions. Equations 3.20 and 3.22 show that for simple beam theory analysis, the stress and elastic modulus have a quadratic and cubic dependence on the measured beam height respectively. It is therefore important the beam dimensions are measured as accurately as possible.

Standard trigonometric techniques are susceptible to measurement errors when the sample isn't perfectly flat and parallel to the microscope stage. In order to avoid these errors a stereoscopic measurement technique was used based on principles outlined by Piazzesi [233], and as used by Hardie [231].

Piazzzesi [233] derived equations for the coordinates of a projection of a point onto a plane when rotated about an axis at angles $\pm\Delta\phi$. These equations can be used to determine the real lengths of features in the analogous situation of pairs of images at two different tilt angles, where coordinates can be calculated on an imaginary imaging plane that lies at the mid angle between them, as illustrated in figure 3.5.

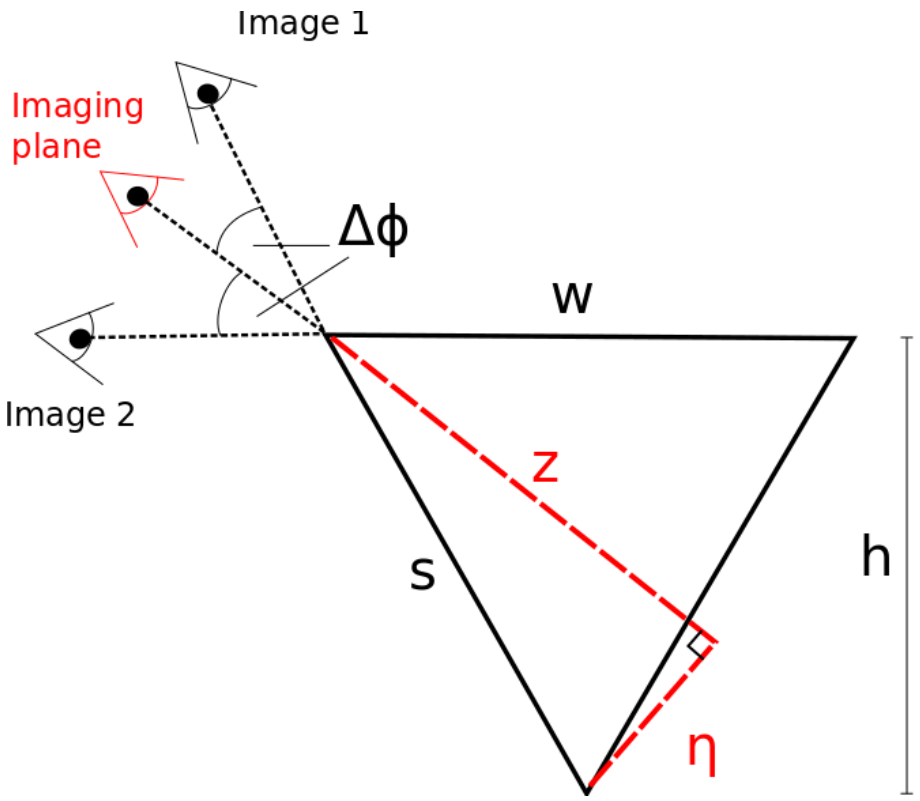


Figure 3.5: Diagram illustrating geometry and measurement variables in the stereoscopic imaging technique.

Suitable pairs of images were taken in the Auriga SEM at tilt angles of 39° and 63° at a working distance of 10 mm. Beams were imaged from the "side view" with the

beam's long axis aligned parallel to the image x axis as shown in figure 3.6.

$$z = \frac{(y_1 - y_2)\cos(\Delta\phi) + y_1 y_2(\frac{1}{d_1} + \frac{1}{d_2})\sin(\Delta\phi)}{\sin(2\Delta\phi)(1 + \frac{y_1 y_2}{d_1 d_2}) + \cos(2\Delta\phi)(\frac{y_1}{d_1} - \frac{y_2}{d_2})} \tag{3.13}$$

$$\eta = \frac{z[(y_1 + y_2)\cos(\Delta\phi) + (d_1 + d_2)\sin(\Delta\phi)] - (y_1 d_1 + y_2 d_2)}{(y_1 - y_2)\sin(\Delta\phi) - (d_1 + d_2)\cos(\Delta\phi)} \tag{3.14}$$

In the above equations, z is the component perpendicular to the imaging plane, and η the in-plane component perpendicular to the tilt axis, of the real dimension of feature y, with lengths y_1 and y_2 in images 1 and 2. d_1 and d_2 are the working distances for each image, and $\Delta\phi$ is half of the difference in tilt angle between the two images. This is shown in figure 3.5.

From each image, the width and side of the beam was measured in 5 places and averaged. η and z are then calculated, and the true beam width w, sidelength s, and height h found using Pythagoras. Values were found from images of both sides of the beam and averaged.

3.2.4 Testing

Microcantilever beams were tested using a nanoindenter. The tip was positioned onto the beam, a short distance from the free end, and displaced to obtain load-displacement data.

The nanoindenter is equipped with a nanopositioning stage, allowing topographical scanning to be performed with the indenter tip in contact scanning mode, used to pre-

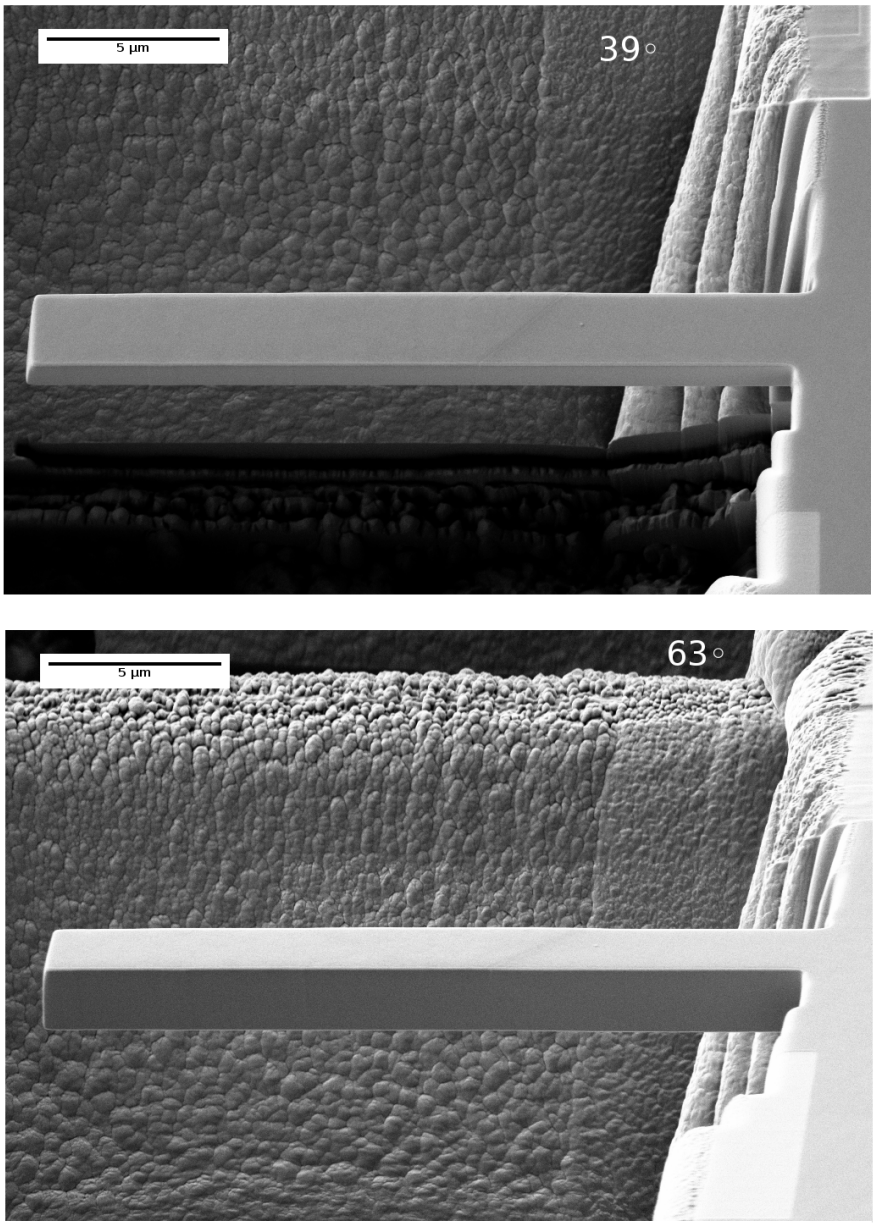


Figure 3.6: A pair of images of the same beam taken at tilt angles of 39° and 63°, used for stereoscopic measurement of real beam height and width. The projected width and side lengths are measured in both images, and used to calculate real measurements using equations 3.13 and 3.14, as described in the text.

cisely locate the beam and select the testing position. In order to avoid scanning over the beam itself, which could damage it (either causing misalignment or inducing strain hardening before testing), additional alignment markings were FIB milled and imaged to aid positioning, as shown in figure 3.7. The line is milled perpendicular to the long direction of the beam, and the centre of the circular hole coincides with the centre of the beam along the same direction. These alignment marks are scanned and the test position is selected as an offset from these, as outlined below.

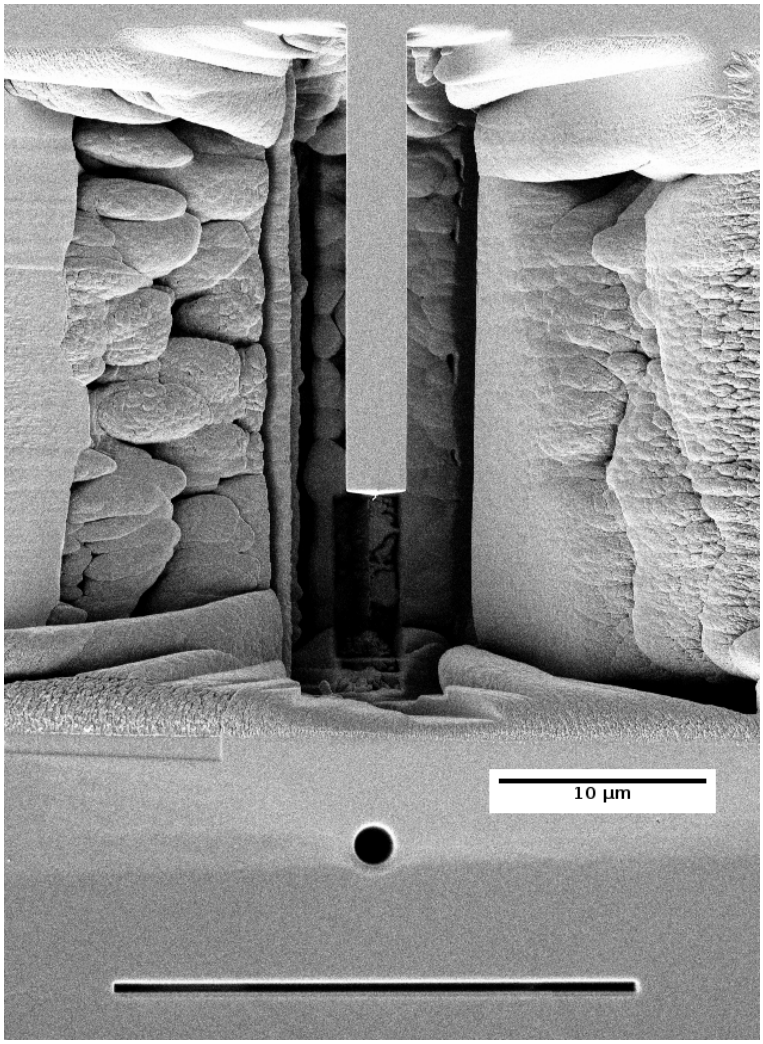


Figure 3.7: SEM image of microcantilever beam and alignment marks.

Firstly, the sample is loaded into the nanoindenter and adjusted so that the beams are in the same orientation as in figure 3.7 by eye. 4 vertical scans of the alignment line are made in order to determine the angle relative to the positioning stage. A scan is then made of the circular feature, with the desired test location selected as an offset from the centre of it using the pre-test image (e.g. figure 3.7) and trigonometry. The effective tested beam length is measured using the pre-test image and the selected test location.

The beam is then tested using a CSM method. It is loaded at a constant displacement rate to a fixed displacement, partially unloaded to 10% of the maximum load, held for 60 s while the thermal drift is measured, and then completely unloaded.

A typical raw load-displacement plot is shown in figure 3.8 (a). Similarly to nanoindentation and discussed in section 3.1.2, the raw load-displacement data produced has contributions from the extension of the indenter support spring and thermal drift, and these need to be compensated for before any analysis.

A straight line was fitted to data before the indenter reached the sample surface, as shown in figure 3.8 (a), in order to find the slope (spring stiffness K_s), and the intercept c_s. The thermal drift, Q, was measured during the hold segment after partial unloading.

The load on sample, P, is then found using equation 3.15:

$$P = P_{raw} - h_{raw}K_s - c_s \tag{3.15}$$

where P_{raw} is the raw load and h_{raw} is the raw displacement.

The bending displacement, h, is given by equation 3.16:

$$h = h_{raw} - h_0 - Qt \tag{3.16}$$

where h_{raw} is the raw displacement, h_0 the displacement at surface contact, Q the thermal drift, and t the time on sample.

After applying these corrections the bending load and displacement can be found, as shown in figure 3.8 (b).

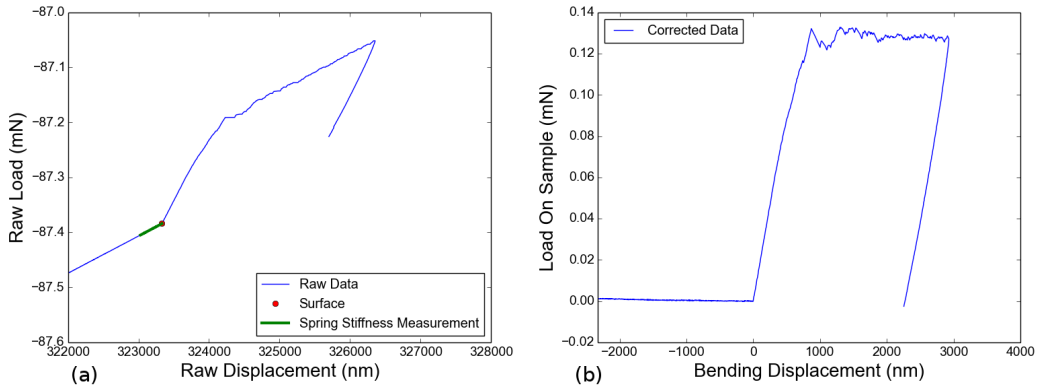


Figure 3.8: (a) Raw load-displacement data, indicating how the spring stiffness is measured. The surface is also marked. (b) Corrected load on sample - bending displacement data.

3.2.5 Simple Beam Theory Analysis

3.2.5.1 Theory

For pure, linear elastic bending of prismatic beams with cross-sections that are constant and symmetrical about the plane of loading, unaffected by irregularities near supports or at stress concentrations, maximum stresses and strains can be calculated from load-displacement data using the following relations [234]:

$$\frac{\sigma}{z} = \frac{M}{I} = E\kappa \tag{3.17}$$

where σ is stress, z the distance from the neutral axis, M the applied moment, I the second moment of inertia of the beam, E the elastic modulus, and $\kappa = \frac{1}{R}$ is the curvature, where R the radius of curvature of the neutral axis of the beam under applied moment. Equation 3.17 is a combination of the moment-curvature equation and flexure formula.

All cantilever beams used in this thesis have triangular cross-sections, for which the second moment of inertia is given by:

$$I = \frac{wh^3}{36} \tag{3.18}$$

where w is the beam width, and h its height.

The moment is:

$$M = PL \tag{3.19}$$

where P is the load, applied at a distance L along the beam.

For triangle cross-section beams, the neutral axis is located at a distance $\frac{1}{3}$ of the height from the top surface, as shown in figure 3.9. The maximum stress occurs at points located furthest from the neutral axis, at the apex on the bottom surface, a distance $\frac{2}{3}h$ from the neutral axis.

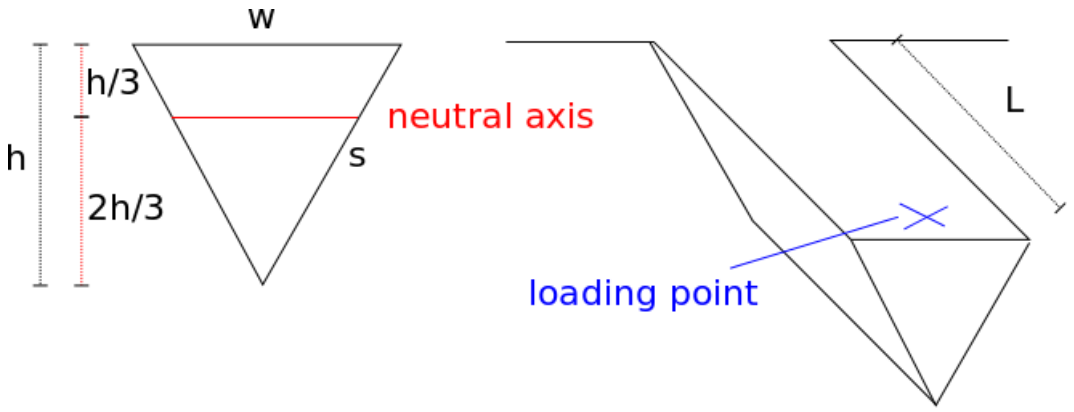


Figure 3.9: Schematic of cantilever geometry and variables

Substituting into equation 3.17, the maximum stress is given by:

$$\sigma_{max} = \frac{24PL}{wh^2} \tag{3.20}$$

The corresponding strain, ε, can be found using:

$$\varepsilon_{max} = \frac{\sigma_{max}}{E} \tag{3.21}$$

From equation 3.17:

$$E = \frac{PL^3}{3I\delta} = \frac{12PL^3}{wh^3\delta} \tag{3.22}$$

where δ is the displacement at the point of the applied load, found by integrating the curvature, κ.

The maximum strain is then given by:

$$\epsilon_{max} = \frac{2h\delta}{L^2} \tag{3.23}$$

3.2.5.2 Analysis

First, the data was corrected for thermal drift and the supporting spring stiffness, as described in section 3.2.4. Equations 3.20 and 3.23 were then used to convert the load-displacement data to simple beam theory maximum stress-strain data.

The elastic modulus is calculated from the slope of the initial linear portion of this simple beam stress-strain curve. This portion was defined as being from the 5th data point after surface contact up to 100 nm bending displacement. The lower limit was chosen to avoid contact and tip embedding effects during the initial contact of the indenter tip with the beam. The upper limit was set such that curves for all beams displayed linearity up to this displacement. This data was fitted to a linear function using a non-linear least squares fitting tool from SciPy [235].

Yield stress was defined as the stress at the strain at which the gradient falls below 0.9 of this value, as used by Armstrong [229]. As shown in figure 3.10, the gradient was measured at each point along the curve using a number of data points either side of the position.

The value of yield stress measured can depend on the number of neighbouring data points used (named *hopsize* in this work). This parameter was optimised for each curve: the use of too few data points meant that local noise affected the result, too many and the slope wasn't measured locally enough. The gradient analysis was run for a range of *hopsize*'s, and the yield stress calculated for each (figure 3.11). For each beam, the modal result for yield stress was selected - where *hopsize* parameter sensitivity was low.

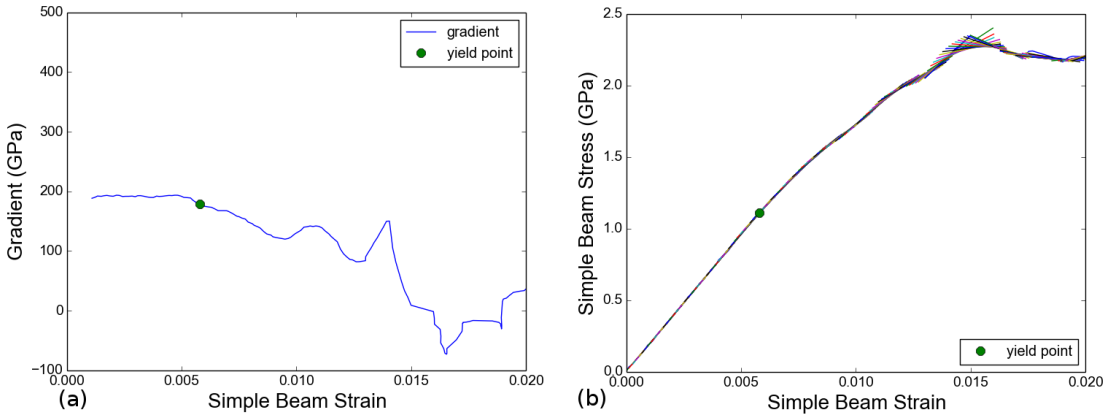


Figure 3.10: (b) illustrates the gradient being measured for each strain, and is plotted in (a). The yield point, where the gradient falls below 0.9 of the reference value is indicated.

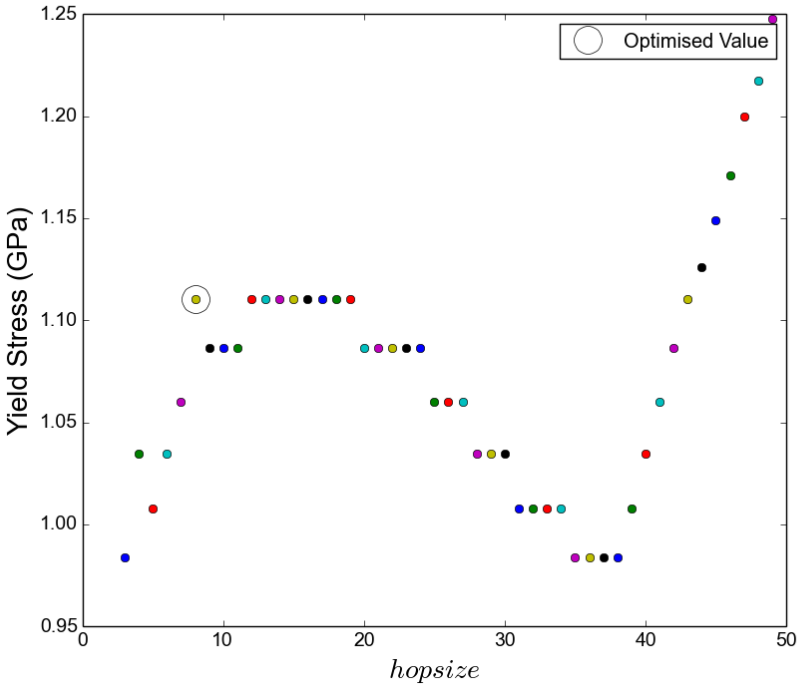


Figure 3.11: Yield stress obtained using different values of the *hopsize* parameter - the number of neighbouring points used to calculate the local gradient. For low values, local noise can cause the gradient to briefly fall below the 0.9 threshold, leading to a lower value of yield stress. For higher values, changes in gradient are felt earlier and so a lower value of yield stress is measured. The optimum value was chosen to be the lowest value that gave the modal result for yield stress.

3.2.6 Finite Element Analysis

Simple beam theory analysis has its limitations, with neglecting any deformation of the "base" near the fixed end of the beam being the most significant for this application. Because of this, finite element analysis was also performed using ABAQUS.

A finite element model was constructed for each microcantilever beam, and the material properties of the model were fitted so that the load-displacement response of the real beam was reproduced.

ABAQUS/CAE 2016 was used with isotropic elasticity and isotropic plasticity constitutive models, with standard, 3D stress, hex 20 node reduced integration quadratic brick elements (C3D20R).

The finite element model was constructed by merging a triangular base part with a triangular beam part, having dimensions matching those of the experimental microcantilever beam being modelled. Boundary conditions are applied to the base, so that it is fixed (encastre) at its rear end and sides, but with the front and top faces being free to move. It has a size determined through a convergence study, large enough so that the fixed faces don't induce artificial stiffness to the beam. Displacement is applied along a line at the free end of the beam.

A typical FEA model used in this work is shown in figure 3.12.

In order to ensure reliable results, convergence studies were performed for both base size and mesh refinement, shown in figure 3.13. These were performed using a beam with dimensions and properties corresponding to a realistic "worst case" in terms of deformation of the base. The beam height and width were set to 3.5 μm, with the length set to 15μm. The elastic modulus was set to 150 GPa and the yield stress to 1.5 GPa.

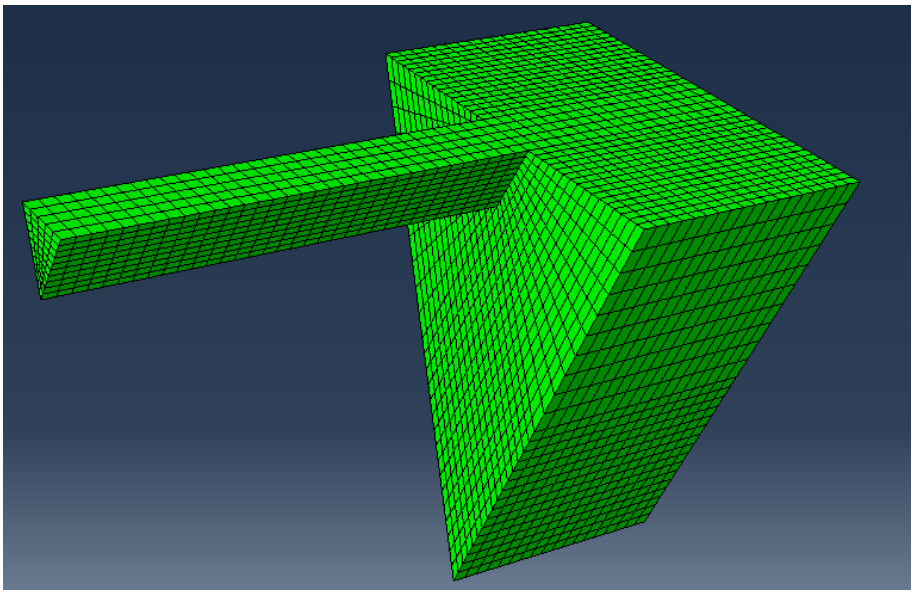


Figure 3.12: Typical FEA model used in this work

The beam stiffness was compared for a variety of base dimensions and mesh sizes to check for convergence (figure 3.13).

Based on this analysis, base height, depth, and width were chosen to be 18, 9, and 15μm respectively, with a mesh size parameter of 0.5 with quadratic elements (C3D20R - 20 node quadratic brick, reduced integration).

For each experimental microcantilever beam a corresponding FE model was created, with the aim of recreating the experimental load-displacement curve by adjusting the material properties of the model. The elastic modulus is first fitted, followed by the yield stress and flow stress at various plastic strains. The procedure was performed using algorithms and scripts based on those used by Hardie [231].

First, as for the simple beam theory analysis, the data is corrected for the support spring stiffness and thermal drift. The elastic region of the corrected load-displacement curve is then manually defined through a graphical user interface. The ABAQUS sim-

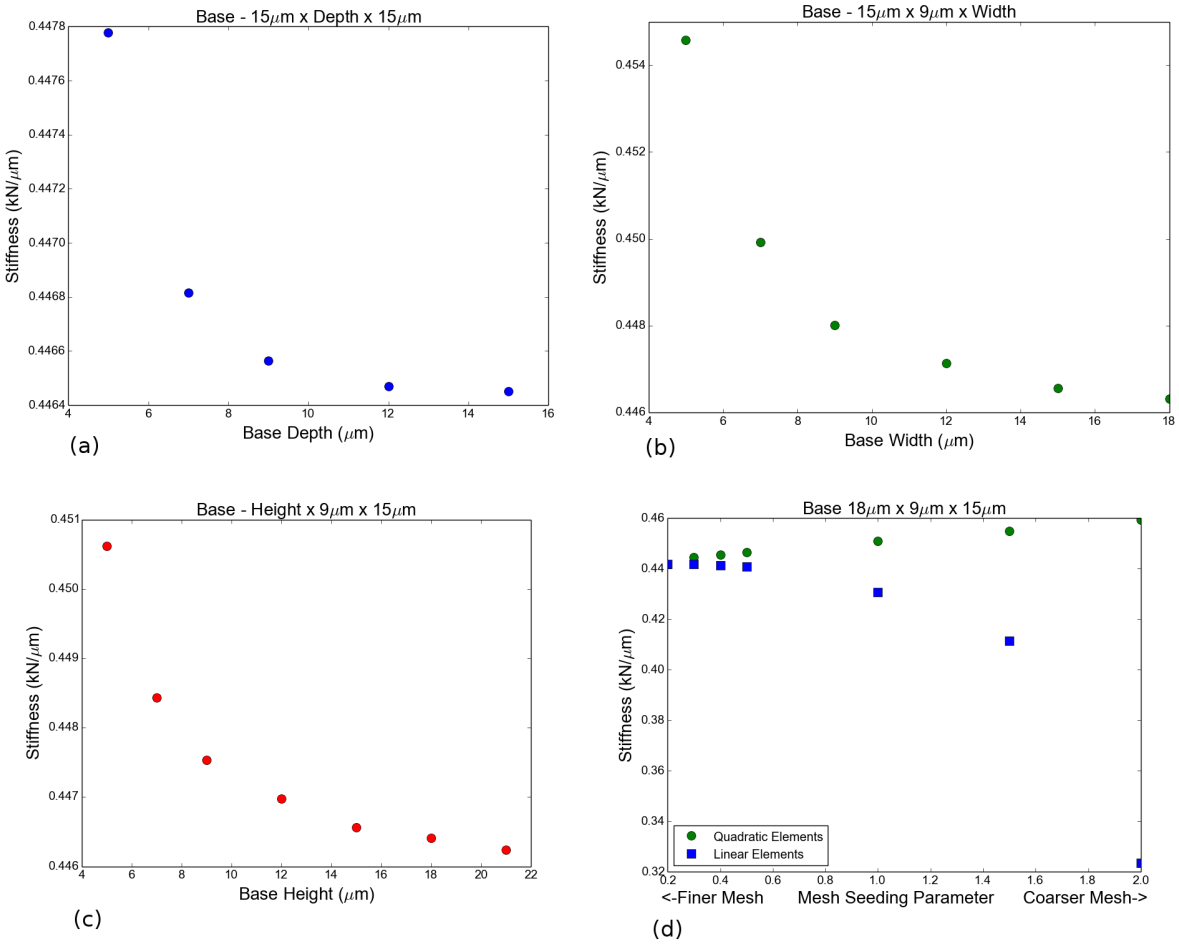


Figure 3.13: Convergence studies for (a) depth, (b) width, (c) height, of the base used in the finite element model, along with the mesh size in (d).

ulation is run iteratively, comparing the load required for the displacement at the end of the elastic region to that in the experimental data. A new value for the elastic modulus of the model material is chosen based on the difference, and repeated until the two load values match.

A polynomial function is then fitted to the plastic part of the curve. The beginning of the plastic part is defined as the yield point calculated by simple beam theory analysis described earlier in section 3.2.5. A number of points along this curve are selected to which the model is fitted progressively. Each fitting point is taken in order of displacement. As with the elastic fitting, the model is displaced to the corresponding displacement and the load compared to the data from the real experiment. The model material properties are adjusted until the model and experimental loads match, and then the procedure is repeated for the next point.

The process is illustrated graphically in figure 3.14.

In ABAQUS, the model's plastic material properties are in the form of a flow stress at a given plastic strain. The analysis aims to find a number of flow stresses at plastic strain corresponding to the number of points selected along the curve. For the first plastic point, the plastic strain is set to 0 (yield stress) and the corresponding flow stress is fitted. For the next plastic point, the plastic strain is set to the maximum plastic strain experienced during the previous point. The process repeats until all points are fitted.

In this work 5 such points were selected, and spaced more closely together at the start of the plastic region in order to capture any yield drop behaviour.

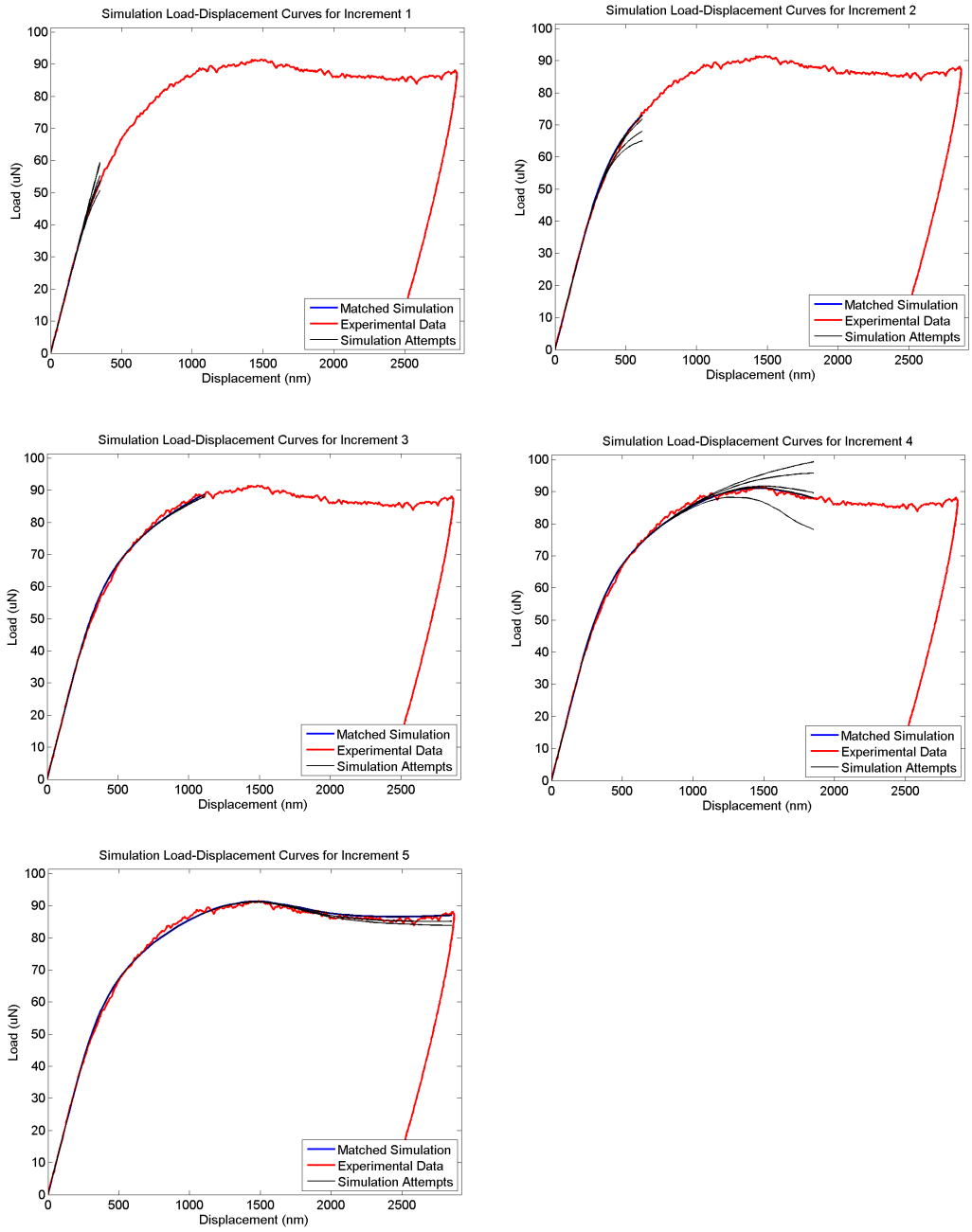


Figure 3.14: Figures illustrating progressive fitting of model load-displacement data to experimental data by adjusting model material properties.

3.3 Size Effects

Small scale mechanical testing techniques are particularly attractive for the study of irradiation damage. For example, the ability to reduce the required sample size of radioactive material reduces the overall activity and lowers the handling requirements for research facilities, allowing active material to be studied more easily and more widely. Where access to such facilities or materials are not available, the simulation of neutron irradiation damage with heavy ion irradiation produces shallow damage layers, also requiring the use of these small scale techniques.

It is however well known that the mechanical strength of a material increases with decreasing specimen size. This "size effect" has been observed in various testing techniques that are commonly used to study irradiated materials, including nanoindentation (Indentation Size Effect) [236, 237], micropillar compression [238] (review), and microcantilever testing e.g. [14,229,239]. For the present application, an understanding of this phenomenon is crucial if these measurements are to be relevant to the larger length scales used for engineering and design considerations.

3.3.1 Mechanisms of Plasticity Size Effects

Several mechanisms have been proposed to explain these observations:

i Strain gradient plasticity

ii Dislocation starvation

iii Truncation hardening

iv Dislocation pile-up

The relevance and relative significance of each mechanism depends on the loading condition, microstructure, and the test volume size [240]. The mechanisms will be briefly explained in turn, and then followed by a discussion focused on the relevance to the work and techniques used in this thesis in section 3.3.2.

i Fleck et al. [241] developed a theory of strain gradient plasticity using the concept of geometrically necessary dislocations [242]. They argue that hardening is caused by the storage of dislocations which can be separated into two populations, termed statistically stored and geometrically necessary. Statistically stored dislocations are accumulated by trapping each other in a random way, whereas geometrically necessary dislocations are required for accommodation of lattice rotations required for compatible shear of various slip planes within the crystal - such as in the presence of a strain gradient. It is argued that when strain gradients are present and large, such as is the case when specimens are small, the geometrically necessary population density becomes significant and a size effect is observed.

ii The dislocation starvation mechanism proposed by Greer et al. [243,244] suggests that in small samples, mobile dislocations may escape from the crystal at free surfaces before they can multiply and interact with other dislocations. This means continuous nucleation of new dislocations is required to accommodate deformation. This theory was used to explain size effects observed in the compression of Au nanopillars, where no strain gradients are present.

iii A similar but alternative hardening mechanism is truncation hardening, proposed by Parthasarathy et al. [245]. Here, the maximum source length is limited by the sample dimensions (or plastic zone size), resulting in shorter source lengths in smaller specimens than would be found in unconstrained volumes, which require higher stresses to activate. Single ended sources formed by the intersection of double ended Frank-

Read sources with free surfaces have been shown to have a similar length-strength relation [246].

iv Dislocation pile-up [239, 247] is a phenomenon where dislocations halted by an obstacle or region of zero stress exert a back stress on following dislocations and the source, requiring a higher stress to continue its operation. This effect can be more prevalent in small samples, where dislocation sources are more scarce and so dislocations are more likely to be concentrated on a small number of slip planes.

3.3.2 Size Effects in Nanoindentation & Microcantilevers

Nix and Gao [236] developed a model for the indentation size effect using strain gradient plasticity, suggesting that the density of geometrically necessary dislocations required to accommodate the indenter tip is responsible for the increase in hardness with decreasing indent size.

"Pop-in" events are often seen during the early stages of nanoindentation, thought to be associated with the nucleation of dislocations. Lilleodden [240] points out that it is somewhat unphysical to transition from a dislocation free regime during the first stages of indentation to one with the highest geometrically necessary dislocation density implied by the Nix-Gao strain gradient plasticity model. The indentation size effect is argued to be controlled by dislocation-starved plasticity in the nanometre regime, and strain gradient plasticity in the micrometre regime by Nix et al. [237].

Similarly to the situation with indentation, Tarleton et al. [248] make the point that a pure strain gradient plasticity interpretation of the size effect in microcantilever bending fails to take into account other changes that occur as the length scale is reduced, such

as the reduced availability of sources. Indeed, Motz et al. [239] argued that geometrically necessary dislocations alone could not produce the $\sim t^{-1}$ dependence on flow stress (where t is the beam thickness) they observed in Cu microcantilever beams. Dislocation pile-up was found to produce the correct beam thickness dependence. Modelling by Tarleton et al. [248] and Motz et al. [249] reconciled these mechanisms, arguing that the limited availability of sources at small length scales leads to dislocations being concentrated on a small number of slip planes where sources are available, leading to localised pileup at regions where stress is relieved.

3.4 Atom Probe Tomography

3.4.1 Introduction

Atom Probe Tomography (APT) is a 3D microscopy technique capable of imaging the chemical distribution of atoms with atomic spatial resolution [250]. Ions are desorbed from the surface of a needle shaped specimen by the process of field evaporation in the presence of an intense electric field and accelerated towards a position sensitive detector. This process requires field strengths of the order of 10 V/nm [251], and this can be achieved by applying a standing voltage of several kV to a specimen with a radius of curvature below 100 nm at the tip.

The standing voltage is typically set to achieve ~80% of this field, with the remainder provided by either HV pulses through a nearby counter-electrode placed in front of the specimen, or with a laser pulse. This provides time controlled evaporation, and allows the determination of the mass to charge ratio of desorbed ions by time of flight measurement.

In standard reconstruction protocols it is assumed that once ions leave the surface, they are accelerated towards the detector quasi-radially from the tip apex. In the 3D reconstruction, x and y positions are calculated using a reverse point projection model [252] from the detector coordinates to find each ion's original position on the surface.

The actual trajectories of ions are not radial, but compressed towards the tip axis relative to that of a sphere due to the presence of the shank behind the tip [253]. The origin of the point projection for reconstruction is positioned along the axis of the tip at a distance of ξr, where ξ is the image compression factor and r the tip radius, to compensate for this. This is illustrated in figure 3.15.

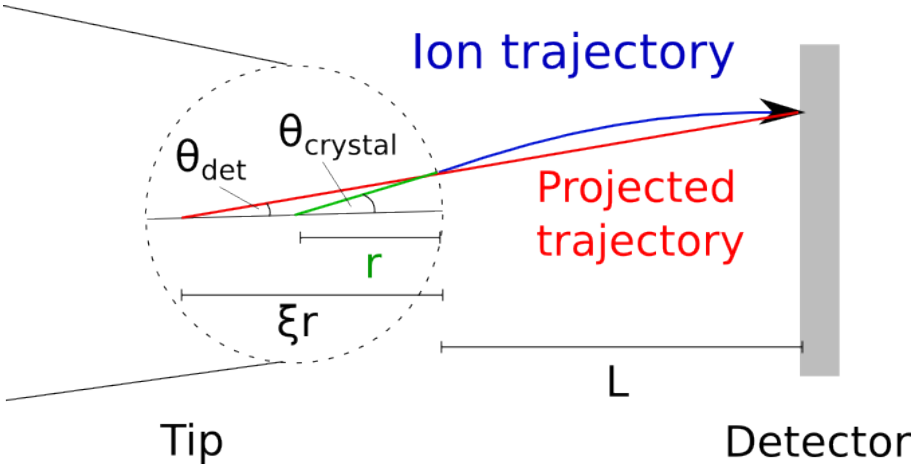


Figure 3.15: Diagram showing lengths and angles used in reconstruction.

The z coordinate is determined from the sequence in which the ions reach the detector. The z increment for each ion is determined from:

$$\mathrm{d}z = \frac{\Omega}{\varepsilon w_V(z)} \tag{3.24}$$

where Ω is the ionic volume, ε the detector efficiency, and $w_V(z)$ a function that describes how the reconstructed tip volume changes with z. The tip radius evolution

can be estimated using the evolution of the standing voltage during the experiment, which increases as the experiment proceeds and ions are evaporated and the tip blunts:

$$r = \frac{V}{k_f F_e} \tag{3.25}$$

where V is the total applied voltage, k_f the field enhancement factor and F_e is the field required for evaporation, 33 V/nm for Fe [254].

In the small angle approximation, the depth increment for an ion hitting a detector of area A_d is given by [254]:

$$\mathrm{d}z = \frac{\Omega(Lk_f F_e)^2}{V^2 \varepsilon A_d \xi^2} \tag{3.26}$$

where L is the tip to detector distance. For atom probes fitted with a reflectron this is not equal to the flight distance, but the distance to the virtual detector positioned before ions enter the reflectron.

3.4.2 Reconstruction Using Crystallography

The point projection model described above requires measurement of the image compression factor ξ and the tip radius r. This section details how these parameters were determined using sample crystallography.

A typical detector hit map (also known as desorption map) acquired in this work is shown in figure 3.16.

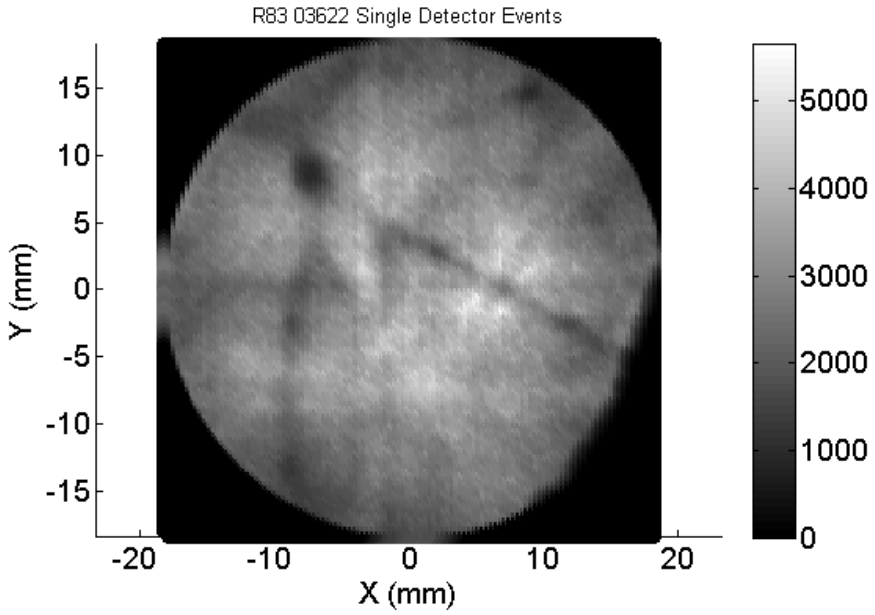


Figure 3.16: Detector hit map (desorption map) showing only single detector events, acquired from an Fe-9Cr alloy in this work.

Regions of high and low ion hit densities originate from variations in local electric field strength due to crystallography [255–257]. These variations cause trajectory aberrations [258–260], where ions are deflected sideways in the early stages of their flight, so their apparent origin on the tip surface is altered slightly. These trajectory aberrations lead to areas of low detector hit densities around poles corresponding to low index crystallographic directions and zone lines, visible in figure 3.16.

Indexing these poles can provide geometric information which can aid accurate tip reconstruction and analysis [261, 262].

The *polefigure* tool from libatomprobe [263] uses the method of Perry and Brandon [264] to simulate the projection coordinates in an APT pole figure. This tool was run with the following parameters:

```
example/polefigure bcc 150 0.2 0.5 42 '(1,0,2)'
```

and 3Depict [265] used to analyse the output file and index the poles. A labelled pole map (shown in figure 3.17) was generated, and used alongside figures in [266] to index hit maps generated in this work.

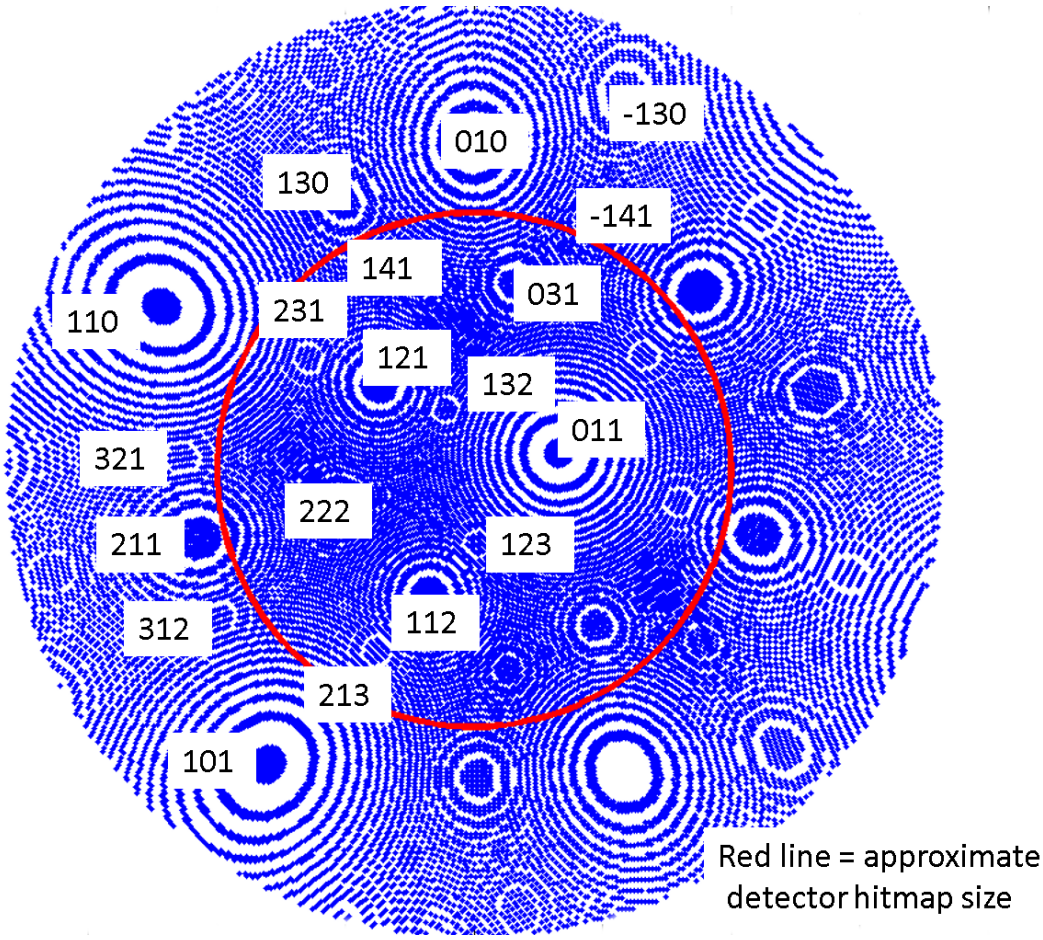


Figure 3.17: Simulated projected coordinates of bcc lattice created using the *polefigure* tool in libatomprobe [263]. Poles were identified by drawing vectors from the origin to each direction in 3Depict [265] and multiplying by the rotation matrix given by the *polefigure* tool.

The image compression factor is given by the ratio of the crystallographic angle between two directions and the same angle observed in the projection [261] (figure 3.15):

$$\xi = \frac{\theta_{\text{crystal}}}{\theta_{\text{det}}} \tag{3.27}$$

θ_{det} was calculated using the detector coordinates of two of the indexed poles, with a value of L of 42 - 44mm found by London [267]. Values of ξ varied between experiments, but were found to be in the range 1.2 - 1.6.

In all experiments the tip radius evolution was determined using the applied voltage. In the IVAS software, the relationship between these two can be calibrated by setting the initial tip radius. The *reconstruction explorer* tool was used to generate spatial distribution maps for a cylindrical section of ions with radius 1 - 2nm around a position containing a crystallographic pole, with the z direction aligned with the projection direction.

The initial radius was adjusted (equivalent to changing k_f in equation 3.26) so that the plane spacings matched those expected for the crystal direction. Other directions were then checked with the same initial radius value to ensure consistency, and confirm the pole indexing. An example is shown in figure 3.18.

To check the angles between crystallographic directions the data was reconstructed with all ionic volumes set to 0, resulting in all ions being positioned on a shell at the same initial radius. Using scripts from AtomProbeLab [268], the .pos files created by IVAS were imported into MATLAB. A 2D histogram of x and y atomic positions was then created, similar to the hitmap shown in figure 3.16 but with reconstructed coordinates, a "reconstructed hitmap". Using the initial radius as the origin, angles between positions corresponding to crystallographic directions were checked. Agreement within ~15% was generally found. For datasets containing features where the crystallography was measured, ξ was adjusted and the whole process repeated to find the best agreement.

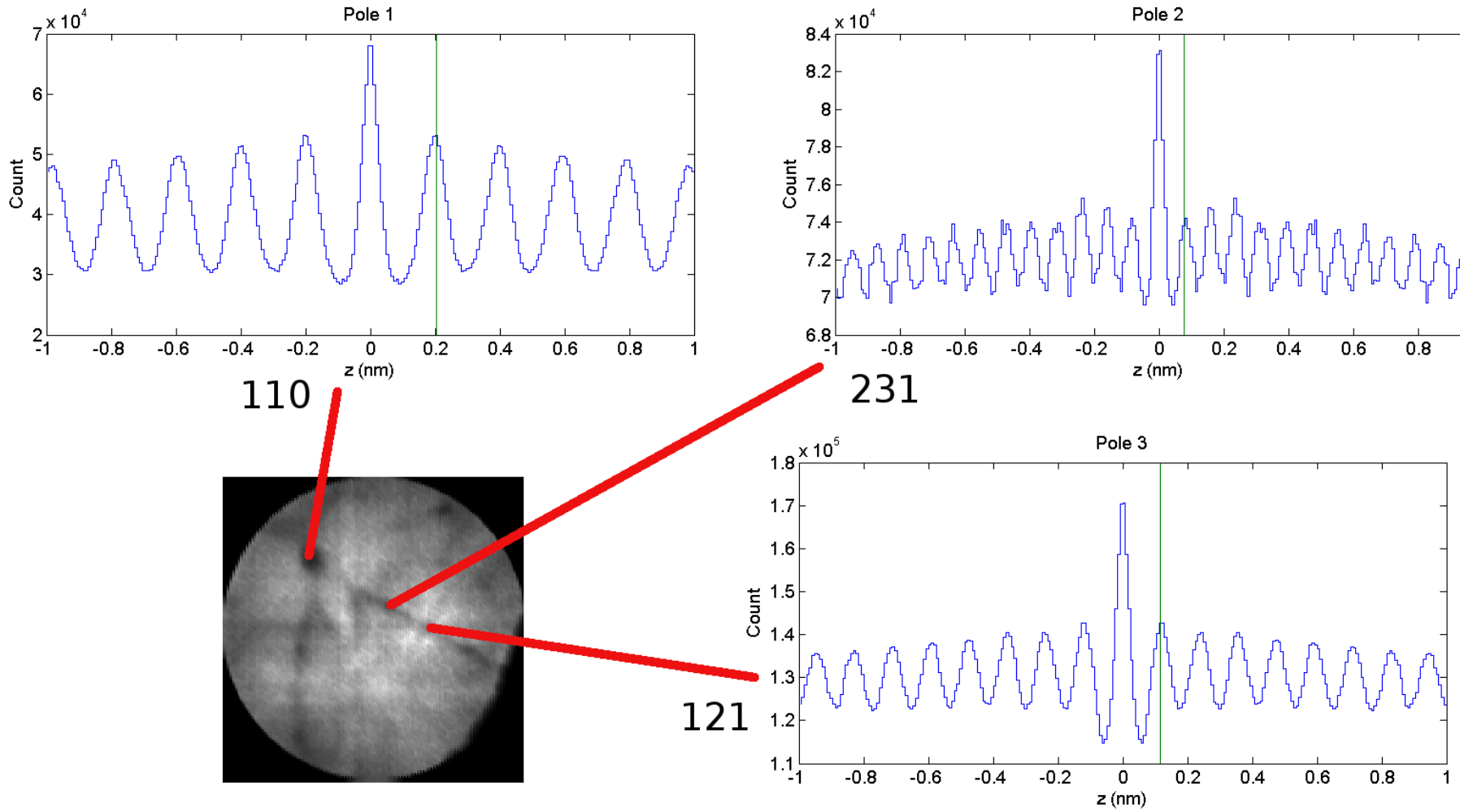


Figure 3.18: Spatial distribution maps created with the *reconstruction explorer* tool in IVAS for 3 crystallographic poles observed in an Fe-9Cr sample in this work. The green vertical lines mark the expected plane spacings.

3.4.3 Crystallography of Features

When the reconstruction is made using crystallography as described above, for a given world direction it is possible to calculate the corresponding crystal direction. This can be used to determine the crystallography of microstructural features, e.g. the habit plane of a dislocation loop found in the reconstructed data. The method used in this thesis is based on the MATLAB code and description given in C. Hirst's part ii thesis [269].

The transformation from world (reconstructed) coordinates to crystal coordinates requires a solution to Wahba's problem [270]. Markley [271] described how the rotation matrix to transform between two coordinate systems could be found using singular-value decomposition (SVD), with the following algorithm:

Construct a matrix $\mathbf{B}$:

$$\mathbf{B} = \sum_{i=1}^{n} \mathbf{w}_i \mathbf{c}_i^T$$

where $\mathbf{w}_i$ and $\mathbf{c}_i$ are unit vectors representing world and corresponding crystal directions respectively.

Perform singular value decomposition of the matrix $\mathbf{B}$:

$$\mathbf{B} = \mathbf{U}\mathbf{S}\mathbf{V}^{\mathbf{T}}$$

where $\mathbf{U}$ and $\mathbf{V}$ are orthogonal matrices, and

$$\mathbf{S} = \mathrm{diag}(s_1, s_2, s_3)$$

with $s_1 \geq s_2 \geq s_3 \geq 0$.

The rotation matrix, $\mathbf{R}$ is given by:

$$\mathbf{R} = \mathbf{U}\mathbf{M}\mathbf{V}^{\mathbf{T}}$$

where $\mathbf{M} = \mathrm{diag}([1, 1, \det(\mathbf{U})\det(\mathbf{V})])$

Transformation between the two coordinate systems is then achieved by either

$$\mathbf{c} = \mathbf{R}^{\mathbf{T}}\mathbf{w}$$

or

$$\mathbf{w} = \mathbf{R}\mathbf{c}$$

In this work MATLAB is used to perform the calculations, using code based on that by C. Hirst [269]. Scripts from AtomProbeLab [268] were also used to import IVAS .pos files into MATLAB for analysis.

The vectors used in $\mathbf{c}$ and $\mathbf{w}$ are determined as when indexing and selecting the reconstruction parameters, using a "reconstructed hitmap" as described in section 3.4.2.

Microstructural feature planes were determined using the MATLAB function affine_fit

[272], which fits a plane to a cloud of points. The function uses principle component analysis [273] to determine a series of vectors whose directions correspond to the maximum covariance of the data, and that are orthogonal to the previous vectors. The first component corresponds to a direction normal to the plane of best fit, and the second and third components lie on that plane.

3.4.4 Atom Probe Sample Preparation

All APT samples were prepared in a Zeiss Auriga dual beam SEM/FIB, using the lift-out technique described by Miller and Russel [274]. First a layer of Pt around 1 μm deep measuring ~2 x 20 μm is deposited with the FIB beam using the gas injection system (GIS). A cantilever beam is then manufactured containing this Pt layer, as described in section 3.2.2. This cantilever is welded to a micromanipulator with Pt and then cut free (see figure 3.19 (a)).

The beam is then transferred to a coupon containing an array of Si posts. The end of the beam is attached to one of these posts with Pt and then cut free from the rest, leaving a piece attached to the post and a shorter beam still attached to the micromanipulator (see figure 3.19 (b)). This process is repeated to create further samples until no beam remains. Pt is then deposited on the other side of the samples to ensure secure attachment.

The samples are annularly milled with the 30 keV Ga beam using progressively lower beam currents to form a sharp tip with a radius smaller than 100 nm (see figure 3.19 (c)). A 5 keV Ga beam is then used to remove the top ~50 nm, which contains implanted Ga.

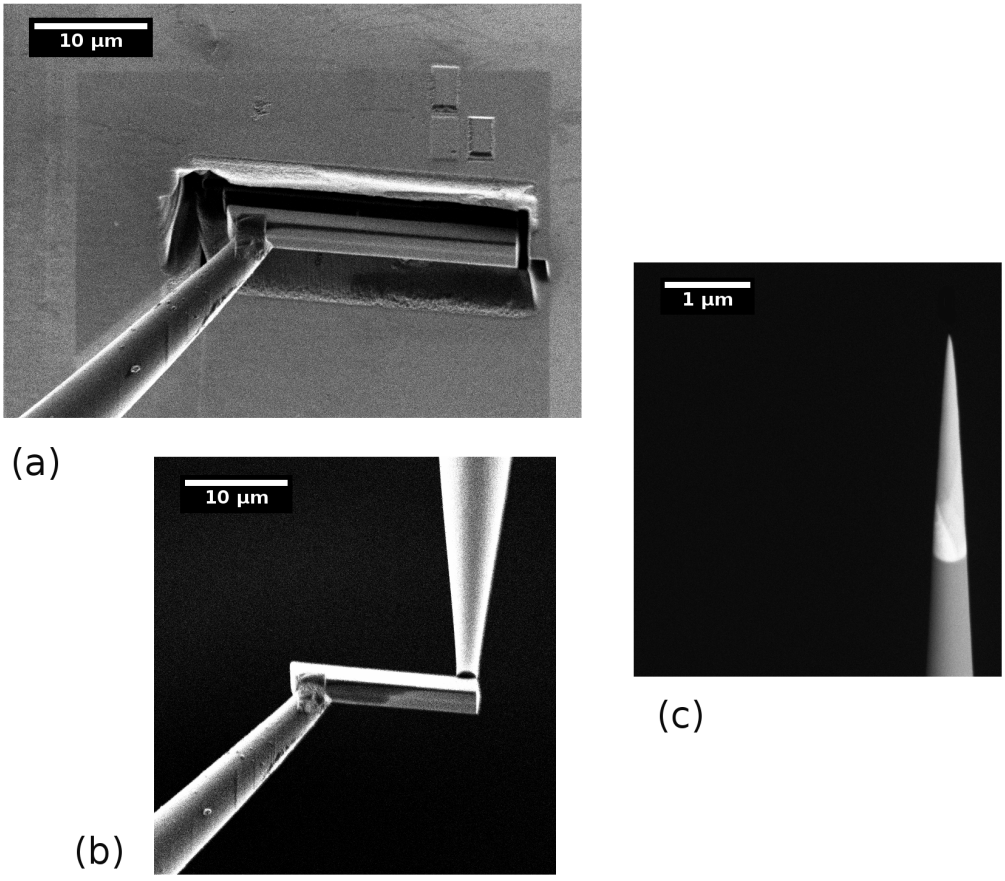


Figure 3.19: FIB lift-out technique used in preparation of samples. (a) Shows the lift-out of a Pt-topped cantilever using a micromanipulator. (b) Shows the beam being mounted onto a Si post. (c) Shows the final sharpened tip.

3.5 SRIM Damage Calculations

The number of displacements per atom (dpa) produced by heavy ion irradiations was calculated using SRIM [21]. The parameters and methods used were those recommended by Stoller et al. [22].

The program was run for using the "Quick Kinchin Pease" option, and using a displacement threshold energy (E_d) of 40 eV and a lattice binding energy of 0. The damage energy, T_{dam}, as a function of depth was calculated from the "PHONONS.txt", "E2RECOIL.txt" and "IONIZ.txt" files as recommended in [22], and the number of vacancies created, N_d, was then found using the NRT formula: $N_d = 0.8T_{dam}/2E_d$. This value was not found to differ from that calculated by summing both columns in the "VACANCIES.txt" file.

To calculate the dpa, this was multiplied by the dose in ions/cm^2 and then divided by the number of atoms /cm^2/angstom - 8.52×10^{14} for Fe.

For irradiations performed at the Surrey Ion Beam Centre (experiments in chapters 4 and 6), the beam energy in the program was set to 2, 1, and 0.5 MeV, and run for 10 000 ions at each energy. Fe targets of thickness 20 000 Angstroms were used for all energies.

For irradiations performed at JANNuS, Saclay (the experiment in chapter 5), the beam energy in the program was set to 24 MeV and the targets for each degrader foil used formed of a layer of Al corresponding the degrader foil thickness, on top of a 100 000 Angstrom Fe target. The simulation was run using 10 000 ions for each degrader foil.

3.6 Materials

3.6.1 EFDA Alloys

These alloys are from a set whose production was specifically commissioned by EFDA in order to study the effects of composition of alloying elements and impurities on radiation induced changes in microstructure due to displacements and H and He implantation, as part of the Fusion Material Programme in reference to the ferritic-martensitic steel EUROFER. As such they are of high purity. All data and details given below are taken from reports on the alloy preparation [275, 276].

Chemical composition of the alloys used in this work are given in table 3.1, grain sizes in table 3.2, and dislocation densities in table 3.3

Alloy	Cr (at%)	C (appm)	S (appm)	O (appm)	N (appm)	P (appm)
Fe	<2 appm	19	3	14	4	< 9
Fe3Cr	3.27	19	5	21	8	-
Fe5Cr	5.78	19	5	21	8	< 9
Fe10Cr	10.77	18	7	14	12	< 9

Table 3.1: EFDA alloy compositions

Alloy	Mean grain size (μm)	min / max grain size (μm)
Fe	183	4 / 650
Fe-3Cr	390	-
Fe-5Cr	68	2 / 170
Fe-10Cr	82	3 / 259

Table 3.2: EFDA alloy grain sizes

All of the alloys consist of a single ferritic phase.

Alloy	Dislocation density (/cm^2)
Fe	1.2×10^8
Fe-3Cr	-
Fe-5Cr	1.2×10^8
Fe-10Cr	$< 1 \times 10^8$

Table 3.3: EFDA alloy dislocation densities

3.6.2 UCSB Alloy

A series of Fe-Cr binary alloys were produced for experiments as part of an effort to understand the superior swelling resistance of martensitic steels over austenitic steels in the 1980s [44]. These alloys were later irradiated in the ATR reactor, with the Fe-9Cr alloy the focus of work reported in chapter 5.

As detailed by Gelles [44], 100 pound (~45 kg) heats of each alloy were produced at the Paul D. Merica Research Laboratory, International Nickel Factory, Sterling Forest, New York. Composition of the Fe-9Cr alloy provided by the vendor, alongside overchecks performed by Lukens Steel Company, Coatsville, Pensylvania, and more recent atom probe analysis [77] are given in table 3.4.

Element	Manufacturer [44]	Overcheck [44]	APT [77]
Cr	9.6	-	8.77
C	0.002	-	0.002
O_2	0.022	~0.01	-
N_2	0.0017	~0.05	-
Ni	-	~0.1	0.01
Mn	-	~0.02	0 01
P	-	~0.005	0.006

Table 3.4: Composition information of UCSB Fe-9Cr alloy given by the manufacturer, orders of magnitude impurities found by chemical analysis overchecks, and recent atom probe analysis (19M ions, neutron irradiated) [77]. All values in wt.%, balance is Fe.

The material was produced as a 1.0 cm diameter extruded bar, and then rolled to a

0.03 cm thick sheet. The sheet was then annealed under argon atmosphere at 950°C for 15min, followed by air cooling. It was then stress relieved at 750°C for 1 hour, followed again by air cooling [277]. This resulted in a simple fully ferritic microstructure, with relatively coarse grains.

3.6.3 Sample Preparation

All samples were prepared using standard metallurgical polishing techniques. First, samples were ground using grit papers of progressively smaller particle sizes, from 240 grade to 4000 grade. For each grade, grinding was performed in one direction until all scratches were parallel, and then rotated 90° and repeated for a perpendicular direction. This ensured all scratches from the previous grade were removed.

After grinding with 4000 grade paper, samples were polished for around 20 min at each stage with 6, 3, and 1 micron diamond suspensions. A final finish was achieved by polishing with colloidal silica for 5-15 min.

3.6.4 Irradiation Conditions

The key details of irradiation conditions used for all experiments in this thesis are shown in table 3.5. All ion irradiations were performed with multi-energy implantations to produce a roughly flat damage profile with depth. This table is provided for easy reference, and full details of conditions can be found in the respective chapters.

Chapter	**Samples**	**Condition**	**Dose (dpa)**	**Dose rate (dpa/s)**	**Temperature (°C)**
4 - Beam Rastering	EFDA Fe, Fe-3Cr, Fe-5Cr	Defocussed	0.3	1.2×10^{-5} Instantaneous 1.2×10^{-5} Global	300
		Scanned	0.3	7.2×10^{-4} Instantaneous 1.2×10^{-5} Global	300
5 - Ions vs Neutrons	UCSB Fe-9Cr	Ion	0.68 - 1.36	$2.98 - 5.96 \times 10^{-5}$	290-310
		Neutron	1.82	3.85×10^{-7}	304-334
6 - Effect of C	Carburised EFDA Fe	HDR	0.3	2.5×10^{-4}	300
		LDR	0.3	1.2×10^{-5}	300

Table 3.5: Table showing irradiation conditions and samples used for the 3 experimental chapters in this thesis. LDR and HDR stand for high and low dose rate respectively.

Chapter 4

Effect of Beam Rastering on Irradiation Hardening in Fe-Cr alloys

This chapter reports an experiment comparing irradiation hardening in low Cr content high purity model Fe-Cr alloys irradiated with a defocussed and scanned beam under otherwise identical conditions.

4.1 Introduction & Background

In ion irradiation experiments the ion beam can be made to irradiate the target area in one of two modes. In the first, known as defocussing, the beam spot size is adjusted to meet that of the target area. This way the whole target area is irradiated continually, but it can be difficult to ensure a spatially homogeneous beam intensity, and therefore the dose delivered (and the rate at which it is delivered) to samples in different areas may vary. In the second, known as beam rastering or beam scanning, the beam is focussed to

a small size and scanned over the target area. This mode is often preferred as it has the advantage of delivering a uniform dose across a large target area, but each area segment is exposed to the beam intermittently, and with a higher intensity than that for a steady beam for the same time averaged dose rate. The impact of this pulsed irradiation is discussed in detail in section 2.4.5, and summarised below.

A rastered beam can be thought of as pulsed source, with each area segment experiencing "beam on" times while the beam reaches its position, with "beam off" times in between as the beam is scanned across the rest of the target. This mode of operation differs from steady state irradiation in 3 ways:

i An increase in instantaneous dose rate due to the dose delivered per unit time being compressed into only the "beam on" periods

ii An induced temporal variation in flux of point defects due to pulsed irradiation

iii The presence of "beam off" periods where annealing can occur

Theoretical analysis is generally based on the Fully Dynamic Rate Theory developed by Ghoniem and Kulcinski [202]. Alongside a body of experimental work around the same period, this focussed on pulse operated reactors rather than scanned ion beams.

Dose rate is discussed in detail in section 2.4.2. In the rate theory an increase in dose rate leads to a higher concentration of point defects per unit time per unit volume, and therefore an increase in mutual recombination, reducing the number of defects available to participate in radiation damage.

Due to the large difference in mobilities of vacancies (lower) and interstitials (higher) in Fe [204], pulsed irradiation can produce a temporal variation in the flux of these point

defects. At the end of an irradiation pulse interstitials quickly arrive at sinks, leaving behind an excess of vacancies, which follow later. Lee et al. [210] and Hishinuma et al. [211] suggested that their observation of a more refined loop population (smaller and higher number density) in steels under pulsed irradiation compared to steady irradiation could be due to this pulsed flux of defects. "Beam off" periods could allow the vacancy population to "nibble away" at the interstitial loops formed during "beam on" times unopposed. Their sizes would be reduced and the net result would be a more refined loop population.

Trinkaus and Ullmaier [204,206] discuss the processes sensitive to point defect flux fluctuations. They argue that insensitive processes are those which mainly depend on the total defect flux accumulated - the growth of stable structures (e.g. cavities and precipitates), and the segregation of impurity atoms to interfaces and grain boundaries. Sensitive processes are those that require the surmounting of a physical or energetic barrier, such as creep by climb controlled dislocation glide or in nucleation processes.

Interpulse annealing allows the system to relax towards equilibrium. More relaxation occurs at higher temperatures and for longer "beam off" times. Microstructures containing less stable structures, such as small voids, are more susceptible to interpulse annealing effects. This was demonstrated experimentally by Brimhall et al. Pure Ni samples were pre-irradiated in a continuous manner at higher [207] and lower [208] temperatures before being subjected to either continuous or pulsed irradiation. Those samples pre-irradiated at the lower temperature showed a coarsening of the void structure under subsequent pulsed irradiation compared to subsequent continuous irradiation, whereas those pre-irradiated at the higher temperature showed little difference. This was thought to be because the pre-irradiation at lower temperature produced a void population with smaller sizes, which can more easily anneal during beam off periods.

Interpulse annealing is also thought to affect void nucleation. Voids become stable and grow by bias driven growth when the vacancy influx is greater than the outflux by thermal emission. Thermal emission is a strong function of void radius, and the radius at which the vacancy influx and outflux become equal is termed the critical radius [57]. In pulsed irradiation there are periods of no vacancy influx, meaning the critical radius can effectively be increased as the influx and outflux must now balance over the whole cycle [203].

Lee et al. [210] observed a reduction in the amount of G-phase and an increase in MC precipitates in a Ti-modified stainless steel after pulsed irradiation compared to steady state irradiation. It was argued that annealing during beam off periods means the system shows preference for the thermal equilibrium MC phase.

Only a relatively small number of experiments have been performed directly comparing irradiation with scanned and defocussed beams, mainly focussing on swelling and void microstructure. The results from these experiments are summarised in table 4.1.

The first was performed in 1973 by Sprague et al. [201] in pure Ni, with more recent studies by Getto et al. [13] in F/M steels and Gigax et al. [12] in pure Fe. All 3 reported reduced void sizes for irradiation with a scanned beam compared to a defocussed one, in agreement with earlier studies comparing pulsed/steady irradiation [208, 209]. Overall swelling was reduced with beam scanning in both of the most recent studies [12, 13], and wasn't directly compared in the earlier study [201]. Only Getto et al. [13] reported loop sizes, and found them to remain unchanged within experimental error. In contrast, earlier pulsing experiments found dislocation structure to develop more slowly under pulsed irradiation in austenitic steels [210, 211], and more rapidly in Mo [209], compared to continuous irradiation. Getto et al. [13] found a reduction in the number

density and size of G-phase precipitates after scanned irradiation compared to continuous irradiation, in agreement with Lee et al.'s [210] pulsing study. Gigax et al. [12] found the void microstructure to be scanning frequency sensitive, and also reported a possible interplay with the injected interstitial effect (see section 2.4.3).

These findings raise concerns about the use of beam scanning in ion irradiation experiments for emulation of typically continuous neutron irradiation. In particular, no study has explicitly focussed on the impact of the change in instantaneous dose rate that occurs with beam scanning. This is of particular significance for low Cr Fe-Cr alloys which have been shown to be sensitive to dose rate [154], which is thought to be an important contributing factor to differences found in microstructure and mechanical properties between ion and neutron irradiation [14]. The present experiment aims to fill this gap in the literature.

4.2 Experimental

Samples of UHP Fe, Fe3Cr and Fe5Cr were prepared for irradiation using the procedure described in section 3.6.3. The materials were selected due to their pronounced dose rate sensitivity demonstrated by Hardie et al. [154] (discussed in detail in section 2.4.2), and are the same as those used in that experiment. These alloys are those referred to as "EFDA alloys" in section 3.6, and detailed compositions and production history can be found there. They are of ultra high purity and have a fairly large grained ferritic microstructure.

Samples were mounted onto a Si wafer with high temperature conductive silver epoxy and irradiated with Fe ions at 300°C at the Surrey Ion Beam centre using either

Ref.	Material	Irradiating species	Temperature (°C)	Dose (dpa)	Dose rate (dpa/s)	Scanning details	Observations of scanning effects
[201]	Pure Ni	2.8 MeV Ni	350 - 750	16	1.4×10^{-2} - 8.3×10^{-2} (global)	2.5ms on/off, 25us on/off sub-pulses	Mean void diameters ↓ diameters ↓ as T ↑
[13]	HT9, T91	5 MeV Fe (+He)	440	140, 150	$0.79 - 1.9 \times 10^{-3}$ (global)	2061 Hz in y 255 Hz in x (full frame every 3.92ms)	Void size+number density ↓ swelling ↓ G-Phase size + number density ↓ loop size slightly ↓ loop number density =
[12]	Pure Fe	3.5 MeV Fe	450	50, 100	1.74×10^{-3} (global) 6.26×10^{-3} (instantaneous)	1 dimension at 0.244, 1.93, 15.625 Hz	Void sizes ↓ number density ↑ Frequency sensitivity of void microstructure and injected interstitial effect

Table 4.1: Table summarising literature experiments comparing effects of irradiation with static and scanned beams.

a scanned or defocussed beam. The temperature was monitored using a thermocouple clamped to the wafer.

For each irradiation three beam energies were used sequentially, beginning with the highest energy and finishing with the lowest, to produce a roughly flat damage profile suitable for mechanical testing. Implantation details are given in table 4.2. SRIM was used to calculate the dose as outlined in section 3.5, giving a dose of approximately 0.3 dpa and a time averaged dose rate of 1.2×10^{-5} dpa/s. The dose as a function of depth is shown in figure 4.1, and the same for dose rate in figure 4.2.

Beam Energy (MeV)	**Dose (ions/cm^2)**	**Doserate (ions/cm^2/s)**
2.0	2.5×10^{14}	1.11×10^{10}
1.0	7.5×10^{13}	1.04×10^{10}
0.5	5×10^{13}	8.87×10^{9}

Table 4.2: Implantation conditions used in this experiment.

Irradiation conditions were chosen based on results from Hardie et al.'s [154] study to be where materials showed the most sensitivity to dose rate, so any changes between the two irradiation modes would be most apparent. Quoted dpa dose values differ due to inconsistencies identified in SRIM between the "Full Cascade" damage calculation mode used by Hardie et al. and the "Quick Kinchen-Pease" mode used in the present work, as recommended by Stoller et al. [22]. The dose in terms of ions/cm^2 are the same for both studies.

The dose delivered experimentally is measured by the charge collected on the stage. In this experiment, an aperture was placed directly in front of the samples, which included an electron suppressor. This ensured the charge measured was unaffected by secondary electrons.

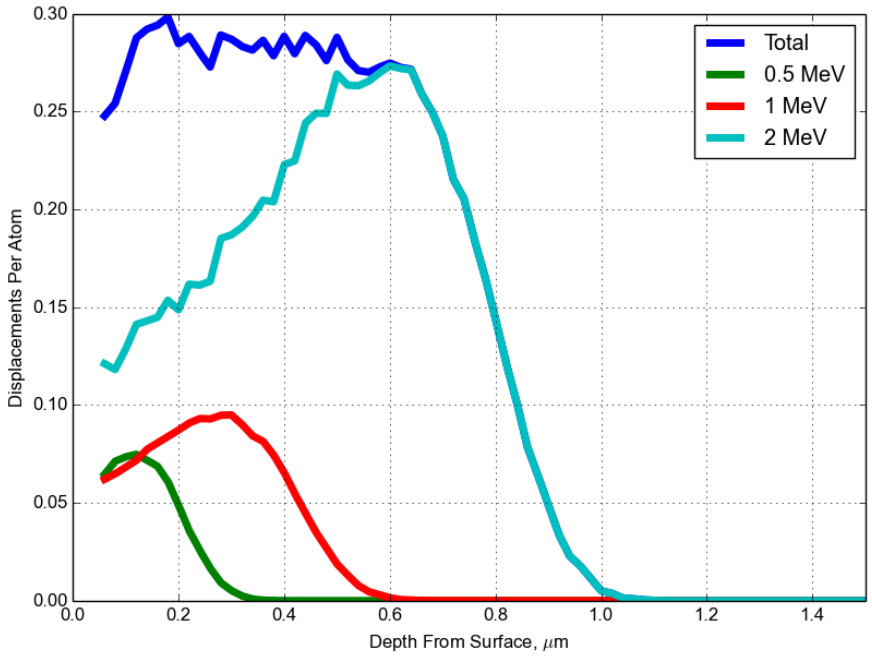


Figure 4.1: Dose as a function of depth, as calculated using SRIM.

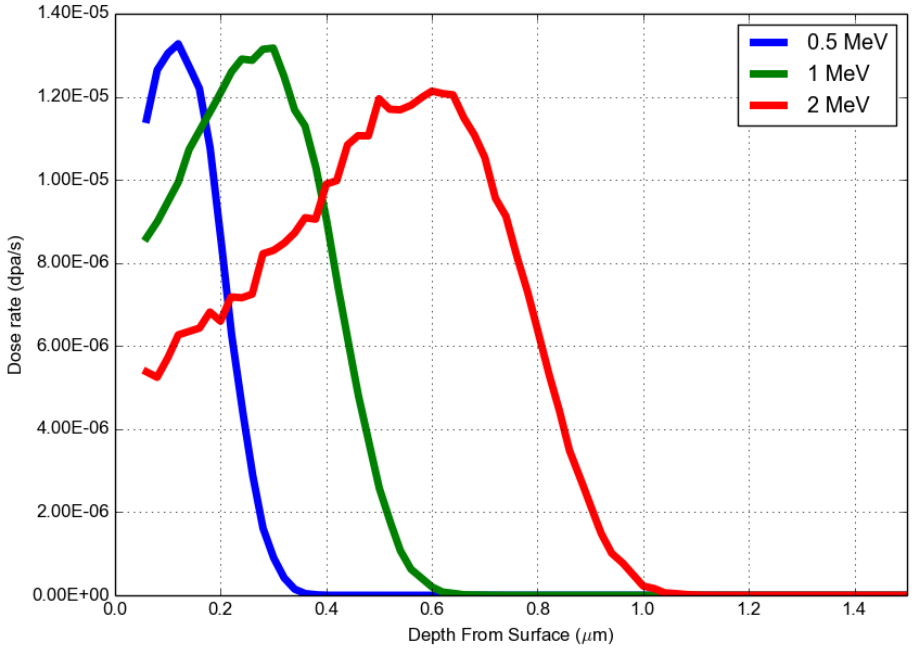


Figure 4.2: Doserate as a function of depth, as calculated using SRIM.

4.2.1 Defocussed Setup

Surrey normally operate their beam in a rastered mode, so this experiment was bespoke and required benchmarking, in particular to assess the uniformity of the beam. A preliminary experiment was performed to do this.

The beam was adjusted to the size of the aperture (20x22 mm). This was verified by adjusting the position of the beam and checking for a drop in current measured on the stage as the aperture obscured part of the beam. A silicon wafer was irradiated with the defocussed beam, implanting ~10^{15}/cm^2 2 MeV Fe ions at 300°C. The concentration of Fe was subsequently measured as a function of position using Proton-Induced X-ray Emission (PIXE). The projected depth of 2 MeV Fe in Si is around 1.6μm, but with diffusion at 300°C will extend to ~30 μm. PIXE is a spectroscopic technique that can give chemical composition information at these depths, inaccessible to surface techniques. This analysis was performed by C. Jeynes and R. Gwilliam of the University of Surrey Ion Beam Centre.

A 2 MeV proton beam was used for analysis as it gave the best signal to noise ratio. The Fe concentration was measured in a 5x5 grid of points with 5 mm spacing. Results are displayed in figure 4.3.

Due to software limitations, the grid position data is preset but only time and concentration are recorded. The position is then inferred from the time data. The scan was run overnight and did not proceed exactly as expected, leading to some uncertainty in the position data. This is likely responsible for the anomalous shape of the beam profile.

Based on this preliminary experiment, samples were placed in a central 15 mm by 15 mm area for the main irradiation, with a small amount of beam wobble applied to

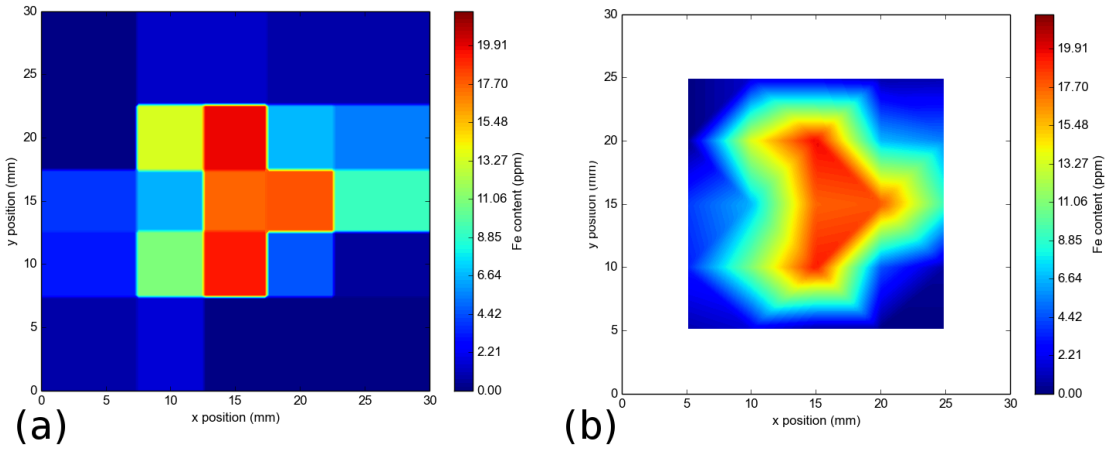


Figure 4.3: Results of PIXE analysis of implanted Si wafer from preliminary experiment to assess uniformity of defocussed beam. The raw data is shown in (a), and (b) is after some linear interpolation.

smooth out any inhomogeneity. Space was left between samples to allow PIXE analysis to check dose uniformity.

4.2.2 Beam Scanning Details

Beam scanning conditions were chosen to match those typically used at the facility for ion irradiation experiments. The beam was focussed to a spot around 3 mm in diameter, and swept horizontally and vertically across the target area (the same 20 mm by 22 mm aperture as in the defocussed experiment). Its position in x and y are controlled by 2 triangle wave signals. Frequencies of 1000 Hz in x and 1004.5 Hz in y produce a spiralling raster, with beam path shown in figure 4.4.

A python script was written to visualise the beam path, and analyse the illumination of a position by the beam as a function of time. The position of the beam is monitored and compared to that of the test position. The test position is said to be illuminated if the difference between the beam and test position is less than the spot size radius. The

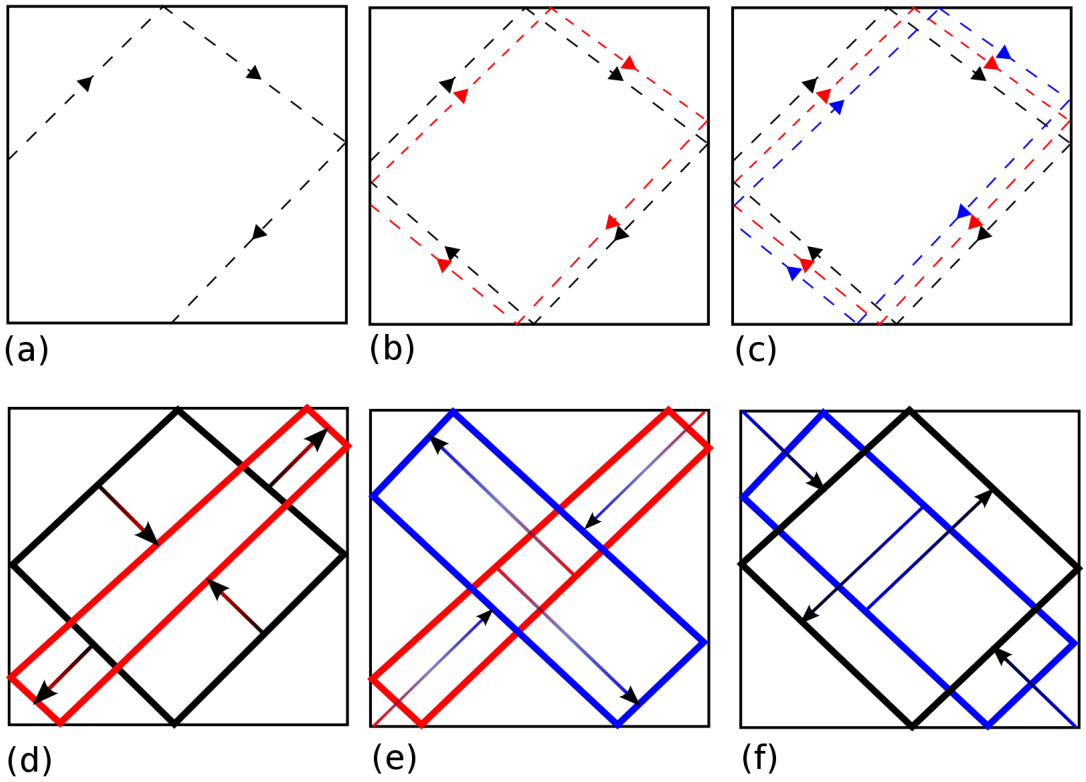


Figure 4.4: Diagrams showing the path of the scanned beam. (a), (b), and (c) show the path the beam follows, and how the shape of the circuit is transformed as each is completed. The difference in frequencies of the waves controlling the x and y position of the beam causes this precession. (d), (e), and (f) show how the shape of the circuits change (from black to red, red to blue, blue to black) with time, and how full coverage is achieved (twice in the progression depicted).

resulting pulsing pattern for the centre of the aperture is shown in figure 4.5 a and b.

The test position is irradiated in pulses, with a sub-pulse structure. The origins of this structure are shown in figure 4.5 c and d. The major pulses occur as the beam's path progresses and comes close enough to the test position. The sub-pulses come from each individual pass of the beam around its path.

Due to the nature of the rastering pattern used, the exact pulse structure varies as a function of position. The time between the main pulses is determined by the time between beam path edges passing the position. This is a function of distance from the major diagonal "parallel" to each edge.

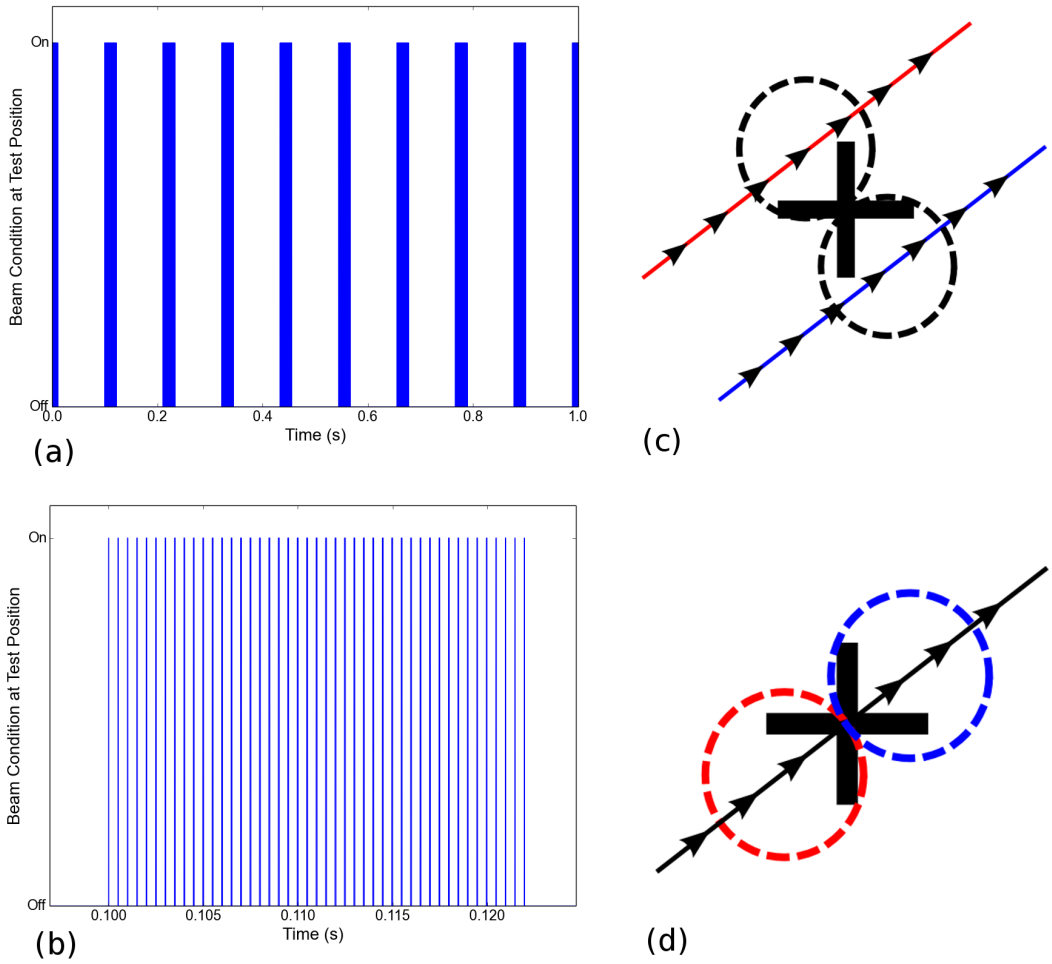


Figure 4.5: Illumination of the centre of the aperture as a function of time for the scanned beam condition. (a) Shows the pulsed nature of the irradiation, with an enlargement of an "on" pulse in (b), showing the sub-pulse structure. (c) Shows the origin of the pulse structure depicted in (a). The beam path moves around the target area as shown in figure 4.4. This is from the red to the blue line in (c). The start of the "beam on" period for the main pulse begins when the beam path gets to the position shown by the red line, within a beam radius of the test position, and ends when it reaches the blue line. The sub-pulse structure is produced as the beam cycles around the beam path, with "on" periods as it moves from the red to the blue position shown in (d) and off periods for the rest of the circuit.

Position (mm,mm)	**Pulse "On" Time (ms)**	**Pulse "Off" Time (ms)**	**Sub-Pulse "On" Time (μs)**	**Sub-Pulse "Off" Time (μs)**
(0,0)	22	89	50	450
(0,7)	22	56, 12	50	950

Table 4.3: Approximate pulse and sub-pulse on and off times for different target positions for the scanned beam condition. The position is given in Cartesian coordinates with the the origin at the centre of the 22 mm x 20 mm aperture.

The time between subpulses is determined by the time it takes for the beam to complete a loop of its path. This will be constant as it depends on the time period of the signal controlling the beam x and y positions. However, close to the major diagonals the beam can irradiate a position twice per circuit if the "parallel" edges are separated by less than the spot size diameter.

The pulse structure was also analysed for a position away from either major diagonal (7 mm above the centre of aperture) with pulse details for both positions given in table 4.3. Each pass of the beam path causes a main "on" pulse lasting 22 ms, separated by a main "off" period by a time which depends on position. These main "off" pulses may alternate between two time values caused by different distances the edges of the beam path must cover to reach the test position. Each main "on" pulse consists of sub pulses lasting ~50 μs, separated by sub-pulse "off" periods of ~950 μs, except near the major diagonals where the position is irradiated twice per circuit of the beam path.

The change in instantaneous dose rate due to beam scanning was calculated by the ratio of "beam on" to total time for 1 period of the pulsing sequence, and remains constant for all positions as is determined by the ratio of beam spot size to aperture size. For these conditions an increase in instantaneous dose rate of 62.1x was calculated.

A summary of radiation conditions for the rastered and defocussed conditions is given in table 4.4.

Beam condition	Temperature (°C)	Dose (dpa)	Time averaged dose rate (dpa/s)	Instantaneous dose rate (dpa/s)
Defocussed	300	0.3	1.2×10^{-5}	1.2×10^{-5}
Rastered	300	0.3	1.2×10^{-5}	7.2×10^{-4}

Table 4.4: Summary of irradiation conditions for the defocussed and rastered beam condition.

4.2.3 Post-Irradiation Analysis

After irradiation, samples were mounted onto pinstubs for nanoindentation using a thin layer of crystalbond and tested, according to procedures outlined in section 3.1. Prior to indentation, the tip area function was calibrated following the procedure described in section 3.1.3.3. For each irradiation condition arrays of 1000 nm deep indents were performed, with each indent spaced atleast 20 μm from any other. Multiple indent arrays were produced, covering multiple grains and areas of the samples.

Indentation was performed using the continuous stiffness measurement technique, with a harmonic displacement of 2 nm and a frequency of 45 Hz. The target strain rate was 0.05 s^{-1}.

4.3 Results

Plots showing hardness and modulus as a function of depth are shown in figure 4.6.

The modulus at depths ~100-300 nm is in agreement with literature values for Fe of around 210 GPa, and falls slightly at larger depths due to increased contribution to the compliance from the crystal bond used to mount the sample at higher loads. In the Fe-3Cr and Fe-5Cr alloys, there is a discrepency between the unirradiated and irradiated modulus at this depth - possibly due to pileup, which causes the contact area to differ

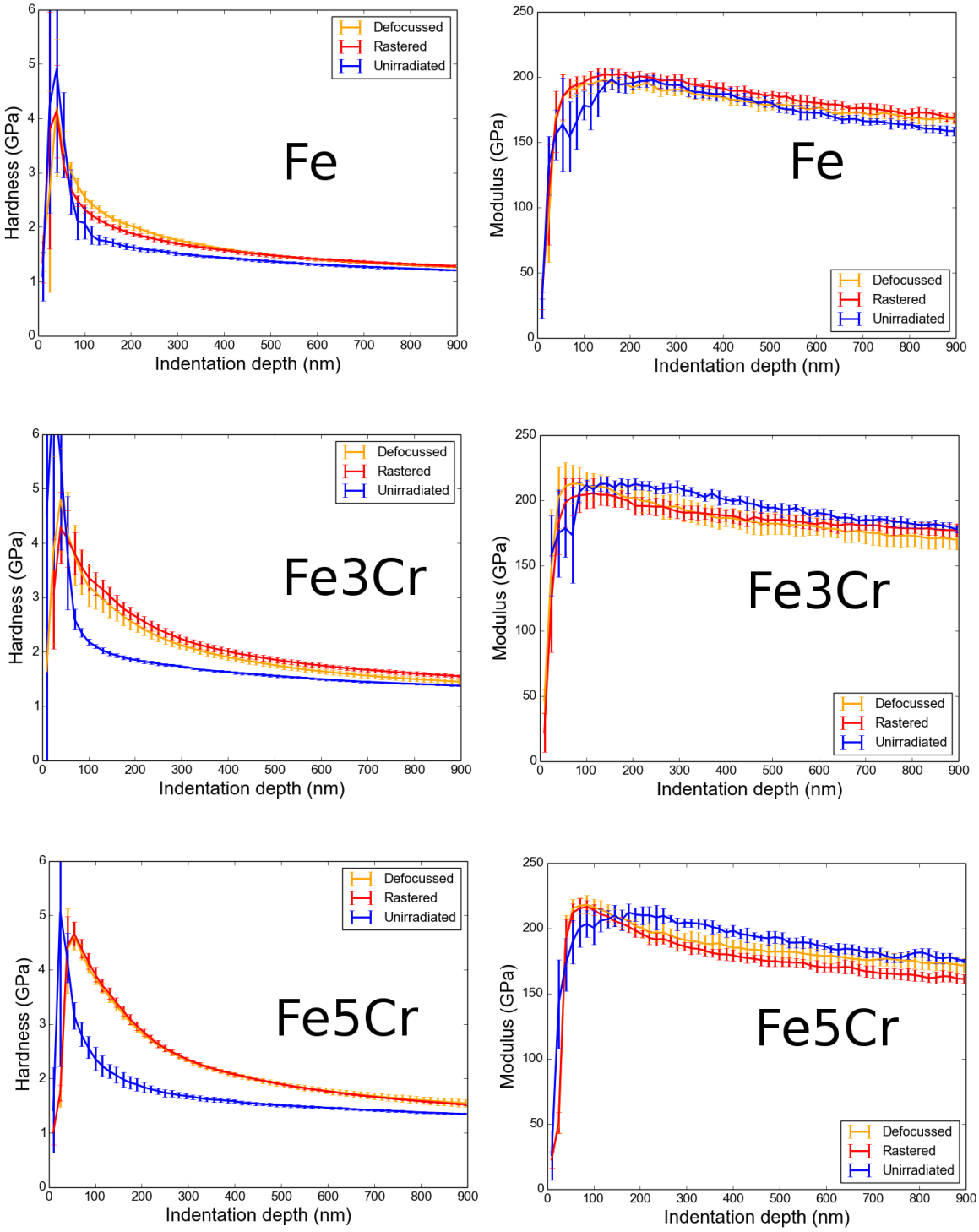


Figure 4.6: Hardness (left) and modulus (right) as a function of indentation depth for high purity Fe, Fe-3Cr and Fe-5Cr irradiated with static and defocussed beams. Error bars represent ± 1 standard deviation.

to that calculated using the area function calibrated using the reference sample prior to the experiment (see section 3.1.3.3).

Hardness data show indent size effect (ISE) behaviour, discussed in section 3.3.2, and those for irradiated specimens tend towards the unirradiated values at larger depths where plastic deformation is mostly occurring beyond the irradiated depth(~1μm). The plastic zone depth is significantly greater than the indent depth, eg. Hardie et al. [278] found it to extend beyond the ~1 μm irradiated layer for indent depths greater than 200 nm.

The hardness at 250 nm for each material and condition are given in figure 4.7. The range of modulus values for all 3 conditions measured at this depth represents an uncertainty in the contact area, possibly due to differing pileup behaviour. This uncertainty in the measured values of E can be propagated into an uncertainty in the contact area by calculating an area correction factor, C_E, as used in [279–281].

Kuksenko et al. [279] give the expression:

$$C_E = \left(\frac{\frac{1-\nu^2}{E} + \frac{1-\nu_i^2}{E_i}}{\frac{1-\nu^2}{E_\mathrm{u}} + \frac{1-\nu_i^2}{E_i}} \right)^2 - 1 \tag{4.1}$$

where ν and ν_i are the Poisson's ratio of the sample and the indenter, E_i the elastic modulus of the indenter, E_u the measured elastic modulus of the sample without correction, and E the "correct" or reference sample modulus.

For this analysis, for each condition E was set to the mean value $\pm$ the standard deviation measured at this depth - producing area correction factors corresponding to the range of contact areas within the uncertainty. This was propagated into an uncertainty

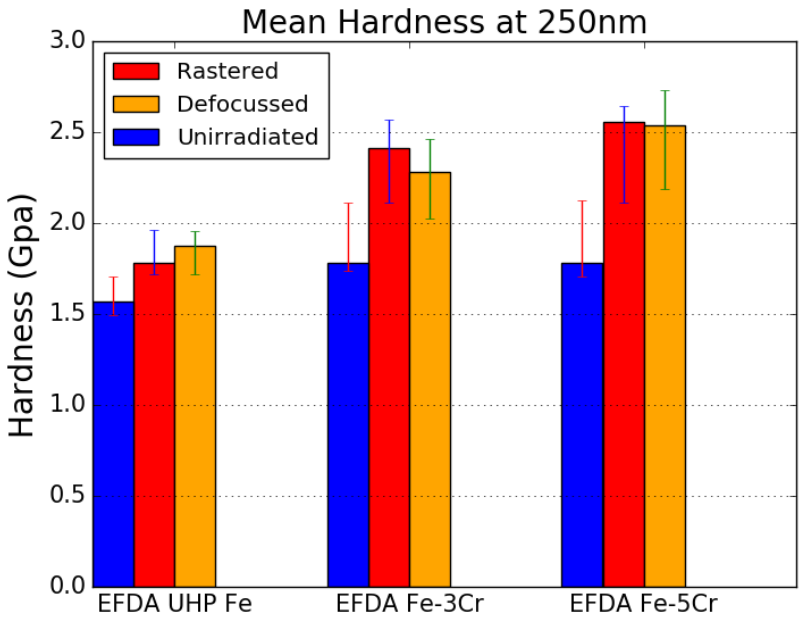


Figure 4.7: Nanoindentation hardness at a depth of 250 nm for unirradiated materials and those irradiated defocussed and rastered beams. Error bars represent the largest possible error due to area propagated from uncertainty in the elastic modulus. This uncertainty could be reduced by measuring the area of the indent impression with e.g. AFM.

in the hardness, H, using:

$$H_c = \frac{H_m}{(C_E + 1)} \tag{4.2}$$

where H_c is the corrected hardness, H_m the measured hardness.

For all alloys, the hardness curves show no statistically significant difference between the rastered and defocussed irradiation conditions.

4.4 Discussion

4.4.1 Dose Rate

The primary aim of this work was to establish whether or not changes in instantaneous dose rate caused by beam scanning would cause similar changes in irradiation induced hardening to that reported by Hardie et al. [154] with changes in time averaged dose rate.

In their experiment, significant changes in hardness were observed in the same Fe-5Cr alloy for a difference in dose rate of ~20x. Hardness as a function of depth is shown in figure 4.8 (a). The "low dose rate" in their experiment corresponds to the same instantaneous dose rate as the defocussed condition in the present experiment. The rastered condition represents an increase in instantaneous dose rate of ~60x. Comparing Hardie et al.'s data with the Fe-5Cr data from the present experiment in figure 4.8 (b), it is clear a similar difference in hardness is not observed.

In order to explain these observations it is first necessary to understand the radiation induced hardening mechanisms in these Fe-Cr alloys, and the origin of the dose rate effect.

Hardie et al. found a lower loop density in the Fe-5Cr sample irradiated at the lower dose rate than for the higher dose rate condtion (16.1×10^{21}/m^2 for the high dose rate and 9.72×10^{21}/m^2 for the low dose rate). Mean loop diameters were found to be 6.7nm and 6.5nm for the high and low dose rate conditions respectively. As discussed in their work, this suggested that the additional hardening observed with a decrease in dose rate was due to the formation of obstacles to dislocation glide other than simple dislocation loops.

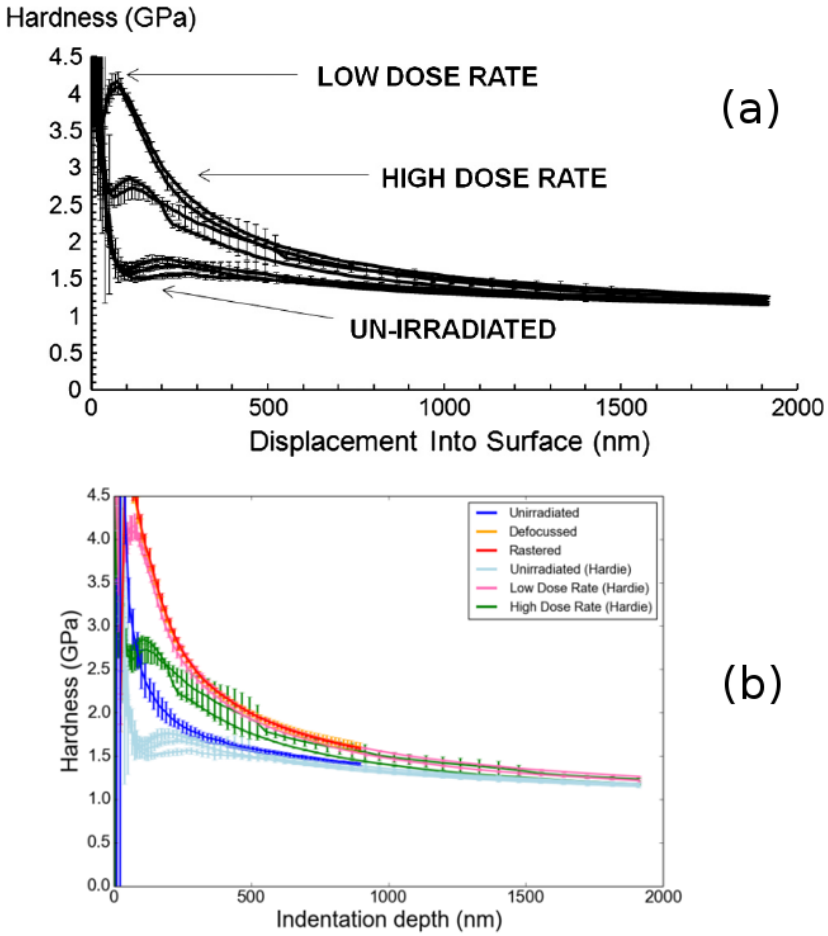


Figure 4.8: (a) Hardness as a function of indentation depth in Fe-5Cr after irradiation at high and low dose rate, from Hardie [154]. (b) Shows data from the present experiment for the same material plotted alongside data from (a). Both rastered and defocussed samples show good agreement with the low dose rate irradiation from [154].

Cr clusters found with atom probe tomography, potentially associated with dislocation loops, were thought to be the obstacles responsible. They were found to be larger and have a higher number density in the lower dose rate condition.

The formation of such clusters requires the diffusion of Cr. Hardie et al. argued that for these large grained materials with low dislocation density, mutual recombination was likely to be the dominant point defect annihilation mechanism. The lower concentration of point defects at the lower dose rate would mean more freely migrating defects [139] would migrate on average over larger distances before recombining, leading to enhanced radiation induced precipitation/segregation, and therefore enhanced hardening.

In Fe, defects are not observed in TEM below a dose of around $10^{12} - 10^{13}$ions/cm^2 [36] - corresponding to ~0.01dpa. This is interpreted as being the "cascade overlap dose", the dose at which remnants of one collision cascade interact with another, allowing the formation TEM-visible defects such as dislocation loops.

For the dose rates used by Hardie et al., the time taken to reach this dose and therefore the time between overlapping cascades is ~40 s and ~14 min for the high and low dose rates of 2.4×10^{-4} and 1.2^{-5}dpa/s respectively. This suggests that defect migration and microstructural evolution occurs over timescales of at least 40 s.

For the instantaneous flux of the rastered beam irradiation in the present experiment, cascade overlap would occur after ~1.5s. This is very long compared to the "beam on" time of ~50 μs during a sub pulse, or ~900 μs during a main pulse. This means that cascade overlap is very unlikely to occur during any pulse, and each cascade is sufficiently far away as to not interact with any subsequent cascades on the pulsing timescale.

Although this approach for deterimining the dose at which cascade overlap occurs

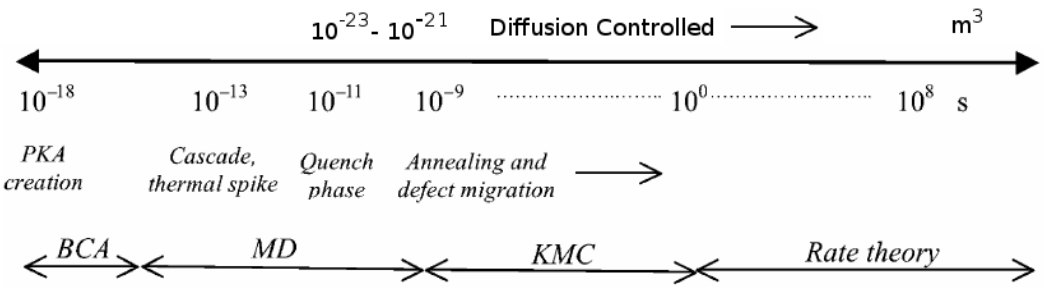


Figure 4.9: Figure modified from [16], showing the stages of damage evolution and their typical timescales and commonly used simulation techniques.

has the advantage of being experimentally verified, it neglects the possibility of interaction between the products of separate cascades before this dose is reached, which may not result in the production TEM visible defects.

An alternative approach is to consider the timescales and characteristic volumes in the development of the damage cascade. Figure 4.9 shows the stages of damage formation and development, and their durations and volumes, with the typically used simulation techniques indicated.

Displacement damage begins with the almost instantaneous formation of a PKA on the order of 10^{-18}s [16]. This PKA goes on to displace other atoms around it, leading to a "thermal spike" phase where the region can be thought of as melted locally. The "quench" stage follows, and after around 10 ps the material recovers and resolidifies [16, 136], leaving behind point defects either individually or in defect clusters. After this, the evolution of damage is controlled by the thermally activated diffusion of these point defects and clusters.

Alongside the timescales, in order to assess the time between overlapping cascades it is also necessary consider the relevant volumes. The damage process can be simulated for up to around 100 ps using molecular dynamics [136], and so this can provide an

estimate for the volume up until this time.

The cascade size depends on the PKA energy, and Stoller et al. [25] used a number of atoms coresponding to a simulated volume from 40 nm^3 to 2.7×10^4 nm^3 for PKAs with energy of 0.1 and 50 keV respectively. The highest energy cascade simulations in Fe, and closest available to those used in this experiment, were performed by Zarkadoula et al. [136] using 0.5 MeV PKAs. Here, the largest separation between atoms in the cascade was found to be 130 nm. Taking a cube of these dimensions gives a volume of ~2.2×10^6 nm^3, or 2.2×10^{-15} cm^3.

This damage volume then grows by the diffusion of point defects, and a higher temperature will allow point defects to diffuse further in a given time. Interstitial defects diffuse faster than vacancy defects in Fe, and so the extent of the damaged volume is controlled by their movement.

Kusunoki [282] modelled the diffusion of self interstitials in α-Fe by dumbell and crowdion migration and found the diffusion coefficient, D_i, to be around 4×10^{-5} cm^2/s at 300°C. For vacancies, the diffusion coefficient D_v was determined from $D = D_0 e^{-\frac{E_v^m}{kT}}$, with $D_0 = 6.7\times10^{-7}\mathrm{cm^2s^{-1}}$ [283], and $E_v^m = 0.55eV$ [100, 101, 107–109]. The characterstic diffusion length, $\sqrt{Dt}$, can be used to estimate the distance a defect can be expected to travel after a time t, and converted into a spherical "damaged volume".

These calculations appear to suggest that the "damaged volume" would grow to $2\times10^{-7}\mathrm{cm^3}$ for interstitials and $4\times10^{-10}\mathrm{cm^3}$ for vacancies during the 22 ms main "on" pulse. This simplistic approach however neglects the presence of traps such as Cr [31, 32, 36, 38] and C [102–106, 115, 116] which greatly reduce the extent to which point defects can diffuse. A more sophisticated model would be required to take these into consideration, and is beyond the scope of this present work.

The fact that the dose corresponding to the onset of visible defects was reported to be the same at 50 K [35] and 573 K [36] in Fe may suggest that diffusion is not that significant.

A simple 2D planar model can be used to calculate whether or not cascades are expected to overlap during a single pulse of the scanned beam. Assuming a cubic cascade volume, for each incident ion, an area can be assigned corresponding to the projected area of the MD cascade volume (neglecting any diffusion). Based on a cascade size of 130 nm x 130 nm, this gives a projected area of 1.7×10^{-10}cm^2, requiring 5.9×10^9 ions to cover 1 cm^2 and overlap. For the instantaneous flux of ~6×10^{11} ions/cm^2/s, this is achieved in around 0.01 s. This is again long compared to the 50μs on period during a sub-pulse, and ~900μs for a main pulse, suggesting that cascades produced in a single pulse are sufficiently separated in space to not interact.

The discrepency between the time until overlap between the two approaches are likely due to the simplifying assumptions in the latter method, where effectively all cascades are assumed to occur at the same depth, and there is no preferential direction for the cascade.

Following the above discussion, it is concluded that no dose rate effect is observed for differences in instantaneous dose rate because the defects produced in a single pulse do not interact. The relevant dose rate is the one averaged over the timescale over which the microstructural evolution occurs, here the diffusion of Cr. This is the dose rate that controls the relevant concentration of point defects which lead to different levels of mutual recombination and the dose rate effect. In the case of this experiment this is averaged over many many pulses, and is therefore the same for both rastered and defocussed beam conditions.

4.4.2 Beam Rastering

At first glance these results may seem to be in contradiction to others reported in the literature, with no beam scanning effect on hardening observed here, unlike the changes in void microstructure reported elsewhere [12, 13, 201]. However, it is important to consider the underlying mechanisms and processes in the microstructural evolution, and how they are affected by differences in the radiation environment.

Although dose rate was the focus of the present experiment, beam scanning can also induce fluctuations in point defect fluxes due to the pulsed nature of the irradiation. Trinkaus and Ullmaier [204, 206] discussed processes sensitive to these fluctuations. They argue that insensitive processes are ones where microstructural changes depend mainly on the total defect flux accumulated and not on any temporal variations. In this category are the growth of stable structures (e.g. cavities and precipitates) and the segregation of impurity atoms to interfaces and grain boundaries. Sensitive processes are those which require the surmounting of a physical or energetic barrier. This category includes creep by climb controlled dislocation glide, and nucleation processes.

In the present experiment the dominant hardening mechanism is the formation of Cr clusters, thought to be associated with dislocation loops. This process is insensitive to fluctuations in point defect fluxes, as the important factor is the total amount of Cr segregated and not any temporal variations in its arrival. It is however sensitive to dose rate, as this affects the total amount of Cr segregated for a given dose.

Void nucleation is sensitive to point defect flux fluctuations as it requires the surmounting of an energetic barrier in reaching a critical size to become stable [57]. The sensitivity of the process forming the microstructure studied, and differences in irradiation conditions may explain the appearance of a beam scanning effect observed else-

where [12, 13, 201]. The higher dose rates (1 or 2 orders of magnitude) and higher temperatures used in other studies may increase the chances of interaction of point defects produced by different cascades on the pulsing timescale.

The main reason for using a rastered beam is to ensure a uniform dose across the whole of the target area. In the present experiment samples were mounted on a Si wafer, with spaces left to allow PIXE analysis of the wafer after irradiation to check the implanted Fe distrubution across the target area. However, unfortunately such analysis wasn't possible as no Fe signal could be collected from the spaces left between the samples. Results from the preliminary experiment and the addition of a small amount of beam wobble during this irradiation gives confidence that any dose inhomogeneity is at least smaller than in the preliminary experiment, but small variations in dose cannot be ruled out for the defocussed irradiation.

4.5 Conclusions

No beam scanning effect was observed in irradiation hardening for any of the Fe or Fe-Cr alloys studied for these irradiation conditions.

It is suggested that changes in the instantaneous dose rate with beam scanning do not produce a dose rate effect because the dose rate averaged over the time scale at which microstructural development occurs (average time for reactions between freely migrating defects) is the same for scanned and defocussed beams under the conditions studied.

The presence of a beam scanning effect may depend on the details of the mecha-

nism of microstructural development in the material studied, as well as the irradiation conditions.

For emulation of neutron irradiation with ion irradiation, the importance of any influence of beam scanning may again depend on the details of damage evolution in the material studied, and the relative sensitivity of processes to pulsing effects compared to other differences in irradiation conditions such as dose rate, injected interstitials, PKA energy, and transmutation gases (see section 2.4).

4.6 Further Work

Further work is required to experimentally establish the conditions where beam scanning effects occur.

Experiments in simple alloys where the damage mechanisms are well understood would help build an understanding of scanning effects on individual microstructural development processes.

Gigax et al.'s work [12] showed a dependence on scanning frequency and this needs to be explored further, particularly given the beam scanning pattern used in the present work produces a pulsing frequency that varies with position.

Their work also suggested an interplay with the injected interstitial effect. This should also be studied further, as implantations using multiple energy ions such as the present study have injected interstitials throughout the damage region.

Chapter 5

Heavy Ion vs Neutron Irradiation in an Fe-9Cr Alloy

This chapter reports an experiment comparing the mechanical properties and microstructure of model Fe-9Cr alloys irradiated with heavy ions or with neutrons under similar conditions.

5.1 Introduction & Background

Reduced Activation Ferritic-Martensitic steels with Cr contents of around 9% are candidate materials for use in future fission and fusion power plants [9, 284, 285], where they will experience high energy neutron fluxes which cause radiation damage. This damage causes a degradation of the material properties, including hardening and embrittlement [87].

The present lack of a dedicated fusion materials testing facility [11], means current efforts to study the effects of neutron irradiation have relied on the use of fission test reactors (e.g. ATR, FFTF, Bor-60) as neutron sources. Such irradiation experiments are costly, and induce radioactivity in samples through transmutation reactions, requiring the use of specialised "hot" facilities which are not routinely available to most researchers. The range of experimental conditions and control are limited to that offered by the reactor, making systematic investigation of parameter effects difficult. Another drawback of these experiments is that they take long periods of time to complete (typically months-years), which not only means that the rate of progress is limited, but also that there isn't an opportunity to "get ahead" of real time reactor conditions (where components may last decades) and make empirically based predictions.

Heavy ion irradiation provides a cheaper, faster method of causing displacement damage in samples, and without inducing radioactivity. Experimental conditions are better controlled and more easily adjusted, and end of life doses can be quickly achieved. There are however some neutron-atypical aspects to heavy ion irradiation, and if these experiments are to be used as a surrogate for neutron irradiation they need to be benchmarked in comparison studies.

Few such studies have been performed in model Fe-Cr alloys, but a more substantial body of literature exists on the influence of the neutron-atypical aspects (discussed in detail in section 2.4), providing a basis with which to interpret comparison experiments.

The available comparison studies in the literature (discussed in more detail in section 2.5) all reveal significant differences between irradiation with the two types of particle.

Model Fe-Cr alloys irradiated to 0.5 and 0.6 dpa at 300°C with heavy ions or with neutrons respectively were analysed in APT by Pareige et al. [82] and in TEM by

Hernandez-Mayoral et al. [218] . The APT study found that in Fe-9Cr and Fe-12Cr, α' precipitates were formed only under neutron irradiation. In the TEM study it was found there were differences in the spatial distribution of dislocation loops. Neutron irradiated alloys containing 5, 9, and 12% Cr were found to have loops preferentially located close to dislocation lines and grain boundaries, whereas in the neutron irradiated 2.5% Cr alloy and all ion irradiated alloys, the loops were homogeneously distributed. Both studies suggested that the difference in dose rate between the two irradiation methods was the most likely cause for the observations.

Hardie et al. [14] compared mechanical properties of an Fe-6Cr model alloy irradiated to 0.82 and 1.83 dpa at 288°C with heavy ions or with neutrons respectively. They found a significantly greater increase in hardness in the neutron irradiated sample, thought to be due to Cr segregation to dislocation loops only observed after neutron irradiation. The authors suggested that a combination of differences in dose rate and PKA energy spectrum were the likely reason for the microstructural difference.

The present work is a comparative study of a fusion-relevant Fe-9Cr model alloy from the same alloy series and neutron irradiation campaign as studied by Hardie et al. [14], but with a heavy ion irradiation using higher beam energies to create a larger damage depth to reduce the distorting impact of size effects (see section 3.3).

5.2 Experimental

5.2.1 Neutron Irradiation

The neutron irradiated specimen was provided courtesy of G.R. Odette of UCSB, irradiated as part of the UCSB Advanced Test Reactor National Scientific Users Facility Irradiation Experiment. Part of a series of Fe-Cr binary model alloys, the Fe-9Cr alloy was chosen for investigation due to its relevance to the reduced activation ferritic-martensitic steel Eurofer. It is refered to as "UCSB alloy" in section 3.6, where more information about its temperature history and composition can be found.

The specimen was from capsule 6a, irradiated in the ATR at position A-10 for cycle 145A over a period of ~54.7 days, at a target temperature of 288°C and to a target dose of 1.7 dpa. Post-experiment analysis however, suggests the temperature and dose received were actually 304-334°C [286] and 1.82 dpa [287] respectively. The neutron fluence as a function of energy is given in [287], and shown in figure 5.1.

After irradiation, the sample was prepared by D. Gragg and P. Wells of UCSB. It was mounted on an SEM pinstub using a thin layer of superglue, and after initial abrasion with 1200 grade grit paper and cleaning in methanol, was vibropolished with 0.3μm alumina for 4 hours.

5.2.2 Ion irradiation

Ion irradiation was performed at JANNuS in Saclay. The facility uses a fixed energy beam and degrader wheel set up, with 6 windows into which degrader foils of different

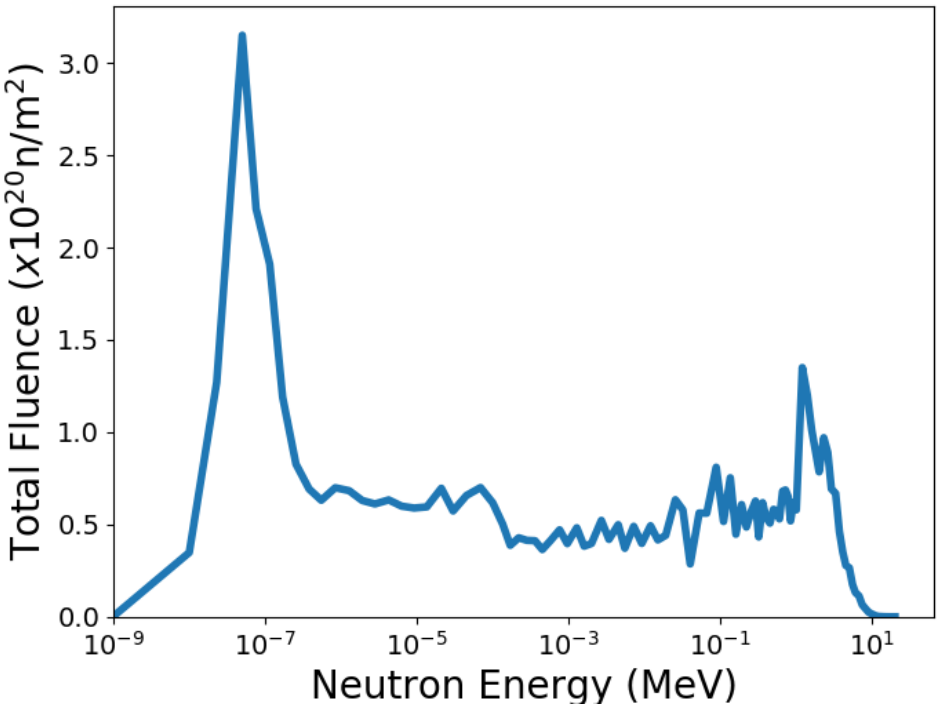


Figure 5.1: Fluence as a function of neutron energy for the neutron irradiated specimen. Data from [287].

thickness are placed. This wheel spins in front of the beam at a rate of 80 Hz. The beam passes through each window in turn, so its energy at the target is effectively curtailed periodically by the foils. In this way a near-uniform damage-depth distribution can be obtained whilst keeping the beam at source at a constant energy. The current is measured as a function of target position using an array of Faraday cups which are intermittently lowered into the beam's path throughout the irradiation. More detailed information about the facility can be found in [288].

Samples were punched from the sheet material, and prepared as outlined in section 3.6.3. For irradiation they were mounted onto a base plate using a high temperature conductive silver epoxy.

The temperature was monitored using both a thermal imaging camera, and two thermocouples - one mounted in a dedicated hole on front of the base plate, and one clamped at the rear of the base plate. Vacuum was maintained below 10^{-6} Torr throughout the experiment.

Conditions were chosen to be as similar to the neutron experiment as possible. Al degrader foils of thickness 0.8, 1.6, 3, 4, and 5 μm were placed in the degrader wheel, leaving one window open. For a beam energy of 24 MeV and a total dose of 5.4×10^{15} ions/cm^2, the estimated displacements per atom in Fe as a function of depth as calculated by SRIM is shown in figure 5.2. Details of the SRIM calculations are given in section 3.5.

Unfortunately, after the experiment was performed a fault was discovered with the beam current measuring apparatus. A difference between the specified and actual dimensions of the Faraday cups meant they did not perform as expected. In particular, the interaction of the beam with the tantalum ring surrounding each cup caused emission

of secondary electrons (and possibly ions). The cups measure the dose (number of ions per area) by measuring beam current. The beam is positively charged, and the loss of secondary electrons appears as a gain in positive charge, causing the beam current and therefore the dose to be overestimated. Secondary electron emission is highly sensitive to local beam parameters, and so this also caused a large spread of measurements across the 7 cups.

Subsequent calibration experiments were performed by staff at the facility, comparing the dose measured by the Faraday cup assembly to that measured by charge collection on an electrically insulated target. For all conditions the Faraday cup assembly overestimated the true dose, and it was suggested that a correction factor of 0.4 - 0.8 be applied to the dose measured using the defective equipment.

The information about the local fluence at the sample of interest's position provided by the Faraday cup assembly was ignored as the secondary electron emission may have introduced significant scatter between cup to cup measurement. Instead an average value was used. Applying the correction factor produces the damage-depth profiles shown in figure 5.2.

Temperature data is given in figure 5.3. Sample temperatures varied between around 290 and 310°C during the irradiation, with an average of approximately 300°C.

A summary of irradiation conditions for both ion and neutron irradiated specimens is given in table 5.1.

Irradiating Species	**Temperature °C**	**Dose (dpa)**	**Dose rate (dpa/s)**
Neutrons (spectrum [287] in fig 5.1)	304-334 [286]	1.82 [287]	3.85×10^{-7} [287]
Fe^{+} ions	~290-310	~0.68-1.36	2.98 - 5.96×10^{-5}

Table 5.1: Summary of irradiation conditions for heavy ion and neutron irradiated specimens.

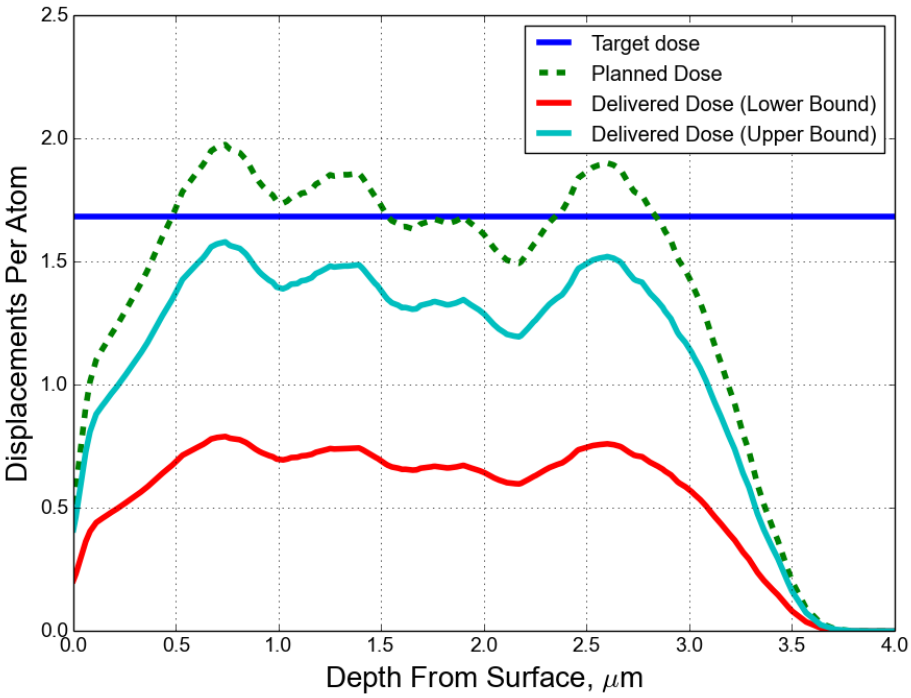


Figure 5.2: SRIM calculation of damage as a function of depth after corrections to dosimetry as advised by the irradiation facility. The lower bound represents a correction factor of 0.4 and the upper bound a correction factor of 0.8.

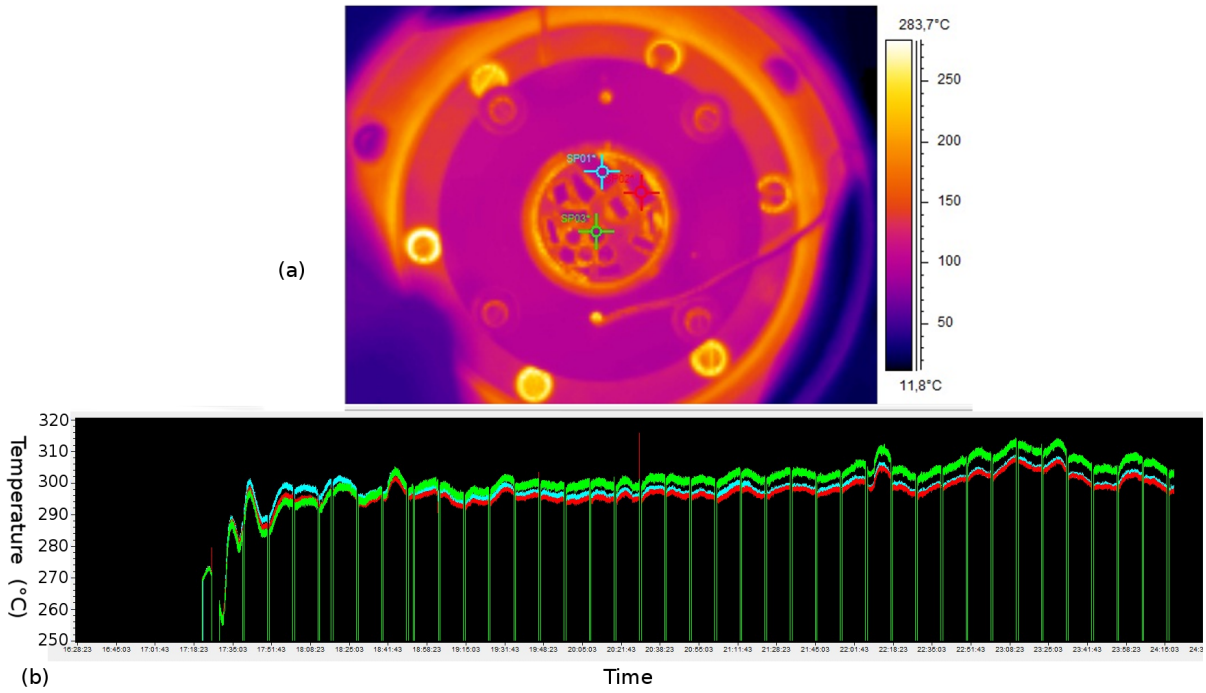


Figure 5.3: (b) Temperature of 3 different target positions (indicated in (a)) during the irradiation experiment, as measured using a thermal imaging camera. The periodic drops in temperature are due to the camera's view being obscured during current measurement by the Faraday cup assembly, at approximately 10 minute intervals.

5.2.3 Post-Irradiation Analysis

After irradiation, samples were analysed using nanoindentation, microcantilever testing, and atom probe tomography, as outlined in table 5.2. Detailed information about the use of these techniques is given in section 3.

Sample	**Nanoindentation**	**Microcantilever Testing**	**APT**
Unirradiated	✓	✓	✓
Ion irradiated	✓	✓	✓
Neutron irradiated	✓	✓	✓ [277] [289] [77]

Table 5.2: Analysis techniques used for each irradiation condition, performed as part of this work unless otherwise specified.

Microcantilevers were produced by FIB milling, and measured using stereoscopic imaging with SEM (see section 3.2). The target beam height was 3μm, corresponding to the damaged depth for the ion irradiation, and measured heights varied between 2 and 4.4μm. The ratio between beam width and the tested beam length was kept above 6 as recommended by Armstrong et al. [230], in order to limit bending around the "base" at the fixed end of the beam. All cantilevers were tested using an Agilent G200 nanoindenter using continuous stiffness measurement (CSM), with a displacement rate of 5nm/s to a total displacement of 3000 nm. The resulting load-displacement data was analysed using simple beam theory analysis, and also with finite element analysis. Further details can be found in sections 3.2.5 (SB) and 3.2.6 (FEA). Before testing, EBSD scans were performed on a number of beams from each sample, and analysed using the MTEX opensource software toolbox [290] to determine the crystallographic orientation of the cantilevers.

Preparation of microcantilevers in the neutron-irradiated sample was performed using the FIB at the Center for Advanced Energy Studies, Idaho Falls, in a rapid turnaround

experiment as part of the National Scientific User Facility (USA). The sample was subsequently shipped to CCFE for micromechanical testing alongside the ion- and un-irradiated samples.

Nanoindentation was also performed using the same Agilent G200 nanoindenter with CSM, to a target depth of 3000 nm at a target strain rate of 0.05 s^{-1}, with a diamond Berkovich tip. Prior to indentation, the tip area function was calibrated following the procedure described in section 3.1.3.3. A minimum of 2 arrays of 3 x 3 indents were performed in each sample, covering different grain orientations. Indents were spaced at least 20x the indent depth from each other. Details of the analysis to extract hardness and elastic modulus data can be found in section 3.1.3.

Atom probe specimens were prepared from a range of depths using the FIB lift-out method. Reconstruction parameters were determined using sample crystallography. Both the specimen preparation procedure and reconstruction methodology are described in detail in section 3.4. All needles were run in voltage mode with a pulse fraction of 0.2 at 50 K with a target evaporation rate of 0.002-0.005 ions per pulse, to match the conditions used in analysis of the neutron irradiated samples by Bachlav et al. [77]. Some tips were run in the LEAP 3000XR and some in the LEAP 5000XR, and IVAS version 3.6.14 was used for reconstruction and analysis of all samples, following the methods detailed in section 3.4.2.

5.3 Results

5.3.1 Nanoindentation

Elastic modulus as a function of depth for each of the three conditions is presented in figure 5.4. At depths below ~1000 nm, the measured moduli are the same for all conditions. The elastic properties of these materials is determined by the atomic bonding, and is not expected to be affected by radiation damage.

At larger depths, the modulus is seen to decrease for all the samples. Samples were mounted on an SEM pin stub using a thin layer of crystal bond, which reduced the load frame stiffness. As the load increases, this layer's contribution to the overall stiffness of the load train increases, resulting in an apparent reduction in the measured elastic modulus.

Hardness as a function of depth is shown in figure 5.5 for all three samples. Both the ion and neutron irradiated samples show an increase in hardness compared to the unirradiated sample. All three samples show a decrease in hardness with increase in indentation depth. For the neutron and unirradiated samples, this is purely due to the indentation size effect (ISE) (discussed in section 3.3). The ion irradiated sample is also affected by a substrate effect, as the irradiated layer sits on top of softer unirradiated material. As the indentation depth increases the plastic zone size increases and expands into the unirradiated region, meaning that unirradiated material becomes an increasing proportion of the volume of material from which the hardness measurement is made. This is the reason that the ion irradiated line tends towards the unirradiated line, but the neutron irradiated line levels off at a higher value as the irradiated depth is much much larger than the sampled volume in this case.

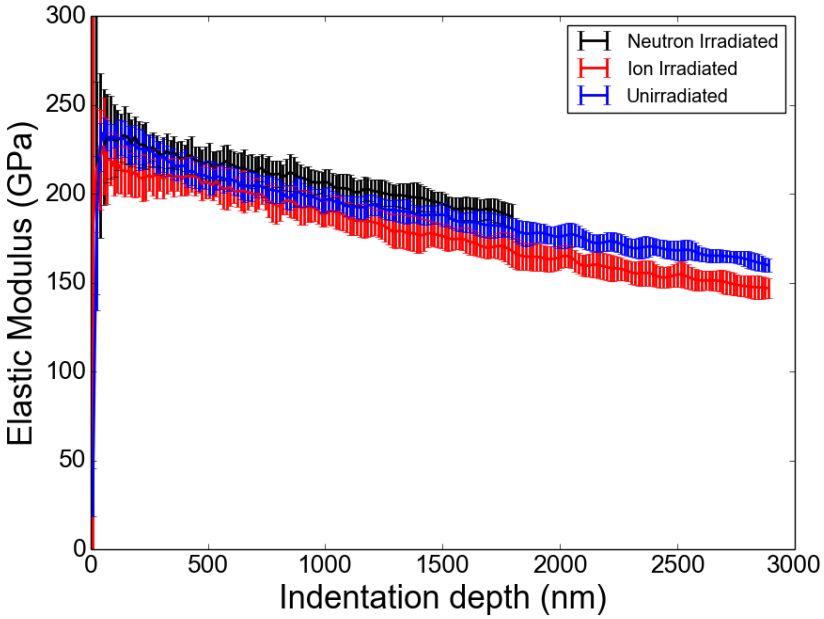


Figure 5.4: Elastic modulus data averaged over at least 18 indents for un-, ion and neutron irradiated Fe-9Cr. Error bars represent 1 standard deviation.

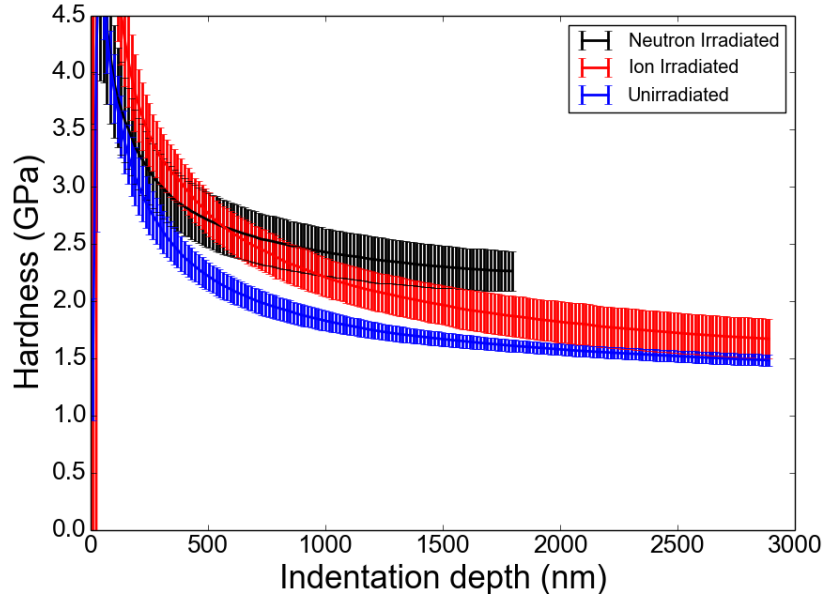


Figure 5.5: Hardness data averaged over at least 18 indents for un-, ion and neutron irradiated Fe-9Cr. Error bars represent 1 standard deviation.

Plastic zones beneath indents have been reported to extend to depths between 4 and 10 times the indentation depth [291]. Hardie et al. [278] performed TEM analysis of the region below a nanoindentation indent in an ion-irradiated Fe-12Cr alloy, and found the main plastic zone to extend to around 5 times the indentation depth.

A depth of 500 nm was therefore chosen for comparison - where the influence of the ISE has fallen such that differences in the hardness of the samples can be distinguished, and the plastic zone is still largely confined to the irradiated region in the ion irradiated sample (~3 μm). Here the ion and neutron irradiated samples show the same hardness within experimental error.

5.3.2 Microcantilevers

In this section results of microcantilever testing are reported, beginning with an analysis of the elastic properties. Yield and plastic properties are then presented afterwards.

5.3.2.1 Elastic properties

Simple beam theory stress-strain curves for un-, ion-, and neutron-irradiated beams are shown in figure 5.6. Details of the simple beam theory analysis can be found in section 3.2.5.

The slope of the initial linear part of the curves represents the elastic modulus of the beam, and the data show a significant spread. This spread may be due to the sensitivity of the elastic modulus to error in the measurement of beam dimensions (cubic dependence on both beam length and height) in simple beam theory analysis, and the

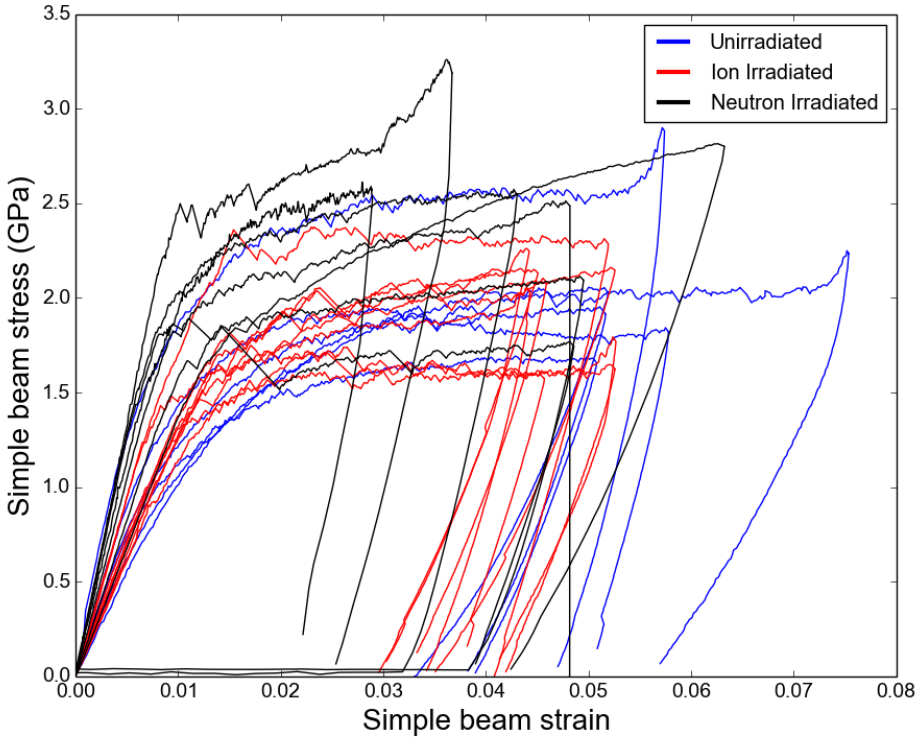


Figure 5.6: Simple beam theory analysis of microcantilever beams. The sharp increase in stress just before unloading for some beams is due to the nanoindenter tip coming into contact with the bulk material around the trench milled for the beam.

fact that Fe is elastically anisotropic. Crystallographic analysis of the beams was performed to ascertain the relative significance of each of these contributions to the spread of gradients observed.

Figure 5.7 shows EBSD scans of cantilever beams in all 3 samples. It is clear that the grains are smaller than the cantilever arrays, and that different beams are made up of differently orientated grains.

In simple bending, the beam is deformed in tension above the neutral axis and in compression below it. Both stresses act primarily along the beam's long axis, so the elastic modulus is measured along this direction. The value obtained should be that of the corresponding crystal direction.

In a cubic crystal, the elastic modulus, E, along a specific crystal direction is given by equation 5.1 [292]:

$$\frac{1}{E} = S_{11} - 2[(S_{11} - S_{12}) - \frac{1}{2}S_{44}](l^2m^2 + m^2n^2 + l^2n^2) \tag{5.1}$$

where S_{11},S_{12}, and S_{44} are elastic compliance constants, with values of 0.76, -0.28, and 0.86 $\times 10^{-10}$ Pa^{-1} for Fe [293], and l, m, and n are the direction cosines.

For each cantilever, the crystal vector along the beam direction for the grain at the fixed end of the beam (where strains are greatest) was found. In figure 5.8 each simple beam stress-strain curve is coloured according to this crystal vector and the key shown. The elastic region of each curve is plotted, alongside lines corresponding to the elastic modulus for major crystal directions calculated using equation 5.1. As can be seen, the range of slopes measured corresponds well to the range expected from crystallographic anisotropy marked by the solid lines. Qualitatively the colours depicting

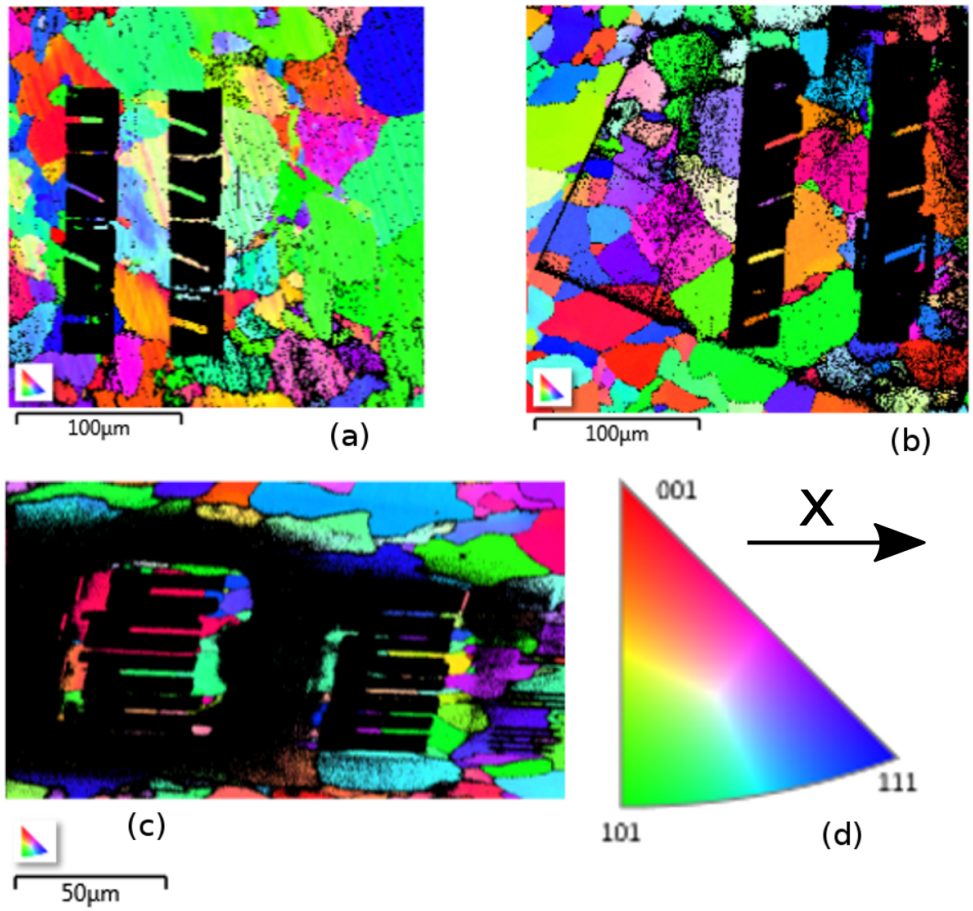


Figure 5.7: Inverse pole figure EBSD scans of cantilevers in (a) unirradiated, (b) ion irradiated, and (c) neutron irradiated specimens. Colours denote crystal orientation in the x direction, according to key in (d). (a) and (b) were taken after the beams were tested and (c) was taken before testing. Black (no solution) pixels are likely due to redeposition during FIB milling (or carbon deposition from a previous scan in (b)).

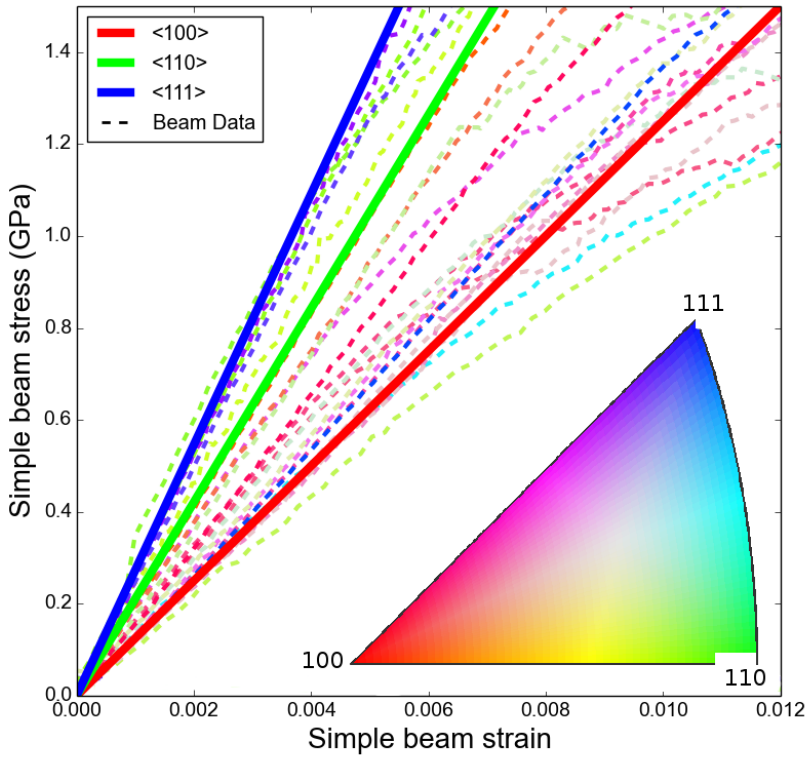


Figure 5.8: The dashed lines represent the elastic regions of simple beam stress-strain curves shown in figure 5.6. They are coloured corresponding to crystal direction along the beam direction, according to the key. Solid lines show the theoretically predicted gradients for major crystal directions in pure Fe.

crystallographic orientation also appear to be in reasonable agreement with the slopes expected: the more compliant <100> directions depicted with red shades have shallower gradients, with the stiffer <110> and <111> directions coloured green and blue having steeper gradients, but there are some exceptions.

Although beam dimensions were chosen to minimize its occurrence, some flexure takes place around the base of the beam at the fixed end during bending. Simple beam theory doesn't take this into account, so for accurate quantitative comparison of differences between the expected modulus value for the beam/crystal orientation and the

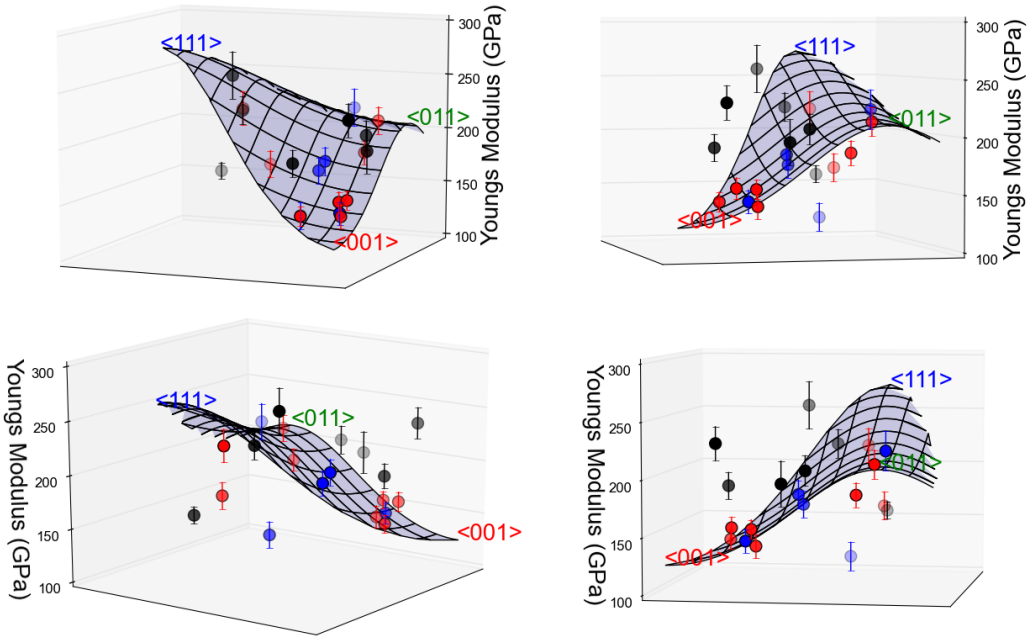


Figure 5.9: Multiple viewpoints of a 3D plot of the Young's modulus as measured by FEA as a function of beam crystal orientation. Crystal orientation along the long beam direction is represented as a stereographic projection on the x and y axes, with the Young's modulus in the z axis. The surface plotted represents the predicted modulus for beams orientated in that crystal direction. Error bars represent errors in modulus for a 100 nm uncertainty in measurement of all beam dimensions.

measured value, finite element analysis (FEA) was performed using ABAQUS. Details of this analysis can be found in section 3.2.6.

In figure 5.9 the Young's modulus measured using FEA is plotted for each beam, with its crystallographic orientation represented as a stereographic projection in x and y. The plotted surface shows the theoretical modulus expected for each crystal direction.

The difference between expected and measured values is plotted more clearly in figure 5.10. The solid and dashed error bars depict uncertainty for an error in measurement in beam dimensions of 0.1 and 0.2 μm respectively.

The errors were calculated by a propogation of errors for the simple beam theory expression for the Young's modulus:

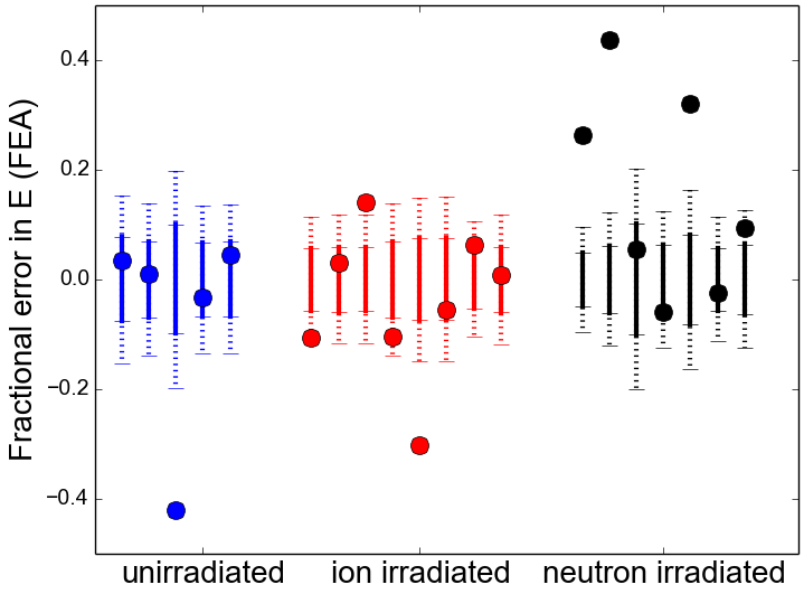


Figure 5.10: Fractional error in E measured by FEA compared to that expected for beam crystal direction. Solid lines represent uncertainty for an error in measurement of all beam dimensions of 100 nm, and dashed lines for 200 nm.

$$E = \frac{12PL^3}{wh^3\delta} \tag{5.2}$$

where P is the load, δ the bending displacement, L the beam length, w the beam width and h the beam height. Uncertainty in P, δ and L was neglected due to being much smaller than for w and h.

The fraction errors were found by:

$$\frac{\Delta E}{E} = \sqrt{\frac{\Delta w^2}{w} + 3\frac{\Delta h^2}{h}} \tag{5.3}$$

with Δh and Δw both set to either 0.1 or 0.2μm.

For the majority of beams, the value of E measured by FEA is in agreement with the expected value within this error. There are however some exceptions.

To produce a fractional error in E of ~0.4, as calculated for some beams, would require an uncertainty in measurement of beam dimensions of 0.4-0.5 μm. For the stereoscopic measurement technique used (see section 3.2.3) this would be unexpectedly large.

As can be seen in the EBSD maps in figure 5.8, some beams are composed of multiple grains with different orientations. During bending the maximum stress occurs at the apex of the underside of the beam at the fixed end, whereas EBSD gives the grain orientation of the near surface atoms. The presence of grain boundaries close to the fixed end of the beam raises the possibility of either a different crystal orientation on the underside of the beam or close to it, meaning the tested crystal direction may be different to that measured by EBSD at the near surface, or a combination of multiple directions. No cross-sectioning of beams was performed to check this, but it could possibly explain the large errors observed for some beams. Differently orientated grains along the beam's length may also contribute to this error.

5.3.2.2 Plastic properties

Load-displacement data was analysed to calculate yield stress using simple beam theory and finite element analysis. Details of this analysis can be found in sections 3.2.5 (SB) and 3.2.6 (FEA).

Results of yield stress calculations using simple beam theory are shown in figure 5.11, where the yield stress is plotted against the measured beam height. The same is

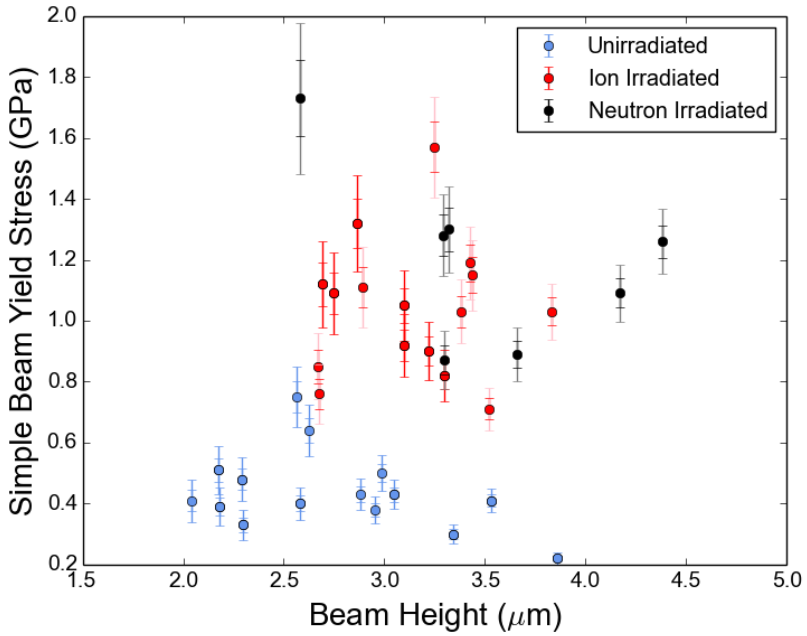


Figure 5.11: Simple beam theory yield stress as a function of measured beam height.

shown for the finite element analysis in figure 5.12. Both Hardie et al. [14] (see figure 5.30 and Motz et al. [239] found the strength of microcantilever beams to vary with beam height, so the data is plotted this way so that any such size effect can be observed.

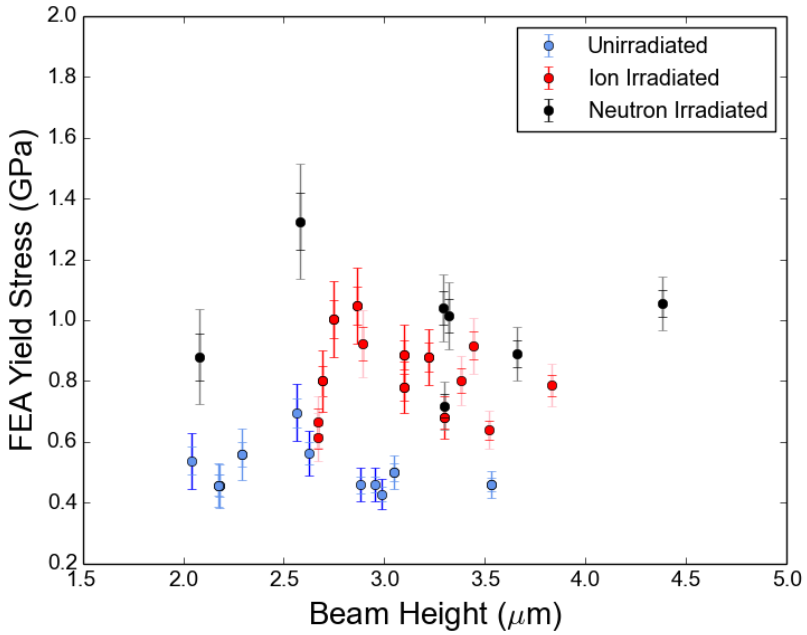


Figure 5.12: FEA yield stress as a function of beam height

Both analysis methods show an increase in yield stress after irradiation. Although there is a large amount of scatter (addressed in section 5.4.2.1), no strong size effect was observed for these beam heights and so mean values were taken to quantify the yield stress for each irradiation condition. These are presented in table 5.3.

Sample	**Simple Beam Theory**	**Finite Element**
Unirradiated	0.44 ± 0.13	0.51 ± 0.07
Ion Irradiated	1.04 ± 0.21	0.82 ± 0.13
Neutron Irradiated	1.20 ± 0.27	0.99 ± 0.18

Table 5.3: Average values and standard deviations of yield stress (in GPa) found by simple beam theory and finite element analysis for microcantilever beams with heights between 2 and 4.5μm.

No statistically significant difference was found in the increase in yield stress between the ion and neutron irradiated specimens with either analysis method.

Figure 5.13 shows load-displacement curves for representative microcantilever beams for the unirradiated, ion irradiated, and neutron irradiated conditions. Simple beam theory stress-strain curves for all beams are shown in figure 5.14. Although not exclusively the case, compared to the unirradiated beams, irradiated beams tended to exhibit a longer elastic regime with a more pronounced transition to plasticity. The unirradiated beams tended to transition to plasticity earlier and more gradually.

Small load drops were observed after yield for all conditions, indicating that at these length scales plasticity is controlled by individual slip events. This is also evident from visible strain localisations in SEM images of the beams after testing, shown in figure 5.15, where deformation is concentrated on a small number of slip planes. Not all beams showed visible slip lines, but examples that did could be found for the un- ion-, and neutron irradiated conditions.

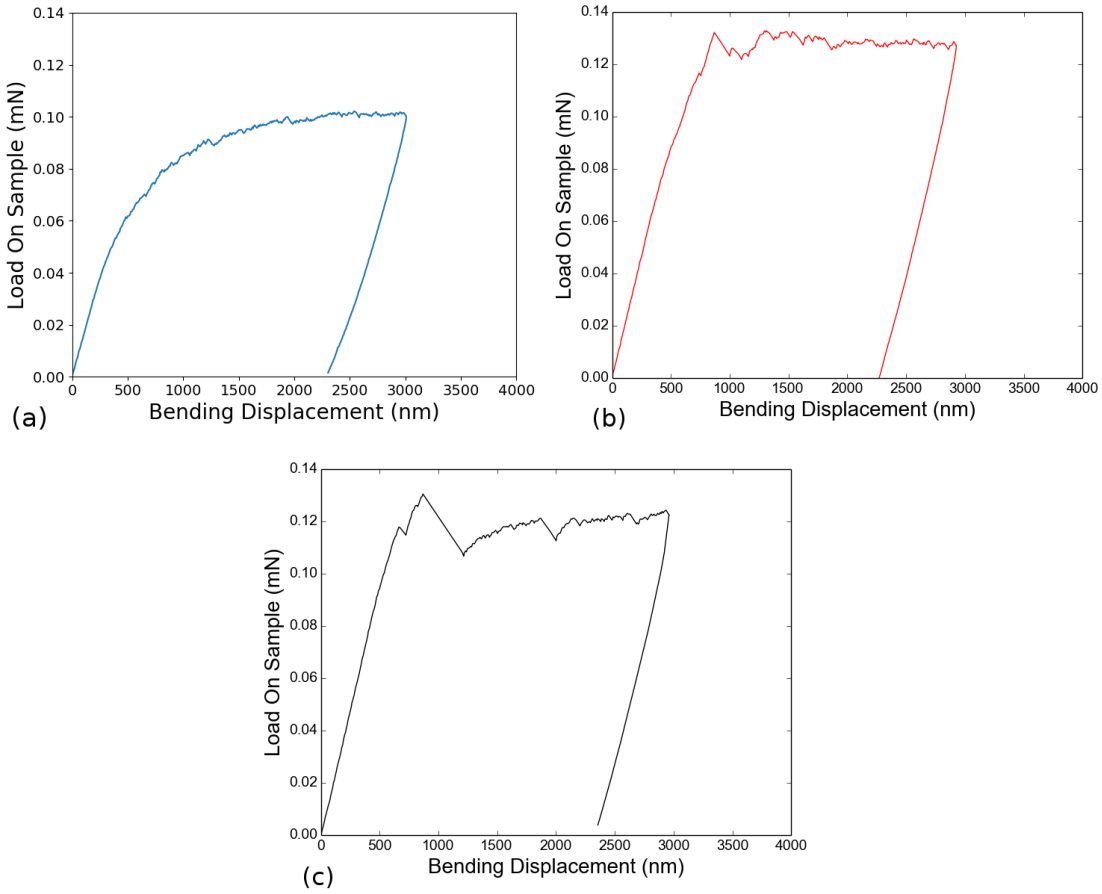


Figure 5.13: Load-displacement graphs for representative (a) unirradiated, (b) ion irradiated, and (c) neutron irradiated microcantilever beams.

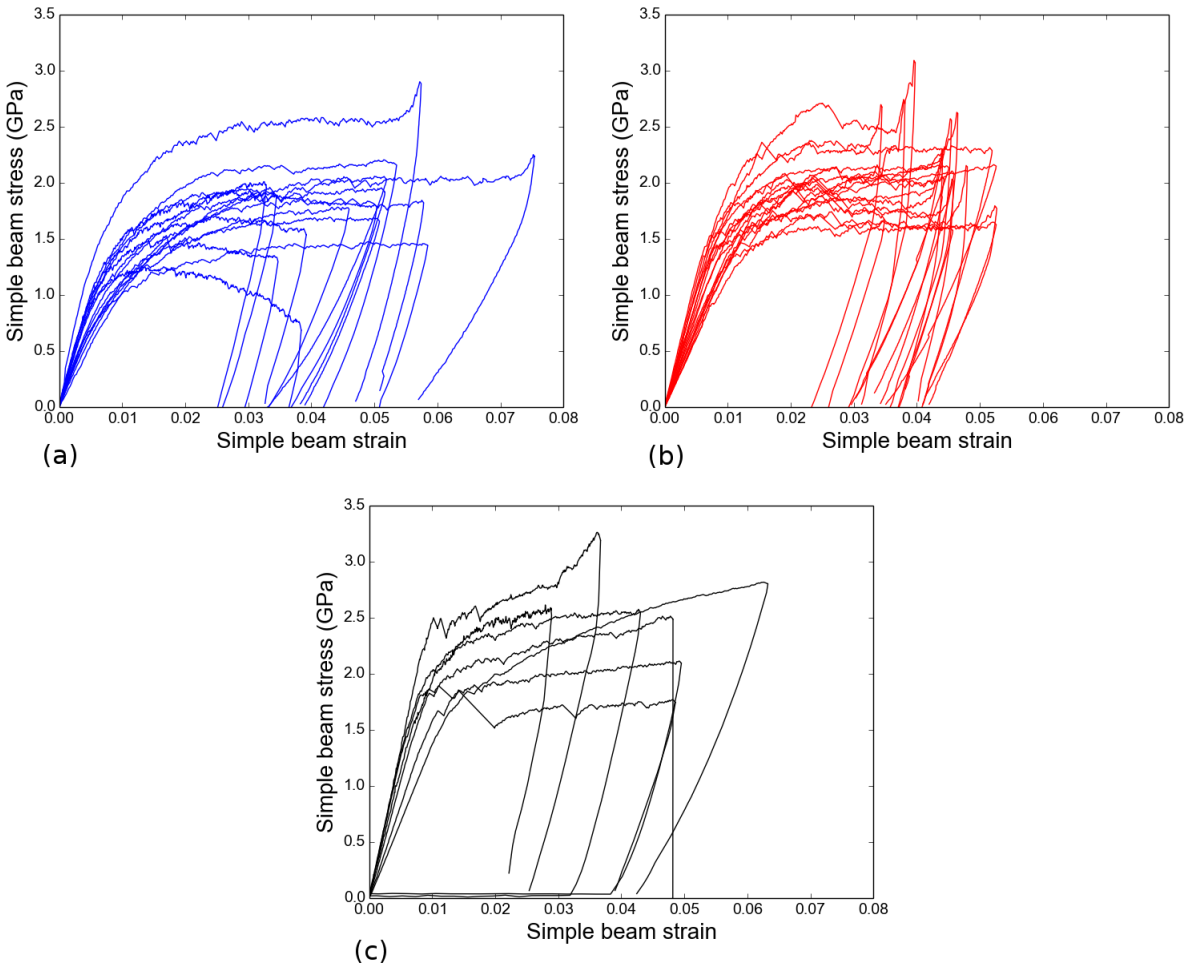


Figure 5.14: Simple beam theory stress-strain curves for all microcantilever beams tested in the (a) unirradiated, (b) ion irradiated and (c) neutron irradiated condition. Sharp increases in stress just before the maximum displacement are due to the indenter tip coming into contact with the bulk material at the edge of the trench surrounding the beam.

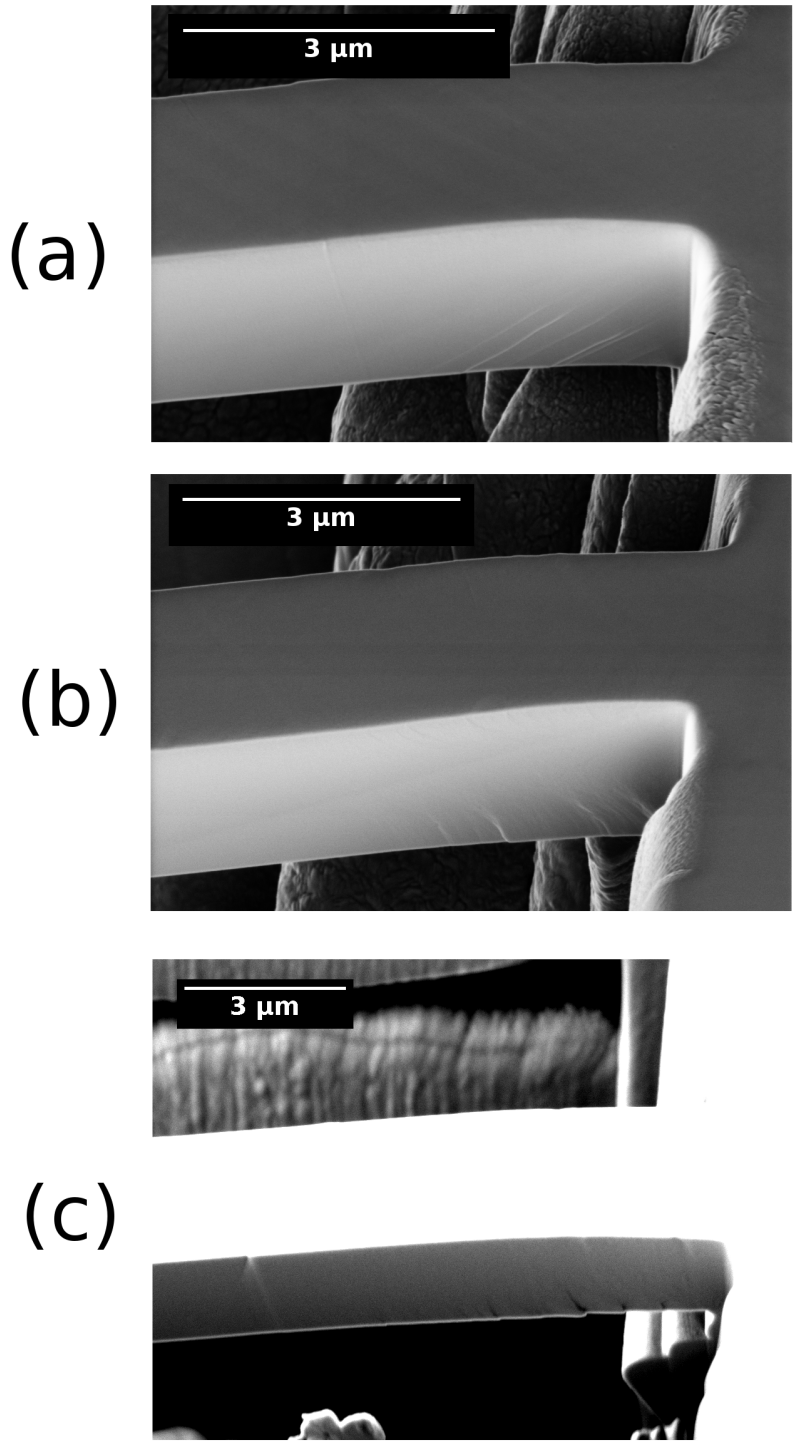


Figure 5.15: SEM images of (a) unirradiated, (b) ion irradiated, and (c) neutron irradiated microcantilever beams taken after testing showing slip lines. Slip lines were not observed for all beams. The images here attempt to capture the variety of appearances of the slip lines observed. No difference was noted between different irradiation conditions.

The load drops likely relate to real phenomena, either the activation of individual dislocation sources or the surmounting of a dislocation glide barrier - after either of which glide becomes easier for a period, but the data recorded during such event is an artefact of a limitation of the testing equipment. The nanoindenter used is inherently load controlled, and uses a feedback loop to adjust the loading rate in order to maintain a constant displacement rate during the test. When a large slip event occurs the beam stiffness drops suddenly. In response the loading rate falls to 0, and the raw load is held constant but does not drop. The increased tip displacement causes the indenter support springs to extend further, causing the load on the beam to fall in proportion to the spring stiffness and tip displacement. The true displacement controlled behaviour is not captured during these events, as the load on the beam doesn't fall correctly in response.

5.3.3 Atom Probe Tomography

5.3.3.1 Composition

Sample compositions were calculate from background-corrected mass spectra. A peak overlap exists at 27 Da between $^{54}Cr^{++}$ and $^{54}Fe^{++}$, and the contribution from each was estimated by comparing the counts recorded here with those expected from the counts at peaks corresponding to other Fe and Cr isotopes, based on natural abundances. As well as peaks where other overlaps occurred, the peak at 28 Da corresponding to $^{56}Fe^{++}$ was avoided as preferential loss of this isotope can occur due to detector pile-up in multiple hits (discussed in section 6.3.1.2).

Sample	**Ions** ($\times 10^6$)	**Cr**	**V**	**C**	**O**	**P**	**Si**	**Ni**	**Mn**
Unirradiated	3.9	9.84 - 9.88	0.01	0.11	0.04	0.005	0.06	-	-
Ion-irradiated	16.3	10.01 - 10.31	0.02	0.08	0.01	0.008	0.06	-	-
Neutron-irradiated [77]	19	9.36	0.02	0.01	-	0.01	0.05	0.01	0.01

Table 5.4: Chemical composition of samples as measured by atom probe. Values for Cr represent minimum and maximum calculated from decomposition of 27 Da using different isotopes. All values in atomic %, balance is Fe.

The decomposed composition for the samples is shown in table 5.4, alongside those found in the neutron irradiated specimen by Bachhav et al. [77]. A table containing the ranges used can be found in appendix A. For Cr, the range of values found by using different Fe and Cr isotopes to perform the peak decomposition is shown.

The material studied by Bachhav et al. [77] is from the same heat as those studied in this work, so the compositions are not expected to differ. The small differences may be due to local inhomogeneities, or differences in analysis equipment (the unirradiated sample was analysed with a LEAP3000XR, the ion irradiated with a LEAP5000XR, and the neutron irradiated with a LEAP4000XR), sample preparation, or analysis technique (peak ranging and decomposition).

5.3.3.2 Clustering - Cr

To check for α' precipitation (observed in the neutron irradiated sample by Bachhav et al. [77]), a nearest neighbour distribution analysis of chromium was performed, revealing it to be close to randomly distributed (figure 5.16). The isoconcentration tool was also used to try to identify areas of higher Cr concentration, but no clustering could be found.

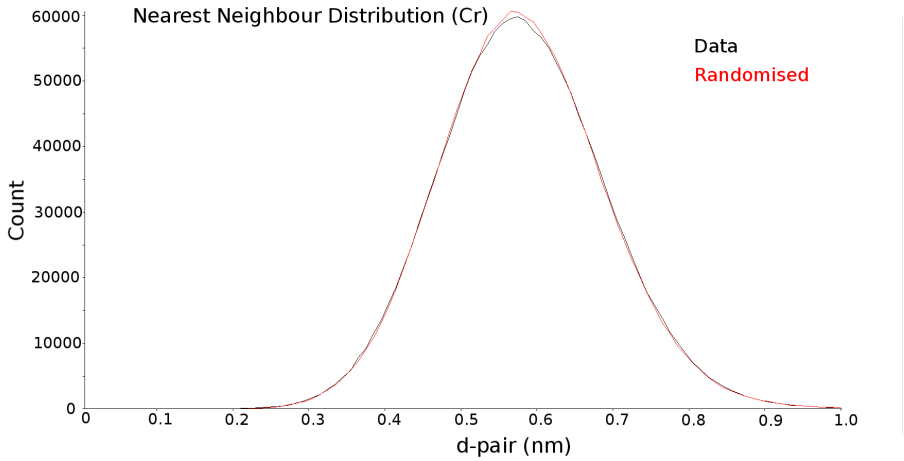


Figure 5.16: Nearest neighbour distributions for Cr in an ion irradiated sample

5.3.3.3 Clustering - P and Si

Clustering of P and Si was identified in the ion-irradiated samples (figure 5.17). Nearest neighbour distributions of P in unirradiated and ion irradiated samples (figure 5.18) shows the distribution of P is close to random in the unirradiated sample, demonstrating that clustering only occurred after irradiation.

Segregation of C, Si, and P to low index crystallographic poles was observed in these samples, as has been reported elsewhere [294,295], and is shown in figure 5.19. In order to separate this artefact from any irradiation-induced cluster formation, a cylindrical

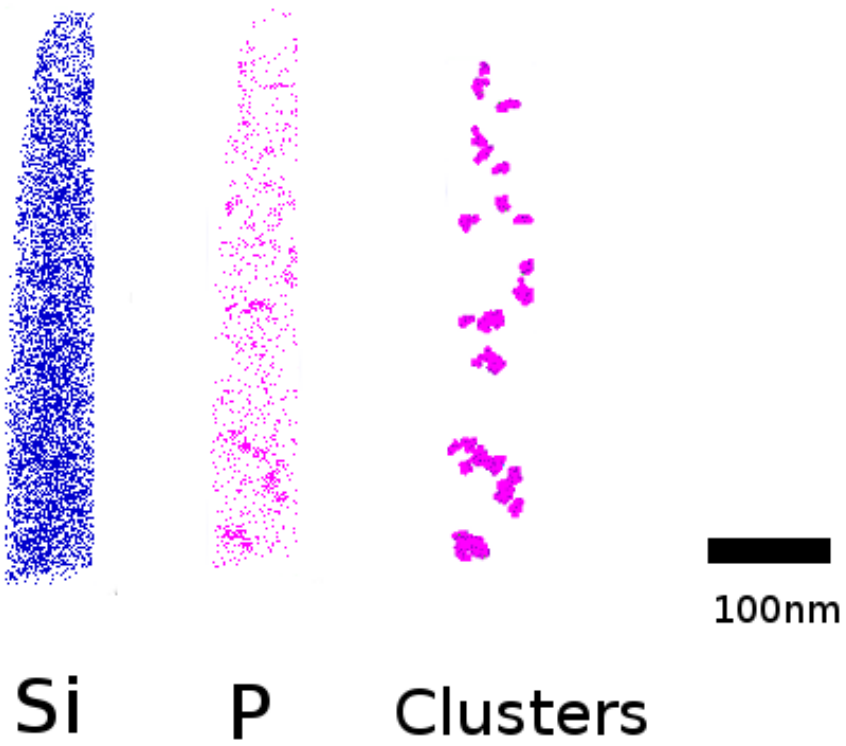


Figure 5.17: Si (blue) and P (pink) atom distributions in selected region of a representative ion-irradiated sample, alongside areas identified as P clusters.

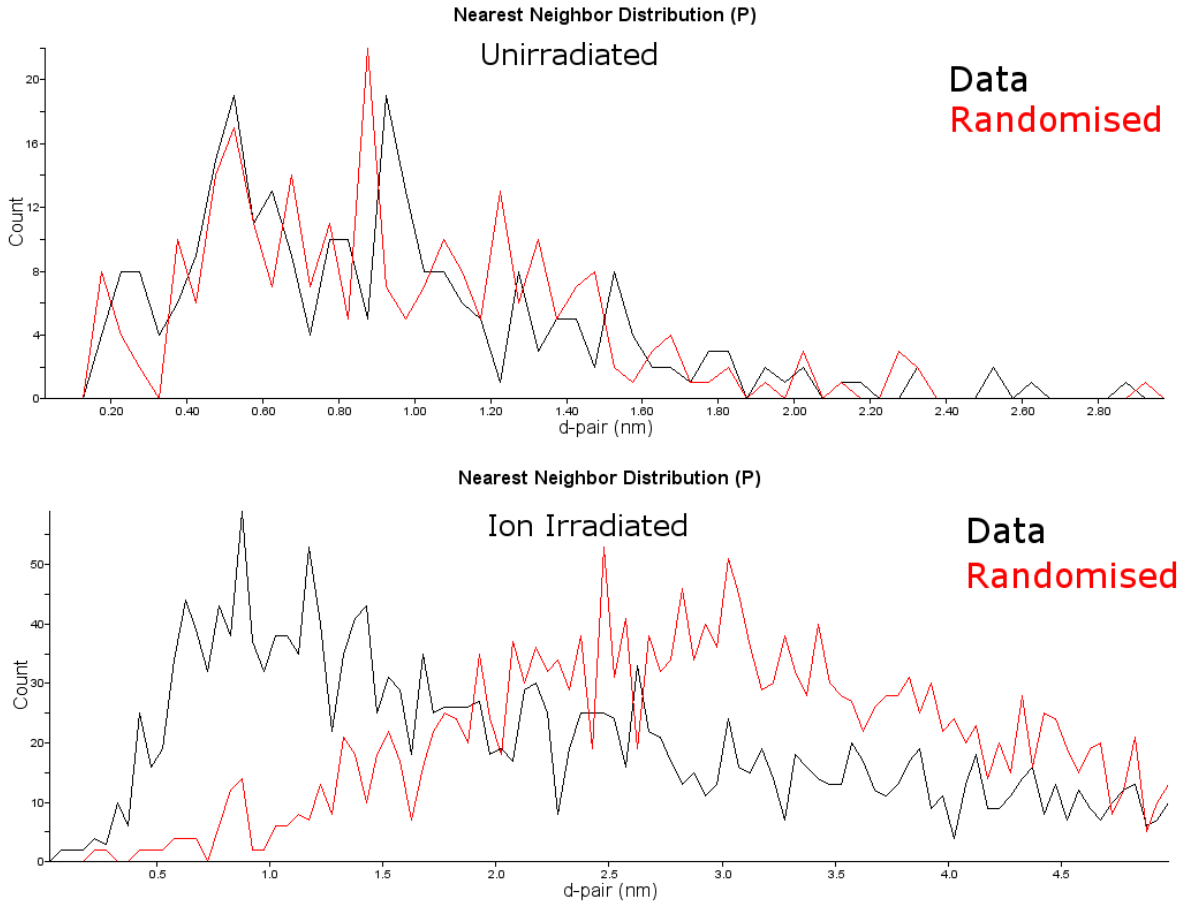


Figure 5.18: Nearest neighbour distributions of P in unirradiated and ion irradiated samples.

section the same depth as the original dataset but not containing these crystallographic poles was isolated from the rest of the data for cluster analysis in 2 samples. This is shown in figure 5.19 (d).

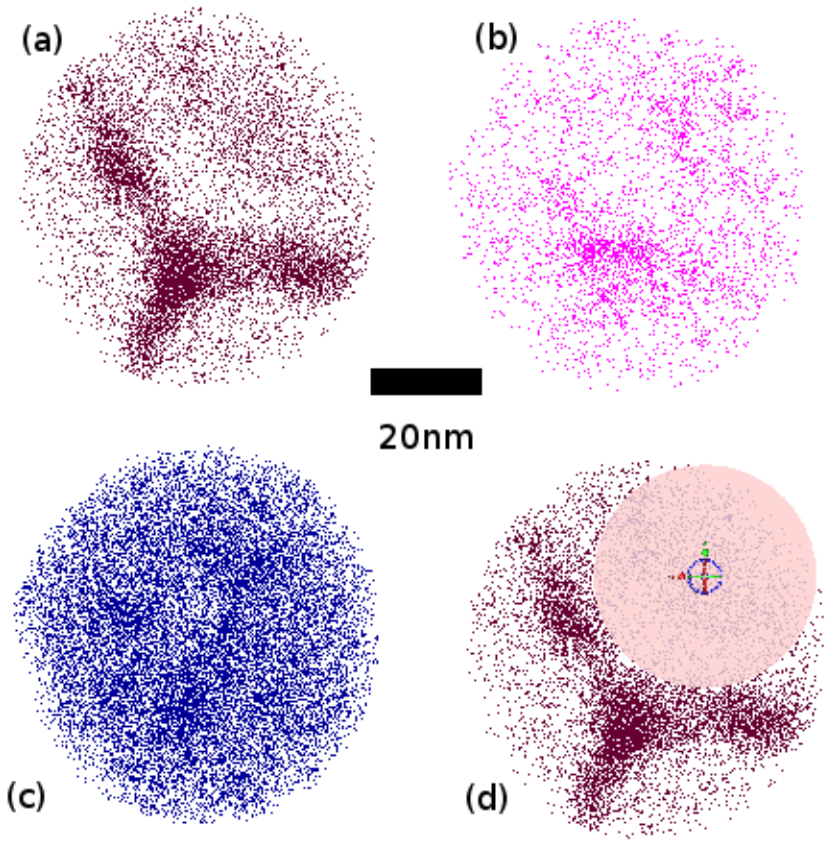


Figure 5.19: Reconstruction of an ion irradiated dataset viewed from above, along the z direction, showing (a) carbon, (b) phosphorus, and (c) silicon segregation to crystallographic poles and zone lines. (d) shows the region isolated for cluster analysis.

Cluster analysis with APT is not standardised, and the selection of the analysis method and parameters used can influence the results obtained - as was revealed in recent interlaboratory round-robin studies [296].

A widely-used "maximum separation" method was used to define clustered ions [297,298], with P as the solute species. P was chosen as it was clear from visual inspection that a larger proportion of this species was clustered, making distinction between

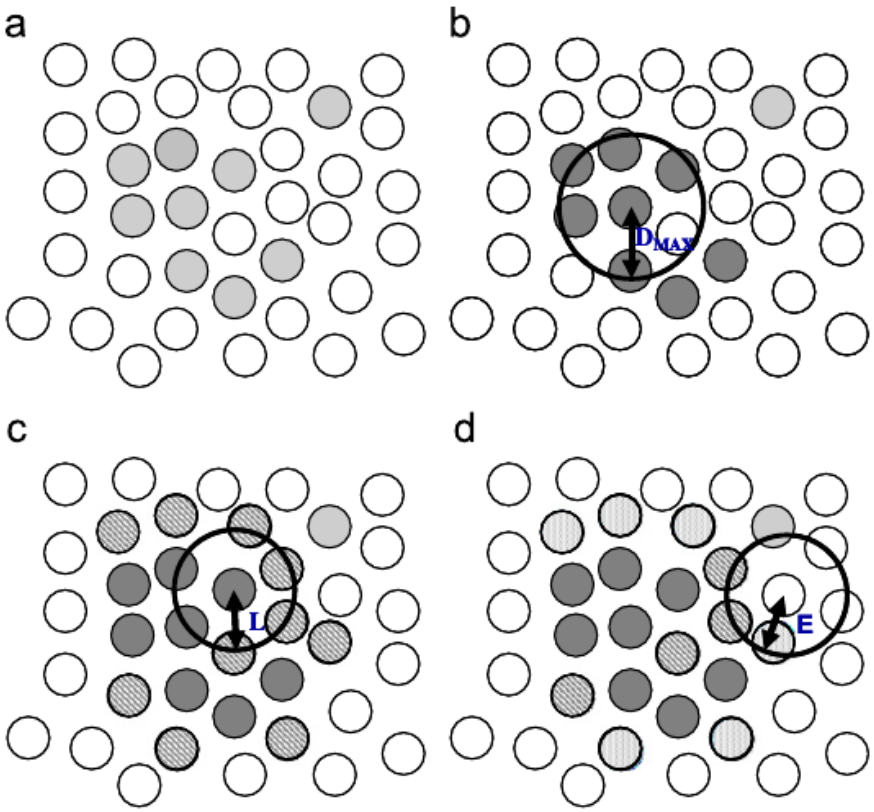


Figure 5.20: Schematic showing the meaning of the cluster finding algorithm parameters. (a) shows the solute atoms shaded (in this case P). (b) atoms within a distance D_{max} are shaded darker. (c) matrix atoms within a distance L of the clustered solute are included in the cluster. (d) atoms within a distance E of atoms outside the cluster are removed. Figure taken from [298].

clusters and matrix by this method more reliable [130, 296]. The physical meaning of the parameters used in the maximum separation method are illustrated in figure 5.20.

In the maximum separation method, atoms are deemed to be clustered if nearest neighbours of order k (1 was used in this analysis) are separated by a distance of less then D_{max}. Too small a value of D_{max} impedes the detection of dilute clusters, and too large a value will include atoms at separation distances expected in a random distribution. N_{min} determines the minimum number of atoms required to constitute a cluster.

The determination of these two linked parameters was performed by iteratively ex-

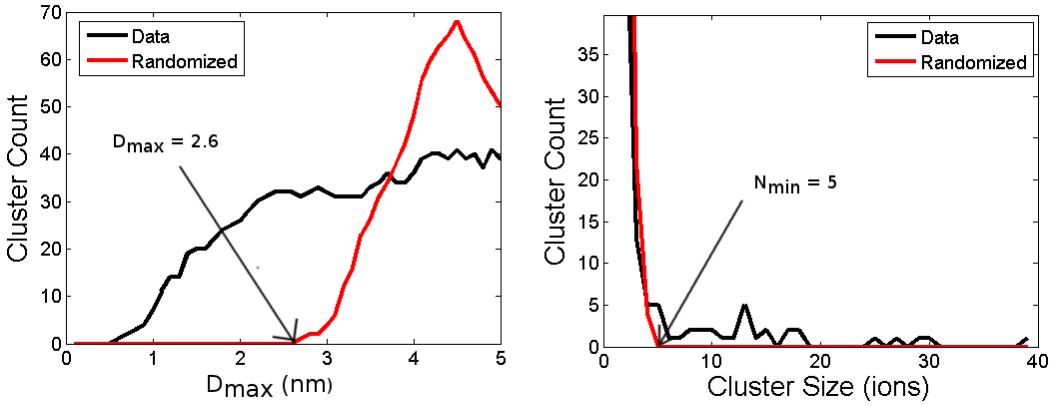


Figure 5.21: Cluster count and cluster size distributions for P in one of the datasets. The cluster sizes are found for a given D_{max}, and the cluster count fount for a given N_{min}. A consistent pair are chosen, where values of D_{max} and N_{min} produce a cluster count in the randomized data that is <1% of that found for the experimental data, as indicated.

amining the cluster size distribution (for a given D_{max}) and cluster count distribution (for a given N_{min}) for the data and a randomized distribution in IVAS to find a consistent pair of values. Cluster size and count distributions are shown in figure 5.21.

A consistent D_{max} and N_{min} pair was chosen to be the smallest value that found the number of clusters in the randomized distribution to be less the 1% of those found in the experimental data. For the two datasets analysed, D_{max} values of 2.2 and 2.6 nm were selected, with an N_{min} of 5 in both cases.

The number density of these clusters was estimated by dividing the number of clusters identified by the analysed volume ((number of ions collected ÷ detector efficiency) × atomic volume). The LEAP5000XR has a detector efficiency of 0.52 [299]. Two datasets were analysed containing a total of 43 million ions, and an average number density of clusters of $1.47 \times 10^{23} \mathrm{m}^{-3}$ was found.

Cluster composition is also sensitive to parameter selection, and difficult to measure for small clusters where statistics are limited. Ions other than P are judged to be con-

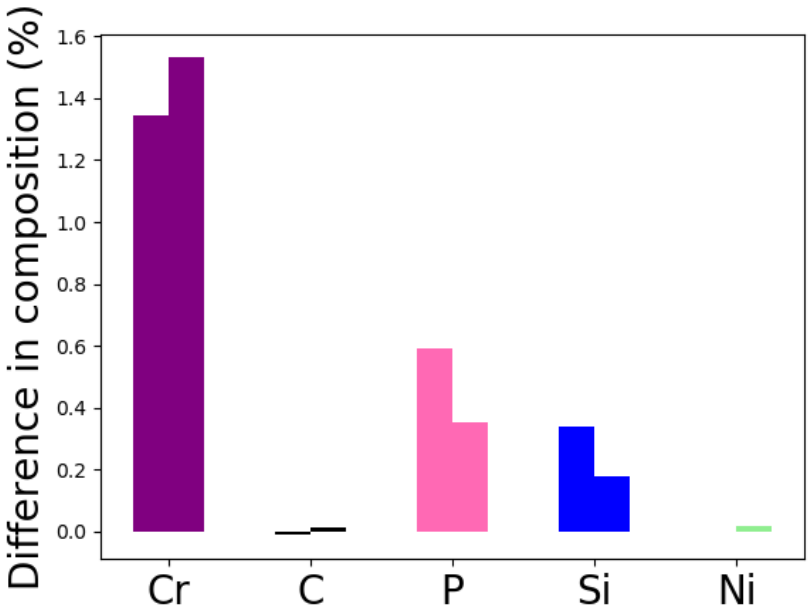


Figure 5.22: Difference in composition between clusters and the matrix, one bar for each dataset. Positive values represent enrichment in the clusters. A small excess in the height of the peak at 29 Da based on isotopic ratios of Fe has been attributed to the presence of $^{58}Ni^{++}$.

tained in the cluster or not based on 2 parameters - the envelope distance L and erosion distance E. L sets the maximum distance from clustered ions (P) at which other elements (not P) are included in the cluster. Atoms within a distance E from non-clustered ions are removed from the cluster. L was set to be half of D_{max} (to avoid two clusters claiming the same ions), and E was set to 0 to include all matrix ions within L.

Separate .pos files were created for ions contained within the clusters, and those outside in the matrix. The mass spectrum analysed in the same way as for the bulk composition, to obtain the average cluster composition and the matrix composition. The difference in composition between clusters and the matrix are shown in figure 5.22 for both data sets.

This analysis revealed Si and Cr enrichment at the site of P clusters. A small excess

in the height of the peak at 29 Da based on that expected from the height of the peak at 28.5 Da from the natural abundances of Fe isotopes may suggest the presence of $^{58}Ni^{++}$ at the clusters.

5.3.3.4 Loop-like Features

Two loop-like features decorated with Si were identified in the ion irradiated samples. They are shown in figure 5.23.

Chemical composition line profiles along the long axis of the cylinders indicated are shown in figure 5.24. It can be seen that these loops are decorated with Si, P and Cr, and are around 20 nm in size.

Analysis was performed to identify the planes on which these loop-like features lie. Full details of this analysis are given in section 3.4.3. Unfortunately, it was only possible to confidently locate and index a required 3 crystallographic poles in one of the datasets.

In order to fit a plane to the loop, firstly isoconcentration surfaces of 0.45 at% Si were created as shown in figure 5.23. The volumes belonging to the loop were then exported to a separate .pos file, and only the Si atoms were used in the plane fitting.

The plane fitting and stereographic projection of the loop habit plane normal are shown in figure 5.25. The feature was found to lie on a plane close to {112}.

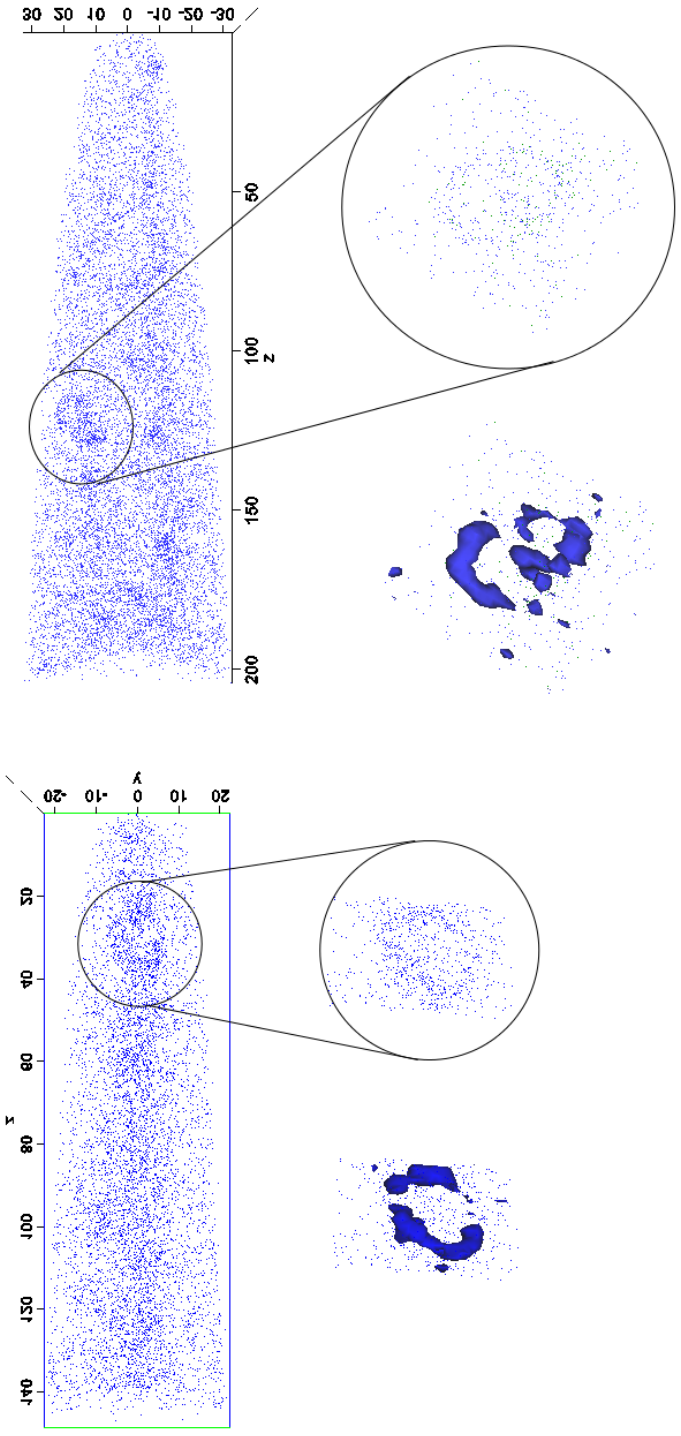


Figure 5.23: Si decorated loop-like features identified in ion irradiated samples. Iso-concentration surfaces of and 0.45% (top) and 0.75% (bottom) Si are shown to aid visualisation.

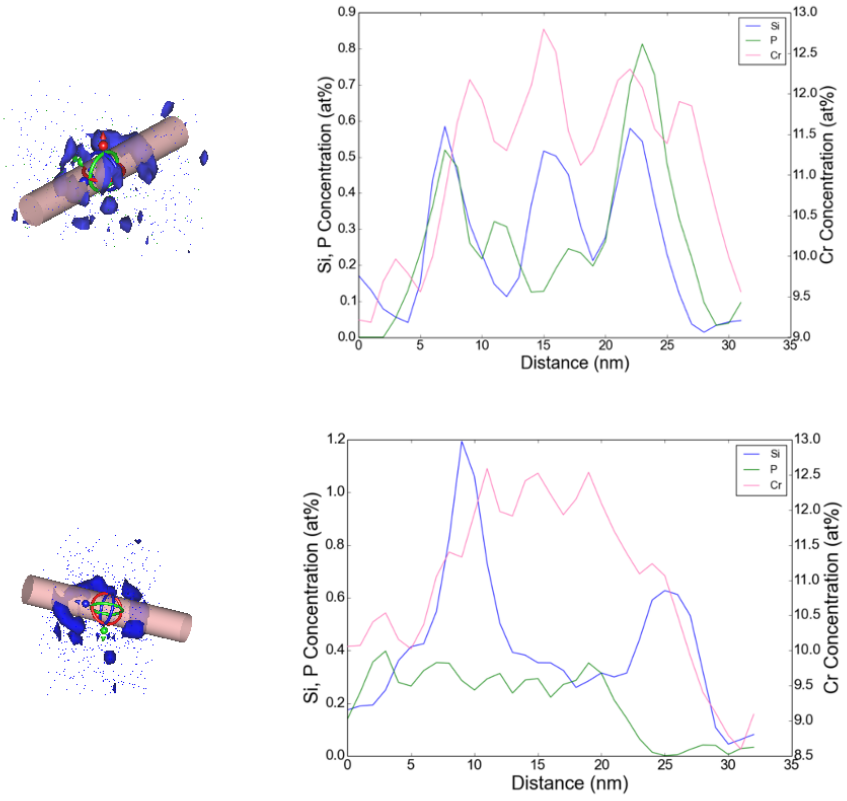


Figure 5.24: Chemical composition line profiles of two loop-like features along the z axis of the cylinders shown. Segregation of Si, P, and Cr can be seen.

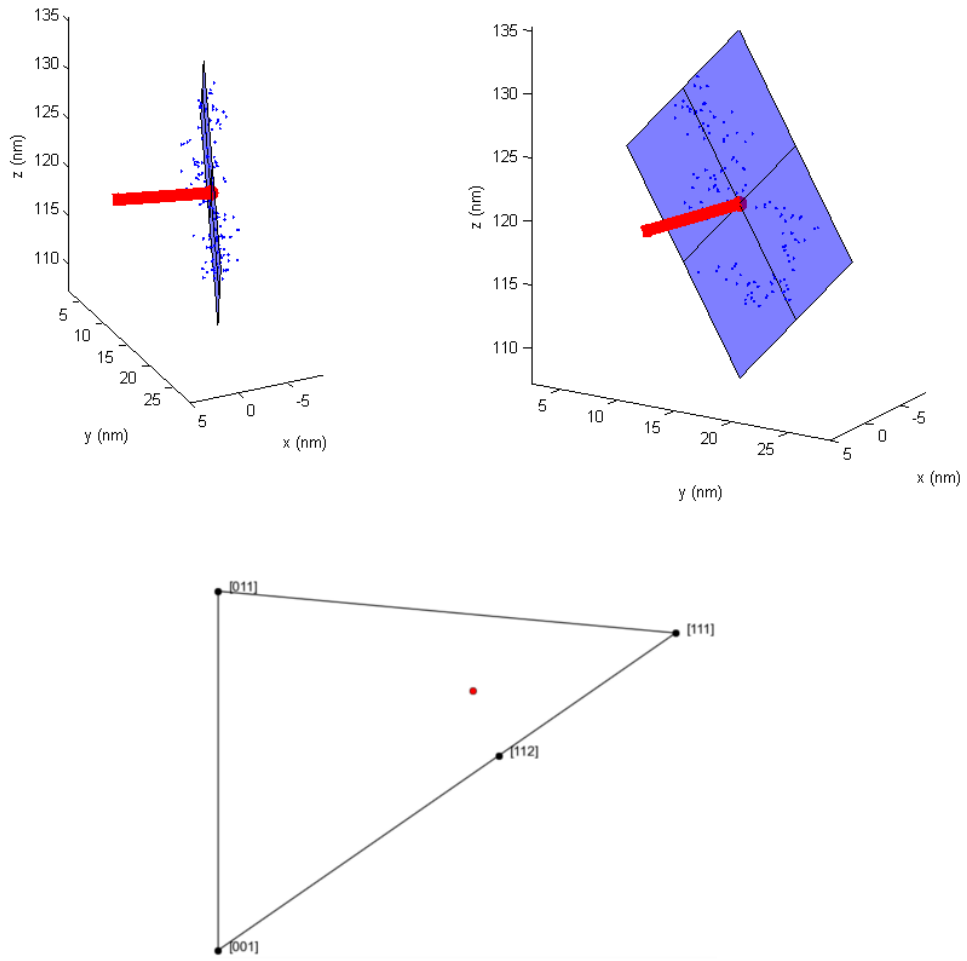


Figure 5.25: Plane fit to Si atoms decorating a dislocation loop, with the stereographic projection of the crystal direction of the plane normal marked with a red circle. The plane normal was found to be closest to $\{112\}$, suggesting it has Burger's vector $\frac{1}{2}$<111> $[300, 301]$.

5.3.3.5 Summary of APT results

A summary of the findings of the APT analysis of the ion irradiated sample, along with those in the literature for the neutron irradiated sample [77, 277, 289] is given in table 5.5.

The main observations in the present study of the ion irradiated sample were: no evidence of α' formation, NiSiPCr clusters with a number density of $1.47 \times 10^{23}\mathrm{m}^{-3}$, and two loop-like features around 20 nm in diameter, decorated with Si, P, and Cr. The habit plane of one of these loops was able to be measured and found to be close to $\{112\}$.

Feature	**Ion Irradiated**	**Neutron irradiated**
α'	Not observed	$8.5 \times 10^{22}/\mathrm{m}^3$, 86.2%Cr, 2.4nm average radius [77]
Loops	~20 nm, decorated with Si, P, Cr	Decorated with Si, Cr [289] [277]
Clusters	NiSiPCr rich clusters $1.47 \times 10^{23}\mathrm{m}^{-3}$	NiSiPCr rich clusters [289]

Table 5.5: Summary of APT observations in ion irradiated (this work) and neutron irradiated specimens (from literature [289] [277] [77]).

5.4 Discussion

In this section the microstructural observations are first discussed, with focus on linking the observations to radiation conditions. This is followed by a discussion of the mechanical properties, with reference to work on the Fe-6Cr alloy from this series by Hardie et al. [14].

5.4.1 Microstructure

5.4.1.1 α' Precipitation

Bachhav et al. [77] examined another specimen of the same neutron-irradiated alloy with APT and found α' precipitates with a number density of $8.5 \times 10^{22}/\mathrm{m}^3$, as shown in figure 5.26. This is in contrast to the present examination of the ion irradiated alloy, where no Cr precipitates or clustering was found.

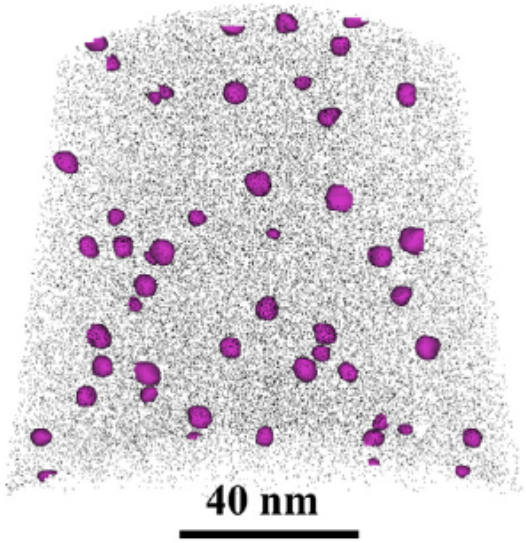


Figure 5.26: α' precipitates in the neutron irradiated Fe-9Cr alloy observed by Bachhav et al. [77]. Purple denotes isoconcentration surfaces of 34 at% Cr. Figure from [77].

The present observations are however in agreement with other experiments comparing ion and neutron irradiation in Fe-Cr alloys. Pareige et al. [82] ion irradiated Fe-Cr model alloys containing nominally 9 and 12% Cr to 0.5 dpa to compare the same alloys neutron-irradiated to 0.6 dpa, both at 300°C. α' precipitates were found in the neutron-irradiated samples with SANS [79] and APT [78], but not in the ion-irradiated samples [82] (APT).

In fact observation of α' precipitation in Fe-Cr alloys after heavy ion irradiation has only been reported once, by Tissot et al. [81] in 2016. In this experiment, a high purity Fe-15Cr alloy was irradiated with 2 MeV Fe ions to ~1 dpa with a dose rate of 3 - 6×10^{-5} dpa/s at 300°C. The sample was analysed by APT at different depths from the surface. Regions containing 45-50 at% Cr were found only at lower depths, away from areas of injected interstitials.

α' precipitation (discussed further in section 2.2.3) is thought to be thermodynamic in origin, with the α-α' phase boundary occurring at around 9%Cr at 300°C [69, 75]. Radiation is thought to enhance diffusion by producing additional vacancies and interstitials, allowing thermodynamic equilibrium to be reached on much shorter timescales than in thermal aging experiments [69].

This radiation-enhanced origin of α' formation is supported by neutron irradiation studies of Fe-Cr model alloys with varying Cr concentrations, at 290°C [77] and 300°C [78,79] finding α' precipitates only in alloys containing 9% or greater Cr, in good agreement with the new proposed phase boundary.

The observation that electron irradiation is particularly efficient at causing α' precipitation [80] also suggests a radiation enhanced mechanism, as electron irradiation tends to produce individual Frenkel pair defects that are able to enhance diffusion more efficiently than other forms of irradiation.

Assuming this radiation-enhanced thermodynamically-driven formation mechanism, the absence of α' precipitation after heavy ion irradiation in the present experiment can be understood to be due to aspects of the irradiation and material that make conditions for its formation unfavourable.

Firstly the material composition. The measured Cr content for this material is around

10 at%, close to the solubility limit of around 9% at 300°C proposed by Bonny et al. [75], meaning that the thermodynamic driving force for phase separation is low.

Secondly dose rate (see section 2.4.2). The ion irradiation dose rate of ~3 - 6×10^{-5} dpa/s is two orders of magnitude faster than the neutron irradiation dose rate of ~4×10^{-7} dpa/s. A higher dose rate leads to a higher average concentration of point defects, meaning these defects are more likely to recombine with each other and annihilate. So on average point defects have shorter lifetimes and migrate over shorter distances for higher dose rates. This means for the same dose, less radiation enhanced diffusion occurs at higher dose rates than at lower dose rates.

Recent work by Reese et al. [302] has suggested that dose rate may have an additional influence via ballistic mixing. The Cr composition in α' clusters in an ion or neutron irradiated Fe-18Cr was found to increase with decreasing dose rate, and this was suggested to be due to ballistic mixing. The authors argue that displacement cascades cause Fe to be mixed into the clusters, and Cr into the matrix, and that thermal recovery occurs in-between cascade events. At higher dose rates there is insufficient time for complete recovery to thermal equilibrium, and a new equilibrium between mixing and unmixing is established at a lower cluster Cr content.

Thirdly, the presence of injected interstitials has been shown to supress α' formation [81]. The concentration of injected interstitials as a function of depth for the target conditions for the present experiment is shown in figure 5.27. The use of multi energy ions produces a roughly flat damage profile across the depth, but also means that injected interstitials are also present in large numbers throughout the damaged region.

Finally, the PKA energy spectrum (see section 2.4.1). While α' is generally not observed after heavy ion irradiation, it has been reported in ferritic-martensitic steels

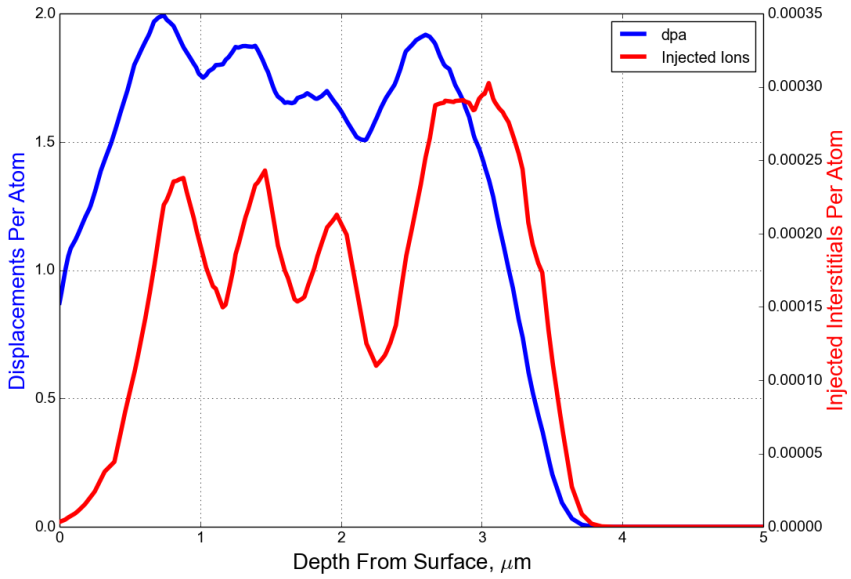


Figure 5.27: Displacements per atom and injected ions as a function of depth for the targeted conditions in the present ion irradiation experiment, as calculated by SRIM.

HCM12A and HT-9 containing 12% Cr after irradiation to 7 dpa at 400°C with 2 MeV protons [303]. Electron irradiation was found to be more efficient than neutron irradiation at inducing α' precipitation [80], with a volume fraction of 6.7% of a Fe-15Cr alloy transformed to α' after a dose of 0.7 dpa with electron irradiation, and a volume fraction of 3.8% after a dose of 1.82 dpa of neutron irradiation. These observations can be explained in terms of the PKA recoil energy spectra produced by each type of irradiating particle. The screened Coulomb interaction between charged ions and lattice atoms produces recoiling atoms with a greater spread of energies than produced by a neutron of the same energy, which interacts as a hard sphere [141]. For this reason irradiation with protons produces more PKAs with lower energies than neutron irradiation does.

There is some debate in the literature as to the meaning of PKA recoil energy spectrum for self ion irradiation. This is discussed in the ion irradiation part of section 2.4.1. For the reasons argued there, it is the author's opinion that the PKA energies should be

taken to be the irradiating ion energy, in the MeV range up to 24 MeV for the present experiment.

Molecular dynamics simulations have shown that in Fe, cascades with lower PKA recoil energies (below 10 keV) tend to have a higher defect survival fraction, and fewer of the surviving defects are clustered for recoil energies below 1 keV [24, 25, 135, 136]. These unclustered defects are known as freely mobile [138–140], and are able to migrate and enhance diffusion.

The higher PKA energy spectrum present in heavy ion irradiation means that fewer freely mobile defects are produced for the same dpa than in neutron and proton irradiation where there are more low energy PKAs. Electron irradiation produces individual frenkel defect pairs, so freely mobile defects are produced with higher efficiency than with other irradiating species. For this reason, radiation enhanced diffusion and therefore α' precipitation is most efficiently enhanced by this irradiation method.

The higher PKA energy spectrum produced in the ion irradiation experiment than in the neutron irradiated experiment may have caused less radiation enhanced diffusion, and so contributed to the lack of α' precipitation found in the ion irradiated sample.

5.4.1.2 Loop-like features

As discussed in section 2.2, dislocation loops in Fe and Fe-Cr alloys form with either <100> or $\frac{1}{2}$<111> type Burgers vectors. <100> loops lie on {100} planes, and $\frac{1}{2}$<111> loops have been observed on {111}, {110} and {112} planes [300,301]. The habit plane of the Si decorated loop-like feature found in section 5.3.3.4 (figures 5.23 and 5.25) was close to {112}, consistent with it being a dislocation loop with Burgers vector $\frac{1}{2}$<111>.

The habit plane and Burgers vector is also consistent with those measured by Bachhav et al. [94] in the neutron irradiated Fe-6Cr alloy from the same alloy series/irradiation campaign.

Comparable TEM studies [41,48,218] report fractions of $\frac{1}{2}$<111> loops of 41-68% for ion or neutron irradiation at 300°C to 0.6-1 dpa in Fe8-10Cr binary alloys. The measured Burgers vector is consistent with those reports.

The measured loop sizes of approximately 20 nm corresponds to around the maximum sizes observed in the TEM studies [41,48,218], and in good agreement with those measured by Bachhav et al. [94] in the Fe-6Cr alloy with APT.

Si and Cr segregation to loops observed in the present work in the ion irradiated specimen was also reported in the neutron irradiated specimen by Reese et al. [277] and Bachhav et al. [289]. Quantitative details about the levels of segregation were not given for the neutron irradiated Fe-9Cr alloy in [277,289] , but these features are at least qualitatively reproduced by heavy ion irradiation.

The segregation of these elements is consistent with other work. For example Kuksenko et al. [216] reported P, Si and Cr segregation to dislocations and grain boundaries in Fe-Cr alloys neutron irradiated to 0.6 dpa at 300°C, and Jiao et al. [304] reported Si, Cr and Ni segregation to dislocation lines, loops, and grain boundaries in HCM12A both after proton irradiation to 7 dpa at 400°C and after Fe irradiation to 100 dpa at 500°C.

5.4.1.3 NiSiPCr Clusters

NiSiPCr rich clusters observed here after ion irradiation were also observed in the corresponding neutron irradiated specimen, and in others from the same neutron irradiation experiment with different Cr contents [289]. No quantitative analysis has yet been published for the Fe-9Cr alloy, but has been for the Fe-6Cr [94] and the Fe-15Cr [305] alloys.

Clustering of the same elements was also observed by Pareige et al. [82] and Kuksenko et al. [216, 217, 306] in similarly ion and neutron irradiated Fe-Cr alloys respectively (300°C and 0.5, 0.6 dpa).

Bachhav et al. [305] and Kuksenko et al. [217] both argue that because these elements are only present at trace impurity levels, there can be no significant thermodynamic driving force for their precipitation, and suggested a radiation induced segregation (RIS) or radiation induced precipitation (RIP) mechanism is most likely. RIS is driven by a coupling of the flux of solute atoms with the flux of point defects [16]. Any preferential association of defects with a species of solute atom will lead to this coupling. Modelling has demonstrated this for these species [33, 307–309]. Point defects migrate to sinks, leading to a build up or depletion of solute atoms at these regions.

Pareige et al [82] found increasing levels of enrichment at clusters with increasing temperature (100, 300 and 420°C), strongly suggesting a RIS mechanism. RIS has a bell shaped relationship with temperature. At low temperatures defect mobility is low and so mutual recombination occurs more frequently and flux of defects to sinks is low. As the temperature increases defect mobility increases and so does the flux to sinks. At higher temperatures back-diffusion of segregated elements becomes more important, leading to a reduction in enrichment and a peak segregation temperature.

The same elements have been observed to segregate to loops, dislocations and grain boundaries [82, 94, 216, 289, 304–306]. This raises the question what features the elements are segregating to, to form the clusters. In a neutron irradiated Fe-12Cr alloy, Kuksenko et al. [217] found that both the number density and spatial distribution of NiSiPCr clusters differed from that of the dislocation loop population reported by TEM [45]. Dislocation loops were found to located preferentially near to line dislocations, whereas the NiSiPCr clusters were homogeneously distributed. The clusters also had a number density 2 orders of magnitude greater than that of the loops, meaning that the clusters are not associated with loops. The authors suggested the clusters could be associated with Ni and Si enriched radiation induced phases observed in F-M steels [310]. In another paper [306] the same authors also suggest possible association with small loops or clusters not visible in TEM. Pareige et al. [82] also suggest small defect clusters, or solute concentration fluctuations which cause trapping of interstitials could be sites for cluster formation by RIS.

In the present experiment NiSiPCr clusters observed after neutron irradiation were at least qualitatively reproduced with heavy ion irradiation. A quantitative comparison would be interesting, as RIS is dose rate sensitive for similar reasons to that of temperature. One might expect a greater level of enrichment for a lower dose rate (neutron irradiation) than for a higher dose rate (ion irradiation), because a lower dose rate means a lower proportion of defects undergo mutual recombination so can migrate to sinks and cause segregation. Differences in PKA energy may also have an effect, with lower energy cascades producing more freely mobile defects able to migrate to sinks.

5.4.1.4 Microstructural Summary

In this work the segregation of Si, P and Cr to dislocation loops, and the formation of NiSiPCr clusters reported by various authors after neutron irradiation was qualitatively reproduced by heavy ion irradiation. Quantitative information about the neutron irradiated Fe-9Cr alloy is not available for comparison. α' precipitation observed in the neutron irradiated specimen was not reproduced by heavy ion irradiation.

The reason NiSiPCr clusters and loop decoration was reproduced but α' precipitates were not is likely due to the differences in mechanisms that lead to their formation. The cluster formation and loop decoration are thought to be due to RIS, whereas α' precipitation is thought to be thermodynamic in origin and enhanced by radiation.

RIS only requires a coupling of defect and solute fluxes, due to interaction of a species with point defects, and a flux of point defects to sinks. These are determined by physics, and are not existentially affected by differences in irradiation conditions. Only the magnitude of the flux of defects to sinks can be affected by differences in irradiation conditions, which may manifest as quantitative differences in levels of segregation.

α' precipitation however has been shown to be sensitive to a number of neutron-atypical aspects of heavy ion irradiation. It is argued that the injected interstitials [81], higher dose rate [302], and PKA energy spectrum [80] in the ion irradiation all act to suppress its formation.

5.4.2 Mechanical Properties

In this section, the results of microcantilever testing will first be discussed, followed by the indentation results with comparison to other work and interpretation with regards to irradiation method and microstructure.

5.4.2.1 Microcantilevers

Microcantilver testing found that both the ion-irradiated and neutron-irradiated samples showed a increase in yield stress compared to the unirradiated sample. No statistically significant difference in the yield stress was observed between the ion- and neutron-irradiated samples. The results showed a reasonably large amount of scatter, likely due to a combination of microstructural variability on these length scales (see size effects discussion in section 3.3), error in determining the value of yield stress, and uncertainty in beam dimension measurement.

In order to assess the influence of beam measurement error on the amount of scatter, further analysis was performed. For those beams where crystallographic orientation information was collected, the theoretical elastic modulus was used to calculate a "fitted" beam height. The "fitted" beam height is the height that gives the theoretical value of the elastic modulus for the beam crystal orientation, assuming that all the difference between the measured and theoretical modulus is due to error in measurement of the beam height. It is calculated using equation 5.4:

$$h_{fitted} = \frac{h_{measured}}{(\frac{E_{theory}}{E_{measured}})^{\frac{1}{3}}} \tag{5.4}$$

where h is the beam height and E the elastic modulus.

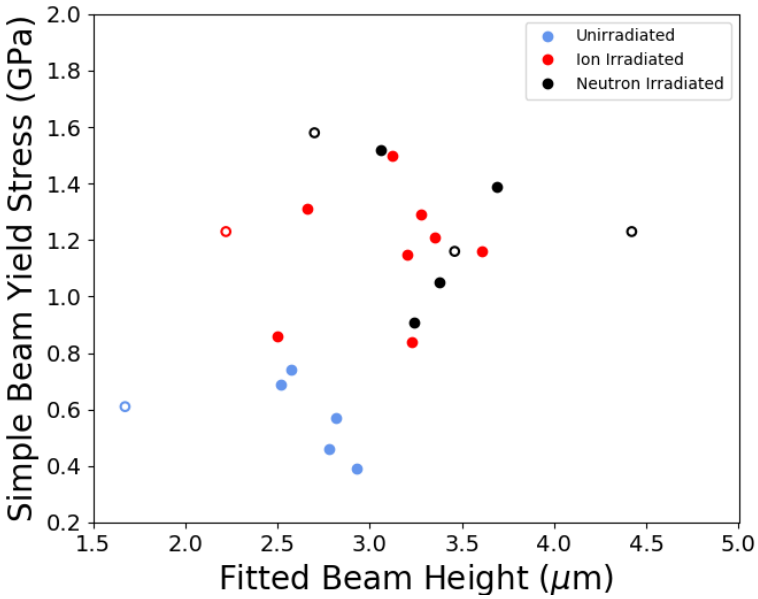


Figure 5.28: Simple beam theory yield stress as a function of fitted beam height. Open symbols identify beams where the deviation from the theoretical modulus was larger than would be expected from beam dimension measurement uncertainty.

The analysis was rerun using the fitted beam heights, with the results plotted in figure 5.28 for simple beam theory and in figure 5.29 for FEA.

As mentioned in the results section , in some beams the difference between the measured and expected elastic moduli was larger than would be expected from uncertainty in beam dimension measurement alone (figure 5.10). This suggested perhaps the crystal orientation at the bottom of the beam may be either different to that measured with EBSD on the surface where a different grain was located, or that a combination of crystal directions were tested due to nearby grain boundaries. If this was the case, the fitting of the beam heights by this method would be inappropriate. The data measured from these beams are marked with open symbols in figures 5.28 and 5.29.

A significant amount of scatter still remains in the data, suggesting some microstructural variability on this scale.

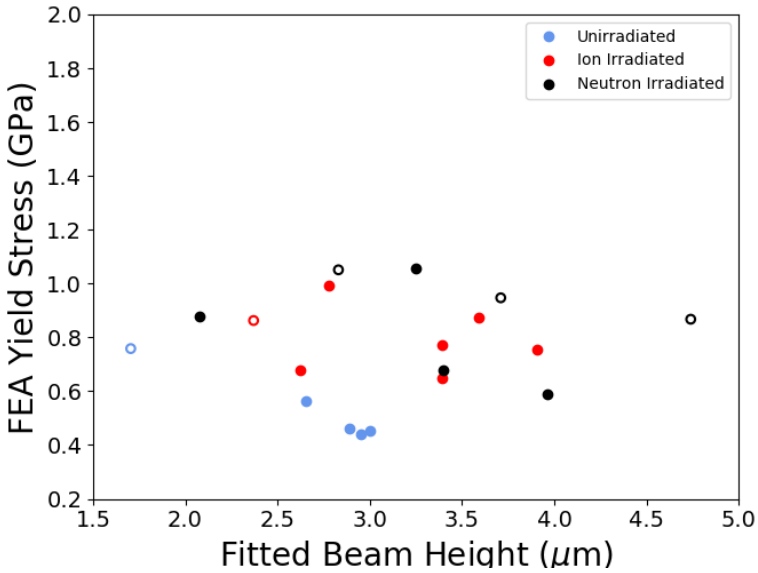


Figure 5.29: FEA yield stress as a function of fitted beam height. Open symbols identify beams where the deviation from the theoretical modulus was larger than would be expected from beam dimension measurement uncertainty.

The scatter is larger in the simple beam theory analysis. As detailed in section 3.2.5, the yield stress in simple beam theory used in this work is based on that used by Armstrong [229] and is defined as the point at which the gradient of the simple beam theory stress-strain curve drops below 0.9 of a reference value measured in the first 100nm of displacement. The gradient is measured at each strain by fitting a straight line to a number of data points either side of the position, with the number of data points used (*hopsize*) being optimised for each curve (see section 3.2.5). A number of factors can affect the value of yield stress measured in this method. Firstly the *hopsize* used - a larger *hopsize* means changes in gradient due to plasticity are felt earlier at lower strains. The method is also sensitive to differences in post yield behaviour - a large drop in gradient post yield will cause the gradient to fall below the 0.9 threshold at a lower strain than a more gradual change in gradient post yield would. Finally due to the elastic anisotropy of this material, cantilever beams with differently orientated grains have different refer-

ence gradients - meaning the absolute drop in gradient required to signify the onset of plasticity is also different. Each of these factors may contribute to the additional scatter observed by this analysis method.

Hardie et al. [14] performed microcantilever testing on the Fe-6Cr alloy from this series, neutron irradiated in the same irradiation campaign and ion irradiated under similar conditions in another experiment. Their results are shown in figure 5.30, where the proof stress is plotted against beam height.

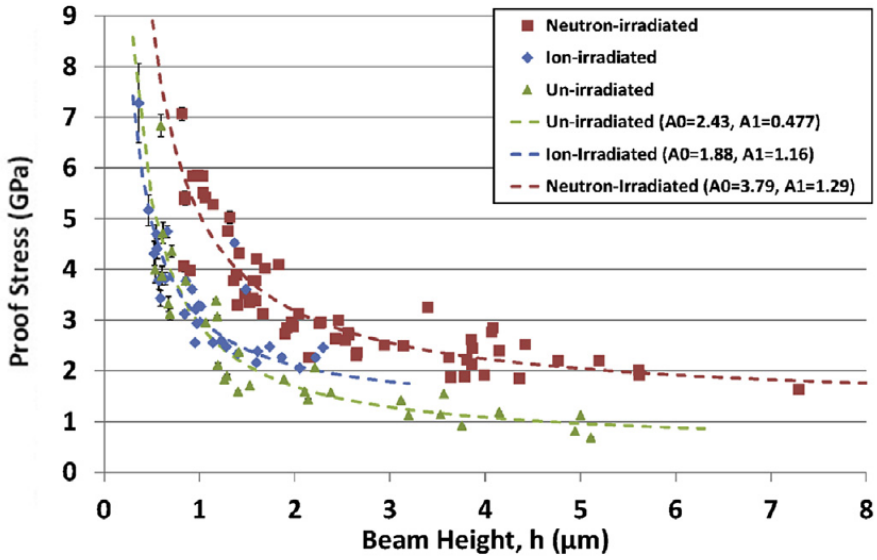


Figure 5.30: Work by Hardie et al. [14] on an identically neutron irradiated and similarly ion irradiated Fe-6Cr alloy from the same series as the Fe-9Cr in the present work, showing proof stress (0.2%) of microcantilever beams as a function of beam height. Data are fitted to $\sigma_{proof} = A_0 h^{-1} + A_1$, where h is the beam height, with the A_0 and A_1 are constants. Figure from [14].

The lack of observation of a strong size effect in the present work is in agreement with that found by Hardie et al. [14], where for beam heights greater than 2 μm a similarly weak size effect is seen. Like that found for flow stress by Motz et al. [239] in Cu, Hardie et al found a h^{-1} dependence on proof stress.

Alongside those of Hardie et al. [14], these results suggest that for these materi-

als an ion implantation depth of at least 2 μm is required to measure radiation induced mechanical property changes with microcantilevers and to avoid strong size effect influences.

5.4.2.2 Indentation

Figure 5.31 shows the results of nanoindentation testing of ion and neutron irradiated Fe-6Cr (by Hardie et al. [14]) and Fe-9Cr alloys, and of Vickers hardness testing (by T Milot, *INL*) of the un- and neutron irradiated specimens. Nanoindentation measurements were all taken at a depth of 500 nm, and Vickers hardness testing using a 500 g load.

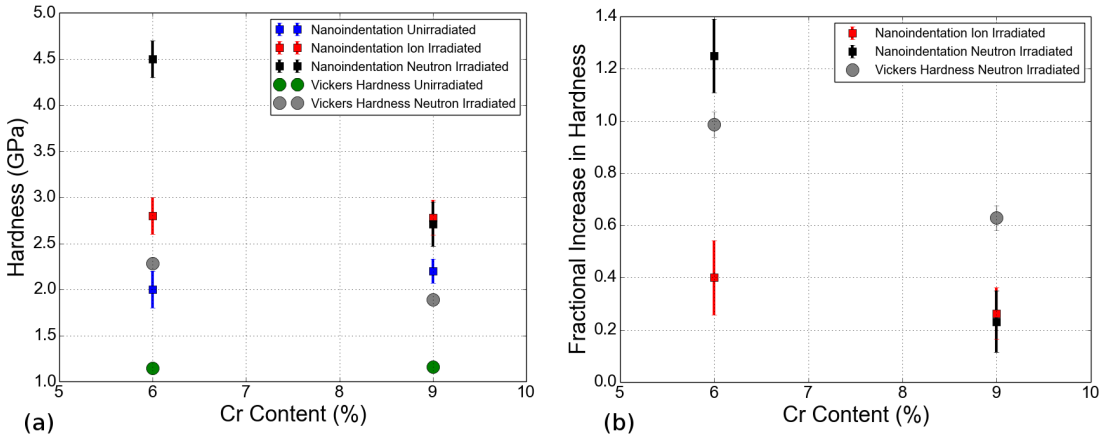


Figure 5.31: (a) Hardness of Fe-6Cr and Fe-9Cr by nanoindentation (at 500nm) after ion and neutron irradiation, and by Vickers testing (500g) after neutron irradiation; (b) fractional increase in hardness (change in hardness/unirradiated hardness). Nanoindentation data for the Fe-6Cr alloy by Hardie et al. [14] (separate ion irradiation, 300°C 0.82 dpa ~2.5×10^{-5} dpa/s). Vickers hardness data by T Milot at INL. Error bars represent 1 standard deviation.

Turning first to data from the present experiment, the measured increase in nanoindentation hardness for the ion and neutron irradiated Fe-9Cr samples is the same within experimental error.

With the differences in microstructure reported here and in [77], namely the presence of α' in the neutron irradiated sample and not in the ion irradiated sample, the similarity found in mechanical properties is somewhat unexpected.

Bergner et al. [90] applied a dispersed-barrier hardening model to Fe-Cr model alloys irradiated to 0.6 dpa at 290°C, using data reported in [45] (yield stress by tensile tests), [311] (α' by SANS), [78] (NiSiPCr clusters by APT), and [45, 218] (dislocation loops by TEM). Their analysis found dislocation loops to be the strongest obstacles, and α' precipitates to be the weakest. The low obstacle strength of α' is not surprising, as they are coherent precipitates and differ in modulus and lattice spacing only a small amount with those of the matrix. Bergner et al. also calculated the contribution from each class of obstacle to the observed increase in yield stress. As can be seen in figure 5.32, in the Fe-9Cr alloy the contribution of α' precipitates is small compared to that of the dislocation loops and NiSiPCr clusters.

A plausible explanation for the similarity in mechanical properties between the two samples in the present experiment is that the α' precipitates observed only after neutron irradiation contribute very little to the hardening, and that other classes of obstacles dominate the overall increase and are well reproduced by ion irradiation. These obstacles consist of dislocation loops (Si decoration observed [277]), and likely NiSiPCr clusters (observed in the neutron irradiated Fe-14Cr alloy from the same irradiation campaign [305]). Microstructural analysis by TEM and APT would be required to confirm this.

This is in contrast to work by Hardie et al. [14] on the Fe-6Cr from the same neutron irradiation campaign, where a significant difference in post irradiation hardening was found between ion and neutron irradiated specimens with nanoindentation, also shown in figure 5.31. They found that loops were present in a higher number density and also

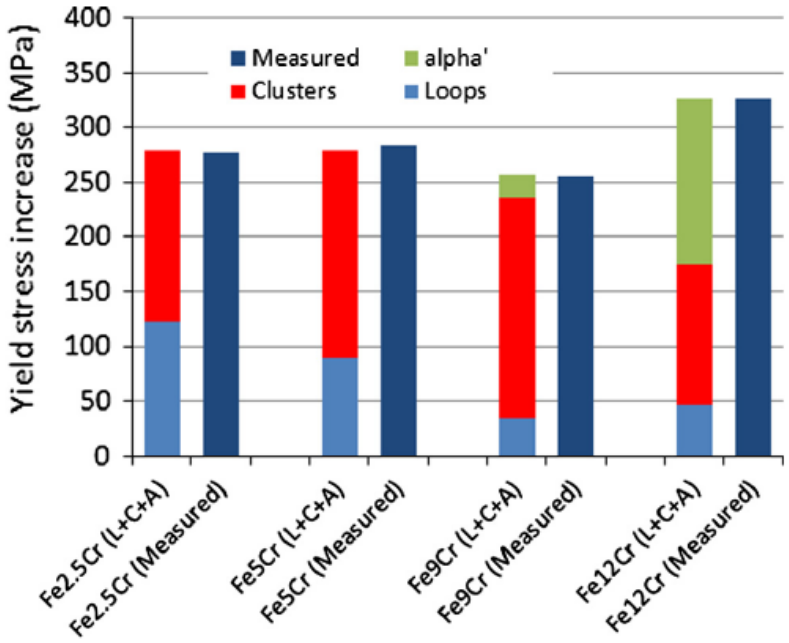


Figure 5.32: Bergner et al.'s work [90] showing contribution of each obstacle class to observed yield stress increase in Fe-Cr alloys neutron irradiated to 0.6 dpa at 290°C. Figure from [90].

had a higher obstacle strength due to Cr decoration in the neutron irradiated sample, compared to a lower loop density and with no Cr decoration in the ion irradiated sample.

The neutron irradiation induced hardness increase is significantly higher for the Fe-6Cr alloy then the Fe-9Cr alloy both from nanoindentation (Hardie et al. [14] and this work), and from Vickers hardness testing (T Milot, *INL*) also shown in figure 5.31. This large difference in hardness suggests obstacles of either a higher number density or higher strength (or a combination of both) exist in the Fe-6Cr compared to the Fe-9Cr sample. The Cr decorated loops found by Hardie et al. [14] could be such obstacles, but again detailed microstructural analysis of the neutron irradiated Fe-9Cr sample by TEM and APT is required to confirm this. Hardie et al. [154] suggested that a higher Cr content in Fe-Cr alloys may act to suppress the flux of defects to sinks by trapping of point defects by Cr [31,32,36,38], leading to reduced RIS. The RIS of Cr and the sensitivity to

conditions is not fully understood, with contradictory results being reported [312–316], and further work is required in this area.

The same trend in relative increases in yield stress with Cr content was also observed in the dataset [45] analysed by Bergner et al. [90].

Work by Hardie et al. [154] on dose rate effects also found greater increases in hardness after ion irradiation (300°C, 0.3dpa) in Fe-5Cr than Fe-10Cr. The Fe-5Cr alloy also showed greater dose rate sensitivity, with the largest difference in hardness between the two conditions. Both alloys were found to have a higher hardness for the low dose rate (1.5×10^{-5} dpa/s) condition than the high dose rate condition (3×10^{-4} dpa/s).

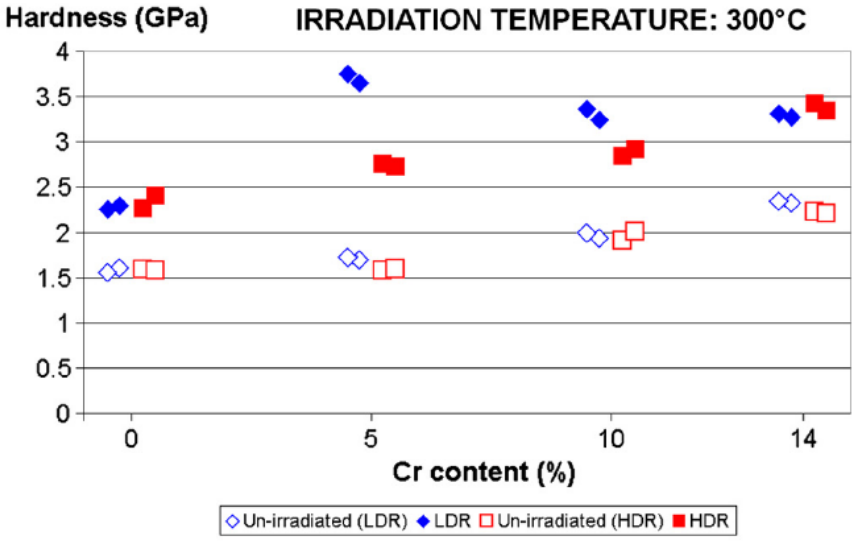


Figure 5.33: Hardie et al.'s work [154] showing post irradiation hardness of UHP Fe-Cr alloys ion irradiated at high (HDR) and low dose rates (LDR). Figure from [154].

Hardie et al.'s results are show in figure 5.33, and mirror those reported here in figure 5.31 - if the ion irradiation is considered as the high dose rate condition ($2.98 - 5.96 \times 10^{-5}$ dpa/s for the Fe-9Cr alloy and ~2.5×10^{-5} dpa/s for the Fe-6Cr alloy [14]) and the neutron irradiation as the low dose rate condition (3.85×10^{-7} dpa/s). Although the alloys studied by Hardie et al. [154] were of ultra high purity and so do not contain

the same impurity clusters as the materials studied in this work, these results suggest that the formation of the microstructure that leads to the larger amount of hardening observed in the Fe-5/6Cr alloys is strongly influenced by dose rate. It also suggests radiation induced hardening in Fe-9/10Cr alloys is relatively dose rate insensitive.

Figure 5.31 (b) shows the fractional increase in hardness ($\frac{\Delta hardness}{unirradiated hardness}$) by nanoindentation for the ion and neutron irradiated specimens, and by Vickers hardness testing (500g, T Milot *INL*) for the neutron irradiated specimens only.

Vickers hardness testing uses a four sided pyramid shaped indenter, which is driven into the surface of the sample with a fixed load, in this case 500g. The hardness is found by dividing this load over the contact area measured by finding the lengths of the diagonals of the indent impression with optical microscopy after the test.

Although both Vickers and Berkovich tips have the same contact area to depth ratio, the Vickers indents discussed here have a depth of around 10μm and so represent a much large testing volume than that of the nanoindentation. ISO standard 6507-1 [317] stipulates the minimum thickness of material to be 1.5× the indent impression diagonal, coresponding to around 10× the indentation depth, and so Vickers testing can only be performed on the neutron irradiated material, where the damage layer is sufficiently thick.

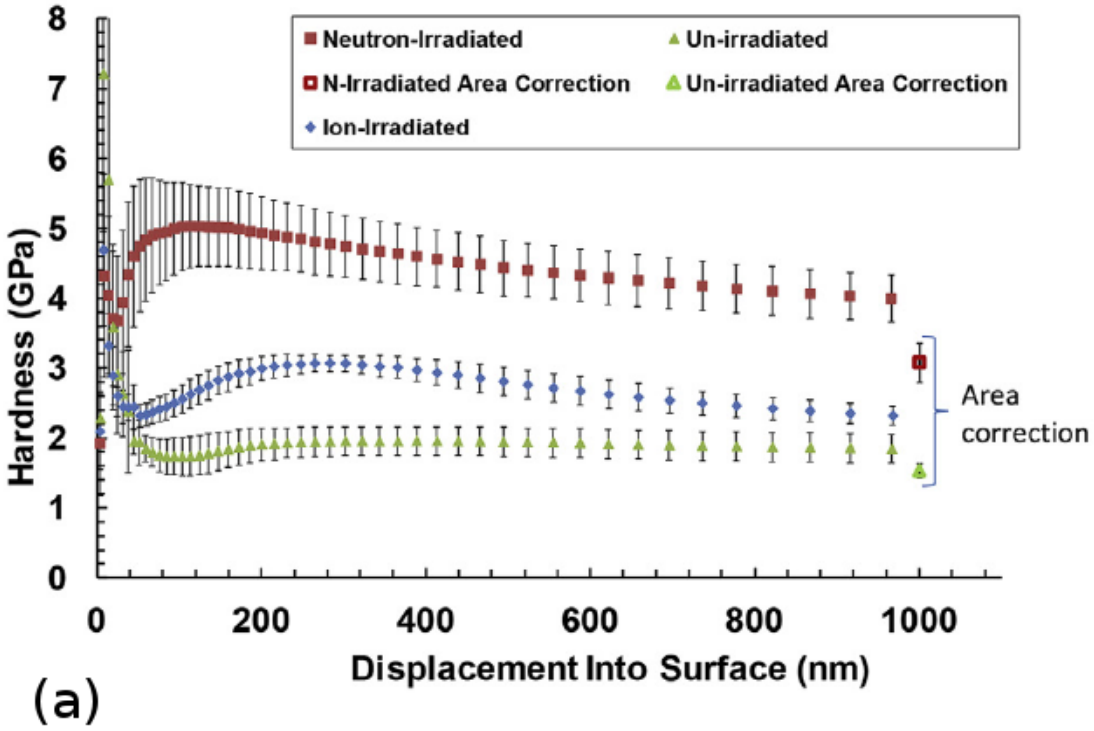
The fractional increase measured by the two methods appears to differ beyond experimental error, with a larger increase being measured by nanoindentation than Vickers indentation for the Fe-6Cr alloy and the opposite for the Fe-9Cr alloy, suggesting a possible indentation size effect. There are however some details to consider regarding the nanoindentation that may exaggerate the differences measured in the Fe-6Cr and Fe-9Cr alloy.

Hardie et al. [14] observed significant pile-up in the neutron irradiated Fe-6Cr alloy. Pile-up is where material piles up on the periphery of the indent and is in contact with the tip during testing, creating additional contact area not accounted for with the calibrated area function, leading to an artificially high measurement of hardness. Such pile-ups were not observed in the Fe-9Cr alloy. The area-corrected values measured by Hardie et al. [14] show a reduced increase in hardness (figure 5.34(a)).

Figure 5.34(b) shows hardness as a function of depth for the unirradiated Fe-9Cr sample measured in this work, and by Hardie. The curves have different shapes, and at 500 nm this work measures a higher hardness than Hardie - resulting in potentially an artificially low hardness increase for both the ion and neutron irradiated Fe-9Cr alloy by nanoindentation. The reason for the discrepancy between measurements may be due to surface condition [318], or differences in tip geometry due to blunting.

Figure 5.35 shows the fractional increases in hardness after applying these "corrections" - using the area-corrected values reported by Hardie et al. [14] for the neutron irradiated Fe-6Cr alloy, and using the lower unirradiated hardness value for the Fe-9Cr measured by Hardie.

The "corrections" move the nanoindentation data closer to the Vickers hardness data, within experimental error for the Fe-6Cr alloy, but the increase is still lower when measured by nanoindentation compared to Vickers testing in the Fe-9Cr alloy. Further work is required, with Vickers testing with lighter weights to bridge the gap in scale with nanoindenation to see if an indentation size effect exists, and whether it is affected by microstructure. Understanding these size effects is crucial to establish the extent to which these small scale tests are representative of macroscopic behaviour, and the required irradiated damage layer depth to extract such data with ion irradiation.



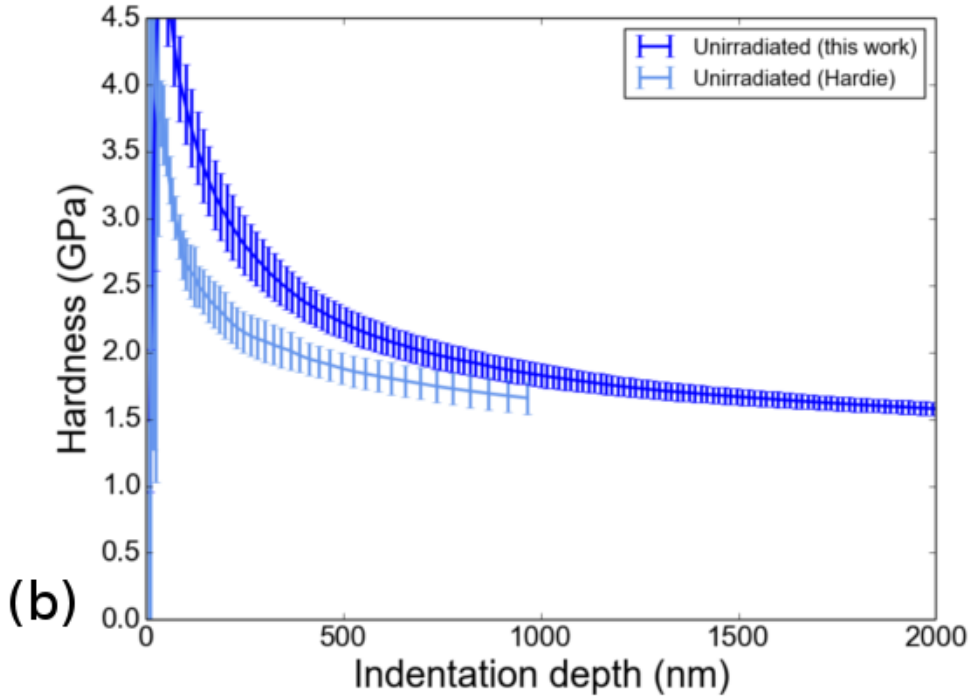


Figure 5.34: (a) Nanoindentation by Hardie et al. [14] of the Fe-6Cr alloy from the same series in the ion, neutron, and unirradiated condition. The area correction due to pileup is shown. (b) Hardness as a function of depth for the Fe-9Cr alloy in the unirradiated condition as measured by Hardie and in this work.

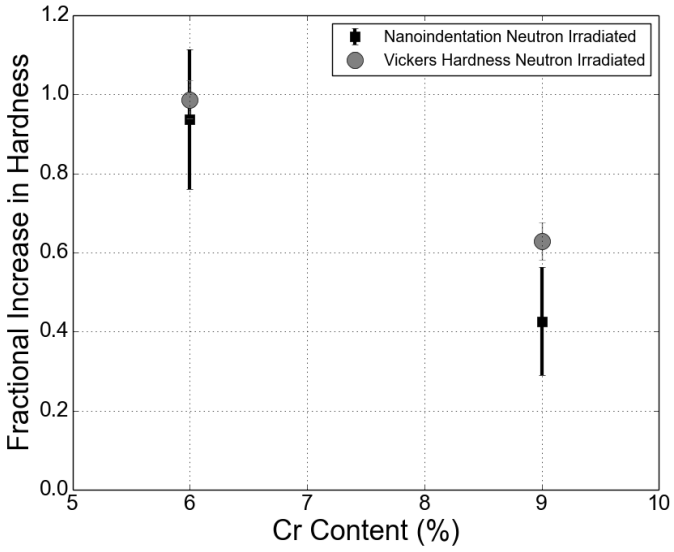


Figure 5.35: Fractional increase in hardness after neutron irradiation by nanoindentation for Fe-6Cr (Hardie et al. [14] area corrected value) and Fe-9Cr (this work, with unirradiated value from Hardie), and by Vickers hardness testing (T Milot, *INL*, 500g)

Wharry et al. [319] argue that meaningful plastic properties can only be measured when the extrinsic size (tested volume) is much greater than intrinsic size (average obstacle spacing). The minimum volume required will therefore depend on the microstructure, and may therefore be different for the two neutron irradiated samples.

This may also, without data on the range of any size effects, bring into question the validity of comparing samples with different microstructures at these length scales. In general, larger irradiated volumes are therefore preferable.

5.5 Conclusions & Further Work

Samples of an Fe-9Cr alloy were irradiated with heavy ions and neutrons under similar conditions, and their mechanical properties analysed using nanoindentation and micro-cantilever testing and compared. The microstructure of the ion irradiated sample was examined with atom probe tomography, and compared to published data for the neutron irradiated sample [77, 277, 289]. A summary of the findings is given in table 5.5.

The decoration of dislocation loops with Si and Cr, and the formation of NiSiPCr rich clusters observed after neutron irradiation was qualitatively reproduced with ion irradiation. Both of these features are thought to occur due to RIS. Further work should include a quantitative comparison.

The most significant microstructural difference was the lack of α' precipitates in the ion irradiated sample that were present in the neutron irradiated one [77]. This finding is consistent with other comparisons of ion and neutron irradiation in Fe-Cr alloys at 300°C, where α' was observed after neutron irradiation [78, 79] but not after ion irradiation [82]. It is argued that a combination of higher dose rate, higher energy PKA spectrum [80], and the presence of injected interstitials [81] in the ion irradiation make conditions less favourable for α' formation than in the neutron irradiation. Further work is required to find ways in which α' can be produced using heavy ion irradiation. This may involve lower dose rate irradiations using only single energy ions, so the region containing the injected interstitial peak can be avoided.

Microcantilever testing and nanoindentation revealed no statistically significant difference in hardness or yield stress between the ion and neutron irradiated samples, but both were found to be harder and have a higher yield stress than the unirradiated sample.

Work by Bergner et al. [90] on similarly irradiated Fe-Cr alloys found that α' precipitates only make a very small contribution to the observed increase in yield stress in Fe-9Cr, and dislocation loops and NiSiPCr clusters play a more significant role. Only incomplete microstructural information is available for the specimens in the present work, most significantly no analysis by TEM to determine loop sizes and number densities in both samples. However, based on the available microstructural information it is possible that the loop population and NiSiPCr clusters found in the neutron-irradiated sample may be well reproduced by the heavy ion irradiation experiment - hence the similarity in mechanical properties.

Hardie et al. [14] performed a similar study on an identically neutron irradiated and similarly ion irradiated Fe-6Cr alloy from the same series. In contrast to the present work, Hardie found the neutron irradiated specimen was significantly harder than the ion irradiated specimen in the Fe-6Cr alloy [14]. The Cr decoration and higher number density of dislocation loops observed in the neutron irradiated specimen is thought to be the reason for this.

Comparing the results of nanoindentation of the neutron irradiated Fe-9Cr specimen with those of Hardie [14] for the Fe-6Cr specimen, it was found that the Fe-6Cr alloy hardened more than the Fe-9Cr alloy, in agreement with other studies [45]. This is thought to be due to additional Cr segregation to loops in the lower Cr content alloy, and that RIS of Cr is reduced for higher Cr contents due to trapping of point defects by Cr [154].

Recreating changes in mechanical properties caused by neutron irradiation means reproducing the damage microstructure that causes these changes. The ability of heavy ion irradiation to reproduce this microstructure depends on the mechanisms by which it forms, and their sensitivity to the neutron atypical aspects of this irradiation method.

Measuring these changes in mechanical properties requires testing on a scale confined to the irradiated layer, but where size effects don't obscure the effects of the radiation induced microstructure. Microcantilever testing revealed no strong size effect for beams with heights greater than ~2 μm, in agreement with the work by Hardie et al. [14]. For these materials, ion irradiation damage layers should be at least this depth for microcantilever testing. Further work is required to investigate whether changes in hardness measured by nanoindentation can be extrapolated to macro-scale Vickers hardness tests.

Chapter 6

Effect of Carbon on Irradiation Hardening in Fe

The work in chapter 5 and work by Bergner et al. [90] has shown that impurities can have a substantial effect on the mechanical properties of Fe based alloys after irradiation. This chapter reports an experiment investigating the effect of carbon on radiation damage in Fe.

6.1 Introduction & Background

Carbon has been long known to interact with vacancies in Fe, as shown in early experiments on Fe-C samples by Wagenblast et al. [96–99]. Evidence for vacancy-carbon complexes was found later [100, 101], and supported by modern density functional theory calculations [102–106]. These complexes are thought to remain stable up to 580 K [114].

Modelling has shown that interstitial carbon and carbon-vacancy complexes can be strong traps for <100> loops and $\frac{1}{2}$<111> loops respectively [114, 120–122]. This could explain the observations of Satoh et al. [115, 116], where dislocation loops in Fe were seen to hop between positions under in-situ electron irradiation. The distance between positions was found to decrease with decreasing sample purity, suggesting that impurities were trapping the loops.

Lambrecht et al. [126, 127] found a significantly greater increase in hardening after neutron irradiation to 0.1 and 0.2 dpa at 290-295°C in the BR2 test reactor at SCK-CEN for an Fe-C alloy containing $\geq$ 50 ppm C compared to pure Fe (< 20 ppm C), measured by tensile testing. The authors suggested that the difference in mechanical properties was likely due to differences in dislocation loop populations, that trapping of self interstitial clusters by C will increase the number of nucleation sites for clusters, and that the reduced mobility will mean coalescence to form loops is reduced, keeping the loop number density higher.

Modelling work by Jansson et al. [124, 125] would support these suggestions.

Terentyev et al. [128] modelled the interaction of edge dislocations with $\frac{1}{2}$<111> loops decorated with carbon. Both small (TEM invisible) and larger loops decorated with C were found to present a stronger obstacle to dislocation glide than naked loops. This may provide an additional or alternate explanation for the observations of Lambrecht et al. [126, 127].

Particularly with the recently raised issue of unintended carbon implantation during ion irradiation [130–132], it is important to understand the effect of carbon on irradiation damage in Fe and its sensitivity to the neutron-atypical aspects of heavy ion irradiation (discussed in 2.4). To this end, the current work investigates the effect of dose rate and

carbon concentration on the mechanical properties and microstructure of ion irradiated UHP Fe.

6.2 Experimental

6.2.1 Materials

A cylindrical length of ultra high purity Fe (referred to as EFDA Fe in section 3.6, where further information about the material can be found) was subject to a carburisation process to form a sample with a carbon concentration gradient in the radial direction.

The cylindrical sample (11 mm ⌀ x 20 mm) was first plated with Ni on the two circular faces to prevent C diffusion into these surfaces, so the C could diffuse solely in the radial direction. This was done using an electroless plating solution consisting of:

18 g Nickel chloride

4.4 g Sodium hypophosphite

40 g Sodium citrate

20 g Ammonium chloride

400 ml Distilled water

The solution is heated to 90-100°C, and Ni plating proceeds at ~0.015 mm/hour. The Ni plating recipe and procedure were taken from [320].

A 2 stage heat treatment was chosen based on numerical modelling of C diffusion in Fe, in order to create as gradual a concentration profile below the solubility limit over as much of the available area as possible. In stage 1, the sample is placed in a large crucible and submerged in carbon powder, allowing carbon to diffuse in from the outer surface. In stage 2, the sample is removed from the powder so no further carbon is added; rather the carbon that was added in stage 1 is allowed to diffuse both inwards radially and back towards the surface, where it is exposed to air.

6.2.1.1 Modelling of Heat Treatments

Due to the circular symmetry, the problem can be treated as 1 dimensional along the radial direction. The solution to the carbon concentration after the first heat treatment is given by equation 6.1 [321]:

$$C(x,t) = C_s - (C_s - C_0)\,\mathrm{erf}\left(\frac{x}{2\sqrt{D(T)t}}\right) \tag{6.1}$$

where $C(x,t)$ is the carbon concentration, $D(T)$ is the diffusivity of C in γ-Fe, t is the carburisation time, and C_s and C_0 are the carbon concentrations at the carburisation surface and the starting matrix composition respectively.

$D(T)$ is given by an Arrhenius equation [321]:

$$D(T) = D_0 e^{-\frac{E_A}{RT}} \tag{6.2}$$

where D_0 is the diffusion coefficient, E_A the activation enthalpy, R the universal

gas constant, and T the absolute temperature. Values of D_0 and E_A were taken to be 7.7×10^{-7} m^2/s and 107.4 kJ/mol respectively [322]. C_s was estimated experimentally, using micrographs of etched carburised samples and the phase diagram as shown in figure 6.1.

Images were analysed using ImageJ [323], and the grey value plotted as a function of distance from the edge of the sample. Where this value begins to fall marks the beginning of the presence of the α phase, at around the eutectoid composition (0.76wt% [324]). Where this value reaches the midpoint between the cementite and alpha grey levels, the composition should be around half the eutectoid composition. The positions of these points and their approximate compositions are fitted to equation 6.1 to find the surface carbon concentration C_s. A value of around 6 at.% was found.

The second stage heat treatment with diffusion both inwards and outwards (to a free surface) was selected to create as gradual a concentration profile as possible in the available material, and leaving a section at the centre of the material with no additional carbon.

$C(x, t)$ after the second heat treatment is found by solving Fick's 2nd law:

$$\frac{\partial C}{\partial \mathcal{T}} = D\frac{\partial^2 C}{\partial X^2} \tag{6.3}$$

where $\mathcal{T}$ and X are time and length respectively.

A python script was written to solve this by finite difference, using an algorithm outlined in [325]: First distance and time are suitably normalised : $x = \frac{X}{L}$ and $t = \frac{\mathcal{T}}{\tau}$. L is chosen to be the maximum length, and τ to be $\frac{L^2}{D}$. Equation 6.3 becomes:

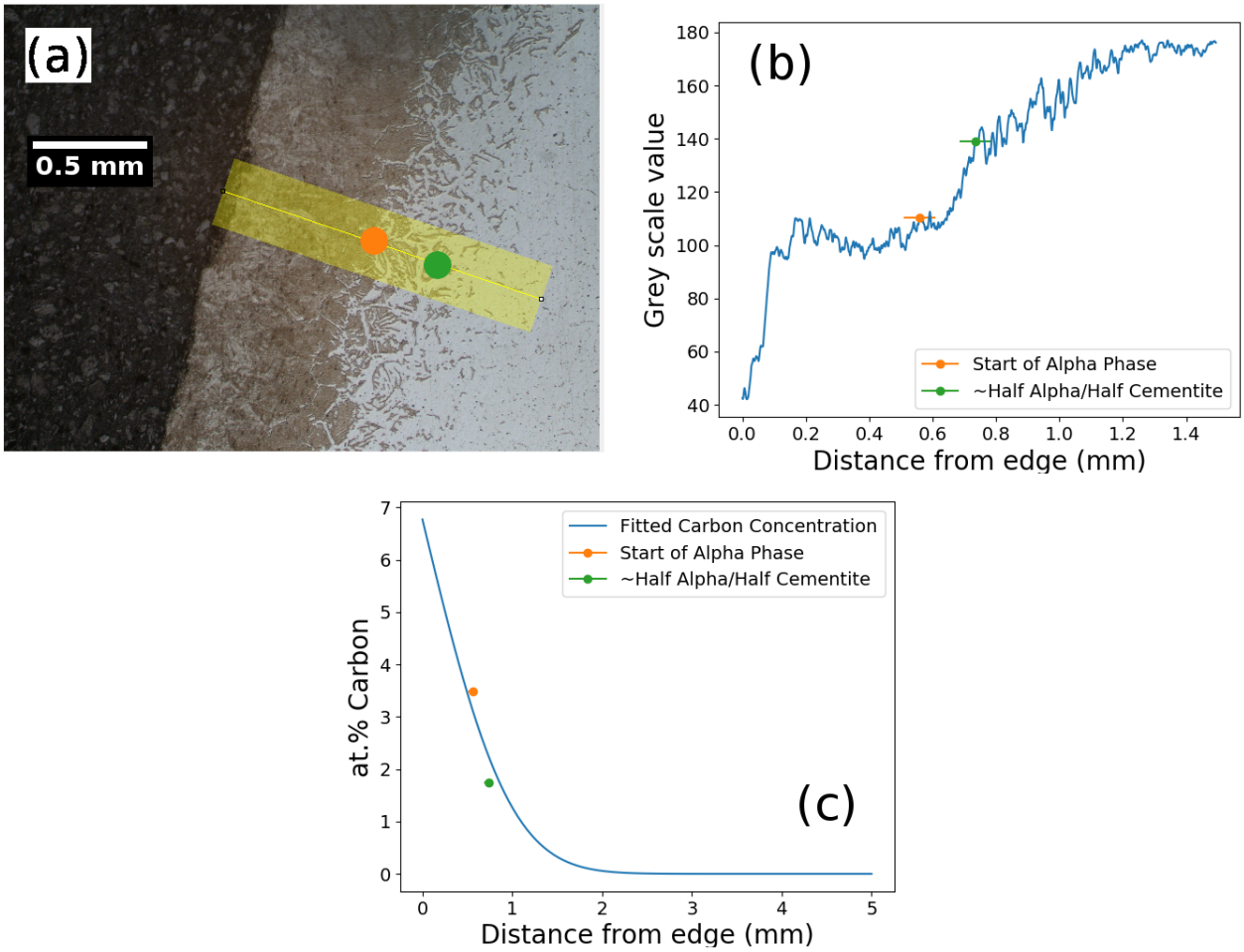


Figure 6.1: Demonstration of how the surface carbon concentration C_s was estimated. (a) Shows the position of the intensity line profile shown in (b). The orange and green circles mark the positions corresponding to the start of the appearance of the alpha phases, and where the alpha/cementite phases are approximately equally observed. (c) Shows the corresponding carbon concentrations and positions of these points, alongside the fitted concentration profile to equation 6.1 to find C_s.

$$\frac{\partial C}{\partial t} = \frac{\partial^2 C}{\partial x^2} \tag{6.4}$$

x and t are discretised, with time and space step sizes δx and δt respectively. Step sizes were chosen to be small enough to reproduce the result of equation 6.1, verified by comparing the areas under the curve (total carbon added) for both results.

For $\lim_{x\to 0}$ and using the notation $C(x_i, t_j) = C_{ij}$ where i and j are indices of the discretised x and t and using central differencing:

$$\left.\frac{\partial^2 C}{\partial x^2}\right|_{x_i,t_j} \approx \frac{C_{i+1,j} - 2C_{i,j} + C_{i-1,j}}{(\delta x)^2} \tag{6.5}$$

Similarly for $\lim_{t\to 0}$ and using forward differencing for time:

$$\left.\frac{\partial C}{\partial t}\right|_{x_i,t_j} \approx \frac{C_{i,j+1} - C_{i,j}}{\delta t} \tag{6.6}$$

Substituting into equation 6.4 gives an expression for the concentration at each x at the $j + 1$ timestep:

$$C_{i,j+1} = C_{i,j} + \frac{\delta t}{(\delta x)^2}(C_{i+1,j} - 2C_{i,j} + C_{i-1,j}) \tag{6.7}$$

The python script takes the solution of equation 6.1 as $C(x, 0)$, and iterates equation 6.7 to find $C(x, \tau)$ after the required period of time. $C(0, t)$ was set to 0 and $C(L, t)$ to C_0, simulating out diffusion from the surface and a sink at L respectively.

Combinations of T and t were explored within the temperature range 950-1200°C

for both stages. A stage one treatment of 2 hours at 1000°C followed by a 1 hour at 1100°C second stage treatment was selected, as it was found to make good use of the available radial length and produce a smooth variation of C content below the solubility limit over an experimentally accessible length scale of around 1.5mm.

The predicted concentration profile for the selected heat treatment is shown in figure 6.2.

6.2.1.2 Experimental Verification of Modelled Heat Treatments

The sample placed in a crucible and submerged in carbon powder, and then loaded into a furnace at 1000°C for 2 hours, followed by air cooling. It was then removed from the crucible and cleaned, then returned to the furnace in an empty crucible, held at 1100°C for a further 1 hour followed again by air cooling.

After both heat treatments a circular slice was taken from the centre of the cylinder and cut into quadrants, then prepared (see section 3.6.3) for analysis and irradiation. A pictorial representation of the whole process is shown in figure 6.3.

One of the quadrants was then etched using nital and imaged in an optical microscope. Micrographs were stitched together to form strips along radial directions (see figure 6.4 (a)), and analysed with ImageJ [323]. The auto local threshold tool using Sauvola and Pietikäinen's algorithm [326] was used to differentiate the regions of α-Fe and Fe_3C carbides (figure 6.4 (b)).

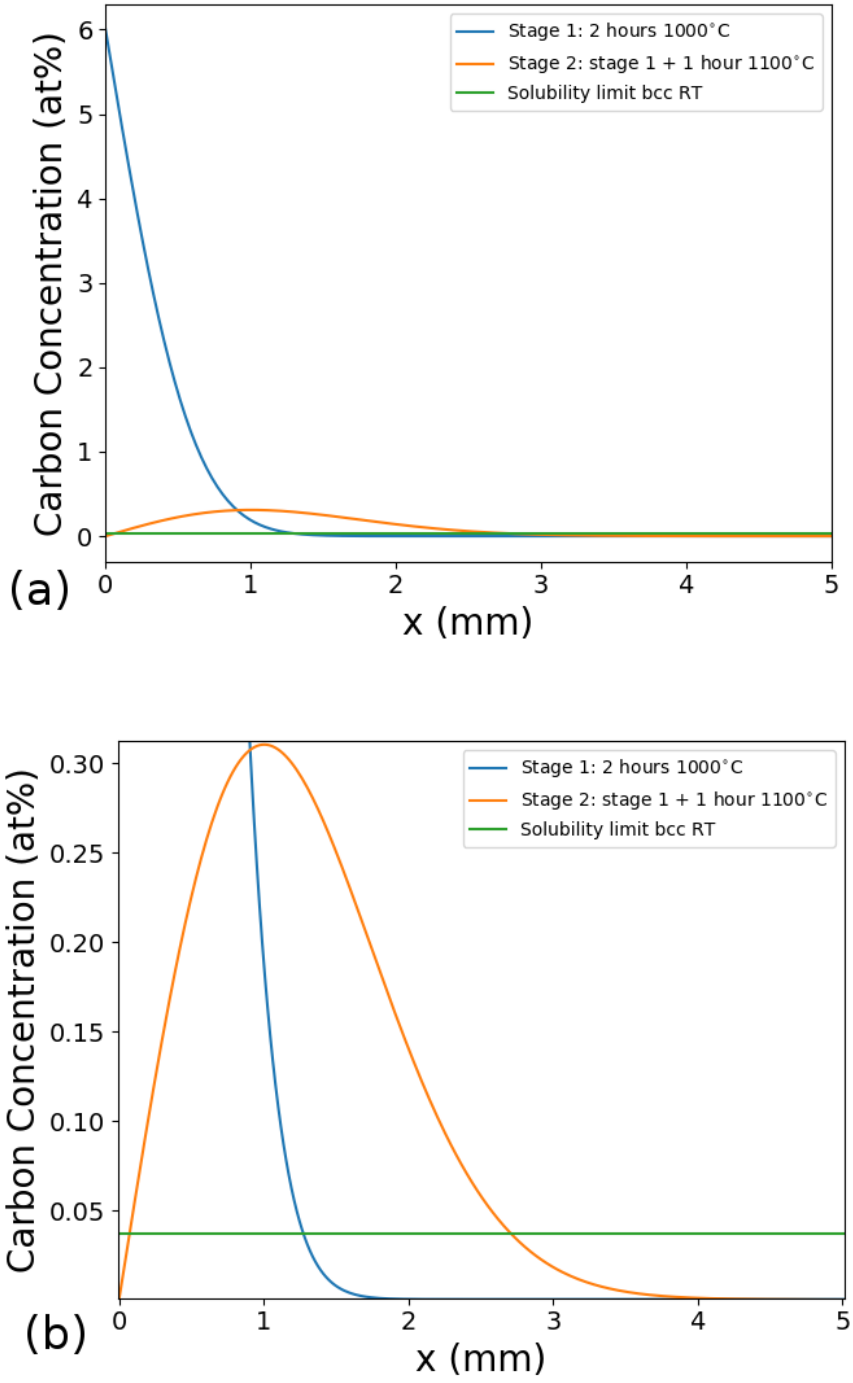


Figure 6.2: Predicted C concentration profile after the 2 stage heat treatment. (a) and (b) show the same profile at different scales.

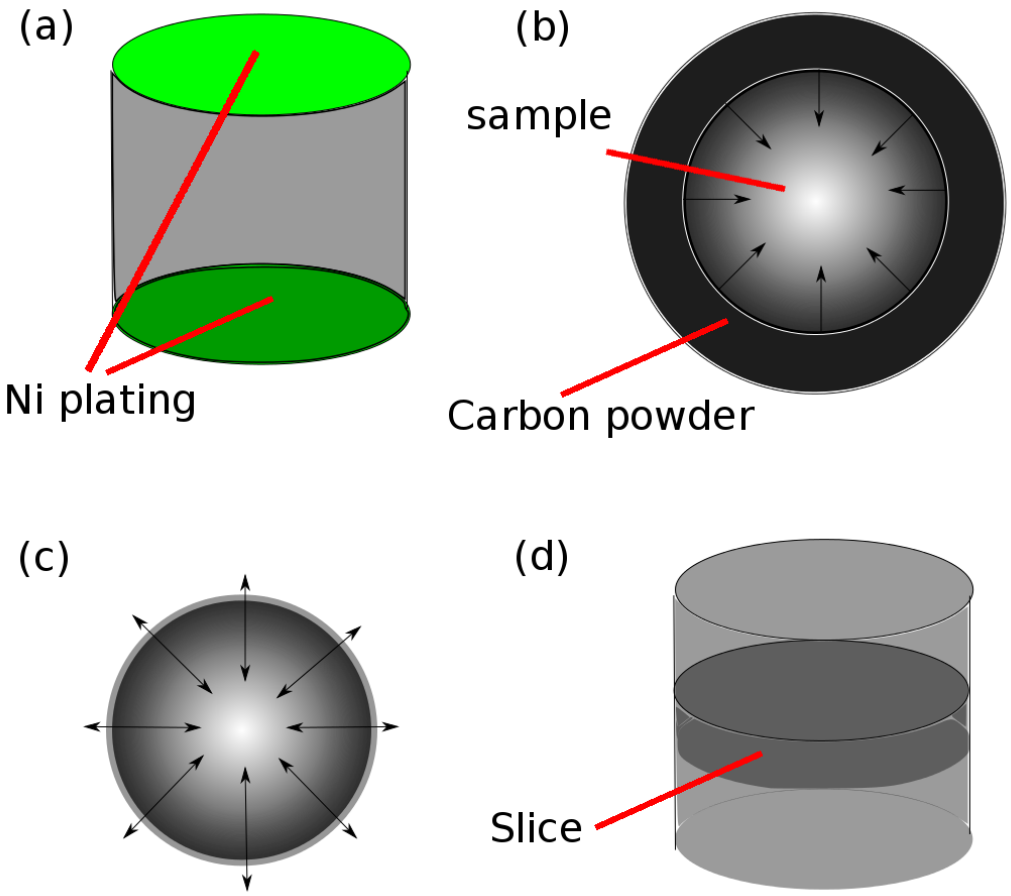


Figure 6.3: Pictorial representation of the carburisation process and sample geometry. (a) Shows the faces where Ni plating was applied to prevent diffusion from these surfaces. (b) Shows the 1st stage heat treatment, where the sample is submerged in carbon powder. (c) Shows the 2nd heat treatment in air. Arrows mark the direction of C diffusion. (d) Shows where the slice of material was cut to form samples for irradiation.

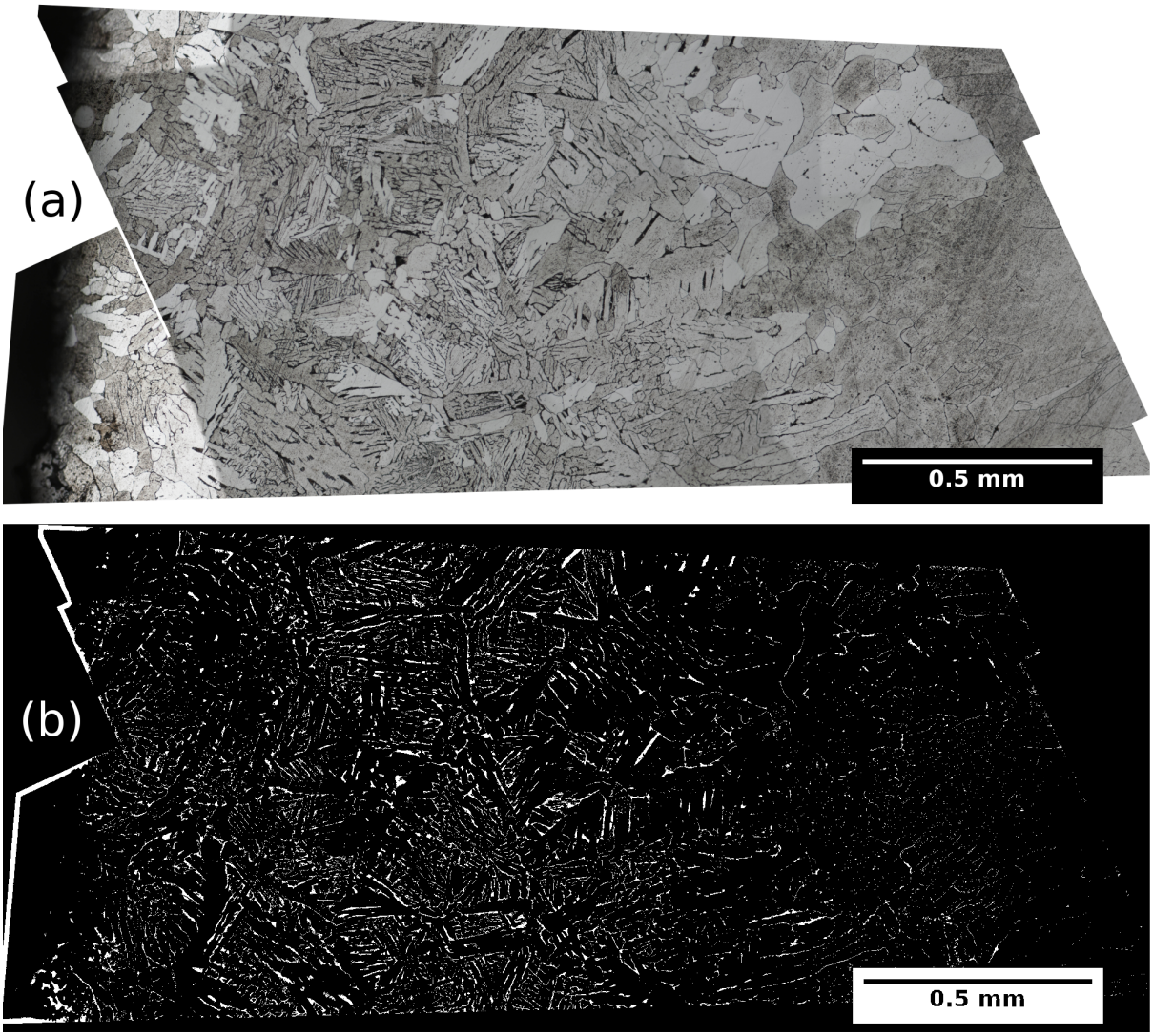


Figure 6.4: (a) Optical micrograph of a radial strip of sample after 2 stage heat treatment, polishing, and etching with nital. The curved, outer edge of the quadrant appears on the left hand side of the image. (b) shows the same image after thresholding to differentiate carbide and α-Fe regions. Carbides are shown in white.

In the thresholded images, white pixels are assigned a greyscale value of 1 and black pixels a value of 0. Each image was cropped to remove areas not containing the sample, and then divided into 100 pixel wide bins in x. The average greyscale value for each bin was taken to find the fraction of Fe_3C as a function of distance from the curved edge. The fraction of C was calculated using the atomic number densities of Fe and Fe_3C.

This process was repeated for 7 different radial strips. The shape of the carbon concentration as a function of distance predicted by the diffusion model, shown in blue in figure 6.2, was interpolated to form a function, $f(x)$ using the SciPy interp1d function [327]. A least squares fit was used to find variables a, b, and c in $C = af(bx) + c$. A fit was found for each radial strip, and an overall fit and error found by taking the mean and standard deviation of these fitted C values at a number of x positions. The data for all radial strips and overall fit are shown in figure 6.5.

The shape and extent of the measured concentration profile fits well with that predicted by the model. The positions of peak concentration are in good agreement, but the measured peak concentration of ~1.5 at.% is higher than the predicted ~0.20 at.%. This may be due to less outward diffusion of C from the free surface in the experiment than was predicted in the model.

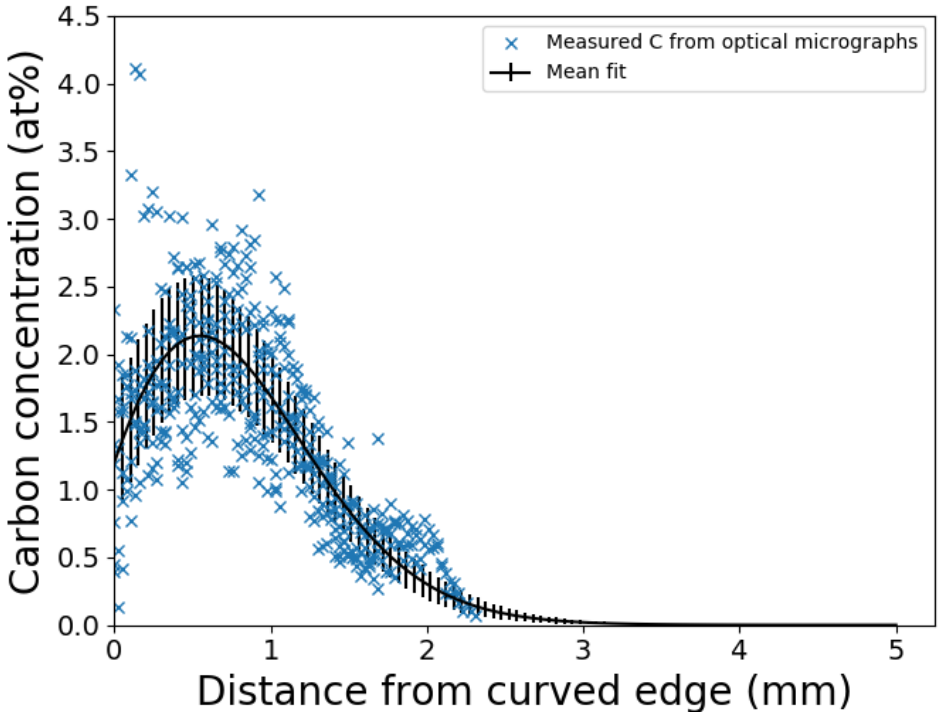


Figure 6.5: Carbon concentration as a function of distance from the curved edge of the sample measured from optical micrographs.

6.2.2 Ion irradiation

Ion irradiation was performed at the Surrey ion beam centre using the hot stage. The setup is shown in figure 6.6.

The stage was heated to 300°C and monitored using a thermocouple attached to one of the sample holders.

The sample holders partially shield the samples from the ion beam, so each sample was mounted such that half of the wedge provided an unirradiated area that has been exposed to the same temperature profile without irradiation as a reference.

Samples were irradiated using 2, 1 and 0.5 MeV Fe^+ ions to give a roughly flat damage profile of ~0.3 dpa. Two irradiations were performed using two different dose rates. Flux and fluence details are given in table 6.1. Results of the SRIM damage calculation (for details see section 3.5) are shown in figure 6.7.

Irradiation	**Temperature (°C)**	**Ion energy (MeV)**	**Fluence (/cm^2)**	**Flux (/cm^2/s)**	**Dose (dpa)**	**Dose rate (dpa/s)**
HDR	300	2.0	2.5×10^{14}	2.28×10^{11}	0.3	2.5×10^{-4}
		1.0	7.5×10^{13}	2.16×10^{11}		
		0.5	5×10^{13}	1.87×10^{11}		
LDR	300	2.0	2.5×10^{14}	1.14×10^{10}	0.3	1.2×10^{-5}
		1.0	7.5×10^{13}	1.08×10^{10}		
		0.5	5×10^{13}	9.35×10^{9}		

Table 6.1: Implantation details for high (HDR) and low dose rate (LDR) experiments.

6.2.3 Post-Irradiation Analysis

Figure 6.8 shows the sample after irradiation. The radial mark on the segment is from where the sample was clamped during irradiation, and divides the irradiated and unirradiated regions. Nanoindentation impressions and FIB milled trenches can be seen.

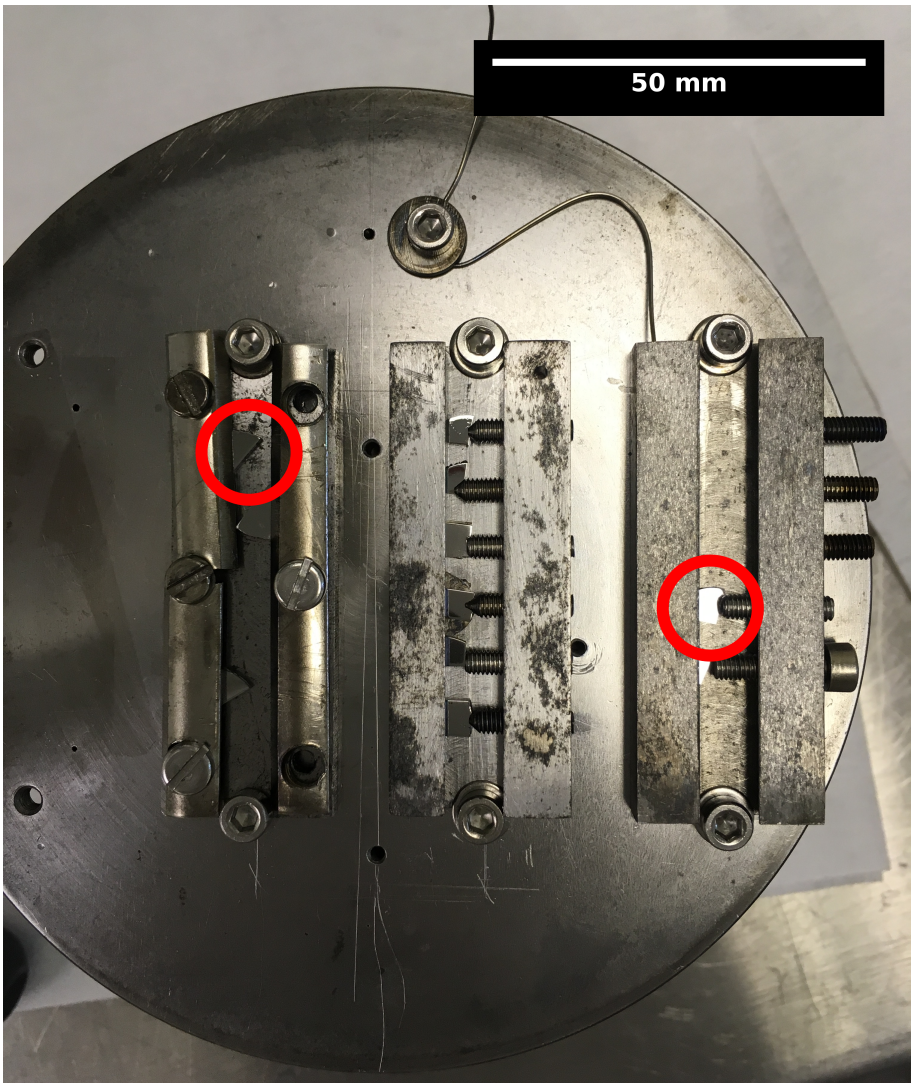


Figure 6.6: Samples mounted on the hot stage at the Surrey ion beam centre, two of which are indicated with circles. The temperature is measured using a thermocouple attached to the rightmost sample holder. Samples are partially covered by the holder, so only part of each sample is exposed to the ion beam. The covered region provides an unirradiated reference that has seen the same temperature.

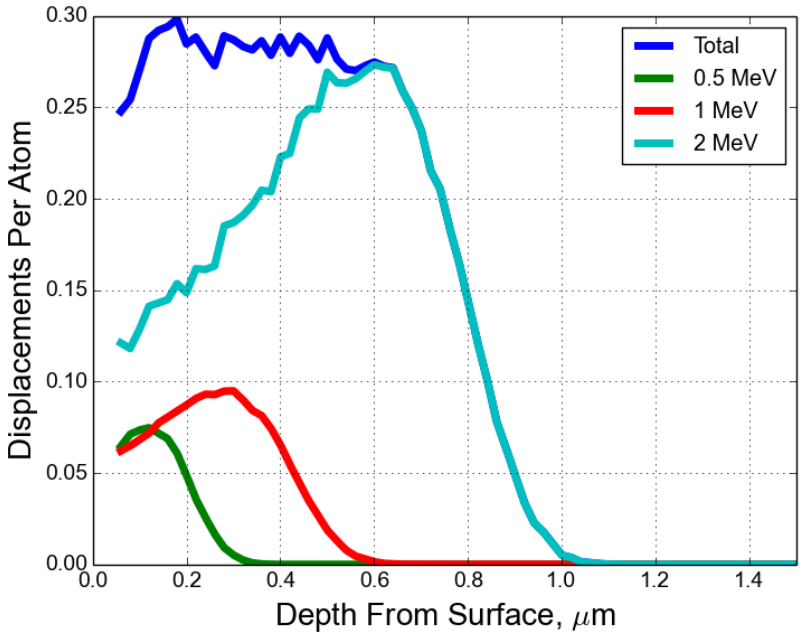


Figure 6.7: Results of SRIM calculation showing dpa as a function of depth for the irradiation conditions.

Indents were performed to a depth of 2000 nm, using continuous stiffness measurement, and a target strain rate of 0.05. A Berkovich tip was used, with the tip area function being calibrated prior to indentation of the samples, following the procedure described in section 3.1.3.3. As can be seen in figure 6.8, multiple rows of indents were made along the radial direction. The spacing between rows was 0.4 mm, and a gap of 50 μm was left between the 5 indents in the same row.

Samples were prepared for atom probe using the FIB lift-out technique described in section 3.4.4, taken from the irradiated region of peak carbon content (0.59 mm from the edge) and from a region of lower carbon content (2.05 mm from the edge), as indicated in figure 6.8. Both were performed on the lower dose rate sample. The aim of this analysis was to quantify the carbon concentration, and to look for any segregation to radiation induced defects or carbide formation.

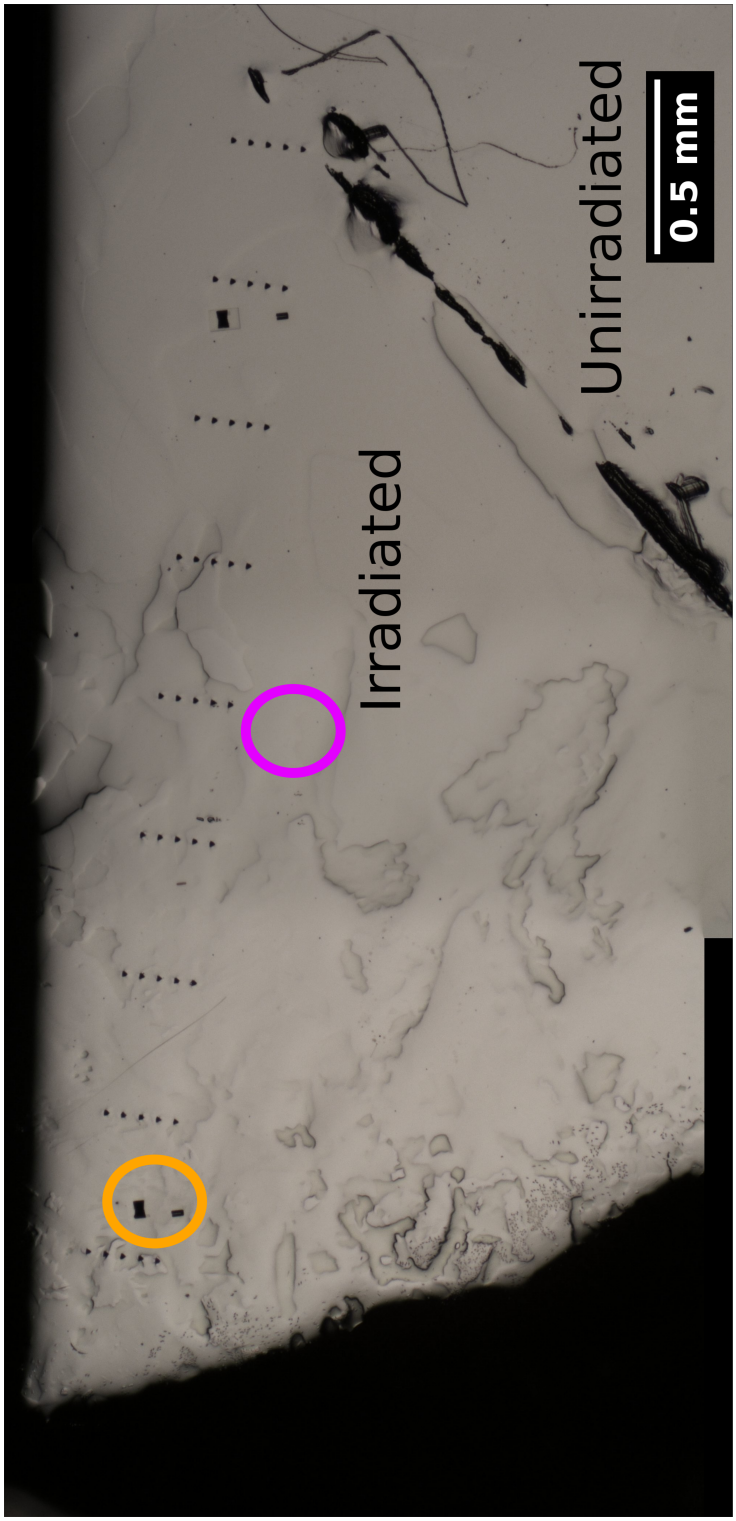


Figure 6.8: Optical micrograph of carburised Fe sample, showing array of indents in the irradiated region. The line-like mark towards the lower right of the image was made where the sample was clamped during irradiation, and divides irradiated and unirradiated regions. The rectangular features close to the indents are from FIB lift-outs. The yellow and pink circles indicate regions where APT needles were taken from.

Analysis of the atom probe tips was performed in a LEAP3000XR, using voltage mode with a pulse fraction of 0.2, a pulse rate of 200 khz, and a target evaporation rate of 0.1-0.25 %. Some tips were run at 50 K, and some at 25 K to investigate the effect of temperature on surface migration of C (discussed in section 6.3.2). Compositional analysis was performed on the tips analysed at 50 K due to the lower number of multiple hits detected at this temperature (discussed in section 6.3.1.2). Laser mode was not used due to concern that tip heating during laser irradiation could enhance surface migration.

Reconstruction of the atom probe tips was performed using IVAS 3.6.14, and the techniques outlined in section 3.4.2. Additional analysis was performed with MATLAB, with the aid of scripts from AtomProbeLab [268] for reading the .pos and .epos file data.

The ranges used to measure the number of counts of each species from the mass to charge ratio spectrum are shown in table 6.2.

Range (Da)	**Ion species**	**Range (Da)**	**Ion species**
5.98 - 6.04	$^{12}C^{++}$	17.95 - 18.04	$^{12}C_3^{2+}$
6.49 - 6.51	$^{13}C^{++}$	23.96 - 24.07	$^{12}C_2^{+}$
6.99 - 7.015	$^{14}N^{++}$	26.90 - 27.07	$^{54}Fe^{++}$
11.98 - 12.06	$^{12}C^{+}$	27.83 - 28.25	$^{56}Fe^{++}$
12.99 - 13.01	$^{13}C^{+}$	28.42 - 28.52	$^{57}Fe^{++}$
13.97 - 14.07	$^{14}N^{+}$	28.93 - 29.00	$^{58}Fe^{++}$
14.99-15.01	$^{15}N^{+}$	34.92 - 35.00	$^{56}Fe\ ^{14}N^{++}$
15.97 - 16.01	$^{16}O^{+}$	35.97 - 36.06	$^{12}C_3^{+}$

Table 6.2: Ranges and ion peak identification used in this work

6.3 Results & Discussion - Atom Probe Tomography

6.3.1 Composition

The composition of the sample at the two measured positions are given in table 6.3.1. All samples were tested at 50 K, and if present any regions of high Ga content near the surface from sample preparation were excluded from the analysis volume.

Sample position	**C**	**N**	**O**	**Ga**	**Number of Ions** ($\times 10^6$)
Peak carbon (0.59mm from edge)	0.109	0.077	0.013	0.029	5.35
Middle (2.05 mm from edge)	0.107	0.022	0.012	0.016	6.35

Table 6.3: Compositional measurement by atom probe tomography. All values in atomic %. Balance is Fe.

The carbon and nitrogen contents as a function of position are additionally shown in figure 6.9, alongside the carbon concentration profile measured using optical microscopy. The APT analysis found the carbon concentration to be the same at both positions, while the nitrogen concentration was measured to decrease with increasing distance from the edge.

The difference between the carbon concentration measurements by optical microscopy and APT are due to the different sizes of analysed volumes between the two techniques. The optical microscopy method measures the carbon concentration averaged over the whole visible area, which includes regions of α-Fe (ferrite) and carbide (Fe_3C), whereas a much smaller volume is analysed in APT. No carbides were found in the volume analysed by APT, indicating that these measurements were made in regions of ferrite, where carbon is in solution. Both measurements are close to the solubility limit - indicating the matrix may be saturated with C in these regions.

For the discussion of the irradiation induced hardness changes (section 6.4), it is argued that the in-solution carbon concentration is the important factor.

Factors affecting the measurement of carbon by APT are discussed in the following sections, but values above the solubililty limit measured here may suggest the concentration is overestimated in this analysis.

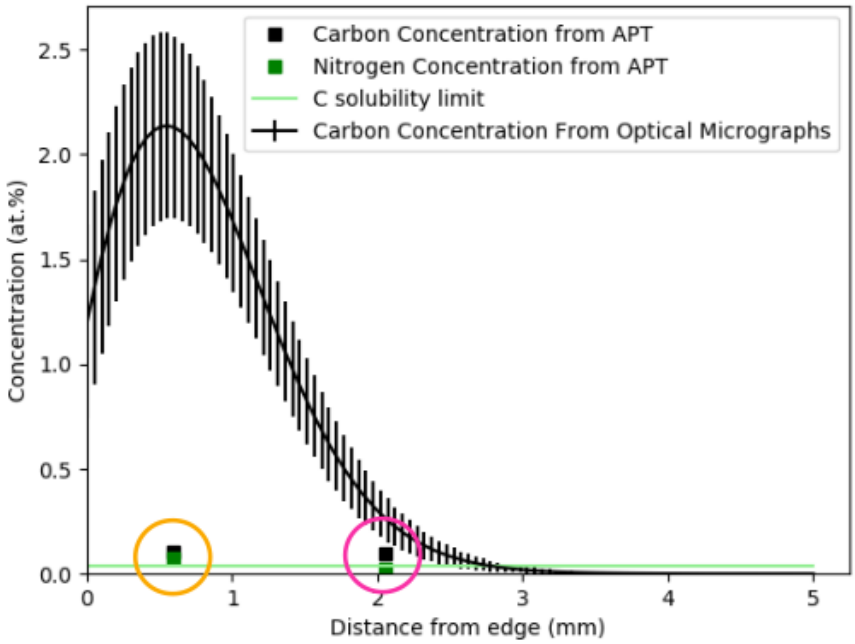


Figure 6.9: Compositional measurement by atom probe tomography as a function of position. The coloured circles indicate the region where the analysed tips were taken from, as in figure 6.8

6.3.1.1 Peak Overlaps

The measured compositions are affected by the identification of ions in peak overlaps, where different ions have the same mass to charge ratio.

For nitrogen, peak overlaps occur at 14 Da for N^+ and N_2^{++}, and at 28 Da for $^{56}Fe^{++}$

and N_2^+. Sha et al. [328] proposed a mechanism to resolve these peaks using an Fe-N sample enriched with ^{15}N, utilising this second isotope. It was found that around 3% of the 14 Da was due to N_2^{++}, and that around 26% of all N ions evaporated as N_2^+ and overlap with $^{56}Fe^{++}$ [329].

The natural isotopic abundance of ^{15}N is only 0.37% [328], and so an insufficient number of these ions were detected in this work to perform a similar analysis. Sha et al.'s [328] samples were tested with voltage pulsing using a pulse fraction of 0.2 at a temperature of 65 K - a higher temperature than the 50 K used in this work. These measured N species ratios were not used to deconvolute the peak overlaps, due to uncertainty about their sensitivity to temperature.

For carbon, the most significant peak overlap occurs at 24 Da between C_2^+ and C_4^{++} [328, 330]. This can be resolved by examining the counts around 24.5 Da, due to $(^{12}C_3{}^{13}C)^{++}$. These ions should constitue 4.29% of all C_4^{++} ions based on natural isotopic abundance [328], and so can be used to calculate the number of counts at 24 Da due to $^{12}C_4^{++}$.

The mass spectra around 24 and 24.5 Da for single, multiple, and all hits for a representative sample is shown in figure 6.10.

No peak can be clearly identified at 24.5 Da, and is certainly lower than 5 counts. 5 counts of $(^{12}C_3{}^{13}C)^{++}$ would mean a contribution of around 10% of the counts at the peak at 24 Da would come from C_4^{++}.

This is significantly lower than ~50% measured by Sha et al. [328] (voltage pulsing with pulse fraction 0.15 at 60-80K), and Kitaguchi et al. [330] who found values of between 64-76 % of counts for laser pulsing, and it to vary with pulse energy and temperature.

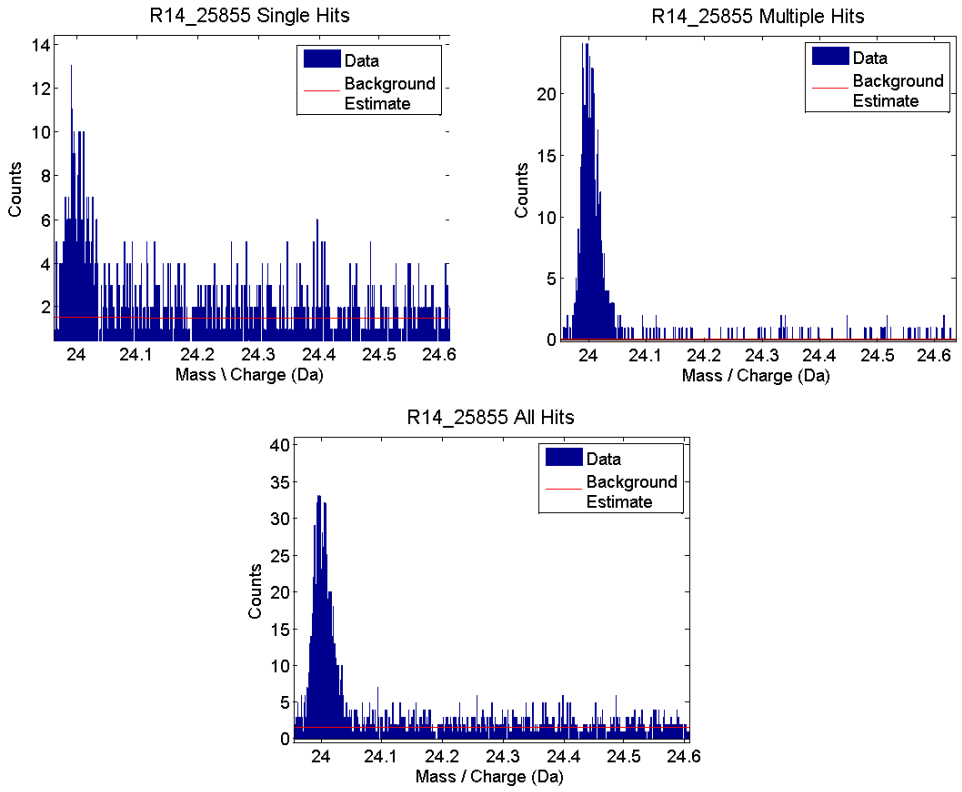


Figure 6.10: Mass spectra around 24 and 24.5 Da for single, multiple and all hits for sample R14_25855.

These observations suggest that either the occurrence of C_4^{++} is a strong function of pulse fraction and temperature for voltage pulsing (50K and 0.2 were used in this work), or that it is a strong function of local composition. In the sample in this work where the carbon concentration was significantly lower than in [328] (Fe-C, 7.89 at.%) and [330] (cementite, 25 at.%), the concentration on the tip surface may rarely have reached levels where C_4^{++} evaporation would become significant.

6.3.1.2 Multiple Hits

In the ideal atom probe experiment each atom is field evaporated from the tip surface and detected one at a time. In reality however, a single pulse may cause the field evaporation of multiple ions which then arrive at the detector only a short time apart.

If two (or more) ions arrive too close together in time and space, the detector cannot resolve them and only records a single hit and the other ions are lost. This is referred to as detector pile-up, and affects simultaneously evaporated ions with the same mass to charge ratio, that arrive at the detector at the same time. It can lead to biased loss for certain species and should be minimised for accurate compositional measurement.

The dataset *R14_25855* - taken from the peak carbon region, containing 6.6×10^6 ions and tested at 50 K - was used to analyse the impact of multiple hits on the data collected in this work.

The length of time between which detector events cannot be resolved is called the dead time, and is dependent on the instrument. This was measured by plotting a histogram of the differences in time of flight between consecutively detected ions in the same multiple hit detector event. This is shown in figure 6.11, where it can be seen that no events were detected less than ~4 ns apart - indicating the detector dead time.

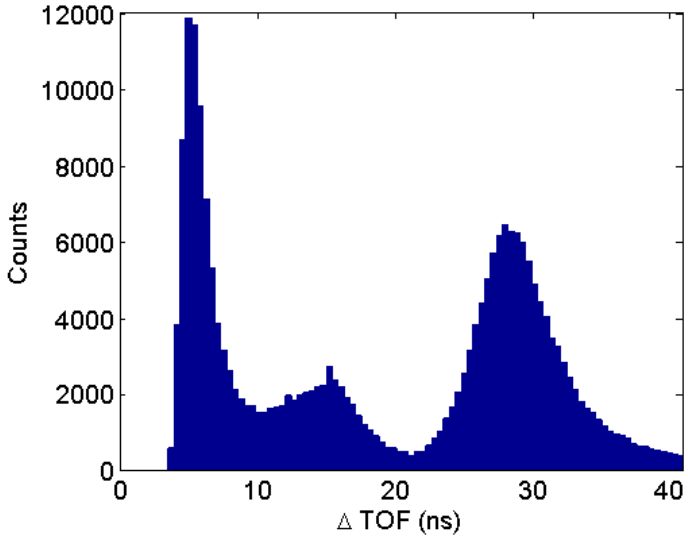


Figure 6.11: Histogram of raw time of flight differences between ions detected in the same multiple hit event.

The situation is complicated in the case of instruments fitted with a reflectron (a device to minimise time of flight differences for ions evaporated with different kinetic energies) as in the present case - where the flight path length, and so the time of flight, varies with detector position. This effect is illustrated in figure 6.12, where the time of flight for $^{56}Fe^{++}$ ions is plotted as a function of detector position.

$^{56}Fe^{++}$-$^{56}Fe^{++}$, and C^{++}-C^{+} pairs were however found to be spatially well correlated, as shown in figure 6.13 where differences in detector x and detector y position are plotted for pairs of ions detected sequentially in the same event. The influence of the reflectron on TOFs can be therefore be assumed to be small.

Carbon is known to commonly be detected in multiple hits [331], and is therefore more prone to being lost due to detector pile-up than other elements. The number of carbon atoms detected as single hits, and in multiple hits containing different numbers of carbon atoms is shown in figure 6.14. It can be see that carbon is preferentially detected in multiple hit events, and that most of these events contain more than one carbon atom.

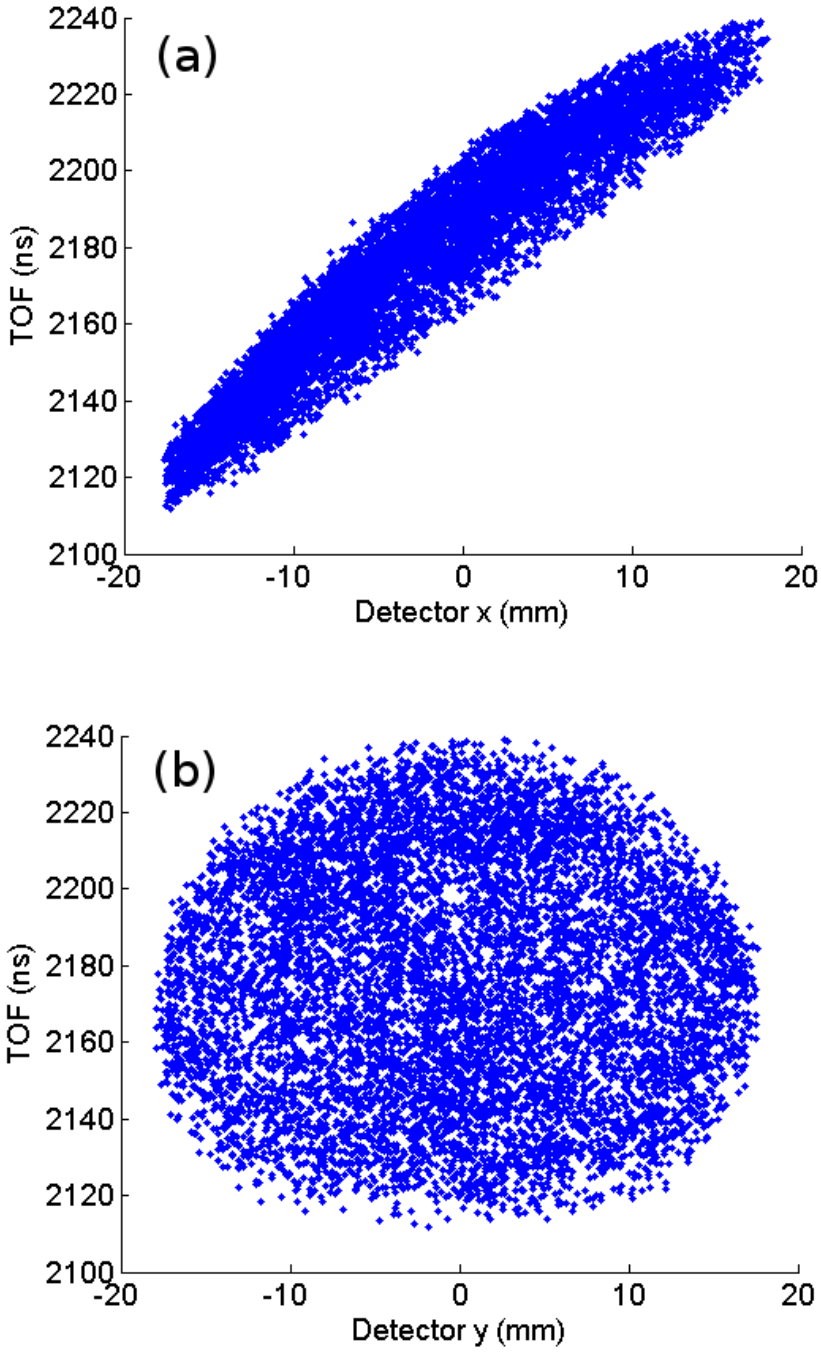


Figure 6.12: Time of flight as a function of (a) x and (b) y detector position for $^{56}Fe^{++}$ ions collected at a standing voltage of between 3 and 3.05 kV.

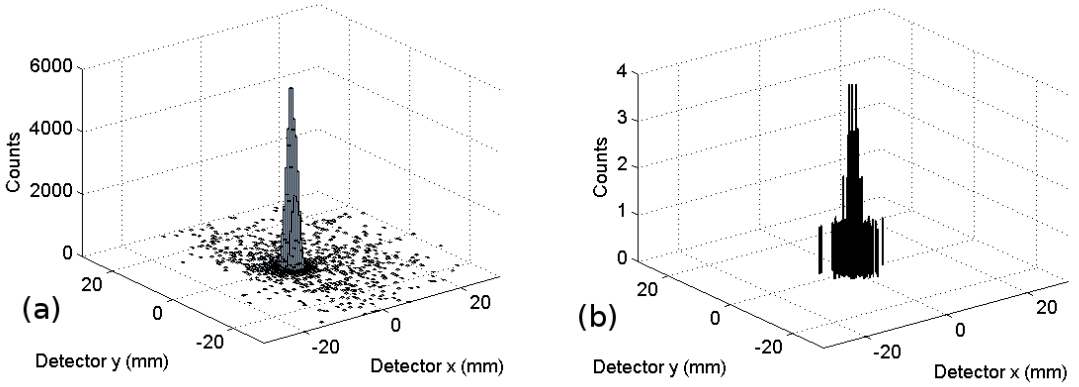


Figure 6.13: Differences in detector coordinates for (a) ^{54}Fe-^{56}Fe and (b) C^{++}-C^{+} pairs detected sequentially within the same multiple hit event.

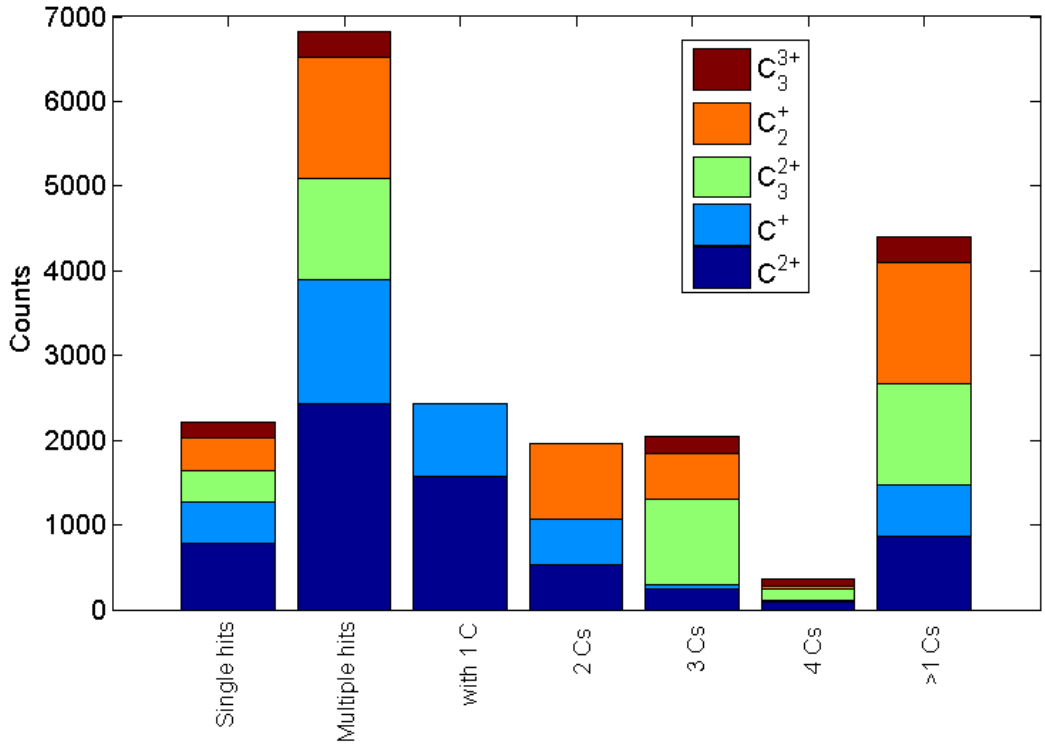


Figure 6.14: Number of carbon atoms detected, and in which species, for single and multiple hit detector events. The multiple hit detector events are also subdivided based on the number of carbon atoms detected in the event. E.g. 2 Cs denotes multiple hit detector events where two carbon atoms are detected.

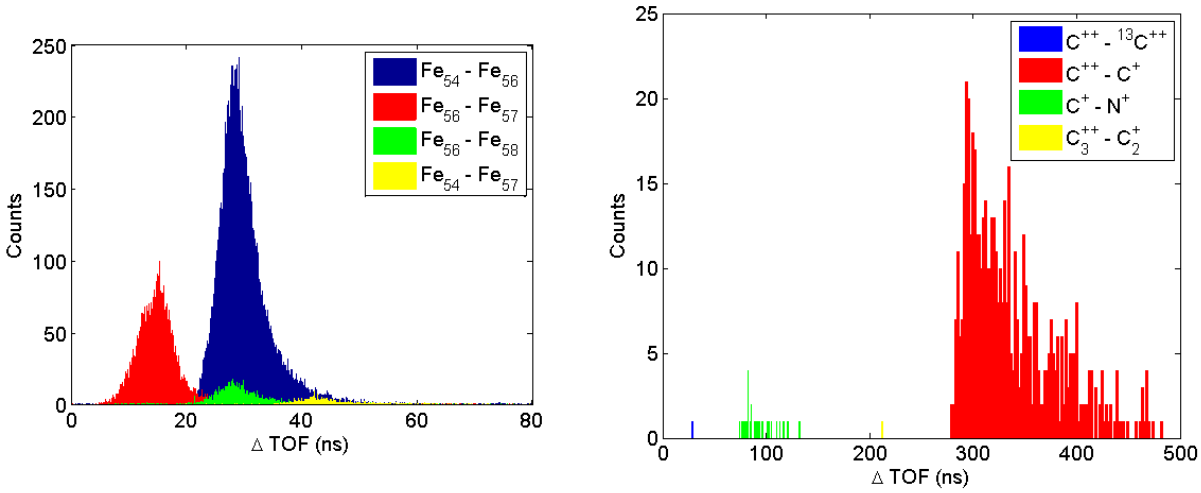


Figure 6.15: Raw time of flight differences for a selection of ion pairs. The applied voltage range is 2.3 - 6.4 kV

Figure 6.15 shows the difference in raw time of flights for different common species pairs. All pairs have time of flight differences longer than the detector dead-time, so only pairs with the same mass to charge ratio should be affected by detector pile-up.

Fe was also observed to be detected in multiple hit events (7.7% of detected Fe was detected in multiples in this dataset), and so is also susceptible to loss due to detector pile-up. The most abundant isotope is ^{56}Fe [332], and so is the most likely to evaporate in a same isotope - same charge pair, leading to ion loss. This preferential loss of ^{56}Fe can be seen as a lower measured fraction of this isotope than the natural abundance [332]. By comparing the measured number of ions of this isotope to that expected based on the measured number of other isotopes, a difference of between 680 000 and 950 000 ions is found in this dataset depending on the isotope used. This represents a significant proportion of the 6 200 000 Fe ions detected.

This compares reasonably well with the number of $^{56}Fe^{++}$-$^{56}Fe^{++}$ pairs expected from natural abundance and the measured number of non-same isotope pairs, and as-

suming only 2+ ions occur. Greater than 99.97 % of Fe ions were in the 2+ charge state in this dataset. Values for the expected number of 56-56 pairs (of which one ion is lost due to detector pile-up) varied between 640 000 and 760 000 are found depending on the isotope pair used.

A similar analysis for C is more challenging as a wider range of molecular ions and charge states are present, and their relative abundances are not easily found and may depend on experimental and local compositional factors. Indeed, the fraction of C detected in molecular ions was found to increase with increasing tip temperature in Fe-C [333, 334], to be greater for laser pulsing than voltage pulsing in WC [335], and to increase with increasing laser pulse energy in cementite [330].

In Kitaguchi et al.'s [330] study on the effect of laser pulse energy on the measured composition of cementite, it is argued that changes in the relative loss of Fe and C due to multiple hit effects are responsible for the observed differences in the measured composition.

Nitrogen concentration measurement may also be affected by this mechanism [336]. There is insufficient data and detailed understanding of the field evaporation processes for carbon and nitrogen and their sensitivity to experimental conditions to confidently deduce the relative proportions of molecular species and charge states required to estimate the relative losses of each due to detector pile-up using this combinatorics approach. Further work is required in this area.

In the present study the composition may be under or over estimated due to this effect, but relative measurements at different positions should remain comparable as the same experimental conditions were used.

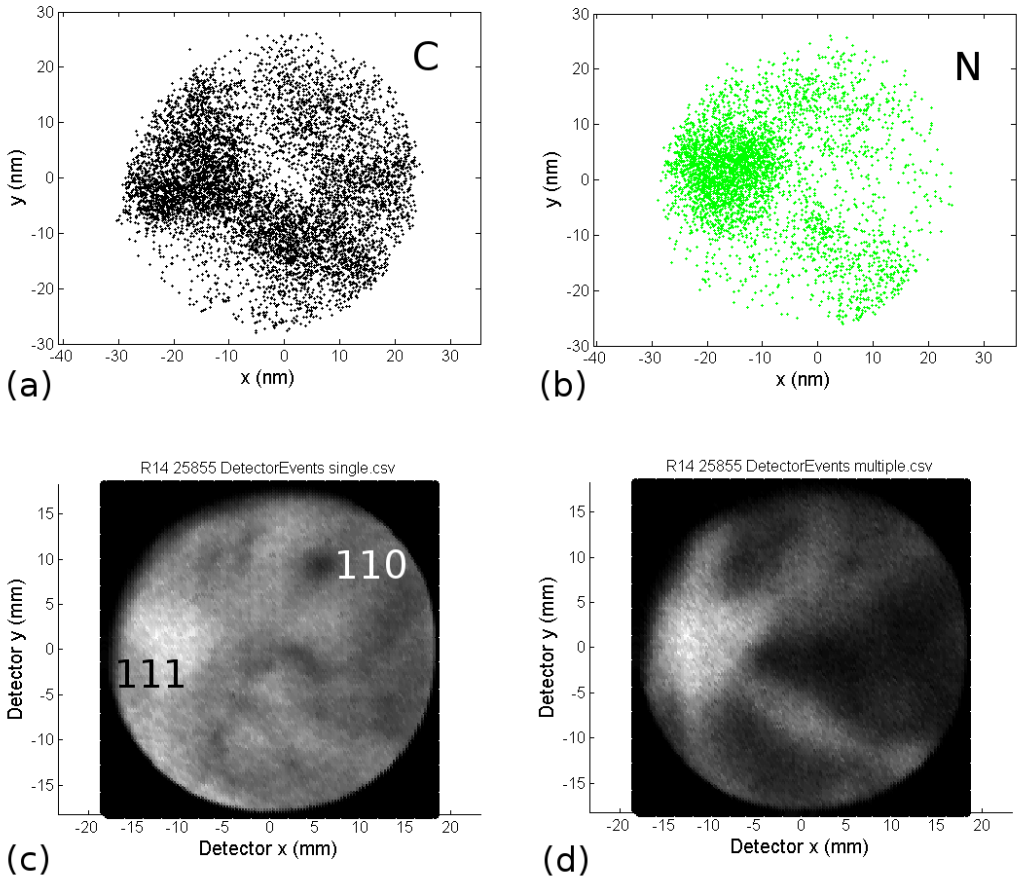


Figure 6.16: (a) and (b) show the reconstructed x and y positions of C and N for a tip from the peak C region, analysed at 50 K. (c) and (d) show the detector hit map for single and multiple hits respectively. Details of the pole indexing can be found in section 3.4.2.

6.3.2 Spatial Distribution of C

In all tips analysed, C and N ions were found to be preferentially located around major crystallographic poles and zone lines, as shown in figures 6.16 and 6.17 for samples tested at 50 K and 27 K respectively. Similar observations have been reported in other ferritic steels [294, 333, 337], and in those studies, changes in experimental parameters (temperature and pulse fraction) were also found to make little difference to the observed spatial distribution of the ions.

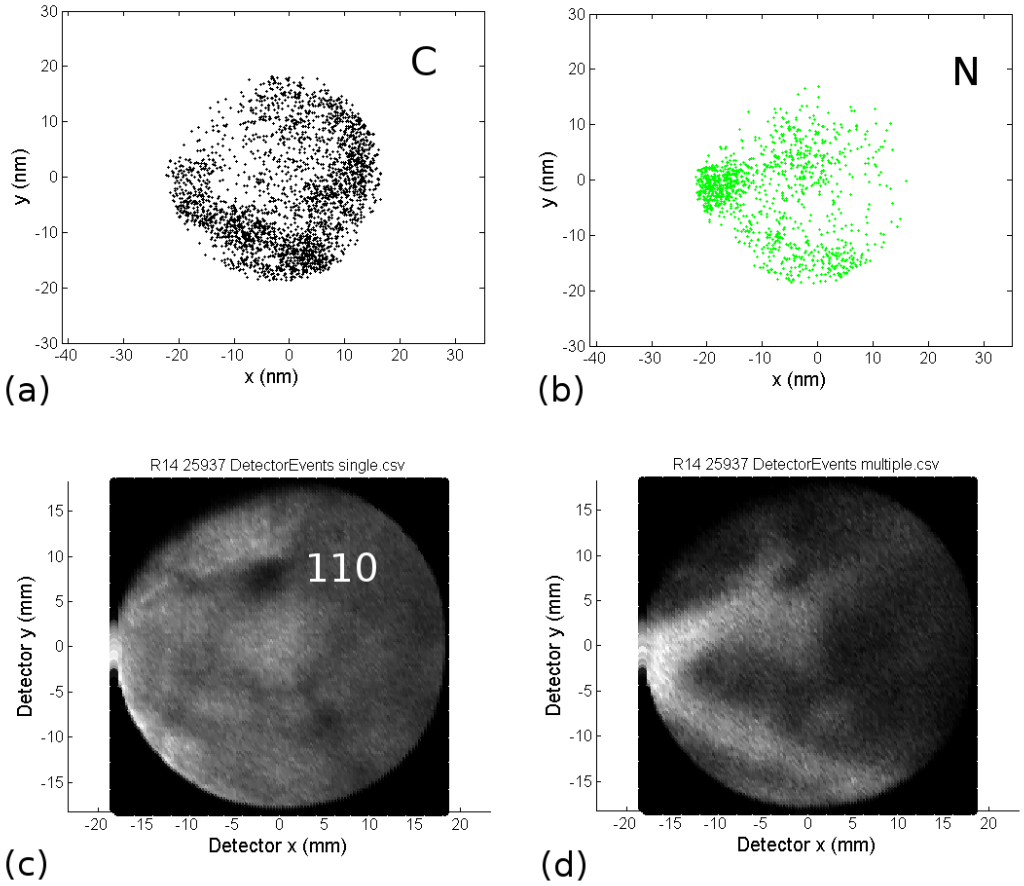


Figure 6.17: (a) and (b) show the reconstructed x and y positions of C and N for a tip from the peak C region, analysed at 27 K. (c) and (d) show the detector hit map for single and multiple hits respectively. Details of the pole indexing can be found in section 3.4.2.

Kobayashi et al. [333] and Gault et al. [337] both found no correlation between the position and form of C detected (single or molecular ion) for any temperature. Kobayashi et al. [333] did however find that the fraction of C evaporated as molecular ions increased with increasing temperature, as did Takahashi et al. [334]. This is said to be due to C ions meeting on the tip during surface migration, and the authors argued this meant that this showed that more surface migration occurred at higher temperatures, and so surface migration could not be the primary reason for the observed spatial distribution and that trajectory aberrations were likely the cause.

However, the relative ratios of different carbon species may be controlled by factors other than the degree of surface migration. For example Yao et al. [338] found the specimen temperature to change field distribution on the tip, evidenced by blurring of crystallographic features in hit maps at increased temperatures, which may affect the C species produced. Thuvander et al. [335] found a higher proportion of C evaporated in molecular species in WC when analysed with laser mode compared to voltage pulsing. No surface migration is observed in this material. Similarly, outside of atom probe tomography different carbon species spectra were observed from high voltage vacuum discharged [339] and N_2 laser ablated [340] graphite [341], showing that temperature driven surface migration is not the only factor which affects the relative populations of C species produced.

Yao et al. [294] and Gault et al. [337] argue that because carbon has a high evaporation energy [342] it is preferentially retained on the tip surface, and moves to regions of higher field strength by thermally-assisted electric field gradient driven migration [343] before evaporating.

This phenomenon reduces the spatial resolution for affected elements, and may limit the technique's ability to image their segregation at microstructural features - the main objective of this analysis in the present work.

Reference	Material	Irradiating species	Temperature (°C)	Dose (dpa)	Dose rate (dpa/s)	Loop number density ($\times 10^{-21}$/m^3)	Mean loop size (nm)
[218]	Fe	neutrons	300	0.19		6.0±1.8	10.2±0.3
[41]	Fe	neutrons	300	0.1		1.2	8.5
[154]	Fe-5Cr	self ions	300	0.3	3×10^{-4}	16.1	6.7
					1.5×10^{-5}	9.72	6.5

Table 6.4: TEM observations of similar irradiations.

Reported loop number densities and mean sizes for Fe and Fe-Cr alloys irradiated under similar conditions from the literature are shown in table 6.4.

The total volume analysed by atom probe in this work was around 1×10^{-21}m^3, so based on the literature observations in table 6.4 it would be reasonable to expect to find at least one dislocation loop in this volume. The results of nanoindentation testing are discussed in section 6.4.2, but the higher hardness observed for higher carbon concentrations may suggest a higher loop number density is present than for pure Fe - making finding a loop more likely. TEM analysis would be required to confirm this.

Segregation of C to line dislocations and grain boundaries is commonly observed with APT (eg. [295, 344, 345]), but preferential retention on the tip surface due to carbon's high evaporation field [342] can lead to a smearing of the boundary along the analysis direction [346]. A combination of this effect, the relatively low concentration of C meaning few such atoms may be present at each loop, and the likely small size of the dislocation loops may make it very difficult to confidently identify whether or not they are present.

Prior TEM analysis of tips to identify loops would clearly demonstrate whether their presence and any C decoration is detectable by atom probe in these samples.

6.3.3 Nitrogen

An N-rich feature was identified in a tip prepared from the region of peak carbon content, and is shown in figure 6.18. The tip was tested at 27 K. The crystal orientation of the plane of the loop was calculated using methods outlined in section 3.4.3, and the stereographic projection of the plane normal is shown in figure 6.19.

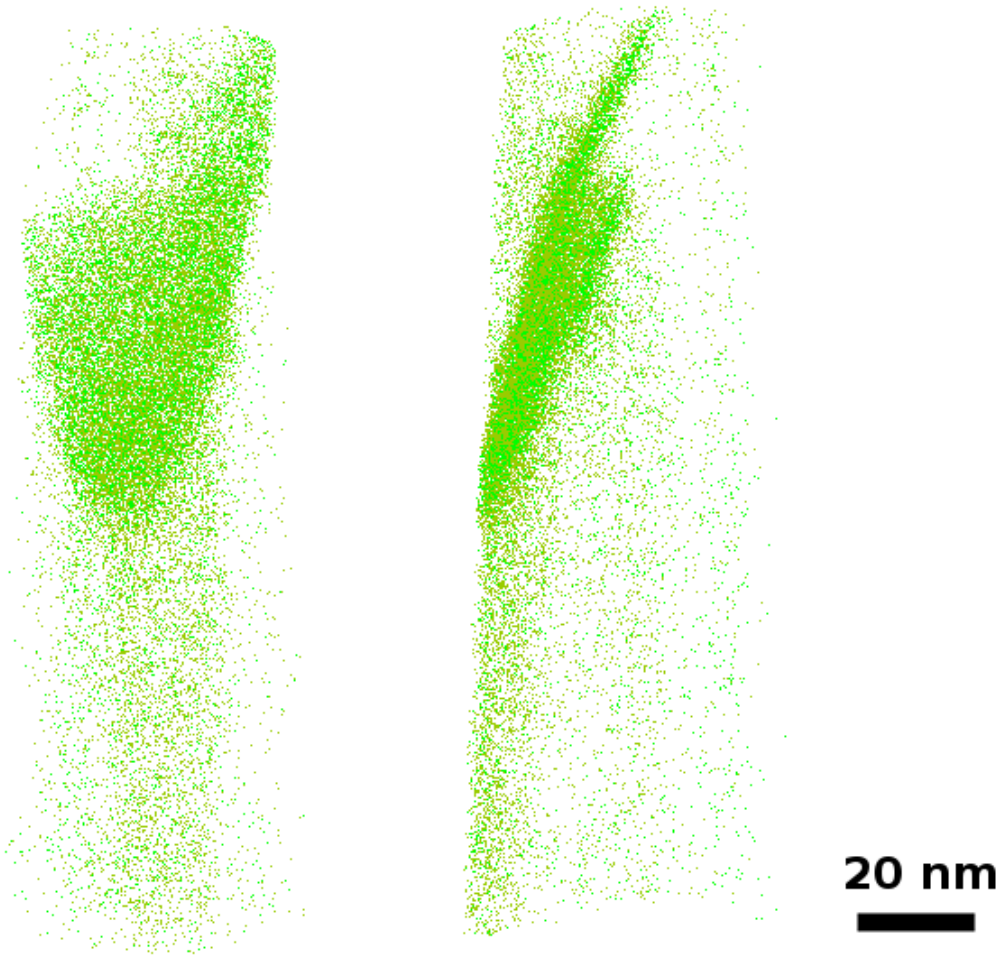


Figure 6.18: Reconstruction showing a nitrogen-rich feature from two views. Only N^{+} (14 Da) and FeN^{++} (35 Da) ions are shown.

The feature is planar, and so could be a grain boundary. However, no difference in the hitmap for ions collected before and after the feature was observed, indicating the crystallographic orientation was the same either side of it.

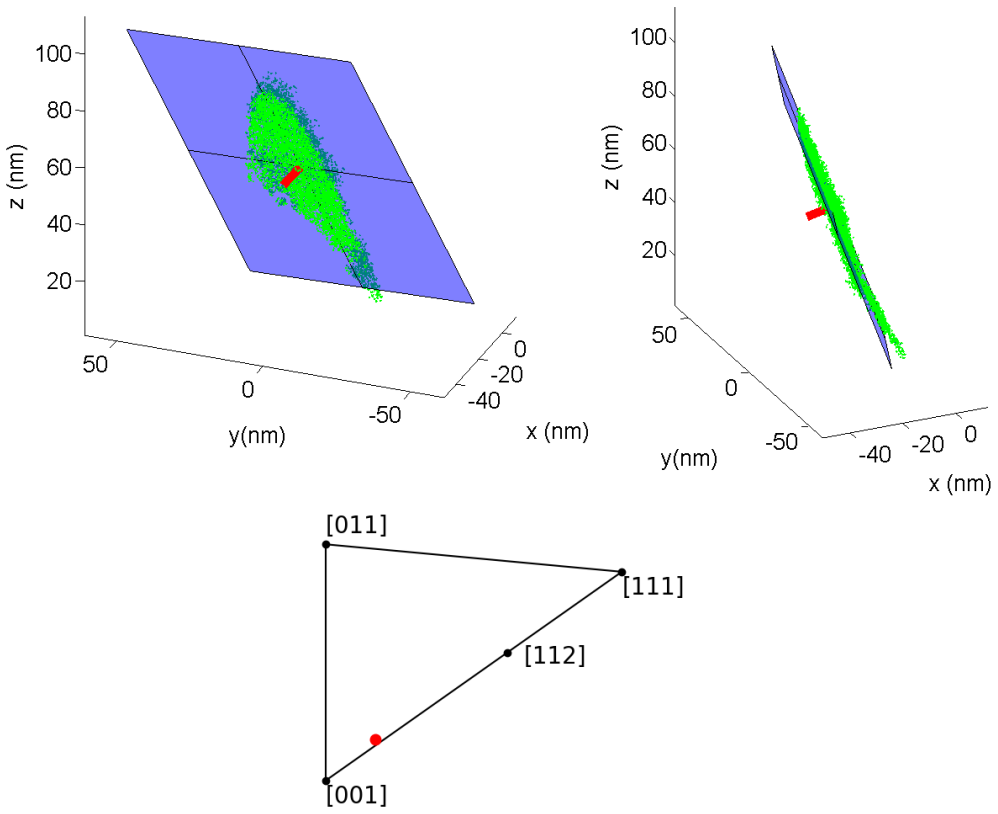


Figure 6.19: Plane fitting and stereographic projection of the plane normal of the N-rich feature, marked in red. A 1% N concentration isosurface was used to isolate the feature.

A second possibility is that it is a dislocation loop. Nitrogen is thought to behave similarly to carbon with regards to radiation damage in α-Fe, and may also interact with dislocation loops [347, 348]. The measured plane is close to {100}, and would be consistent with being a <100> loop [300]. However, given that it is much larger (at around 60 nm at its widest point) than the loops reported for similar irraditions (table 6.4), this would seem unlikely. Its appearance also differs from the loops observed in the work in chapter 5 (figure 5.23), where only the outline was found to be decorated.

The third possibility is that it is a nitride. The feature was found to contain 4.40 at.% N, most consistent with an $Fe_{16}N_2$ nitride (11.1 at.% N) [349]. These nitrides occur as disks on {100} planes [349], also consistent with the present observations.

The lower N composition may be due to N lost in detector pile-up caused by multiple hits (see section 6.3.1.2). Another factor could be trajectory aberrations due to differences in electric field between the precipitate and the matrix [277, 350], which has the effect of Fe outside of the precipitate appearing to originate from within it, leading to an artificially high Fe content being measured. There also exists an N-deficient $Fe_{16}N_2$ transition nitride, which transforms to the perfect nitride with further aging [336].

The composition of the alloy prior to carburisation is given in table 3.1 in section 3.6. The N concentration is stated as 4 appm. This is much lower than the 0.077-0.022 at% measured by APT in the carburised sample (table 6.3.1). Both the presence of the nitride, and the measured decreasing N concentration with increasing distance from the edge of the sample suggest that nitrogen was introduced during the carburisation process - most likely during the second stage where the sample was exposed to air. This was unforeseen and unfortunate, as N also interacts with point defects in Fe [102, 105, 351, 352] and may influence the mechanical properties after irradiation [347].

The concentration of N was measured to be lower than that of C, and should be expected to be lower still at greater distances from the exposed edge, but may still have an influence on the post irradiation microstructure and mechanical properties.

6.3.4 Carbon Contamination

Recently there has been much concern over the possibility of unintended carbon implantation during heavy ion irradiation [130–132]. Although no quantification of the amount of carbon unintentionally implanted was made in this work, the results of nanoindentation testing would suggest that any amount should be low compared to that added intentionally by carburisation. In figure 6.21, a clear effect of carbon on post-irradiation hardness is observed for all regions, even where the amount added by carburisation is only calculated to be around 0.01 at% and below.

Additionally, no difference in contrast in the FIB/SEM was noted between irradiated and unirradiated regions, which is sometimes observed and due to carbon contamination of the surface during irradiation.

It was however found that carbon could be implanted in the FIB during APT needle preparation. In samples where siginifcant quantities of Ga could be detected near the tip apex (due to insufficient final polish with 5 keV ions), higher concentrations of C were also found. An example depth composition profile for such a tip is shown in figure 6.20.

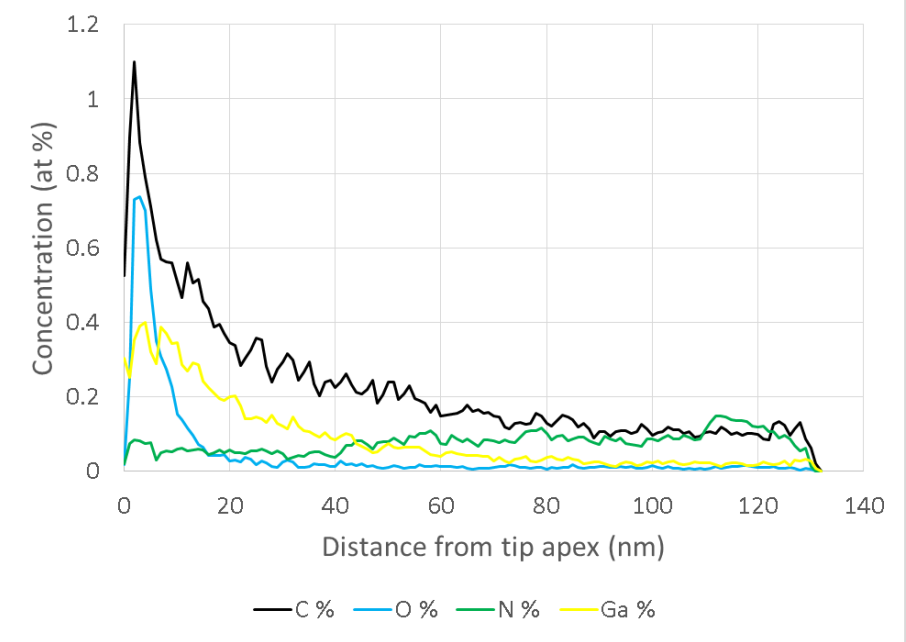


Figure 6.20: Concentration of minor elements as a function of depth for a sample with significant Ga concentration from FIB preparation. This near surface region was not used for compositional analysis.

It can also be seen that this region is depleted in nitrogen. Langelier et al. [353] found Fe-Mn-N samples prepared by FIB to have lower N concentrations than those prepared by electropolishing, and suggested this could be due to heating during preparation leading to N diffusing to the sample surface and outgassing.

Any near surface regions showing elevated Ga content were not used for composition analysis.

6.4 Results & Discussion - Nanoindentation

Results of nanoindentation testing are shown in figure 6.21. For each indent, the hardness at an indenter penetration of 200 nm was measured and plotted, along with the average for all indents in each row. This depth was chosen to avoid the region of surface and strong size effects at low depths, but low enough so that the main plastic zone of the indent is confined to the irradiated layer (around 5 times the indentation depth in irradiated Fe-Cr alloys [278]). An optical micrograph of a non-irradiated quadrant etched with nital is also shown, so that the microstructure at each position can be seen.

In the unirradiated regions, the hardness remains constant with increasing carbon concentration until it reaches a point where significant carbide formation can be seen, at a distance less than around 1 mm from the edge of the sample. The value of hardness measured for these low C concentrations is in good agreement with that measured in the unirradiated pure Fe.

In the irradiated regions however, the hardness increases with increasing (modelled) carbon concentration throughout the whole sample. There is no observable difference between samples irradiated at high and low dose rates for any carbon concentration. The hardness at the lowest measured carbon concentration corresponds well to that measured in pure Fe.

6.4.1 Unirradiated Behaviour

Carbon in solution adds strength to Fe and steels by forming Cottrell atmospheres around dislocations [15]. The dislocation becomes locked, and an additional stress is required to remove the atmosphere before the dislocation is free to move.

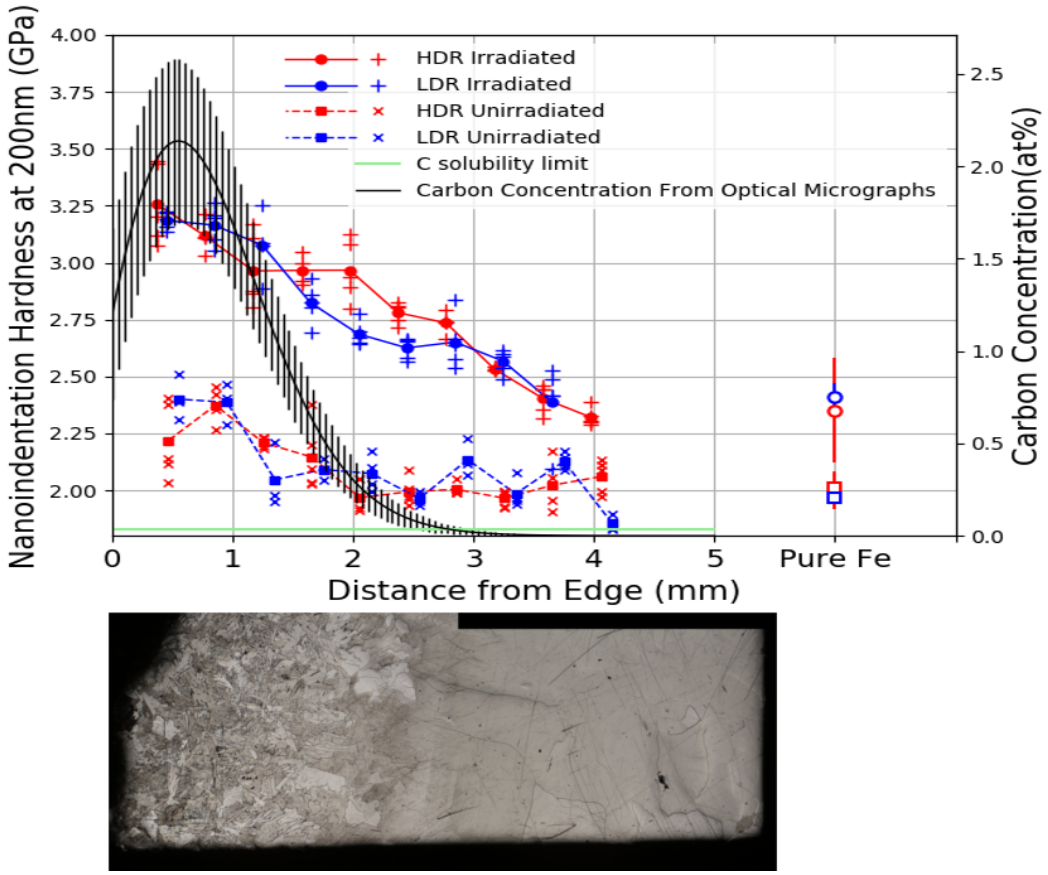


Figure 6.21: Nanoindentation hardness at 200 nm, plotted alongside the carbon concentration measured with optical microscopy. Red markers and lines denote those corresponding to the high dose rate and blue to the low dose rate. Dashed lines mark unirradiated data, whilst irradiated data is marked with solid lines. The average of each row of indents is marked with either a circle or a square, with the individual values marked with + and × for irradiated and unirradiated data respectively. Values for a pure Fe sample are shown with open symbols. An optical micrograph of a non-irradiated quadrant etched with nital is below to show microstructure, approximately to scale.

Near the surface of a well prepared, well annealed material, few dislocations exist around which Cottrell atmospheres can form. During nanoindentation, dislocations are nucleated, multiply, and rapidly move through the material. Under these circumstances at room temperature, Cottrell atmospheres do not have chance to form - and any carbon present does little to affect the flow stress of the material. For this reason, the unirradiated material behaves the same way as the pure Fe at low carbon concentrations. At higher carbon concentrations an increase in hardness is observed, corresponding well with the region of carbide formation seen in the optical micrographs in figures 6.4 and 6.21.

No difference between the unirradiated regions of the high and low dose rate samples was observed, suggesting any affect of thermal aging for these times and temperatures is negligible.

6.4.2 Irradiated Behaviour

In the irradiated regions, carbon was found to have a strong effect on hardening at all concentrations. For regions of the sample at a distance greater than ~2 mm from the carburised edge, where no carbides were observed in the etched sample and carbon is present only in solution, the post-irradiation increase in hardness as a function of carbon concentration is plotted in figure 6.22. The carbon concentration was calculated using the fitted curve in figure 6.5 from the indent row position, and the increase is shown relative to the mean unirradiated hardness of 2.0 $\pm$ 0.1 GPa for these carbon concentrations.

The observation of hardness increasing with increasing carbon concentration in solution is consistent with the findings of Lambrecht et al. [126, 127] who performed

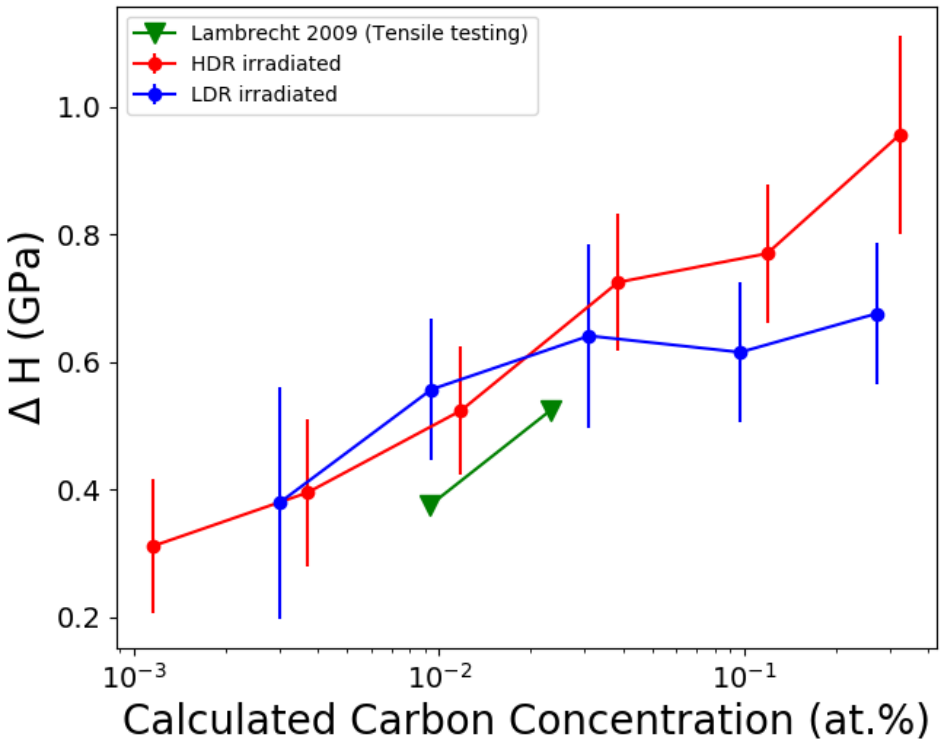


Figure 6.22: Increase in hardness as a function of calculated carbon concentration from the optical micrograph fitted curve in figure 6.5. Also shown are tensile testing data by Lambrecht et al. [126, 127] of neutron irradiated Fe-C alloys to 0.2 dpa at 290-295°C. The yield stress values were multipled by 3 for comparison with nanoindentation hardness data from the present work.

tensile testing on Fe (< 20 ppm C) and Fe-C (≥ 50 ppm C) alloys neutron irradiated to both 0.1 and 0.2 dpa at 290-295°C in the BR2 test reactor at SCK-CEN. The reported increases in yield stress were converted to hardness increases by multiplying by 3 [354], and are also plotted alongside the present work in figure 6.22.

This direct comparison of the two experiments must be performed with caution, firstly due to the different testing methods, and secondly due to the different testing length scales. The quantitative increases in hardness are in good agreement, although in Lambrecht et al.'s macro-scale tested samples this likely represents a larger relative increase (no values for yield stress for the unirradiated samples are given in [127], but are estimated to be around 110 MPa from figures in [126]). Additionally, the effect of carbon on the strength of the unirradiated specimens may be relatively underrepresented by nanoindentation compared to in macro-scale tests, as discussed in section 6.4.1.

The work in chapter 5 and by Hardie et al. [14] suggest that further work is required to understand the influence of size effects on the measurement of radiation induced mechanical property changes. Nonetheless, the present work and that of Lambrecht et al. [126, 127] show good agreement on the magnitude and trend of the influence of carbon concentration on the post-irradiated mechanical properties of Fe-C.

The increase in yield stress caused by a periodic array of obstacles of class x ($\Delta\sigma_{yx}$) is often modelled using [90]:

$$\Delta\sigma_{yx} = \alpha_x M \mu b \sqrt{N_x d_x} \tag{6.8}$$

where M is the Taylor factor, μ the shear modulus, b the magnitude of the Burgers vector, N and d are the obstacle number density and average size, and α is the obstacle's

Reference	Material	Irradiation Conditions	$\frac{(N_L d_L)_{FeCr}}{(N_L d_L)_{Fe}}$
[52]	Fe-2Cr	neutron irradiation, 26 dpa at 400°C	4.7
[46]	Fe-2Cr	neutron irradiation, 6.2 dpa at 400°C	12.3
[41]	Fe-10,16Cr	neutron irradiation, 1 dpa at 300°C	2.2, 2.5

Table 6.5: Literature data on the effect of Cr addition to Fe on dislocation loop number densities and average sizes.

strength.

In this model, there are several possible explanations for the influence of carbon on irradiation hardening. The first possibility is that the in-solution concentration of carbon alters the dislocation loop population. This is the explanation suggested by Lambrecht et al. [126,127], and is supported by modelling work by Jansson et al. [124,125]. Trapping of self interstitial clusters by C and carbon-vacancy complexes [114, 120–122] leads to an increase in the number of nucleation sites for clusters. The reduction in their mobility also means coalescence to form loops is reduced, making the loop number density higher.

Outside of the region of carbide formation, the hardness increase at the highest in-solution carbon concentration is around 3 times that at the lowest carbon concentration (figure 6.22). This would require a factor of 9 difference in $N_L d_L$ between the two regions, where $_L$ signifies dislocation loops.

Literature data on the effect of Cr addition to Fe on loop number density and average size are shown in table 6.5. Cr also traps dislocation loops [36,38,49] and so may have a similar effect to that of C on loop sizes and number densities.

A factor of 9 difference in $N_L d_L$ for the highest and lowest C contents would fit within the range of values observed for the addition of Cr compared to Fe shown in table 6.5, suggesting it is possible that the differences in hardness could be due to dif-

ferences in loop sizes and number densities. However, the irradiation conditions differ significantly from those used in the present work, and the influence of C may not be the same as that of Cr. TEM analysis should be performed to compare the loop populations at the high and low C concentrations.

A second possibility is the decoration of dislocation loops by C, increasing the obstacle strength α_L. Terentyev et al. [128] modelled the interaction of edge dislocations with $\frac{1}{2}$<111> loops decorated with carbon, and found that they presented a significantly stronger obstacle to the passaged of dislocations than naked loops. For 1 nm loops, α_L was found to increase by at least a factor of 2 compared to undecorated loops, and for 2.5 nm loops a 25-40% increase was found.

If the measured hardness increase was due solely to a strengthening of loops by C decoration, an increase in α_L of around 3 would be required. Based on the modelling work by Terentyev et al. [128], this may be plausible. Although loop decoration with C was not observed with atom probe tomography, it cannot be ruled out by this method for the reasons discussed in section 6.3.2.

A third possibility is the presence of a new class of obstacle due to the presence of carbon, such as irradiation induced carbides. Carbides do not present the same problem for analysis as carbon decorated dislocation loops may, and are routinely detected and analysed using atom probe tomography. The fact that none were found by APT during the course of this analysis suggests that either none are present or that their number density is low.

The two mentioned loop population hardening mechanisms are of course not mutually exclusive, and it is plausible based on other observations and modelling that a combination of the two may be responsible for the change in hardness increase with carbon concentration. An additional class of obstacle would not appear necessary to

explain the observations.

In the region closer to the carburised edge, carbides were observed in the non-irradiated sample. The contribution to hardness from these carbides sums with that due to the irradiation induced dislocation loop population to produce the observed hardness.

The presence of nitrogen may have also contributed to the increase in hardness [347], as its concentration was found to increase over this region.

6.4.3 Dose rate

No effect of dose rate was observed on the post-irradiated hardness for any carbon concentration for these irradiation conditions.

Jansson et al. [125] modelled the effect of dose rate using object kinetic Monte Carlo simulations in Fe-C at 70°C up to 0.23 dpa, with dose rates varying from 1×10^{-11} to 1×10^{-3} dpa/s and a trap density of 100 ppm. It was found the interstitial and vacancy cluster densities increased with increasing dose rate, and their mean sizes decreased.

In this work no TEM was performed to quantify the dislocation loop sizes and number densities, but considering the results of nanoindentation, it would appear that any differences due to dose rate are not significant enough to cause changes to the mechanical properties of the material.

6.5 Conclusions & Future Work

An ultra high purity Fe sample was subjected to a carburisation treatment to produce quarter circle shaped samples with a carbon concentration gradient along the radial direction. Two samples were self-ion irradiated to 0.3 dpa at 300°C at different dose rates: 2.5×10^{-4} and 1.2×10^{-5} dpa/s, and analysed by nanoindentation and atom probe tomography.

Nanoindentation revealed the post-irradiation hardness to vary along the radial direction - showing that carbon has a strong influence on the mechanical effects of radiation damage in Fe.

No effect of dose rate was observed.

It is suggested that the presence of carbon in solution affected post-irradiation hardness in a combination of two ways. First it may produce a more refined loop population by trapping small interstitial clusters leading to more nucleation sites for loops, and by decreasing loop mobility leading to less coalescence. In future, TEM analysis should be performed to verify this.

Secondly the decoration of loops with C may increase their barrier strength to dislocation glide. APT did not reveal any decorated dislocation loops, despite analysing a volume large enough to expect to observe some. This may be due to artefacts relating to the detection of carbon in the atom probe. TEM examination of tips prior to atom probe analysis would reveal for certain whether observation of loop decoration with carbon is possible.

Atom probe analysis revealed the presence of a nitride at the region of peak carbon content, and that the nitrogen concentration decreased with distance from the carburised

edge of the sample. The measured concentration of nitrogen was significantly higher than is specified for the as received material, strongly suggesting that nitrogen was introduced to the sample during the carburisation or heat treatment process. This may have influenced the post-irradiated properties of the material.

The nitrogen concentration was measured to be lower than that of carbon, although the relative losses of these ions due to multiple hit effects and peak overlaps requires detailed knowledge of the field evaporation processes for these elements not found in the literature. Artefacts from sample preparation may also influence composition measurement. Further work is required in this area.

The natural continuation of this work is to study the effect of carbon in Fe-Cr alloys. Fe-3Cr and Fe-10Cr alloys with carbon concentration profiles were irradiated alongside the Fe sample in this work, and nanoindentation results are shown in appendix B. The results are not included here due to strong concerns that the surface quality of these samples may have had an influence on the observations [318].

Chapter 7

Summary, Discussion, & Conclusions

The work in this thesis aimed to answer questions around the use of heavy ion irradiation to emulate neutron irradiation for the study radiation damage in nuclear fusion-relevant materials, in the absence of a fusion neutron source. In chapter 4, the issue of instantaneous dose rate changes during beam rastering was addressed, and its potential impact on radiation induced microstructural changes. Chapter 5 compared directly the effects of heavy ion and neutron irradiation on the microstructure and mechanical properties of an Fe-9Cr alloy. Lastly, in chapter 6 the effect of carbon concentration on radiation damage in Fe and its sensitivity to dose rate was investigated.

In this chapter, the work from all 3 experimental chapters is discussed firstly in terms of the emulation of neutron irradiation induced microstructural changes with heavy ions in section 7.1, then in terms of the reproduction of mechanical property changes in section 7.2. In section 7.3 the impact of impurities on radiation damage in ferritic steels is discussed.

7.1 Emulation of Irradiation-induced Microstructural Changes

The theme that runs through this work in regards to the emulation of microstructure changes is that the details of the mechanism that leads to the change, and its sensitivity to the neutron-atypical aspects of heavy ion irradiation are important.

In chapter 4, no difference in the post-irradiation hardness of any of the materials studied was found for irradiations performed with a static, defocussed or a scanned, focussed beam. This appeared to be in contradiction to reports in the literature of differences in void populations for samples irradiated using each of the two modes [12, 13, 201]. It was argued in section 4.4 that these observations can be explained by considering the different mechanisms that lead to the microstructural changes; a summary is given below.

In the low Cr content Fe-Cr alloys studied, irradiation hardening is thought to be due to the formation of dislocation loops, and in particular the segregation of Cr to them [14, 154]. This process is sensitive to dose rate [14, 154], but, it is argued, due to the low dose delivered per pulse the defects produced during a single pulse do not interact, and the relevant dose rate is the one over the timescale on which microstructural development occurs (reactions between freely migrating point defects). This timescale includes many pulses, and is therefore the same for the rastered and defocussed beams.

RIS is argued to not be sensitive to any fluctuations in the flux of point defects, that only the total point defect fluence is imporant [204, 206]. Void nucleation however requires the surmounting of an energetic barrier before reaching a critical size and becoming stable [57], and is therefore sensitive to the beam scanning-induced point defect flux variations [204, 206].

The work in chapter 5 tells a similar story. There, the segregation of Si, P, and Cr to dislocation loops observed after neutron irradiation in the same Fe-9Cr alloy [277, 289] and other similar alloys [94, 216, 217, 305, 306], was at least qualitatively reproduced by heavy ion irradiation, but the neutron irradiation induced α' precipitation [77] was not. It was argued again in section 5.4.1 that differences in the mechanisms leading to these microstructural changes and their sensitivity to neutron-atypical aspects of heavy ion irradiation is the reason ones is reproduced successfully and the other is not.

Segregation of Si, P, and Cr to dislocation loops occurs due to RIS [82, 217, 305], driven by a coupling of point defect and solute fluxes [16]. Any preferential association of defects with a species of solute atom will lead to this coupling, and has been demonstrated by modelling for these species [33, 307–309]. As point defects migrate to sinks, this leads to a build up or depletion of solute atoms at these regions. Differences in radiation conditions between irradiation with heavy ion and neutron irradiation may alter the magnitude of the defect flux to sinks, but should not fundamentally change the segregation mechanism, and so the segregation should be at least qualitatively the same for irradiation with the two particle types. α' precipitation on the other hand, is thought to be a radiation-enhanced, thermodynamically-driven process [69, 75], which has been shown to be sensitive to a number of the neutron-atypical aspects of heavy ion irradiation, including PKA energy [80], injected interstitials [81], and dose rate and ballistic mixing [302].

α' precipitation causes embrittlement in ferritic steels [65, 355], and is a key issue for their use in fusion environments [87]. For the study of radiation damage in such materials and environments, it is therefore essential that any emulation technique used is able to reproduce this microstructural feature. This might be best achieved with heavy ion irradiation by using single energy irradiations to avoid the influence of injected interstitials [81], and at lower dose rates [302].

Some success in inducing α' formation has been reported in ferritic-martensitic steels HCM12A and HT-9 containing 12% Cr after irradiation to 7 dpa at 400°C with 2 MeV proton irradiation [303], and this irradiation technique should also be explored more thoroughly. The lower PKA energy spectrum in proton irradiation than heavy ion irradiation may allow more faithful reproduction of the α' formed under neutron irradiation.

7.2 Emulation of Mechanical Property Changes

Heavy ion irradiation faces two challenges in emulating the mechanical property changes induced by neutron irradiation. The first is the emulation of the microstructural changes, discussed above. The second is to produce these microstructural changes in a volume large enough for the mechanical properties to be measured.

In the investigation of the effect of carbon concentration on radiation damage in Fe in chapter 6, the results of nanoindentation testing of the ion irradiated sample were compared to literature data on similarly neutron irradiated specimens characterised by tensile testing [126, 127]. The results are shown in figure 7.1. The same trend was found - the change in hardness increased with increasing carbon concentration, and the quantitative hardness increases were in good agreement.

As discussed in 6.4.2, this quantitative comparison of mechanical properties across length scales needs to be made with caution. The similar increases in hardness represent vastly different fractional changes - the unirradiated hardness was measured to be 2.0 GPa by nanoindentation in this work, and around 0.33 GPa by macro-sized tensile testing in Lambrecht et al.'s study [126]. It may be that indentation size effects are obscuring some of the hardness increase.

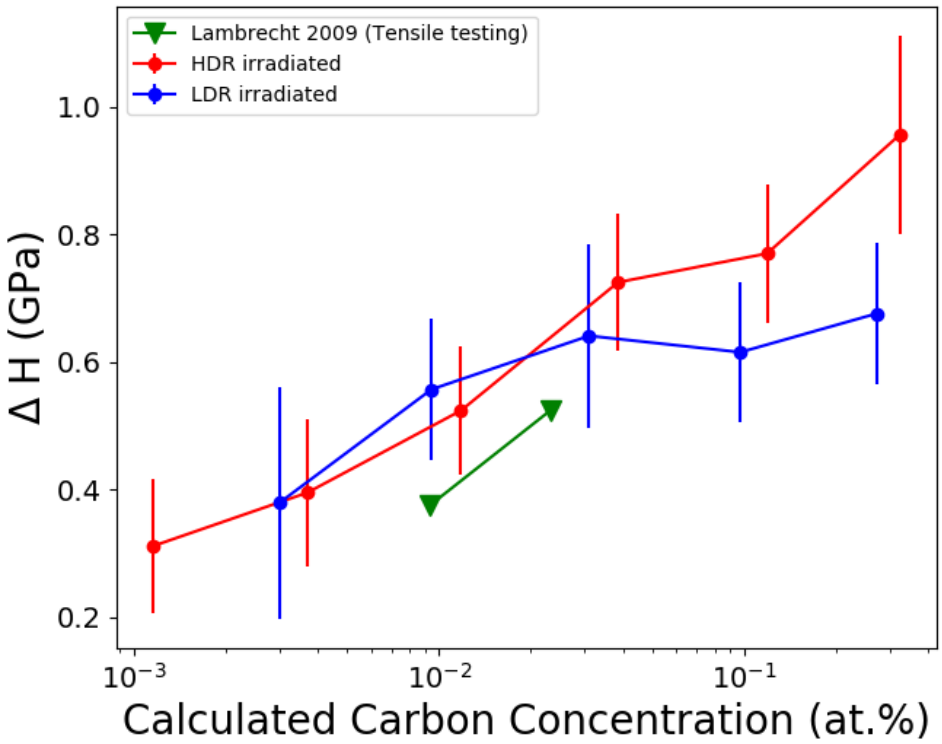


Figure 7.1: Increase in hardness as a function of calculated carbon concentration, alongside results from similarly neutron irradiated specimens characterised by tensile testing data by Lambrecht et al. [126, 127]. The yield stress values were multiplied by 3 for comparison with nanoindentation hardness data from the present work [354]. Full details are given in chapter 6 (section 6.4.2).

Additionally another "size effect" was observed in the unirradiated material tested by nanoindentation - where the strengthening effect of interstitial carbon was not observed at these scales. In section 6.4.1 it was argued that Cottrell atmospheres [15] are not able to form around the freshly nucleated dislocations produced during nanoindentation at room temperature. This effect may cause the hardness of materials containing interstitial carbon to be measured to be relatively lower at small length scales than at macroscopic scales. Further work could investigate to what extent and at what scale this effect is present in indentation and other small scale testing techniques.

In chapter 5, the results of nanoindentation testing of neutron irradiated Fe-Cr samples conducted in this work and by Hardie et al. [14] were compared to Vickers hardness testing performed on the same materials by T Milot. The results are shown in figure 7.2. Figure (a) shows relative hardness increases for the as measured data, and (b) is after correction for pileup in the Fe-6Cr data and a potentially artificially high unirradiated reference hardness in the Fe-9Cr data. Full details are given in section 5.4.2.2. After these "corrections", the relative increases in hardness are fairly well reproduced, but further work should include Vickers testing with a series of lighter weights to bridge the gap in length scales and observe the relative hardness increase as a function of indent size. The relationship between microstructure and this indentation size effect should also be investigated.

In similar work, Hardie et al. [14] found a size effect existed between the yield stress measured using microcantilever beams and that measured with Vickers hardness testing. A strong size effect was also found in microcantilever beams with beam heights below ~2μm - suggesting that irradiations should produce damage layers of at least this depth in order to usefully use this testing method in these materials. The present work used microcantilever beams with beam heights between 2.0 and 4.5 μm, and no strong size effect was observed.

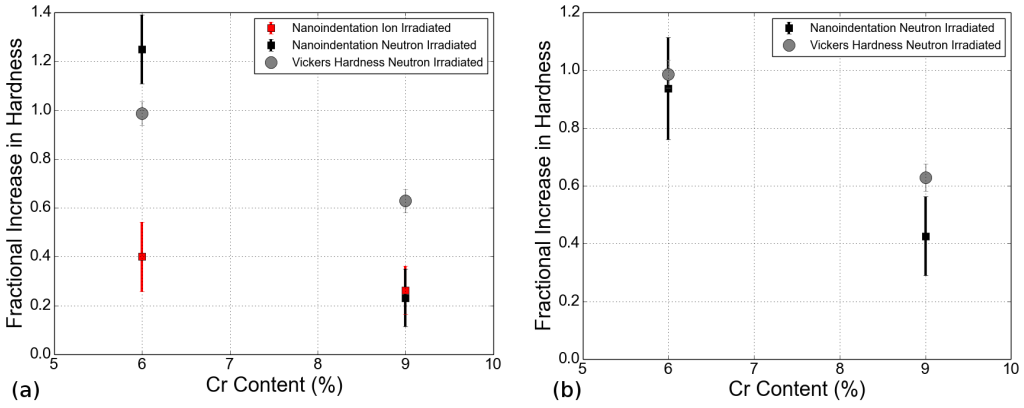


Figure 7.2: Fractional increases in hardness by nanoindentation for neutron irradiated Fe-6Cr (Hardie et al. [14]) and Fe-9Cr (this work), and Vickers testing (T Milot, *INL*), (a) as measured, (b) corrected for indentation pile up (Fe-6Cr) and unirradiated reference (Fe-9Cr). For full details see section 5.4.2.2.

In order for heavy ion irradiation to be a useful tool for the study of irradiation induced mechanical property changes, a robust understanding of the influence of size effects and their relationship to microstructure is necessary, and further work is required in this area.

With heavy ion irradiation, it is common practice to produce a relatively flat damage profile with depth by using multiple energy implantations. While this can increase the irradiated volume available for mechanical testing, it leads to injected interstitials being present throughout the damage depth. These injected interstitials have been shown to have an impact on heavy ion irradiation's ability to reproduce faithfully the microstructure changes caused by neutron irradiation, particularly void structure [168] and α' precipitation [81]. For these reasons it may be preferable to use single energy irradiations with high energy (>~30MeV), to create a large damage layer of approximately uniform damage away from the peak damage region, where the number of injected interstitials is low, as used in e.g. [302].

Depending on the method used, multi-energy implantation can also introduce differences in dose rate at different damage depths. For the sequential energy method, where each beam energy is used in turn, at depths shallower than the maximum depth there are contributions to the total damage from each beam energy. The damage-depth profile for a single beam energy is strongly peaked, so although different currents are used to achieve an approximately uniform dose rate with depth some variation will inevitably occur.

A degrader foil wheel set up will induce a cyclically time varying dose rate at a given depth as each beam energy is effectively cycled through in turn, with intermittent "beam off" periods where the beam is periodically blocked by the arms separating each window in the degrader foil wheel.

These effects have not been explored in the literature, and should be kept in mind when using multiple energy implantations.

7.3 Effect of Impurities

The work in both chapters 5 and 6 have both shown that impurities (P, Si, and C) have a significant effect on the post-irradiated mechanical properties of Fe-9Cr and Fe.

In chapter 5, the microstructure and mechanical properties of a neutron irradiated sample and an ion irradiated Fe-9Cr sample were compared. Microstructural analysis of the neutron irradiated sample was performed by another group, and reported in [77, 277, 289]. Both samples were found to contain NiSiPCr clusters, and dislocation loops decorated with Si, P, and Cr. Ni, Si, and P were present at impurity levels. Only the

neutron irradiated sample was found to contain α' precipitates [77].

Despite these microstructural differences, the ion and neutron irradiated samples were found to have the same hardness and yield stress, as measured by nanoindentation and microcantilever testing respectively (Table 7.1). This would suggest that the α' precipitates only play a minor role, and that the mechanical properties are mostly determined by microstructural features formed by the impurity elements. A similar finding was made by Bergner et al. [90], who applied Orowan-type analysis to literature data on Fe-Cr alloys neutron irradiated at the same temperature and to a similar dose as those studied in this work.

Sample	**Microcantilever Testing Yield Stress (GPa)**		**Nanoindentation Hardness (GPa)**
	Simple Beam Theory	*Finite Element*	
Unirradiated	0.44 ± 0.13	0.51 ± 0.07	2.2 ± 0.1
Ion irradiated	1.04 ± 0.21	0.82 ± 0.13	2.78 ± 0.19
Neutron irradiated	1.20 ± 0.27	0.99 ± 0.18	2.71 ± 0.24

Table 7.1: Average values and standard deviations of yield stress found by simple beam theory and finite element analysis for microcantilever beams with heights between 2 and 4.5 μm. Nanoindentation hardness measurements were made at an indenter displacement of 500 nm.

In chapter 6 the effect of carbon concentration on radiation damage in Fe was studied, and it was found to have a strong impact on post-irradiation hardness even at very low concentrations (<0.1 at%). The post-irradiation hardness increased with increasing carbon concentration, with a maximum increase in hardness of around 3 times that observed in pure Fe. These findings are in agreement with a study on neutron irradiated Fe samples containing different concentrations of carbon under similar irradiation conditions [126, 127]. The results are shown in figure 7.1.

It is important to understand the influence of impurities on radiation damage - both from the point of view of alloy design, and for making comparisons between experiments using samples of different purity. The unintentional implantation of carbon during heavy ion irradiation [130–132, 356] makes it significant also for ion-neutron irradiation correlation.

7.4 Conclusions

The key findings of the work in this thesis are summarised below:

- No impact of beam rastering on the post-irradiation hardness of Fe or Fe-Cr alloys was observed.
- In an Fe-9Cr alloy, heavy ion irradiation was found to reproduce the segregation to dislocation loops and clustering of Si, P, and Cr, but not the α' precipitation reported in the literature for the neutron irradiated specimen.
- The post-irradiation hardness and yield stress of the ion and neutron irradiated specimens were found to be the same, as measured by nanoindentation and microcantilever testing respectively. This suggests that the microstructural features formed by impurity elements Si and P dominate the observed hardening.
- The increase in nanoindentation hardness of 0.81 ± 0.26 GPa for the neutron irradiation Fe-9Cr sample was found to be less than 1.5 ± 0.28 GPa the reported for the Fe-6Cr sample.
- The irradiation hardening of Fe was found to increase with increasing carbon concentration, with carbon creating an increase in hardness up to 3 times greater than that observed in pure Fe. This was argued to be likely due to increases in the dislocation loop number density, and their decoration with C.
- No effect of dose rate on the post irradiation hardening of the Fe-C sample was observed.

This work suggests that the ability of heavy ion irradiation to recreate the damage caused by neutron irradiation depends on the details of the damage mechanism, and its

sensitivity to the differences between irradiation with the two particle types. A major concern around the use of heavy ion irradiation for the study of Fe-Cr alloys is the apparent difficulty of inducing the α' precipitation observed after neutron irradiation.

Although these precipitates were found to play only a minor role in the irradiation hardening of the Fe-9Cr alloy studied in chapter 5, in other work they found to make a more significant contribution at higher Cr contents [90] and in higher purity materials [41]. Further work is required in this area, investigating the use of single energy irradiations [81] at lower dose rates [302].

This work has also shown that impurity elements such as P, Si, and C can have a significant effect on the post-irradiation hardening of Fe and Fe-Cr alloys. Care should be taken when comparing experiments on alloys of different purity.

Although in both chapters 5 and 6 the qualitative trends of macro scale mechanical tests were reproduced by nanoindentation, size effects may inhibit quantitative comparison. Further work is required in this area to determine the magnitude and microstructural sensitivity of such size effects.

The above-mentioned limitations of heavy ion irradiation for these purposes suggest that it should not be used as a stand-alone method for the study of radiation damage in Fe-Cr alloys, and requires benchmarking against neutron irradiated specimens. Facilities such as CAES in Idaho Falls, and the MRF at CCFE play a vital role in providing access to study such neutron irradiated materials.

7.5 Recommendations & Considerations

Based on the findings of work described in this thesis and other available literature, this section details recommendations and considerations to be made when designing experiments using heavy ion irradiation as a proxy to neutron irradiation (in particular for Fe and Fe-Cr alloys, but may apply more widely) - what differences can be expected, and how they can be minimised.

A general recommendation, as discussed in section 7.1, is to consider the underlying mechanisms that lead to radiation induced microstructural changes, and how they are affected by the neutron atypical aspects of heavy ion irradiation.

PKA spectrum differences between heavy ion and neutron irradiation are unavoidable, and the higher PKA spectrum produced by heavy ions will inherently lead to fewer freely mobile [138–140] defects than produced by the lower PKA energy cascades present in neutron irradiation [25, 134, 137]. This will lead to reduced RIS, creep, swelling, and radiation-enhanced diffusion processes for the same dpa for heavy ion irradiation compared to neutron irradiation.

Dose rate is often cited as a major cause for differences in microstructure between ion and neutron irradiated specimens. The literature on dose rate effects is discussed in detail in section 2.4.2, with dose rate having been shown to affect a number of radiation damage mechanisms: RIS [152, 154] and radiation creep rate [155] have both been found to be enhanced at lower dose rate; peak swelling is shifted to a higher temperature with higher dose rate [146], and a reduction in incubation dose before steady state swelling observed with lower dose rate [149, 150]; dislocation loop density was found to increase with increasing dose rate [47, 153].

For these reasons it is recommended that the ion irradiation dose rate should be chosen to be as close as possible to the neutron irradiation experiment. A small number of experiments [160, 162] have found some success employing a Mansur [147, 159] temperature shift to compensate for differing dose rates, but this has yet to be explored thoroughly.

The work in chapter 4 showed that differences in instantaneous dose rate between scanned and defocussed beams did not affect post irradiation hardness in Fe, Fe-3Cr and Fe-5Cr alloys. However, based on other literature [12, 13, 201] it is recommended that the use of scanned beams is avoided, particularly for the study of swelling and microstructures containing voids.

The presence of injected interstitials should be minimized, as they have been shown to inhibit both α' formation [81] and swelling [168]. This can be achieved with the use of single energy implantations and careful selection of the analysis depth.

For the mechanical testing of implanted layers as large a damage depth as possible is desirable, to minimise any size effects. For microcantilever testing of Fe and Fe-Cr alloys, this depth should be at least 2μm [14] (see also section 5.4.2.1).

This can be achieved ideally using a single high energy beam (> ~30 MeV), using the initial pre-peak, approximately uniform damage region. If such high beam energies are not available and multiple energy implantations are used, researchers should be aware that: injected interstitials will be present throughout the damaged depth; for degrader foil wheel-type setups a pulsed beam flux will be present; and that any effects of sequential beam energy implantations have not yet been explored.

The work in chapter 6 shows that interstitial carbon affects the post irradiation hardness of Fe, thought to be due to refining and decoration of the dislocation loop popu-

lation. Alongside recent work on unintended carbon implantation during ion irradiation [130–132, 356], it is recommended to take measures to minimize any such implantation, and to attempt to quantify any that does occur.

It should be noted that as the dose increases, all of these potential issues become more difficult to mitigate. Practical time constraints mean that higher dose rates are necessarily used, the number of injected interstitials increases with increasing fluence, as does likely the amount of carbon implantation. It is therefore suggested that lower dose heavy ion irradiation experiments are more likely to be able to reproduce corresponding neutron irradiation experiments than those at higher doses.

Appendices

Appendix A

APT ranges for UCSB Fe-9Cr alloy

Range	Ion	Range	Ion
5.9900 - 6.0350	$^{12}C^{2+}$	24.9180 - 25.0350	$^{50}Cr^{2+}$
10.3130 - 10.3490	$^{31}P^{3+}$	25.4460 - 25.4990	$^{51}V^{2+}$
11.9890 - 12.0450	$^{12}C^{+}$	25.8620 - 26.0930	$^{52}Cr^{2+}$
13.9720 - 14.0240	$^{28}Si^{2+}$	26.3960 - 26.5400	$^{53}Cr^{2+}$
14.4820 - 14.5050	$^{29}Si^{2+}$	26.8870 - 27.0650	$^{54}Fe^{2+}$ / $^{54}Cr^{2+}$
14.9770 - 15.0030	$^{30}Si^{2+}$	27.5070 - 28.2844	$^{56}Fe^{2+}$
15.4760 - 15.5080	$^{31}P^{2+}$	28.4070 - 28.5440	$^{57}Fe^{2+}$
15.9750 - 16.0250	$^{16}O^{+}$	28.9240 - 29.0150	$^{58}Fe^{2+}$ / $^{58}Ni^{2+}$
17.9780 - 18.0280	$^{12}C_3^{2+}$	34.4260 - 34.4940	$^{69}Ga^{2+}$
18.6270 - 18.6600	$^{56}Fe^{3+}$	35.4140 - 35.4960	$^{71}Ga^{2+}$
23.9670 - 24.0300	$^{12}C_2^{+}$	55.7440 - 56.0720	$^{56}Fe^{+}$

Table A.1: Ranges used in APT analysis of UCSB Fe-9Cr alloy, extending to background noise level.

Appendix B

Nanoindentation results of Fe-Cr-C alloys

Here results of nanoindentation testing of carburised Fe3Cr and Fe10Cr samples are presented. The irradiation conditions and heat treatments are the same as those for the Fe sample described in chapter 6, with the exception that they were cooled slowly in the furnace after the 2nd stage treatment to avoid martensite formation.

The reason these results are placed in the appendix rather than in chapter 6 is because of doubts over the surface quality, which may give a misleading presentation and interpretation of results.

An optical image of the Fe3Cr sample is shown in figure B.1, and an SEM/EBSD scan for the Fe10Cr sample prior to irradiation in figure B.2.

Both images suggest a good quality of surface finish. However upon etching to study the microstructure and measure the carbon concentration profile, a large number of scratches were revealed. This suggests that during an early polishing stage mechanical damage was not completely removed, and that the near surface region was then polished hiding it from view.

This sub-surface region may have a high density of dislocations and affect the mechanical properties of the material, and result in greater scatter of hardness between indents [318].

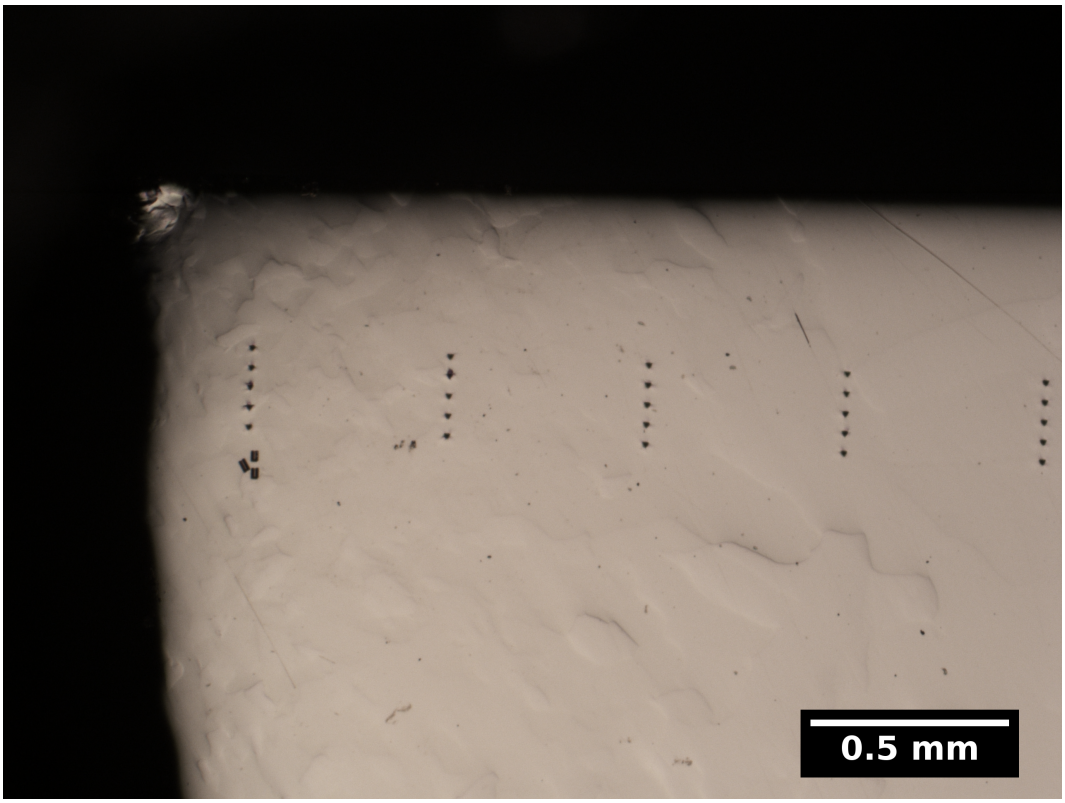


Figure B.1: Optical micrograph of the carburised Fe3Cr sample.

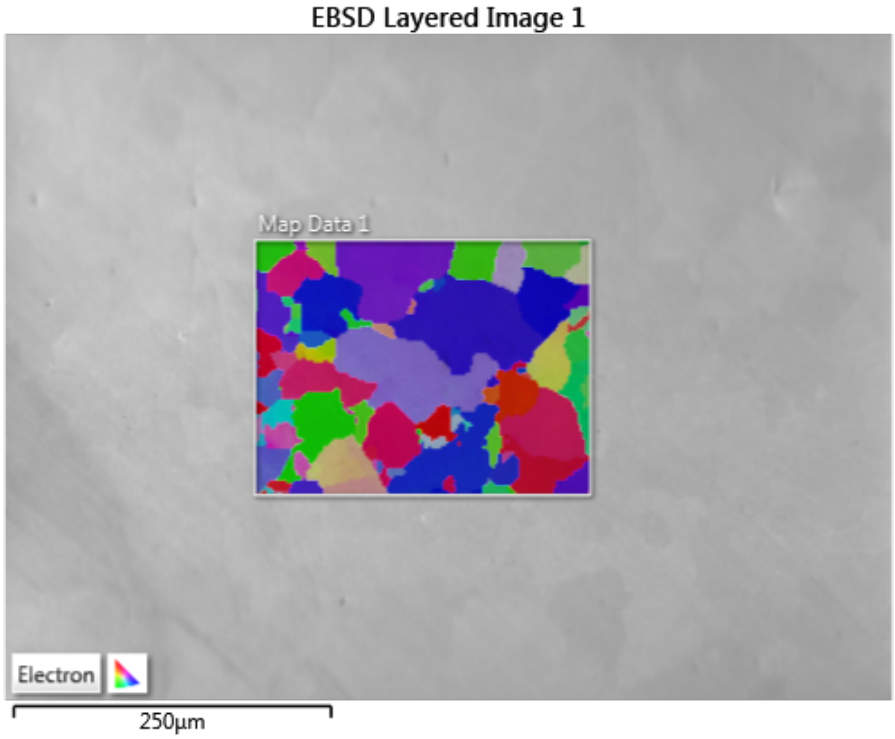


Figure B.2: EBSD scan of the carburised Fe10Cr sample prior to irradiation. Good quality patterns were achieved.

The nanoindentation results are presented in figures B.3 and B.4 for the Fe3Cr and Fe10Cr samples respectively. The scratches revealed by etching made it difficult to measure the carbon concentration, so the composition curve plotted is that for the Fe sample.

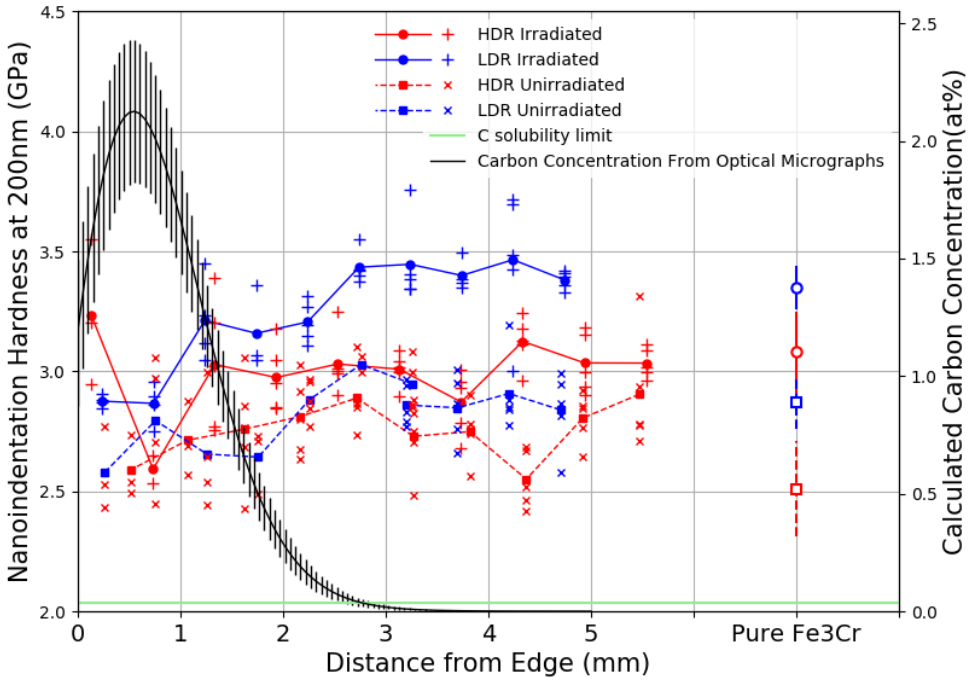


Figure B.3: Nanoindentation results for the carburised Fe3Cr alloy.

There is a large amount of scatter in the data for the carburised Fe3Cr alloy in figure B.3 (probably due to surface finish), but it tenatively it appears that carbon may reduce post-irradiation hardening in this alloy at higher concentrations. This may be due to trapping of vacancies by C, which may reduce Cr segergation to dislocation loops thought to be the mechanism for hardening in this alloy [154].

There is less scatter in the data for the carburised Fe10Cr alloy in figure B.4, possibly due to a better quality surface. Carbon appears to have little affect on the irradiation hardening in this material, in contrast to that found in Fe. This may be due to the high concentration of Cr atoms, which can also trap point defects [31, 32, 36, 38].

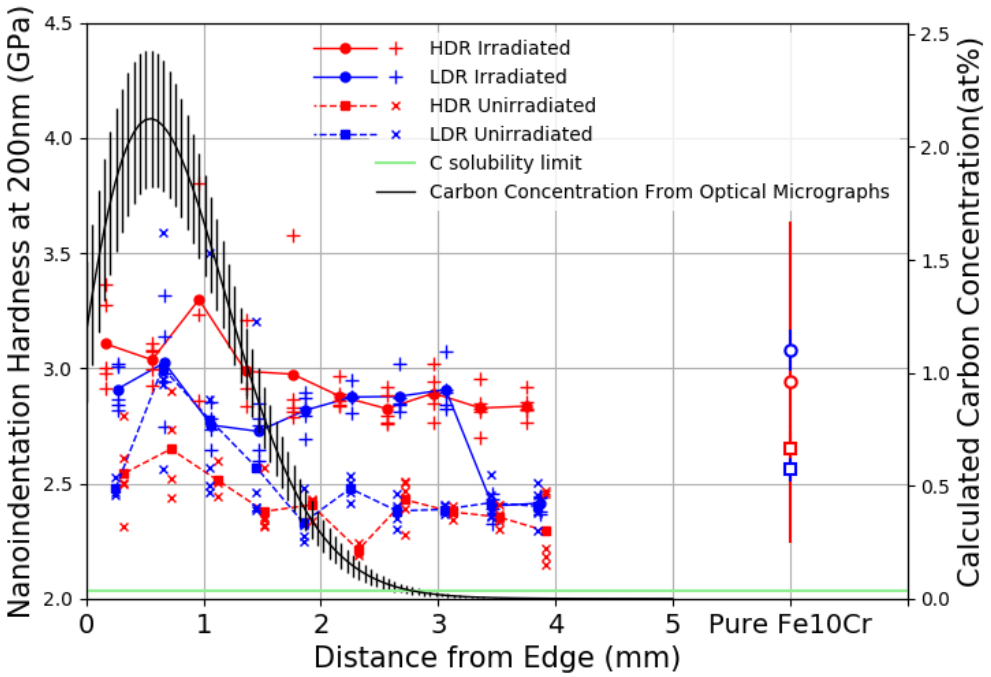


Figure B.4: Nanoindentation results for the carburised Fe10Cr alloy.

Bibliography

[1] V. Masson-Delmotte, P. Zhai, H.O. Pörtner, D. Roberts, J. Skea, P.R. Shukla, A. Pirani, W. Moufouma-Okia, C. Péan, R. Pidcock, S. Connors, J.B.R. Matthews, Y. Chen, X. Zhou, M.I. Gomis, E. Lonnoy, T. Maycock, M. Tignor, and T. Waterfield. IPCC, 2018: Summary for Policymakers. In: Global warming of 1.5 C. An IPCC Special Report on the impacts of global warming of 1.5 C above pre - industrial levels and related global greenhouse gas emission pathways, in the context of strengthening the ... pages 1–2, 2018.

[2] A. Einstein. Ist die Trägheit eines Körpers von seinem Energieinhalt abhängig? *Annalen der Physik*, 323(13):639–641, 1905.

[3] H. Bosch and G.M. Hale. Improved Formulas for Fusion Cross-Sections and Thermal Reactivities. *Nuclear Fusion*, 32(4):611–631, 1992.

[4] S. Cowley. Hot fusion. *Physics World*, 23(10):46–51, 2010.

[5] Jet Team. Fusion energy production from a deuterium-tritium plasma in the JET tokamak. *Nuclear Fusion*, 32(2):187–203, 1992.

[6] S.J. Zinkle and J.T. Busby. Structural materials for fission & fusion energy. *Materials Today*, 12(11):12–19, nov 2009.

[7] A.-A.F. Tavassoli, E. Diegele, R. Lindau, N. Luzginova, and H. Tanigawa. Current status and recent research achievements in ferritic/martensitic steels. *Journal of Nuclear Materials*, 455(1-3):269–276, 2014.

[8] F.A. Garner, M.B Toloczko, and B.H Sencer. Comparison of swelling and irradiation creep behavior of fcc-austenitic and bcc-ferritic/martensitic alloys at high neutron exposure. *Journal of Nuclear Materials*, 276(1-3):123–142, jan 2000.

[9] H. Tanigawa, E. Gaganidze, T. Hirose, M. Ando, S.J. Zinkle, R. Lindau, and E. Diegele. Development of benchmark reduced activation ferritic / martensitic steels for fusion energy applications. *Nuclear Fusion*, 57:92004, 2017.

[10] E.E Bloom, S.J Zinkle, and F.W Wiffen. Materials to deliver the promise of fusion power - progress and challenges. *Journal of Nuclear Materials*, 329-333(2004):12–19, aug 2004.

[11] J. Knaster, S. Chel, U. Fischer, F. Groeschel, R. Heidinger, a. Ibarra, G. Micciche, a. Möslang, M. Sugimoto, and E. Wakai. IFMIF, a fusion relevant neutron source for material irradiation current status. *Journal of Nuclear Materials*, 453(1-3):115–119, oct 2014.

[12] J.G. Gigax, E. Aydogan, T. Chen, D. Chen, L. Shao, Y. Wu, W.Y. Lo, Y. Yang, and F.A. Garner. The influence of ion beam rastering on the swelling of self-ion irradiated pure iron at 450 C. *Journal of Nuclear Materials*, 465:343–348, 2015.

[13] E. Getto, Z. Jiao, A.M. Monterrosa, K. Sun, and G.S. Was. Effect of irradiation mode on the microstructure of self-ion irradiated ferritic-martensitic alloys. *Journal of Nuclear Materials*, 465:116–126, 2015.

[14] C.D. Hardie, G.R. Odette, Y. Wu, S. Akhmadaliev, and S.G. Roberts. Mechanical properties and plasticity size effect of Fe-6%Cr irradiated by Fe ions and by neutrons. *Journal of Nuclear Materials*, 482:236–247, 2016.

[15] A.H. Cottrell and B.A. Bilby. Dislocation Theory of Yielding and Strain Ageing of Iron. *Proceedings of the Physical Society. Section A*, 62(1):49–62, jan 1949.

[16] G.S. Was. *Fundamentals of Radiation Materials Science: Metals and Alloys [Hardcover]*. Springer; 2007 edition, 2007.

[17] M.J. Norgett, M.T. Robinson, and I.M. Torrens. A proposed method of calculating displacement dose rates. *Nuclear Engineering and Design*, 33:50–54, 1975.

[18] G.H. Kinchin and R.S. Pease. The Displacement of Atoms in Solids by Radiation. *Reports on Progress in Physics*, 18(1):1–51, jan 1955.

[19] I. Cook. Materials research for fusion energy. *Nature materials*, 5(2):77–80, 2006.

[20] J. Lindhard and M. Scharff. Energy Dissipation by Ions in the kev Region. *Physical Review*, 124(1):128–130, oct 1961.

[21] J.F. Ziegler, M.D. Ziegler, and J.P. Biersack. SRIM - The stopping and range of ions in matter (2010). *Nuclear Instruments and Methods in Physics Research Section B: Beam Interactions with Materials and Atoms*, 268(11-12):1818–1823, jun 2010.

[22] R.E. Stoller, M.B. Toloczko, G.S. Was, A.G. Certain, S. Dwaraknath, and F.A. Garner. On the use of SRIM for computing radiation damage exposure. *Nuclear Instruments and Methods in Physics Research Section B: Beam Interactions with Materials and Atoms*, 310:75–80, sep 2013.

[23] R.E. Stoller, G.R. Odette, and B.D. Wirth. Primary damage formation in bcc iron. *Journal of Nuclear Materials*, 1:49–60, 1997.

[24] R.E. Stoller. Point defect survival and clustering fractions obtained from molecular dynamics simulations of high energy cascades. *Journal of Nuclear Materials*, 237(1996):999–1003, 1996.

[25] R.E. Stoller. The role of cascade energy and temperature in primary defect formation in iron. *Journal of Nuclear Materials*, 276(2000):22–32, 2000.

[26] A. De Backer, A.E. Sand, K. Nordlund, L. Luneville, D. Simeone, and S.L. Dudarev. Subcascade Formation and Defect Cluster Size Scaling in High-Energy Collision Events in Metals epl draft Subcascade formation and defect cluster size scaling in high- energy collision events in metals. *EPL (Europhysics Letters)*, 115:26001, 2016.

[27] W. Setyawan, A.P. Selby, N. Juslin, R.E. Stoller, B.D. Wirth, and R.J. Kurtz. Cascade morphology transition in bcc metals. *Journal of Physics: Condensed Matter*, 27(22):225402, 2015.

[28] E. Antoshchenkova, L. Luneville, D. Simeone, R.E. Stoller, and M. Hayoun. Fragmentation of displacement cascades into subcascades: A molecular dynamics study. *Journal of Nuclear Materials*, 458:168–175, 2015.

[29] D.J. Bacon, A.F. Calder, J.M. Harder, and S.J. Wooding. Computer simulation of low-energy displacement events in pure bcc and hcp metals. *Journal of Nuclear Materials*, 205:52–58, 1993.

[30] K. Vörtler, C. Björkas, D. Terentyev, L. Malerba, and K. Nordlund. The effect of Cr concentration on radiation damage in FeâĂŞCr alloys. *Journal of Nuclear Materials*, 382(1):24–30, nov 2008.

[31] D. Terentyev, L. Malerba, R. Chakarova, K. Nordlund, P. Olsson, M. Rieth, and J. Wallenius. Displacement cascades in FeâĂŞCr: A molecular dynamics study. *Journal of Nuclear Materials*, 349(1-2):119–132, feb 2006.

[32] P. Olsson, C. Domain, and J. Wallenius. Ab initio study of Cr interactions with point defects in bcc Fe. *Physical Review B*, 75(1):014110, jan 2007.

[33] D. Terentyev, P. Olsson, T.P.C. Klaver, and L. Malerba. On the migration and trapping of single self-interstitial atoms in dilute and concentrated Fe-Cr alloys: Atomistic study and comparison with resistivity recovery experiments. *Computational Materials Science*, 43(4):1183–1192, oct 2008.

[34] I.M. Robertson, M.L. Jenkins, and C.A. English. Low-dose neutron-irradiation damage in α-iron. *Journal of Nuclear Materials*, 108-109:209–221, jul 1982.

[35] I.M. Robertson, M.A. Kirk, and W.E. King. Formation of Dislocation Loops In Iron by Self-Ion Irradiations at 40K. *Scripta Metallurgica*, 18(c):317–320, 1984.

[36] Z. Yao, M. Hernández-Mayoral, M.L. Jenkins, and M.A. Kirk. Heavy-ion irradiations of Fe and Fe-Cr model alloys Part 1: Damage evolution in thin-foils at lower doses. *Philosophical Magazine*, 88(21):2851–2880, jul 2008.

[37] B.C. Masters. Dislocation loops in irradiated iron. *Philosophical Magazine*, 11(113):881–893, 1965.

[38] M.L. Jenkins, Z. Yao, M. Hernández-Mayoral, and M.A. Kirk. Dynamic observations of heavy-ion damage in Fe and Fe-Cr alloys. *Journal of Nuclear Materials*, 389(2):197–202, 2009.

[39] B.L. Eyre and A.F. Bartlett. An electron microscope study of neutron irradiation damage in alpha-iron. *Philosophical Magazine*, 12(116):261–272, 1965.

[40] C.A. English, B.L. Eyre, and M.L. Jenkins. Heavy-ion damage in α Fe. *Nature*, 263(5576):400–401, sep 1976.

[41] W-Y. Chen, Y. Miao, J. Gan, M.A. Okuniewski, S.A. Maloy, and J.F. Stubbins. Neutron irradiation effects in Fe and Fe-Cr at 300 C. *Acta Materialia*, 111:407–416, jun 2016.

[42] S.L. Dudarev, R. Bullough, and P.M. Derlet. Effect of the α-γ Phase transition on the stability of dislocation loops in bcc iron. *Physical Review Letters*, 100(13):1–4, 2008.

[43] Z. Yao, M.L. Jenkins, M. Hernández-Mayoral, and M.A. Kirk. The temperature dependence of heavy-ion damage in iron: A microstructural transition at elevated temperatures. *Philosophical Magazine*, 90(35-36):4623–4634, 2010.

[44] D.S. Gelles. Microstructural examination of neutron-irradiated simple ferritic alloys. *Journal of Nuclear Materials*, 109:515–526, 1982.

[45] M. Matijasevic and A. Almazouzi. Effect of Cr on the mechanical properties and microstructure of Fe-Cr model alloys after n-irradiation. *Journal of Nuclear Materials*, 377(1):147–154, jun 2008.

[46] S.I. Porollo and A.M. Dvoriashin. The microstructure and tensile properties of Fe-Cr alloys after neutron irradiation at 400 C to 5.5-7.1 dpa. *Journal of Nuclear Materials*, 256(February):1–7, 1998.

[47] S. Xu. *A Study of Irradiation Damage in Iron and Fe-Cr Alloys*. PhD thesis, University of Oxford, 2013.

[48] S. Xu, Z. Yao, and M.L. Jenkins. TEM characterisation of heavy-ion irradiation damage in FeCr alloys. *Journal of Nuclear Materials*, 386-388(C):161–164, 2009.

[49] D. Terentyev, M. Klimenkov, and L. Malerba. Confinement of motion of interstitial clusters and dislocation loops in BCC Fe-Cr alloys. *Journal of Nuclear Materials*, 393(1):30–35, aug 2009.

[50] H. Xu, R.E. Stoller, Y.N. Osetsky, and D. Terentyev. Solving the Puzzle of <100> Interstitial Loop Formation in bcc Iron. *Physical Review Letters*, 110(26):265503, jun 2013.

[51] L.K. Béland, Y.N. Osetsky, R.E. Stoller, and H. Xu. Interstitial loop transformations in FeCr. *Journal of Alloys and Compounds*, 640:219–225, 2015.

[52] Y.V. Konobeev, A.M. Dvoriashin, S.I. Porollo, and F.A. Garner. Swelling and microstructure of pure Fe and Fe-Cr alloys after neutron irradiation to 26dpa at 400 C. *Journal of Nuclear Materials*, 355(1-3):124–130, sep 2006.

[53] M. Hernández-Mayoral, Z. Yao, M.L. Jenkins, and M.A. Kirk. Heavy-ion irradiations of Fe and Fe-Cr model alloys Part 2: Damage evolution in thin-foils at higher doses. *Philosophical Magazine*, 88(21):2881–2897, 2008.

[54] A. Okada, H. Maeda, K. Hamada, and I. Ishida. Defect structure development in a pure iron and dilute iron alloys irradiated with neutrons and electrons. *Journal of Nuclear Materials*, 271-272:133–138, 1999.

[55] C. Cawthorne and E.J. Fulton. Voids in Irradiated Stainless Steel. *Nature*, 216(5115):575–576, nov 1967.

[56] A.D. Brailsford and R Bullough. The rate theory of swelling due to void growth in irradiated metals. *Journal of Nuclear Materials*, d:121–135, 1972.

[57] A. Hishinuma and L.K. Mansur. Critical radius for bias-driven swelling - a further analysis and its application to bimodal cavity size distributions. *Journal of Nuclear Materials*, 118:91–99, 1983.

[58] S.J. Zinkle, L.E. Seitzman, and W.G. Wolfer. I. Energy calculations for pure metals. *Philosophical Magazine A*, 55(1):111–125, jan 1987.

[59] S.J. Zinkle, W.G. Wolfer, G.L. Kulcinski, and L.E. Seitzman. II. Effect of oxygen and helium on void formation in metals. *Philosophical Magazine A*, 55(1):127–140, jan 1987.

[60] A. Bhattacharya, E. Meslin, J. Henry, A. Barbu, S. Poissonnet, and B. Décamps. Effect of chromium on void swelling in ion irradiated high purity Fe-Cr alloys. *Acta Materialia*, 108:241–251, 2016.

[61] E.A. Little and D.A. Stow. Void-swelling in irons and ferritic steels: II. An experimental survey of materials irradiated in a fast reactor. *Journal of Nuclear Materials*, 87:25–39, 1979.

[62] D.S. Gelles. Void swelling in binary Fe-Cr alloys at 200 dpa. *Journal of Nuclear Materials*, 225:163–174, 1995.

[63] Y. Katoh, A. Kohyama, and D.S. Gelles. Swelling and dislocation evolution in simple ferritic alloys irradiated to high fluence in FFTF/MOTA. *Journal of Nuclear Materials*, 225:154–162, 1995.

[64] J.O. Andersson and B. Sundman. Thermodynamic properties of the CrFe system. *Calphad*, 11(1):83–92, 1987.

[65] P.J. Grobner. The 885 F (475 C) embrittlement of ferritic stainless steels. *Metallurgical transactions*, 4(4), 1973.

[66] S.J. Zinkle and N.M. Ghoniem. Operating temperature windows for fusion reactor structural materials. *Fusion Engineering and Design*, 51-52(2000):55–71, 2000.

[67] A.W. Bowen and G.M. Leak. Solute Diffusion in Alpha- and Gamma-Iron. *Metallurgical transactions*, 1(June):1695–1696, 1970.

[68] M.K. Miller, R.E. Stoller, and K.F. Russell. Effect of neutron-irradiation on the spinodal decomposition of Fe-32% Cr model alloy. *Journal of Nuclear Materials*, 230(3):219–225, 1996.

[69] G. Bonny, D. Terentyev, and L. Malerba. On the α-α' miscibility gap of Fe-Cr alloys. *Scripta Materialia*, 59(11):1193–1196, dec 2008.

[70] W. Xiong, M. Selleby, Q. Chen, J. Odqvist, and Y. Du. Phase Equilibria and Thermodynamic Properties in the Fe-Cr System. *Critical Reviews in Solid State and Materials Sciences*, 35(2):125–152, may 2010.

[71] P. Olsson, I.A. Abrikosov, L. Vitos, and J. Wallenius. Ab initio formation energies of Fe-Cr alloys. *Journal of Nuclear Materials*, 321(1):84–90, 2003.

[72] P. Olsson, I.A. Abrikosov, and J. Wallenius. Electronic origin of the anomalous stability of Fe-rich bcc Fe-Cr alloys. *Physical Review B - Condensed Matter and Materials Physics*, 73(10):1–8, 2006.

[73] T. P C Klaver, R. Drautz, and M. W. Finnis. Magnetism and thermodynamics of defect-free Fe-Cr alloys. *Physical Review B - Condensed Matter and Materials Physics*, 74(9):1–11, 2006.

[74] G. Bonny, P. Erhart, A. Caro, R. C. Pasianot, L. Malerba, and M. Caro. The influence of short range order on the thermodynamics of Fe-Cr alloys. *Modelling and Simulation in Materials Science and Engineering*, 17(2), 2009.

[75] G. Bonny, D. Terentyev, and L. Malerba. New contribution to the thermodynamics of fe-cr alloys as base for ferritic steels. *Journal of Phase Equilibria and Diffusion*, 31(5):439–444, 2010.

[76] M.H. Mathon, Y. de Carlan, G. Geoffroy, X. Averty, A. Alamo, and C.H. de Novion. A SANS investigation of the irradiation-enhanced α-αâĂš phases separation in 7-12 Cr martensitic steels. *Journal of Nuclear Materials*, 312(2-3):236–248, feb 2003.

[77] M. Bachhav, G. Robert Odette, and E.A. Marquis. α' precipitation in neutron-irradiated Fe-Cr alloys. *Scripta Materialia*, 74:48–51, mar 2014.

[78] V. Kuksenko, C. Pareige, and P. Pareige. Cr precipitation in neutron irradiated industrial purity Fe-Cr model alloys. *Journal of Nuclear Materials*, 432(1-3):160–165, jan 2013.

[79] C. Heintze, F. Bergner, A. Ulbricht, and H. Eckerlebe. The microstructure of neutron-irradiated Fe-Cr alloys: A small-angle neutron scattering study. *Journal of Nuclear Materials*, 409(2):106–111, 2011.

[80] O. Tissot, C. Pareige, E. Meslin, B. Decamps, and J. Henry. Kinetics of α' precipitation in an electron-irradiated Fe15Cr alloy. *Scripta Materialia*, 122:31–35, 2016.

[81] O. Tissot, C. Pareige, E. Meslin, B. Décamps, and J. Henry. Influence of injected interstitials on α' precipitation in Fe-Cr alloys under self-ion irradiation. *Materials Research Letters*, 5(2):117–123, mar 2017.

[82] C. Pareige, V. Kuksenko, and P. Pareige. Behaviour of P, Si, Ni impurities and Cr in self ion irradiated Fe-Cr alloys - Comparison to neutron irradiation. *Journal of Nuclear Materials*, 456:471–476, 2015.

[83] C. Heintze, F. Bergner, M. Hernández-Mayoral, R. Kögler, G. Müller, and A. Ulbricht. Irradiation hardening of Fe-9Cr-based alloys and ODS Eurofer: Effect of helium implantation and iron-ion irradiation at 300 C including sequence effects. *Journal of Nuclear Materials*, 470:258–267, 2016.

[84] G. Bonny, D. Terentyev, J. Elena, A. Zinovev, B. Minov, and E.E. Zhurkin. Assessment of hardening due to dislocation loops in bcc iron: Overview and analysis of atomistic simulations for edge dislocations. *Journal of Nuclear Materials*, 473:283–289, 2016.

[85] R. Nakai, K. Yabuuchi, S. Nogami, and A. Hasegawa. The effect of voids on the hardening of body-centered cubic Fe. *Journal of Nuclear Materials*, 471:233–238, 2016.

[86] D. Terentyev, G. Bonny, and L. Malerba. Strengthening due to coherent Cr precipitates in Fe-Cr alloys: Atomistic simulations and theoretical models. *Acta Materialia*, 56(13):3229–3235, aug 2008.

[87] A. Kohyama, A. Hishinuma, D.S. Gelles, R.L. Klueh, W. Dietz, and K. Ehrlich. Low-activation ferritic and martensitic steels for fusion application. *Journal of Nuclear Materials*, 233-237(PART 1):138–147, 1996.

[88] A. Kohyama, Y. Kohno, K. Asakura, and H. Kayano. R&D of low activation ferritic steels for fusion in japanese universities. *Journal of Nuclear Materials*, 212-215(PART 1):684–689, 1994.

[89] R.L. Klueh and D.J. Alexander. Impact behavior of reduced-activation steels irradiated to 24 dpa. *Journal of Nuclear Materials*, 233-237(PART 1):336–341, 1996.

[90] F. Bergner, C. Pareige, M. Hernández-Mayoral, L. Malerba, and C. Heintze. Application of a three-feature dispersed-barrier hardening model to neutron-irradiated Fe-Cr model alloys. *Journal of Nuclear Materials*, 448(1-3):96–102, 2014.

[91] C. Heintze, F. Bergner, and M. Hernández-Mayoral. Ion-irradiation-induced damage in Fe-Cr alloys characterized by nanoindentation. *Journal of Nuclear Materials*, 417(1-3):980–983, 2011.

[92] S. Lozano-Perez, M.L. Jenkins, and J.M. Titchmarsh. Evidence for deformation-induced transformations of Cu-rich precipitates in an aged FeCu alloy. *Philosophical Magazine Letters*, 86(6):367–374, 2006.

[93] M. Hiratani and V.V. Bulatov. Solid-solution hardening by point-like obstacles of different kinds. *Philosophical Magazine Letters*, 84(7):461–470, 2004.

[94] M. Bachhav, L. Yao, G.R. Odette, and E.A. Marquis. Microstructural changes in a neutron-irradiated Fe-6 at.%Cr alloy. *Journal of Nuclear Materials*, 453(1-3):334–339, 2014.

[95] D. Terentyev, F. Bergner, and Y. Osetsky. Cr segregation on dislocation loops enhances hardening in ferritic Fe-Cr alloys. *Acta Materialia*, 61(5):1444–1453, mar 2013.

[96] H. Wagenblast and A.C. Damask. Kinetics of carbon precipitation in irradiated iron. *Journal of Physics and Chemistry of Solids*, 23:221–227, 1962.

[97] F.E. Fujita and A.C. Damask. Kinetics of carbon precipitation in irradiated iron - II electrical resistivity measurements. *Acta metallurgica*, 1964.

[98] R.A. Arndt and A.C. Damask. Kinetics of carbon precipitation in irradiated iron - III. Calorimetry. *Acta Metallurgica*, pages 0–4, 1964.

[99] H. Wagenblast, F.E. Fujita, and A.C. Damask. Kinetics of carbon precipitation in irradiated iron - IV electron microscope observations. *Acta Metallurgica*, 1964.

[100] A. Vehanen and P. Hautojarvi. Vacancies and carbon impurities in alpha-iron: Electron irradiation. *Physical Review B*, 25(2):762–780, 1982.

[101] S. Takaki, J. Fuss, H. Kuglers, U. Dedek, and H. Schultz. The resistivity recovery of high purity and carbon doped iron following low temperature electron irradiation. *Radiation Effects*, 79(1-4):87–122, jan 1983.

[102] C. Domain, C. Becquart, and J. Foct. Ab initio study of foreign interstitial atom (C, N) interactions with intrinsic point defects in α-Fe. *Physical Review B*, 69(14):144112, apr 2004.

[103] C. Först, J. Slycke, K. Van Vliet, and S. Yip. Point Defect Concentrations in Metastable Fe-C Alloys. *Physical Review Letters*, 96(17):175501, may 2006.

[104] C.S. Becquart, J.M. Raulot, G. Bencteux, C. Domain, M. Perez, S. Garruchet, and H. Nguyen. Atomistic modeling of an Fe system with a small concentration of C. *Computational Materials Science*, 40(1):119–129, jul 2007.

[105] T. Ohnuma, N. Soneda, and M. Iwasawa. First-principles calculations of vacancy - solute element interactions in body-centered cubic iron. *Acta Materialia*, 57(20):5947–5955, dec 2009.

[106] T. Jourdan, C.C. Fu, L. Joly, J.L. Bocquet, M.J. Caturla, and F. Willaime. Direct simulation of resistivity recovery experiments in carbon-doped α-iron. *Physica Scripta*, T145:014049, dec 2011.

[107] D. Terentyev, G. Bonny, A. Bakaev, and D. Van Neck. On the thermal stability of vacancy - carbon complexes in alpha iron. *Journal of Physics: Condensed Matter*, 24(38):385401, sep 2012.

[108] K. Tapasa, A. Barashev, D. Bacon, and Y. Osetsky. Computer simulation of carbon diffusion and vacancy - carbon interaction in α-iron. *Acta Materialia*, 55(1):1–11, jan 2007.

[109] C-C Fu, J.D. Torre, F. Willaime, J-L Bocquet, and A. Barbu. Multiscale modelling of defect kinetics in irradiated iron. *Nature Materials*, 4(1):68–74, dec 2004.

[110] J. Diehl, U. Merbold, and M. Weller. Information on vacancy migration in α-iron from annealing experiments. *Scripta Metallurgica*, 11(9):811–816, sep 1977.

[111] M. Kiritani, H. Takata, K. Moriyama, and F.E. Fujita. Mobility of lattice vacancies in iron. *Philosophical Magazine A: Physics of Condensed Matter, Structure, Defects and Mechanical Properties*, 40(6):779–802, 1979.

[112] L. Malerba, G.J. Ackland, C.S. Becquart, G. Bonny, C. Domain, S.L. Dudarev, C.-C. Fu, D. Hepburn, M.C. Marinica, P. Olsson, R.C. Pasianot, J.M. Raulot, F. Soisson, D. Terentyev, E. Vincent, and F. Willaime. Ab initio calculations and interatomic potentials for iron and iron alloys: Achievements within the Perfect Project. *Journal of Nuclear Materials*, 406(1):7–18, nov 2010.

[113] A.F. Calder, D.J. Bacon, A.V. Barashev, and Y.N. Osetsky. Computer simulation of cascade damage in α-iron with carbon in solution. *Journal of Nuclear Materials*, 382(2-3):91–95, dec 2008.

[114] D. Terentyev, N. Anento, A. Serra, V. Jansson, H. Khater, and G. Bonny. Interaction of carbon with vacancy and self-interstitial atom clusters in α-iron studied using metallic - covalent interatomic potential. *Journal of Nuclear Materials*, 408(3):272–284, jan 2011.

[115] Y. Satoh, H. Matsui, and T. Hamaoka. Effects of impurities on one-dimensional migration of interstitial clusters in iron under electron irradiation. *Physical Review B*, 77(9):094135, mar 2008.

[116] Y. Satoh and H. Matsui. Obstacles for one-dimensional migration of interstitial clusters in iron. *Philosophical Magazine*, 89(18):1489–1504, jun 2009.

[117] B.D. Wirth, G.R. Odette, D. Maroudas, and G.E. Lucas. Dislocation loop structure, energy and mobility of self-interstitial atom clusters in bcc iron. *Journal of Nuclear Materials*, 276(1):33–40, 2000.

[118] D. Terentyev, L. Malerba, and M. Hou. Dimensionality of interstitial cluster motion in bcc-Fe. *Physical Review B*, 75(10):104108, mar 2007.

[119] K. Arakawa, K. Ono, M. Isshiki, K. Mimura, M. Uchikoshi, and H. Mori. Observation of the one-dimensional diffusion of nanometer-sized dislocation loops. *Science*, 318(5852):956–959, 2007.

[120] D. Terentyev, N. Anento, and A. Serra. Interaction of <100> loops with Carbon atoms and <100> dislocations in BCC Fe: An atomistic study. *Journal of Nuclear Materials*, 420(1-3):9–15, jan 2012.

[121] N. Anento and A. Serra. Carbon - vacancy complexes as traps for self-interstitial clusters in Fe-C alloys. *Journal of Nuclear Materials*, 440(1-3):236–242, sep 2013.

[122] Y. Abe, T. Suzudo, S. Jitsukawa, T. Tsuru, and T. Tsukada. Effects of Carbon Impurity on Microstructural Evolution in Irradiated α-Iron. *Fusion Science and Technology*, 62(1):139–144, aug 2012.

[123] V. Jansson and L. Malerba. Simulation of the nanostructure evolution under irradiation in Fe-C alloys. *Journal of Nuclear Materials*, 443(1-3):274–285, nov 2013.

[124] V. Jansson, M. Chiapetto, and L. Malerba. The nanostructure evolution in Fe-C systems under irradiation at 560K. *Journal of Nuclear Materials*, 442(1-3):341–349, nov 2013.

[125] V. Jansson and L. Malerba. OKMC simulations of Fe-C systems under irradiation: Sensitivity studies. *Journal of Nuclear Materials*, 452(1-3):118–124, sep 2014.

[126] M. Lambrecht, L. Malerba, and A. Almazouzi. Influence of different chemical elements on irradiation-induced hardening embrittlement of RPV steels. *Journal of Nuclear Materials*, 378(3):282–290, sep 2008.

[127] M. Lambrecht and A. Almazouzi. Positron annihilation study of neutron irradiated model alloys and of a reactor pressure vessel steel. *Journal of Nuclear Materials*, 385(2):334–338, 2009.

[128] D. Terentyev, N. Anento, and A. Serra. Interaction of dislocations with carbon-decorated dislocation loops in bcc Fe: an atomistic study. *Journal of physics. Condensed matter : an Institute of Physics journal*, 24(45):455402, nov 2012.

[129] Yu N. Osetsky and D.J. Bacon. An atomic-level model for studying the dynamics of edge dislocations in metals. *Modelling and Simulation in Materials Science and Engineering*, 11(4):427–440, 2003.

[130] E.A. Marquis, B.D. Wirth, and G.S. Was. Characterization and Modeling of Grain Boundary Chemistry Evolution in Ferritic Steels under Irradiation: Nuclear Energy Advanced Modeling and Simulation. Technical report, 2016.

[131] J.G. Gigax, H. Kim, E. Aydogan, F.A. Garner, S. Maloy, and L. Shao. Beam-contamination-induced compositional alteration and its neutron-atypical consequences in ion simulation of neutron-induced void swelling. *Materials Research Letters*, 0(0):1–8, may 2017.

[132] G.S. Was, S. Taller, Z. Jiao, A.M. Monterrosa, D. Woodley, D. Jennings, T. Kubley, F. Naab, O. Toader, and E. Uberseder. Resolution of the carbon contamination problem in ion irradiation experiments. *Nuclear Instruments and Methods in Physics Research, Section B: Beam Interactions with Materials and Atoms*, 412:58–65, 2017.

[133] L. Malerba. Molecular dynamics simulation of displacement cascades in α-Fe: A critical review. *Journal of Nuclear Materials*, 351(1-3):28–38, 2006.

[134] D. Terentyev, C. Lagerstedt, P. Olsson, K. Nordlund, J. Wallenius, C.S. Becquart, and L. Malerba. Effect of the interatomic potential on the features of displacement cascades in α-Fe: A molecular dynamics study. *Journal of Nuclear Materials*, 351(1-3):65–77, jun 2006.

[135] R.E. Stoller and L.R. Greenwood. Subcascade formation in displacement cascade simulations: Implications for fusion reactor materials. *Journal of Nuclear Materials*, 271-272:57–62, may 1999.

[136] E. Zarkadoula, S.L. Daraszewicz, D.M. Duffy, M.A. Seaton, I.T. Todorov, K. Nordlund, M.T. Dove, and K. Trachenko. The nature of high-energy radiation damage in iron. *J. Phys. Condens. Matter*, 25:125402, 2013.

[137] C. Björkas, K. Nordlund, and M.J. Caturla. Influence of the picosecond defect distribution on damage accumulation in irradiated α-Fe. *Physical Review B - Condensed Matter and Materials Physics*, 85(2):1–8, 2012.

[138] H. Wiedersich. Effects of the primary recoil spectrum on microstructural evolution. *Journal of Nuclear Materials*, 179-181(PART 1):70–75, 1991.

[139] L.E. Rehn. Production of freely-migrating defects. *Journal of Nuclear Materials*, 174(2-3):144–150, 1990.

[140] L.E. Rehn and R.C. Birtcher. Experimental studies of free defect generation during irradiation - Implications for reactor environments. *Journal of Nuclear Materials*, 205(C):31–39, 1993.

[141] R.S. Averback. Atomic displacement processes in irradiated metals. *Journal of Nuclear Materials*, 216(C):49–62, 1994.

[142] S.J. Zinkle and L.L. Snead. Opportunities and limitations for ion beams in radiation effects studies: Bridging critical gaps between charged particle and neutron irradiations. *Scripta Materialia*, 2016.

[143] R.S. Nelson, D.J. Mazey, and J.A. Hudson. The use of ion accelerators to simulate fast neutron-induced voidage in metals. *Journal of Nuclear Materials*, 37:1–12, 1970.

[144] S. Ishino. Implications of fundamental radiation damage studies in the research and development of materials for a fusion reactor. *Journal of Nuclear Materials*, 239:24–33, dec 1996.

[145] C. Abromeit. Aspects of simulation of neutron damage by ion irradiation. *Journal of Nuclear Materials*, 216:78–96, oct 1994.

[146] N.H. Packan, K. Farrell, and J.O. Stiegler. Correlation of neutron and heavy-ion damage: I. The influence of dose rate and injected helium on swelling in pure nickel. *Journal of Nuclear Materials*, 78:143–155, 1978.

[147] L.K. Mansur. Correlation of Neutron and Heavy-Ion Damage II. The predicted temperature shift if swelling with changes in radiation dose rate. *Journal of Nuclear Materials*, 78:156–160, 1978.

[148] N.M. Ghoniem and G.L. Kulcinski. The effect of damage rate on void growth in metals. *Journal of Nuclear Materials*, 82(2):392–402, 1979.

[149] T. Okita, T. Kamada, and N. Sekimura. Effects of dose rate on microsturctural evolution and swelling in austenitic steels under irradiation. *Journal of Nuclear Materials*, 287:220–223, 2000.

[150] T. Okita, T. Sato, N. Sekimura, F.A. Garner, and L.R. Greenwood. The primary origin of dose rate effects on microstructural evolution of austenitic alloys during neutron irradiation. *Journal of Nuclear Materials*, 307-311:322–326, dec 2002.

[151] T. Okita, T. Sato, N. Sekimura, T. Iwai, and F.A. Garner. The synergistic influence of temperature and displacement rate on microstructural evolution of ion-irradiated FeâĂŞ15CrâĂŞ16Ni model austenitic alloy. *Journal of Nuclear Materials*, 367-370:930–934, aug 2007.

[152] T.R. Allen, J.I. Cole, C.L. Trybus, D.L. Porter, H. Tsai, F.A. Garner, E.A. Kenik, T. Yoshitake, and Joji Ohta. The effect of dose rate on the response of austenitic stainless steels to neutron radiation. *Journal of Nuclear Materials*, 348(1-2):148–164, 2006.

[153] T. Muroga, H. Watanabe, and N. Yoshida. Correlation of fast neutron, fusion neutron and electron irradiations based on the dislocation loop density. *Journal of Nuclear Materials*, 174(2-3):282–288, nov 1990.

[154] C.D. Hardie, C.A. Williams, S. Xu, and S.G. Roberts. Effects of irradiation temperature and dose rate on the mechanical properties of self-ion implanted Fe and Fe-Cr alloys. *Journal of Nuclear Materials*, 439(1-3):33–40, aug 2013.

[155] G.W. Lewthwaite and D. Mosedale. The effects of temperature and dose-rate variations on the creep of austenitic stainless steels in the dounreay fast reactor. *Journal of Nuclear Materials*, 90(1-3):205–215, 1980.

[156] T. Okita, N. Sekimura, and F.A. Garner. Effects of dpa rate on swelling in neutron-irradiated FeâĂŞCr and FeâĂŞCrâĂŞMo alloys. *Journal of Nuclear Materials*, 417(1-3):944–948, 2011.

[157] L. Boulanger and Y. Serruys. Dislocation loops in Eurofer and a Fe-Cr alloy irradiated by ions at 350 and 550 C at 3 dpa: Effect of dose rate. *Journal of Nuclear Materials*, 386-388(C):441–444, 2009.

[158] A.E. Sand, M.J. Aliaga, M.J. Caturla, and K. Nordlund. Surface effects and statistical laws of defects in primary radiation damage: Tungsten vs. iron. *EPL (Europhysics Letters)*, 115(3):36001, 2016.

[159] L.K. Mansur. Theory of transitions in dose dependence of radiation effects in structural alloys. *Journal of Nuclear Materials*, 206(2-3):306–323, nov 1993.

[160] G.S. Was, J.T. Busby, T.R. Allen, and E.A. Kenik. Emulation of neutron irradiation effects with protons: validation of principle. *Journal of Nuclear Materials*, 300:198–216, 2002.

[161] G.S. Was and T. Allen. Radiation-induced segregation in multicomponent alloys: Effect of particle type. *Materials Characterization*, 32(4):239–255, 1994.

[162] G.S. Was, Z. Jiao, E. Getto, K. Sun, A.M. Monterrosa, S.A. Maloy, O. Anderoglu, B.H. Sencer, and M. Hackett. Emulation of reactor irradiation damage using ion beams. *Scripta Materialia*, 88:33–36, oct 2014.

[163] M. Kiritani, T. Yoshiie, and S. Kojima. Fission-fusion correlation by fission reactor irradiation with improved control. *Journal of Nuclear Materials*, 174:327–351, 1990.

[164] A.D. Brailsford and L.K. Mansur. Effect of self-ion injection in simulation studies of void swelling. *Journal of Nuclear Materials*, 71:110–116, 1977.

[165] D.L. Plumton, H. Attaya, and W.G. Wolfer. Conditions for the Suppression of Void Formation During Ion-Bombardment. *Journal of Nuclear Materials*, 122 & 123:650–653, 1984.

[166] D.L. Plumton and W.G. Wolfer. Supression of void nucleation by injected interstitials during heavy ion bombardment. *Journal of Nuclear Materials*, 120:245–253, 1984.

[167] E.H. Lee, L.K. Mansur, and M.H. Yoo. Spatial variation in void volume during charged particle bombardment - the effects of injected interstitials. *Journal of Nuclear Materials*, 85-86(PART 1):577–581, 1979.

[168] L. Shao, C.-C. Wei, J. Gigax, A. Aitkaliyeva, D. Chen, B.H. Sencer, and F.A. Garner. Effect of defect imbalance on void swelling distributions produced in pure iron irradiated with 3.5 MeV self-ions. *Journal of Nuclear Materials*, 453(1-3):176–181, 2014.

[169] M.A. Kirk and L.R. Greenwood. Determination of the neutron flux and energy spectrum in the low-temperature fast-neutron facility in CP-5, calculations of primary-recoil and damage-energy distributions, and comparisons with experiment. *Journal of Nuclear Materials*, 80(1):159–171, 1979.

[170] P. Jung. Average atomic-displacement energies of cubic metals. *Physical Review B*, 23(2):664–670, 1981.

[171] C. Jaouen, J.P. Rivikre, C. Templier, and J. Delafond. Production de Defauts dans des Films de Fer; Etude en Fonction de la Densite d'Energie Deposee dans les Cascades. *Journal of Nuclear Materials*, 131:11–19, 1985.

[172] S. Takamura, T. Aruga, and K. Nakata. Fission-neutron displacement cross sections in metals. *Journal of Nuclear Materials*, 136(2-3):159–163, 1985.

[173] G. Wallner, M.S. Anand, L.R. Greenwood, M.A. Kirk, W. Mansell, and W. Waschkowski. Defect production rates in metals by reactor neutron irradiation at 4.6 K. *Journal of Nuclear Materials*, 152(2-3):146–153, 1988.

[174] C.E. Klabunde and R.R. Coltman. Fission neutron damage rates and efficiencies in several metals. *Journal of Nuclear Materials*, 108-109(C):183–193, 1982.

[175] J.A. Horak and T.H. Blewitt. Fast neutron irradiation induced resistivity in metals. *Physica Status Solidi (a)*, 9(2):721–730, 1972.

[176] M. Hernández-Mayoral and D. Gómez-Briceño. Transmission electron microscopy study on neutron irradiated pure iron and RPV model alloys. *Journal of Nuclear Materials*, 399(2-3):146–153, 2010.

[177] M.R. Gilbert, S.L. Dudarev, S. Zheng, L.W. Packer, and J.-Ch. Sublet. An integrated model for materials in a fusion power plant: transmutation, gas production, and helium embrittlement under neutron irradiation. *Nuclear Fusion*, 52(8):083019, 2012.

[178] R. Schäublin, J. Henry, and Y. Dai. Helium and point defect accumulation: (i) microstructure and mechanical behaviour. *Comptes Rendus Physique*, 9(3-4):389–400, apr 2008.

[179] M.R. Gilbert, S.L. Dudarev, D. Nguyen-Manh, S. Zheng, L.W. Packer, and J.Ch Sublet. Neutron-induced dpa, transmutations, gas production, and helium embrittlement of fusion materials. *Journal of Nuclear Materials*, 442(1-3 SUPPL.1):S755–S760, 2013.

[180] N. Hashimoto, R.L. Klueh, and K. Shiba. Pros and cons of nickel- and boron-doping to study helium effects in ferritic/martensitic steels. *Journal of Nuclear Materials*, 307-311:222–228, dec 2002.

[181] T. Yamamoto, G.R. Odette, P. Miao, D.T. Hoelzer, J. Bentley, N. Hashimoto, H. Tanigawa, and R.J. Kurtz. The transport and fate of helium in nanostructured ferritic alloys at fusion relevant He/dpa ratios and dpa rates. *Journal of Nuclear Materials*, 367-370:399–410, aug 2007.

[182] T. Tanaka, K. Oka, S. Ohnuki, S. Yamashita, T. Suda, S. Watanabe, and E. Wakai. Synergistic effect of helium and hydrogen for defect evolution under multi-ion irradiation of FeâĂŞCr ferritic alloys. *Journal of Nuclear Materials*, 329-333:294–298, aug 2004.

[183] A. Prokhodtseva, B. Décamps, A. Ramar, and R. Schäublin. Impact of He and Cr on defect accumulation in ion-irradiated ultrahigh-purity Fe(Cr) alloys. *Acta Materialia*, 61(18):6958–6971, oct 2013.

[184] D. Brimbal, B. Décamps, J. Henry, E. Meslin, and A. Barbu. Single- and dual-beam in situ irradiations of high-purity iron in a transmission electron microscope: Effects of heavy ion irradiation and helium injection. *Acta Materialia*, 64:391–401, feb 2014.

[185] B. Kaiser, C. Dethloff, E. Gaganidze, D. Brimbal, M. Payet, P. Trocellier, L. Beck, and J. Aktaa. TEM study and modeling of bubble formation in dual-beam He+/Fe3+ ion irradiated EUROFER97. *Journal of Nuclear Materials*, 484:59–67, 2017.

[186] T. Yamamoto, G.R. Odette, P. Miao, D.J. Edwards, and R.J. Kurtz. Helium effects on microstructural evolution in tempered martensitic steels: In situ helium implanter studies in HFIR. *Journal of Nuclear Materials*, 386-388(C):338–341, 2009.

[187] E.M. Grieveson. *Irradiation Effects on the Deformation of Oxide Dispersion Strengthened Steels*. PhD thesis, University of Oxford, 2015.

[188] L. Peng and Y. Dai. Helium-induced hardening effect in ferritic/martensitic steels F82H and Optimax-A irradiated in a mixed spectrum of high energy protons and spallation neutrons. *Journal of Nuclear Materials*, 417(1-3):996–1000, 2011.

[189] E.M. Grieveson and S.G. Roberts. Investigation into irradiation effects in ODS steels using ion implantation and micromechanical testing. In *2013 IEEE 25th Symposium on Fusion Engineering, SOFE 2013*, pages 6–9, 2013.

[190] S.M. Hafez Haghighat, G. Lucas, and R. Schäublin. Atomistic simulation of He bubble in Fe as obstacle to dislocation. *IOP Conference Series: Materials Science and Engineering*, 3:012013, jul 2009.

[191] R. Schäublin and Y.L. Chiu. Effect of helium on irradiation-induced hardening of iron: A simulation point of view. *Journal of Nuclear Materials*, 362(2-3):152–160, may 2007.

[192] W.R. Wampler, T. Schober, and B. Lengeler. Precipitation and trapping of hydrogen in copper. *Philosophical Magazine*, 34(1):129–141, 1976.

[193] K. Shiraishi, A. Hishinuma, and Y. Katano. Radiation-generated prismatic loops around gas bubbles in alumnium-lithium alloy. *Radiation Effects*, 21(3):161–164, 1974.

[194] Y. Dai, J. Henry, Z. Tong, X. Averty, J. Malaplate, and B. Long. Neutron/proton irradiation and He effects on the microstructure and mechanical properties of ferritic/martensitic steels T91 and EM10. *Journal of Nuclear Materials*, 415(3):306–310, aug 2011.

[195] P. Jung, J. Henry, J. Chen, and J.-C. Brachet. Effect of implanted helium on tensile properties and hardness of 9% Cr martensitic stainless steels. *Journal of Nuclear Materials*, 318:241–248, may 2003.

[196] L. Zhang, C.C. Fu, E. Hayward, and G.H. Lu. Properties of He clustering in α-Fe grain boundaries. *Journal of Nuclear Materials*, 459:247–258, 2015.

[197] E. Wakai, N. Hashimoto, Y. Miwa, J.P. Robertson, R.L. Klueh, K. Shiba, and S. Jistukawa. Effect of helium production on swelling of F82H irradiated in HFIR. *Journal of Nuclear Materials*, 283-287(2000):799–805, 2000.

[198] F.A. Garner, D.S. Gelles, L.R. Greenwood, T. Okita, N. Sekimura, and W.G. Wolfer. Synergistic influence of displacement rate and helium/dpa ratio on swelling of Fe-(9, 12)Cr binary alloys in FFTF at 400 C. *Journal of Nuclear Materials*, 329-333(1-3 PART B):1008–1012, 2004.

[199] E. Wakai, T. Sawai, K. Furuya, A. Naito, T. Aruga, K. Kikuchi, S. Yamashita, S. Ohnuki, S. Yamamoto, H. Naramoto, and S. Jistukawa. Effect of triple ion beams in ferritic/martensitic steel on swelling behavior. *Journal of Nuclear Materials*, 307-311:278–282, dec 2002.

[200] E. Wakai, K. Kikuchi, S. Yamamoto, T. Aruga, M. Ando, H. Tanigawa, T. Taguchi, T. Sawai, K. Oka, and S. Ohnuki. Swelling behavior of F82H steel irradiated by triple/dual ion beams. *Journal of Nuclear Materials*, 318(SUPPL):267–273, 2003.

[201] J.A. Sprague, F.A. Smidt, Jr., J.E. Westmoreland, and P.R. Malmberg. The effect of Ion-Beam Scanning on the Microstructure of Nickel-Ion Bombarded Nickel. *Report of NRL Progress*, (February 1973):45–47, 1973.

[202] N.M. Ghoniem and G. Kulcinski. A rate theory approach to time dependent microstructural development during irradiation. *Radiation Effects*, 39(1):47–56, jan 1978.

[203] E.P. Simonen, N.M. Ghoniem, and N.H. Packan. Pulsed flux effects on radiation damage. *Journal of Nuclear Materials*, 123:391–401, 1984.

[204] H. Trinkaus and H. Ullmaier. Conditions for effects of radiation pulsing. *Journal of Nuclear Materials*, 307-311:1705–1709, dec 2002.

[205] H. Gurol and N. M. Ghoniem. Irradiation creep by the climb-controlled glide mechanism in pulsed fusion reactors. *Radiation Effects*, 52(1-2):103–125, jan 1980.

[206] H. Trinkaus and H. Ullmaier. Does pulsing in spallation neutron sources affect radiation damage? *Journal of Nuclear Materials*, 296, 2001.

[207] J.L. Brimhall, L.A. Charlot, and E.P. Simonen. Effect of pulsed irradiation on void swelling in nickel. *Journal of Nuclear Materials*, 104:1147–1150, 1981.

[208] J.L. Brimhall, E.P. Simonen, and L.A. Charlot. Void growth in a pulsed irradiation environment. *Journal of Nuclear Materials*, 117:118–122, 1983.

[209] J.L. Brimhall, E.P. Simonen, and L.A. Charlot. Pulsed ion irradiated microstructures in molybdenum. *Journal of Nuclear Materials*, 123:579–583, 1984.

[210] E.H. Lee, N.H. Packan, and L.K. Mansur. Effects of pulsed dual-ion irradiation on phase transformations and microstructure in Ti-modified austenitic alloy. *Journal of Nuclear Materials*, 117:123–133, 1983.

[211] A. Hishinuma and N.H. Packan. Effects of pulsed and/or dual ion irradiation on microstructural evolution in a Ti and Si modified austenitic alloy. *Journal of Nuclear Materials*, 123:260–265, 1984.

[212] N.H. Packan. The effect of pulsed irradiation on microstructural evolution. *Radiation Effects*, 101(1-4):189–198, jan 1987.

[213] L.K. Mansur. Theory and experimental background on dimensional changes in irradiated alloys. *Journal of Nuclear Materials*, 216(C):97–123, 1994.

[214] N.M. Ghoniem and G.L. Kulcinski. The effect of pulsed irradiation on the swelling of 316 stainless steel in fusion reactors. *Nuclear Engineering and Design*, 52:111–125, 1979.

[215] L.K. Mansur, W.A. Coghlan, and A.D. Brailsford. Swelling with inhomogeneous point defect production - a cascade diffusion theory. *Journal of Nuclear Materials*, 86:591–595, 1979.

[216] V. Kuksenko, C. Pareige, C. Genevois, and P. Pareige. Characterisation of Cr, Si and P distribution at dislocations and grain-boundaries in neutron irradiated Fe-Cr model alloys of low purity. *Journal of Nuclear Materials*, 434(1-3):49–55, mar 2013.

[217] V. Kuksenko. *Model Oriented Irradiation Experiments in Fe-Cr Model Alloys*. PhD thesis, Université de Rouen, 2011.

[218] M. Hernández-Mayoral, C. Heintze, and E. Oñorbe. Transmission electron microscopy investigation of the microstructure of Fe-Cr alloys induced by neutron and ion irradiation at 300 C. *Journal of Nuclear Materials*, 474:88–98, 2016.

[219] Y. Wu, P. Wells, G.R. Odette, T. Yamamoto, S.G. Roberts, C.D. Hardie, A. Bhattacharya, M. Bachhav, and E.A. Marquis. Microstructural characterization of a Fe + irradiated Fe-6 % Cr alloy. *Report on the Fusion Reactor Materials Program*, pages 8–11, 2015.

[220] Z. Jiao, J. Michalicka, and G.S. Was. Self-ion emulation of high dose neutron irradiated microstructure in stainless steels. *Journal of Nuclear Materials*, 501:312–318, 2018.

[221] J.B. Pethica, R. Hutchings, and W.C. Oliver. Hardness measurement at penetration depths as small as 20 nm. *Philosophical Magazine A*, 48(4):593–606, apr 1983.

[222] W.C. Oliver and G.M. Pharr. Nanoindentation in materials research: past, present, and future. *MRS bulletin*, 35(November), 2010.

[223] W.C. Oliver and G.M. Pharr. An improved technique for determining hardness and elastic modulus using load and displacement sensing indentation experiments. *Journal of materials research*, 7(6):1564–1583, 1992.

[224] M.R. Vanlandingham. Review of Instrumented Indentation. *Journal of Research of the National Institue of Standards and Technology*, 108(4):249–265, 2003.

[225] I.N. Sneddon. The Relation Between Load and Penetration in the Axisymmetric Boussinesq Problem for a Punch of Arbitrary Profile. *International Journal of Engineering Science*, 3(638):47–57, 1965.

[226] G.M. Pharr, W.C. Oliver, and F.R. Brotzen. On the generality of the relationship among contact stiffness , contact area , and elastic modulus during indentation. *Journal of Materials Research*, 7(3):613–617, 1992.

[227] R.B. King. Elastic analysis of some punch problems for a layered medium. *International Journal of Solids and Structures*, 23(12):1657–1664, 1987.

[228] D. Di Maio and S.G. Roberts. Measuring fracture toughness of coatings using focused-ion-beam-machined microbeams. *Journal of Materials Research*, 20(02):299–302, mar 2011.

[229] D.E.J. Armstrong. *Measuring Elastic , Plastic and Fracture Properties using Micro-Cantilever Testing*. PhD thesis, University of Oxford, 2009.

[230] D.E.J. Armstrong, A.J. Wilkinson, and S.G. Roberts. Measuring anisotropy in Young's modulus of copper using microcantilever testing. *Journal of Materials Research*, 24(11):3268–3276, jan 2011.

[231] C.D. Hardie. *Micro-Mechanics of Irradiated Fe-Cr Alloys for Fusion Reactors*. PhD thesis, University of Oxford, 2013.

[232] D.E.J. Armstrong, C.D. Hardie, J.S.K.L. Gibson, A.J. Bushby, P.D. Edmondson, and S.G. Roberts. Small-scale characterisation of irradiated nuclear materials: Part II nanoindentation and micro-cantilever testing of ion irradiated nuclear materials. *Journal of Nuclear Materials*, 462:374–381, 2015.

[233] G. Piazzesi. Photogrammetry with the scanning electron microscope. *Journal of Physics E: Scientific Instruments*, 6:392–396, 1973.

[234] J.M. Gere. *Mechanics of Materials*. 6th edition, 2006.

[235] https://docs.scipy.org/doc/scipy-0.13.0/reference/generated/scipy.optimize.curve_fit.html.

[236] W.D. Nix and H.J. Gao. Indentation size effects in crystalline materials: A law for strain gradient plasticity. *Journal of the Mechanics and Physics of Solids*, 46(3):411–425, 1998.

[237] W.D. Nix, J.R. Greer, G. Feng, and E.T. Lilleodden. Deformation at the nanometer and micrometer length scales: Effects of strain gradients and dislocation starvation. *Thin Solid Films*, 515(6):3152–3157, 2007.

[238] M.D. Uchic, P.A. Shade, and D.M. Dimiduk. Plasticity of Micrometer-Scale Single Crystals in Compression. *Annual Review of Materials Research*, 39(1):361–386, 2009.

[239] C. Motz, T. Schöberl, and R. Pippan. Mechanical properties of micro-sized copper bending beams machined by the focused ion beam technique. *Acta Materialia*, 53:4269–4279, 2005.

[240] E.T. Lilleodden. Coupled finite-volume and microstructural length-scale effects on the deformation of metals. In *35th Riso International Symposium on Materials Science. New Frontiers of Nanometals*, 2014.

[241] N.A. Fleck, G.M. Muller, M.F. Ashby, and J.W. Hutchinson. Strain Gradient Plasticity: Theory and Experiment. *Acta Metallurgica et Materialia*, 42(2):475–487, 1994.

[242] M.F. Ashby. The deformation of plastically non-homogeneous materials. *Philosophical Magazine*, 21(170):399–424, 1970.

[243] J.R. Greer, W.C. Oliver, and W.D. Nix. Size dependence of mechanical properties of gold at the micron scale in the absence of strain gradients. *Acta Materialia*, 53(6):1821–1830, 2005.

[244] J.R. Greer and W.D. Nix. Nanoscale gold pillars strengthened through dislocation starvation. *Physical Review B - Condensed Matter and Materials Physics*, 73(24):1–6, 2006.

[245] T.A. Parthasarathy, S.I. Rao, D.M. Dimiduk, M.D. Uchic, and D.R. Trinkle. Contribution to size effect of yield strength from the stochastics of dislocation source lengths in finite samples. *Scripta Materialia*, 56(4):313–316, 2007.

[246] S.I. Rao, D.M. Dimiduk, M. Tang, T.A. Parthasarathy, M.D. Uchic, and C. Woodward. Estimating the strength of single-ended dislocation sources in micron-sized single crystals. *Philosophical Magazine*, 87(30):4777–4794, 2007.

[247] B. Pan, Y. Shibutani, X. Zhang, and F. Shang. Effect of dislocation pile-up on size-dependent yield strength in finite single-crystal micro-samples. *Journal of Applied Physics*, 118(1), 2015.

[248] E. Tarleton, D.S. Balint, J. Gong, and A.J. Wilkinson. A discrete dislocation plasticity study of the micro-cantilever size effect. *Acta Materialia*, 88:271–282, 2015.

[249] C. Motz, D. Weygand, J. Senger, and P. Gumbsch. Micro-bending tests: A comparison between three-dimensional discrete dislocation dynamics simulations and experiments. *Acta Materialia*, 56(9):1942–1955, 2008.

[250] B. Gault, M.P. Moody, F. De Geuser, D. Haley, L.T. Stephenson, and S.P. Ringer. Origin of the spatial resolution in atom probe microscopy. *Applied Physics Letters*, 95(3), 2009.

[251] T.T. Tsong. Field ion image formation. *Surface Science*, 70(1):211–233, 1978.

[252] P. Bas, A. Bostel, B. Deconihout, and D. Blavette. A general protocol for the reconstruction of 3D atom probe data. *Applied Surface Science*, 87-88(C):298–304, 1995.

[253] V. Migunov, A. London, M. Farle, and R.E. Dunin-Borkowski. Model-independent measurement of the charge density distribution along an Fe atom probe needle using off-axis electron holography without mean inner potential effects. *Journal of Applied Physics*, 117(13), 2015.

[254] M.K. Miller and R.G. Forbes. *Atom-Probe Tomography : The Local Electrode Atom Probe*. Springer, 1 edition, 2014.

[255] F. Vurpillot, A. Bostel, and D. Blavette. The shape of field emitters and the ion trajectories in three- dimensional atom probes. *Journal of Microscopy*, 196(3):332–336, 1999.

[256] F. Vurpillot, A. Bostel, E. Cadel, and D. Blavette. The spatial resolution of 3D atom probe in the investigation of single-phase materials. *Ultramicroscopy*, 84(3-4):213–224, 2000.

[257] F. Vurpillot, A. Bostel, and D. Blavette. A new approach to the interpretation of atom probe field-ion microscopy images. *Ultramicroscopy*, 89(1-3):137–144, 2001.

[258] A.R. Waugh, E.D. Boyes, and M.J. Southon. Investigations of field evaporation with a field-desorption microscope. *Surface Science*, 61(1):109–142, 1976.

[259] M.K. Miller and M.G. Hetherington. Local magnification effects in the atom probe. *Surface Science*, 246(1-3):442–449, 1991.

[260] F. Vurpillot, A. Bostel, and D. Blavette. Trajectory overlaps and local magnification in three-dimensional atom probe. *Applied Physics Letters*, 76(21):3127–3129, 2000.

[261] B. Gault, M.P. Moody, F. De Geuser, G. Tsafnat, A. La Fontaine, L.T. Stephenson, D. Haley, and S.P. Ringer. Advances in the calibration of atom probe tomographic reconstruction. *Journal of Applied Physics*, 105(3), 2009.

[262] B. Gault, M.P. Moody, J.M. Cairney, and S.P. Ringer. Atom probe crystallography. *Materials Today*, 15(9):378–386, 2012.

[263] D. Haley. Libatomprobe - https://bitbucket.org/mycae_gmx/libatomprobe.

[264] A.J. Perry. The bond structure of computer-simulated field-ion images. *Philosophical Magazine*, 16(139):119–130, 1967.

[265] D. Haley. 3Depict - Visualisation & Analysis for Atom Probe.

[266] B. Gault, M.P. Moody, J.M. Cairney, and S.P. Ringer. *Atom Probe Microscopy*, volume 160 of *Springer Series in Materials Science*. Springer New York, New York, NY, 2012.

[267] A.J. London. *Irradiation Damage of Oxide Dispersion Strengthened Steels*. PhD thesis, Univeristy of Oxford, 2015.

[268] A.J. London. AtomProbeLab - https://sourceforge.net/projects/atomprobelab/.

[269] C. Hirst. *Atom probe tomography of element distributions in unirradiated and proton irradiated Zircaloy fuel cladding*. Part ii thesis, University of Oxford, 2015.

[270] G. Wahba. A Least Squares Estimate of Satellite Attitude. *SIAM Review*, 7(3):409–409, jul 1965.

[271] F.L. Markley. Attitude Determination Using Vector Observations and the Singular Value Decomposition. *Journal of the Astronautical Sciences*, 36(3):245–258, 1988.

[272] A Leygue. affine_fit(X) - https://uk.mathworks.com/matlabcentral/fileexchange/60502-affine_fit-x, 2013.

[273] K. Pearson. LIII. On lines and planes of closest fit to systems of points in space. *The London, Edinburgh, and Dublin Philosophical Magazine and Journal of Science*, 2(11):559–572, nov 1901.

[274] M.K. Miller and K.F. Russell. Atom probe specimen preparation with a dual beam SEM/FIB miller. *Ultramicroscopy*, 107(9):761–766, 2007.

[275] J. Le Coze, C. Varillon, D. Juhem, A. Reynaud, C. Collas, C. Lettori, G. Blanc, P. Leveque, Y. Garnier, C. Genevois, and A. Fraczkiewicz. EFDA âĂŞ Contract 06 âĂŞ 1901 TW6 âĂŞ TTMS 007- PUREFE Procurement of Pure Fe Metal and Fe-Based Alloys with Controlled Chemical Alloying Contents and Microstructure Final Report on Model Alloy Prepartion. Technical report, 2007.

[276] C. Varillon. Fe-3, Fe-8 et Fe-12%Cr Resultats d'Analyses Chimiques # 1586-1. Technical report, 2001.

[277] E.R. Reese, M. Bachhav, P. Wells, T. Yamamoto, G.R. Odette, and E.A. Marquis. On α' precipitate composition in thermally annealed and neutron-irradiated Fe-9-18Cr alloys. *Journal of Nuclear Materials*, 500:192–198, mar 2018.

[278] C.D. Hardie and S.G. Roberts. Nanoindentation of model Fe-Cr alloys with self-ion irradiation. *Journal of Nuclear Materials*, 433(1-3):174–179, feb 2013.

[279] V. Kuksenko, S. Roberts, and E. Tarleton. The hardness and modulus of polycrystalline beryllium from nano- indentation. *International Journal of Plasticity*, 116(September 2018):62–80, 2019.

[280] C.E. Beck, F. Hofmann, J.K. Eliason, A.A. Maznev, K.A. Nelson, and D.E.J. Armstrong. Correcting for contact area changes in nanoindentation using surface acoustic waves. *Scripta Materialia*, 128:83–86, 2017.

[281] C. Heintze, F. Bergner, S. Akhmadaliev, and E. Altstadt. Ion irradiation combined with nanoindentation as a screening test procedure for irradiation hardening. *Journal of Nuclear Materials*, 472:196–205, 2016.

[282] K. Kusunoki. Molecular-Dynamics Study of Self-Interstitial Diffusion in bcc-Iron. *Materials Transactions*, 47(8):1906–1909, 2006.

[283] . Huang, D.L. Worthington, M. Asta, V. Ozolins, G. Ghosh, and P.K. Liaw. Calculation of impurity diffusivities in a -Fe using first-principles methods. *Acta Materialia*, 58(6):1982–1993, 2010.

[284] N. Baluc, D.S. Gelles, S. Jitsukawa, a. Kimura, R.L. Klueh, G.R. Odette, B. van der Schaaf, and Jinnan Yu. Status of reduced activation ferritic/martensitic steel development. *Journal of Nuclear Materials*, 367-370:33–41, aug 2007.

[285] R.J. Kurtz, a. Alamo, E. Lucon, Q. Huang, S. Jitsukawa, a. Kimura, R.L. Klueh, G.R. Odette, C. Petersen, M.a. Sokolov, P. Spätig, and J.-W. Rensman. Recent progress toward development of reduced activation ferritic/martensitic steels for fusion structural applications. *Journal of Nuclear Materials*, 386-388:411–417, apr 2009.

[286] T.L. Maddock, S.M. Wilson, and P.E. Murray. As-Run Thermal Analysis for the UCSB-1 Experiment in the Advanced Test Reactor. Technical report, 2015.

[287] J.W. Nielsen. As-Run Physics Analysis for the UCSB–1 Experiment in the Advanced Test Reactor. (September), 2015.

[288] L. Beck, Y. Serruys, S. Miro, P. Trocellier, E. Bordas, F. Leprêtre, D. Brimbal, T. Loussouarn, H. Martin, S. Vaubaillon, S. Pellegrino, and D. Bachiller-Perea. Ion irradiation and radiation effect characterization at the JANNUS-Saclay triple beam facility. *Journal of Materials Research*, 30(9):1183–1194, 2015.

[289] M. Bachhav, G.R. Odette, and E.A. Marquis. Clustering and Radiation Induced Segregation in Neutron Irradiated Fe-(3-18)Cr Alloys. *Microscopy and Microanalysis*, 21(S3):581–582, 2015.

[290] F. Bachmann, Ralf Hielscher, and Helmut Schaeben. Texture Analysis with MTEX - Free and Open Source Software Toolbox. *Solid State Phenomena*, 160:63–68, 2010.

[291] G. M. Pharr and W. C. Oliver. Measurement of Thin Film Mechanical Properties Using Nanoindentation. *MRS Bulletin*, 17(7):28–33, 1992.

[292] J.F. Nye. *Physical Properties of Crystals: Their Representation by Tensors and Matrices*. Oxford University Press, 1985.

[293] J.J. Adams, D.S. Agosta, R.G. Leisure, and H. Ledbetter. Elastic constants of monocrystal iron from 3 to 500 K. *Journal of Applied Physics*, 100(11), 2006.

[294] L. Yao, B. Gault, J.M. Cairney, and S.P. Ringer. On the multiplicity of field evaporation events in atom probe: A new dimension to the analysis of mass spectra. *Philosophical Magazine Letters*, 90(2):121–129, 2010.

[295] J.M. Hyde, M.G. Burke, B. Gault, D.Wf. Saxey, P. Styman, K.B. Wilford, and T.J. Williams. Atom probe tomography of reactor pressure vessel steels: An analysis of data integrity. *Ultramicroscopy*, 111(6):676–682, 2011.

[296] Y. Dong, A. Etienne, A. Frolov, S. Fedotova, K. Fujii, K. Fukuya, C. Hatzoglou, E. Kuleshova, K. Lindgren, A. London, A. Lopez, S. Lozano-perez, Y. Miyahara, Y. Nagai, K. Nishida, B. Radiguet, D.K. Schreiber, N. Soneda, M. Thuvander, T. Toyama, J. Wang, F. Sefta, P. Chou, and E.A. Marquis. Atom Probe Tomography Interlaboratory Study on Clustering Analysis in Experimental Data Using the Maximum Separation Distance Approach. *Microscopy and Microanalysis*, pages 1–11, 2019.

[297] E.A. Jaegle, P-P. Choi, and D. Raabe. The Maximum Separation Cluster Analysis Algorithm for Atom-Probe Tomography: Parameter Determination and Accuracy. *Microscopy and Microanalysis*, 20(6):1662–1671, 2014.

[298] J.M. Hyde, E.A. Marquis, K.B. Wilford, and T.J. Williams. A sensitivity analysis of the maximum separation method for the characterisation of solute clusters. *Ultramicroscopy*, 111(6):440–447, 2011.

[299] Z. Peng, F. Vurpillot, P.P. Choi, Y. Li, D. Raabe, and B. Gault. On the detection of multiple events in atom probe tomography. *Ultramicroscopy*, 189:54–60, 2018.

[300] J. Chen, N. Gao, P. Jung, and T. Sauvage. A new mechanism of loop formation and transformation in bcc iron without dislocation reaction. *Journal of Nuclear Materials*, 441(1-3):216–221, 2013.

[301] S.J. Zinkle and B.N. Singh. Microstructure of neutron-irradiated iron before and after tensile deformation. *Journal of Nuclear Materials*, 351(1-3):269–284, jun 2006.

[302] E.R. Reese, N. Almirall, T. Yamamoto, S. Tumey, G.R. Odette, and Emmanuelle A. Marquis. Dose rate dependence of Cr precipitation in an ion-irradiated Fe-18Cr alloy. *Scripta Materialia*, 146:213–217, 2018.

[303] Z. Jiao, V. Shankar, and G.S. Was. Phase stability in proton and heavy ion irradiated ferritic-martensitic alloys. *Journal of Nuclear Materials*, 419(1-3):52–62, 2011.

[304] Z. Jiao and G.S. Was. Segregation behavior in proton- and heavy-ion-irradiated ferritic-martensitic alloys. *Acta Materialia*, 59(11):4467–4481, jun 2011.

[305] M. Bachhav, G.R. Odette, and E.A. Marquis. Microstructural changes in a neutron-irradiated Fe-15 at.%Cr alloy. *Journal of Nuclear Materials*, 454(1):381–386, 2014.

[306] V. Kuksenko, C. Pareige, and P. Pareige. Intra granular precipitation and grain boundary segregation under neutron irradiation in a low purity Fe-Cr based alloy. *Journal of Nuclear Materials*, 425(1-3):125–129, 2012.

[307] C. Domain and C. S. Becquart. Diffusion of phosphorus in α-Fe: An ab initio study. *Physical Review B - Condensed Matter and Materials Physics*, 71(21):1–13, 2005.

[308] E. Meslin, C.C. Fu, A. Barbu, F. Gao, and F. Willaime. Theoretical study of atomic transport via interstitials in dilute Fe-P alloys. *Physical Review B - Condensed Matter and Materials Physics*, 75(9):1–8, 2007.

[309] E. Vincent, C. S. Becquart, and C. Domain. Ab initio calculations of self-interstitial interaction and migration with solute atoms in bcc Fe. *Journal of Nuclear Materials*, 359(3):227–237, 2006.

[310] P.J. Maziasz. Formation and stability of radiation-induced phases in neutron-irradiated austenitic and ferritic steels. *Journal of Nuclear Materials*, 169(C):95–115, 1989.

[311] F. Bergner, A. Ulbricht, and C. Heintze. Estimation of the solubility limit of Cr in Fe at 300 C from small-angle neutron scattering in neutron-irradiated Fe-Cr alloys. *Scripta Materialia*, 61(11):1060–1063, 2009.

[312] R.G. Faulkner, N.C. Waite, E.A. Little, and T.S. Morgan. Radiation-induced grain boundary segregation in dilute alloys. *Materials Science and Engineering: A*, 171(1-2):241–248, 1993.

[313] J.P. Wharry, Z. Jiao, V. Shankar, J.T. Busby, and G.S. Was. Radiation-induced segregation and phase stability in ferritic-martensitic alloy T 91. *Journal of Nuclear Materials*, 417(1-3):140–144, 2011.

[314] J.P. Wharry, Z. Jiao, and G.S. Was. Application of the inverse Kirkendall model of radiation-induced segregation to ferritic-martensitic alloys. *Journal of Nuclear Materials*, 425(1-3):117–124, 2012.

[315] S. Choudhury, L. Barnard, J.D. Tucker, T.R. Allen, B.D. Wirth, M. Asta, and D. Morgan. Ab-initio based modeling of diffusion in dilute bcc Fe-Ni and Fe-Cr alloys and implications for radiation induced segregation. *Journal of Nuclear Materials*, 411(1-3):1–14, apr 2011.

[316] Z. Lu, R.G. Faulkner, G. Was, and B.D. Wirth. Irradiation-induced grain boundary chromium microchemistry in high alloy ferritic steels. *Scripta Materialia*, 58(10):878–881, may 2008.

[317] ISO. ISO 6507-1:2005(E) Metallic materials - Vickers hardness test. Technical report, 2005.

[318] S. Pathak, D. Stojakovic, R. Doherty, and S.R. Kalidindi. Importance of surface preparation on the nano-indentation stress-strain curves measured in metals. *Journal of Materials Research*, 24(3):1142–1155, 2009.

[319] J.P Wharry, K.H. Yano, and P.V. Patki. Intrinsic-extrinsic size effect relationship for micromechanical tests. *Scripta Materialia*, 162:63–67, 2019.

[320] E.M. Grieveson. *Micromechanical Testing Of Fusion Reactor Materials*. Part ii thesis, University of Oxford, 2010.

[321] D.A. Porter and K.E. Easterling. Phase Transformations in Metals and Alloys. 1981.

[322] X. Zhang, R. Takahashi, T. Akiyama, and J. Yagi. Carburization Rate into Solid Iron at CO-CO2 Atmosphere. *Tetsu-to-Hagane*, 83(5):299–304, 1997.

[323] J. Schindelin, I. Arganda-Carreras, E. Frise, V. Kaynig, M. Longair, T. Pietzsch, S. Preibisch, C. Rueden, S. Saalfeld, B. Schmid, J.Y. Tinevez, D.J. White, V. Hartenstein, K. Eliceiri, P. Tomancak, and A. Cardona. Fiji: An open-source platform for biological-image analysis. *Nature Methods*, 9(7):676–682, 2012.

[324] W.D. Callister Jr. and D.G. Rethwisch. *Materials Science and Engineering: An Introduction*. Wiley, 7 edition, 2007.

[325] J.M. Moehlis. Solution of the diffusion equation by finite differences. https://me.ucsb.edu/˜moehlis/APC591/tutorials/tutorial5/node3.html, 2001.

[326] J. Sauvola and M. Pietikäinen. Adaptive document image binarization. *Pattern Recognition*, 33(2):225–236, 2000.

[327] SciPy - scipy.interpolate.interp1d - https://docs.scipy.org/doc/scipy-0.13.0/reference/generated/scipy.interpolate.interp1d.html.

[328] W. Sha, L. Chang, G. D W Smith, Liu Cheng, and E. J. Mittemeijer. Some aspects of atom-probe analysis of FeC and FeN systems. *Surface Science*, 266(1-3):416–423, 1992.

[329] J. Takahashi, K. Kawakami, K. Ushioda, S. Takaki, N. Nakata, and T. Tsuchiyama. Quantitative analysis of grain boundaries in carbon- and nitrogen-added ferritic steels by atom probe tomography. *Scripta Materialia*, 66(5):207–210, mar 2012.

[330] H.S. Kitaguchi, S. Lozano-Perez, and M.P. Moody. Quantitative analysis of carbon in cementite using pulsed laser atom probe. *Ultramicroscopy*, 147:51–60, dec 2014.

[331] M. Thuvander, A. Kvist, L.J.S. Johnson, J. Weidow, and H-O. Andrén. Reduction of multiple hits in atom probe tomography. *Ultramicroscopy*, 132:81–85, sep 2013.

[332] G.E. Valley and H.H. Anderson. A Comparison of the Abundance Ratios of the Isotopes of Terrestrial and of Meteoritic Iron. *Journal of the American Chemical Society*, 69(8):1871–1875, 1947.

[333] Y. Kobayashi, J. Takahashi, and K. Kawakami. Anomalous distribution in atom map of solute carbon in steel. *Ultramicroscopy*, 111(6):600–603, 2011.

[334] J. Takahashi, K. Kawakami, and Y. Kobayashi. Quantitative analysis of carbon content in cementite in steel by atom probe tomography. *Ultramicroscopy*, 111(8):1233–1238, 2011.

[335] M. Thuvander, J. Weidow, J. Angseryd, L.K.L. Falk, F. Liu, M. Sonestedt, K. Stiller, and H.-O. Andrén. Quantitative atom probe analysis of carbides. *Ultramicroscopy*, 111(6):604–608, may 2011.

[336] M.J. van Genderen, S.J. Sijbrandij, A. Böttger, E.J. Mittemeijer, and G.D.W. Smith. Atomprobe analysis of initial decomposition of Fe-N martensite. *Materials Science and Technology*, 13(10):806–812, 1997.

[337] B. Gault, F. Danoix, K. Hoummada, D. Mangelinck, and H. Leitner. Impact of directional walk on atom probe microanalysis. *Ultramicroscopy*, 113:182–191, 2012.

[338] L. Yao, J.M. Cairney, C. Zhu, and S.P. Ringern. Optimisation of specimen temperature and pulse fraction in atom probe microscopy experiments on a microalloyed steel. *Ultramicroscopy*, 111(6):648–651, 2011.

[339] I. Cornides and L. Morvay. Investigation of the evaporation of graphite in high-voltage vacuum discharge: The formation mechanism of carbon clusters. *Rapid Communications in Mass Spectrometry*, 6(12):758–759, 1992.

[340] A. Kasuya and Y. Nishina. Transient chemical forms of molecular ions emitted from a graphite surface by N2 laser excitation. *Physical Review B*, 28(11):6571–6574, 1983.

[341] H. Hogreve. Ab initio study of the dication carbon trimer C32+. *The Journal of Chemical Physics*, 102(8):3281–3291, 1995.

[342] D.G. Brandon. Resolution Of Atomic Structure - Recent Advances In Theory And Development Of Field Ion Microscope. *British Journal of Applied Physics*, 14(8):474, 1963.

[343] S.C. Wang and T.T. Tsong. Field and temperature dependence of the directional walk of single adsorbed W atoms on the W(110) plane. *Physical Review B*, 26(12):6470–6475, 1982.

[344] C. Lerchbacher, S. Zinner, and H. Leitner. Atom probe study of the carbon distribution in a hardened martensitic hot-work tool steel X38CrMoV5-1. *Micron*, 43(7):818–826, 2012.

[345] J.B. Seol, B.H. Lee, P. Choi, S.G. Lee, and C.G. Park. Combined nano-SIMS/AFM/EBSD analysis and atom probe tomography, of carbon distribution in austenite/ϵ-martensite high-Mn steels. *Ultramicroscopy*, 132:248–257, 2013.

[346] P.J. Felfer, B. Gault, G. Sha, L. Stephenson, S.P. Ringer, and J.M. Cairney. A new approach to the determination of concentration profiles in atom probe tomography. *Microscopy and Microanalysis*, 18(2):359–364, 2012.

[347] K.L. Murty. Interstitial-impurity radiation-defect interactions in ferritic steels. *JOM*, (October):34–39, 1985.

[348] E.A. Little and D.R. Harries. Radiation-Hardening and Recovery in Mild Steels and the Effects of Interstitial Nitrogen. *Metal Science Journal*, 4(1):188–195, jan 1970.

[349] D.H. Jack and K.H. Jack. Invited review: Carbides and nitrides in steel. *Materials Science and Engineering*, 11(1):1–27, jan 1973.

[350] A. Morley, G. Sha, S. Hirosawa, A. Cerezo, and G.D.W. Smith. Determining the composition of small features in atom probe: bcc Cu-rich precipitates in an Fe-rich matrix. *Ultramicroscopy*, 109(5):535–540, 2009.

[351] N. Hashimoto, S. Sakuraya, J. Tanimoto, and S. Ohnuki. Effect of impurities on vacancy migration energy in Fe-based alloys. *Journal of Nuclear Materials*, 445(1-3):224–226, feb 2014.

[352] C. Barouh, T. Schuler, C.C. Fu, and M. Nastar. Interaction between vacancies and interstitial solutes (C, N, and O) in α- Fe: From electronic structure to thermodynamics. *Physical Review B - Condensed Matter and Materials Physics*, 90(5):1–20, 2014.

[353] B. Langelier, H.P. Van Landeghem, G.A. Botton, and H.S. Zurob. Interface Segregation and Nitrogen Measurement in Fe-Mn-N Steel by Atom Probe Tomography. *Microscopy and Microanalysis*, 23(2):385–395, 2017.

[354] J.T. Busby, M.C. Hash, and G.S. Was. The relationship between hardness and yield stress in irradiated austenitic and ferritic steels. *Journal of Nuclear Materials*, 336(2-3):267–278, 2005.

[355] P. Dubuisson, D. Gilbon, and J.L. Séran. Microstructural evolution of ferritic-martensitic steels irradiated in the fast breeder reactor Phénix. *Journal of nuclear materials*, 205:178–189, 1993.

[356] J. Král and J. Zemek. Carbon contamination of ion implanted layers. *Vacuum*, 36:555–557, 1986.